

# AN HBT MAGNETIC SENSOR WITH INTEGRATED 3-DIMENSIONAL MAGNETIC STRUCTURES

A THESIS SUBMITTED TO  
THE DEPARTMENT OF ELECTRONICS AND ELECTRICAL ENGINEERING  
FACULTY OF ENGINEERING  
UNIVERSITY OF GLASGOW  
IN FULFILMENT OF THE REQUIREMENTS  
FOR THE DEGREE OF  
DOCTOR OF PHILOSOPHY

By  
Richard K. Oxland  
April 2009

© Richard K. Oxland 2009  
All Rights Reserved

In my line of work, the laws of physics rarely seem to apply.

Fox Mulder, *Special Agent, FBI.*

# Abstract

The applicability and functionality of high frequency digital and millimetre wave circuits can be enhanced by the integration of sensor elements into the circuits. It is furthermore advantageous to utilise or modify the pre-existing fabrication process flow in creating this added functionality. This thesis describes a work on magnetic field sensors based on an InP/InGaAs heterojunction bipolar transistor (HBT) which has been fabricated to be compatible with high frequency epilayer structure and processes.

In this work, the complete fabrication process for the HBT magnetic sensors has been developed, using standard, transferrable process modules. Ohmic contact metallisations were optimised and D.C. electrical characterisations are also reported upon. The effects of several surface treatments on device performance have been studied and characterised. Surface passivation using two distinct sulphur containing compounds of different phases was shown to enhance performance and an ion bombardment process was developed that degraded surface quality and increased surface leakage currents for enhanced sensor performance.

In order to improve the sensitivity of an HBT to magnetic field 3-dimensional magnetic structures were designed to be incorporated onto the surface of the extrinsic base. This design process was informed by simulation of magnetic field profiles of the magnetic elements and fabrication processes were created that would allow for arbitrary 3-dimensional structures.

The response to magnetic field applied both parallel and perpendicular to the normal of the wafer of an as-fabricated HBT was investigated. Two different emitter structures were compared, a simple square emitter and a multiple finger emitter, and the ability of the devices to resolve applied field angle was uncovered. The effects of device bias on the field response was also looked at and the optimal bias conditions determined. An analysis of the temperature variation of the magnetic field response was conducted with lower temperatures resulting in higher sensitivity to applied field.

Finally, the response of an HBT with integrated 3-dimensional magnetic structures was investigated. A passivated device was found to be less sensitive to applied magnetic field and a device treated with ion bombardment to be more sensitive to magnetic field applied parallel to the normal. The signal to noise ratio for an HBT with integrated magnetic structures was 36.4 dB with an equivalent noise of 0.002 T. The maximum magnetic field strength sensitivity was  $0.339 \text{ T}^{-1}$  and the maximum magnetic field applied angle sensitivity was  $0.119 \text{ rad}^{-1}$ . The maximum change in normalised D.C. current gain was 0.019. A mathematical description of the change in current gain caused by a given

magnetic field applied at a given angle was also determined.

# Publications

The peer-reviewed publications arising from the work done in completion of this thesis are listed below.

R. K. OXLAND AND F. RAHMAN (2007), *Technology for an HBT Magnetic Sensor with Integrated 3-D Magnetic Structures*, Compound Semiconductors UK, Sheffield, UK, D01.

R. K. OXLAND AND F. RAHMAN (2008), *Magnetic Field Sensors Based on Charge Transport in Indium Phosphide Heterojunction Bipolar Transistors*, UK Semiconductors, Sheffield, UK, D04.

R. K. OXLAND AND F. RAHMAN (2008), *Fluid Phase Passivation and Polymer Encapsulation of InP/InGaAs Heterojunction Bipolar Transistors*, Semiconductor Science and Technology, **23**(8), 085020–6.

R. K. OXLAND, A. R. LONG AND F. RAHMAN (accepted for publication, 2009), *Magnetotransport Characterization of Surface-treated InP/InGaAs Heterojunction Bipolar Transistors*, Microelectronics Engineering.

R. K. OXLAND, G. W. PATERSON, A. R. LONG AND F. RAHMAN (under review), *Indium Phosphide Heterojunction Bipolar Transistors as Magnetic Field Sensors*, IEEE Transactions on Electronic Devices.

R. K. OXLAND, G. W. PATERSON, A. R. LONG AND F. RAHMAN (in progress), *Magnetotransport and Magnetic Field Sensing with Ferromagnet-Bipolar Transistor Hybrid Devices*.

# Acknowledgements

Thanks must go primarily to my supervisor, Faiz Rahman, whose initial ideas prompted this work. His knowledge and his focus on the end product and his engineering solutions helped immeasurably in my transition from graduate physicist to postgraduate engineer as well as in the successful completion of the project.

Of course my family receives the most hearty ‘thank you’; I am indebted to their unwavering support and was constantly buoyed by their confidence in me.

I must also mention Doctors Harold Chong, Corrie Farmer, Richard Hill and David Moran in the Department of Electronics and Electrical Engineering for gladly transferring to me that knowledge they possessed that I required. Needless to say this was ever done with patience and in good humour. The smooth running of the facilities provided for me by the Department is a credit to those academic and technical staff who work very hard at it. I’m thinking particularly of the James Watt Nanofabrication Centre, where most of this work was undertaken. The Solid State Physics Group in the Department of Physics was kind enough to give me the use of some of their test and measurement equipment. Equally important (if not more so) was the expertise and time which Doctor Gary Paterson (Physicist) was able to donate to help me towards my goals and for that I am very grateful indeed.

The highlight of every day in the Department is undoubtedly lunchtime, where relief from the often solitary pursuit of a Ph.D. comes with hours of laughter with Dave, Rich, Griogair, Steven and Kevin, as it once did with Paul, Ed, Anna and others. Would that we could still share it with Simon Triger.

Finally my friends, flatmates, acquaintances and accomplices, for whose continued company I would endure a working life somewhat less gratifying than I do today (well, probably), who have entertained me and shared my most enjoyable experiences, I salute you.

# Contents

<b>1</b>	<b>Introduction</b>	<b>1</b>
1.1	History . . . . .	1
1.2	The InP Material System . . . . .	3
1.3	Advantages of HBTs . . . . .	4
1.4	High Frequency HBTs . . . . .	6
1.5	Sensor Technologies . . . . .	8
<b>2</b>	<b>The Bipolar Junction Transistor</b>	<b>12</b>
2.1	P–n Junctions . . . . .	12
2.2	Bipolar Junction Transistors . . . . .	20
2.2.1	Ideal Operational Characteristics . . . . .	24
2.2.2	Deviations from Ideal . . . . .	26
2.3	Heterojunctions . . . . .	29
2.4	Heterojunction Bipolar Transistors . . . . .	30
2.5	The Hall Effect in Semiconductors . . . . .	33
2.6	Figures of Merit for Transistor Magnetic Sensors . . . . .	35
2.7	Charge Transport and Magnetic Field. . . . .	35
<b>3</b>	<b>HBT Fabrication</b>	<b>41</b>
3.1	Wafer Epilayer Structure . . . . .	41
3.2	Fabrication Processes . . . . .	44
3.2.1	Sample Preparation . . . . .	44
3.2.2	Lithography . . . . .	44
3.2.3	Metallisation . . . . .	47
3.2.4	Etching . . . . .	48

3.2.5	Thin Film Deposition . . . . .	.49
3.2.6	Bonding. . . . .	.50
3.3	Ohmic Contacts . . . . .	.51
3.4	HBT Process Flow . . . . .	.55
3.5	Design Considerations . . . . .	.58
3.6	Device Testing . . . . .	.60
3.6.1	In-line Testing . . . . .	.60
3.6.2	End-of-line Testing . . . . .	.64
<b>4</b>	<b>Semiconductor Surface Effects</b>	<b>69</b>
4.1	Semiconductor Surfaces . . . . .	.69
4.1.1	Work Function . . . . .	.69
4.1.2	Surface Space-Charge . . . . .	.70
4.1.3	Surface States . . . . .	.73
4.1.4	Equilibrium and Non-equilibrium Surface Carrier Conditions. . . . .	.75
4.2	Plasma Processing . . . . .	.78
4.3	Passivation of Semiconductor Surfaces . . . . .	.79
4.4	Lattice Defects. . . . .	.81
4.4.1	Dislocations . . . . .	.81
4.4.2	Point Defects. . . . .	.82
4.5	Experimental Results . . . . .	.82
4.5.1	Ammonium Sulphide. . . . .	.83
4.5.2	Gas Phase Sulphur . . . . .	.83
4.5.3	Ion Bombardment of Semiconductor Surface . . . . .	.87
<b>5</b>	<b>Magnetic Materials and Structures</b>	<b>90</b>
5.1	Magnetism . . . . .	.90
5.2	Classification of Magnetic Materials . . . . .	.91
5.2.1	Ferromagnetism. . . . .	.92
5.2.2	Paramagnetism and Diamagnetism . . . . .	.93
5.3	Origins of Magnetic Effects . . . . .	.94
5.3.1	Microscopic Magnetism. . . . .	.94
5.3.2	Magnetic Domains . . . . .	.95

5.4	Applications of Magnetic Materials . . . . .	.96
5.5	Design of 3-D Structures . . . . .	.97
5.5.1	Cross-sectional Design . . . . .	.98
5.5.2	Material Choice . . . . .	102
5.5.3	Base Volume Analysis . . . . .	102
5.6	Fabrication of 3-D Magnetic Structures . . . . .	106
<b>6</b>	<b>HBTs in Magnetic Field</b>	<b>111</b>
6.1	Experimental Setup . . . . .	111
6.2	Calibrating the Applied Magnetic Field Intensity . . . . .	114
6.3	Experimental Results . . . . .	118
6.3.1	Measurement of Mobility . . . . .	118
6.3.2	An LA-HBT in Magnetic Field . . . . .	121
6.3.3	An MEF-HBT in Magnetic Field . . . . .	124
6.3.4	Effect of Bias Conditions . . . . .	127
6.3.5	Low Temperature Parallel Field Dependence . . . . .	132
<b>7</b>	<b>HBTs as Magnetic Field Sensors</b>	<b>135</b>
7.1	HBT Sensitivity . . . . .	135
7.2	Surface Treated Sensors . . . . .	137
7.3	Integrated Magnetic Structures . . . . .	139
7.4	Sensor Noise and Dynamic Range . . . . .	143
7.5	HBT Sensor Calibration . . . . .	144
<b>8</b>	<b>Conclusions</b>	<b>149</b>
	<b>Appendix</b>	<b>154</b>
	<b>References</b>	<b>161</b>

# List of Tables

1.1	Semiconductor material properties . . . . .	4
1.2	Figures of merit for several magnetotransistors . . . . .	10
2.1	Heterojunction bandgap offsets . . . . .	30
3.1	InGaAs/InP Wafer Structure . . . . .	42
3.2	Diode ideality factors . . . . .	63
3.3	Variation in $\beta_{dc}$ across a sample . . . . .	66
3.4	Typical HBT parameters . . . . .	67
5.1	Results of magnetic structure simulation . . . . .	102
5.2	Results of magnetic structure material simulation . . . . .	103
5.3	Total flux densities over the base area (perpendicular field) . . . . .	106
5.4	Total flux densities over the base area (parallel field) . . . . .	108
6.1	Relative change in the electromagnet in consecutive sweeps . . . . .	117
6.2	DC r.m.s noise and device bias . . . . .	131
7.1	Current gain magnetic field sensitivity for an MEF-HBT. . . . .	136
7.2	Magnetic field angle sensitivity for an MEF-HBT. . . . .	136
7.3	Relative strengths of the field effects . . . . .	137
7.4	Noise data before and after surface treatment . . . . .	138
7.5	Equivalent noise . . . . .	144
7.6	Signal-to-noise ratio . . . . .	145

# List of Figures

1.1	The Lorentz force . . . . .	8
1.2	Silicon BMT designs . . . . .	9
2.1	A 1-D p-n junction. . . . .	13
2.2	Electrostatics of a 1-D p-n junction . . . . .	14
2.3	1-D p-n junction energy bands . . . . .	15
2.4	P-n junction under forward bias. . . . .	17
2.5	P-n junction under reverse bias . . . . .	19
2.6	Diode I-V characteristics . . . . .	19
2.7	BJT bands and schematic . . . . .	21
2.8	Common emitter and common base configurations . . . . .	24
2.9	Ideal and real BJT common base characteristics . . . . .	27
2.10	Ideal and real BJT common base characteristics . . . . .	27
2.11	An example HBT band structure . . . . .	29
2.12	Hall effect . . . . .	34
2.13	Electrons accelerated in a circular path by magnetic field. . . . .	37
3.1	HBT band diagram . . . . .	43
3.2	Ohmic contact TLM metallisation . . . . .	51
3.3	P-type contact leakage measurement metallisation . . . . .	52
3.4	Contact resistance of annealed n-type metallisation . . . . .	53
3.5	Contact resistance of annealed p-type metallisation . . . . .	53
3.6	Leakage current of annealed, isolated p-type metallisation . . . . .	54
3.7	Alignment marks. . . . .	56
3.8	HBT mesa with metal contacts . . . . .	57
3.9	Completed HBT . . . . .	58

3.10	HBTs bonded into an LCC. . . . .	.59
3.11	A section of the HBT layout file. . . . .	.59
3.12	In-line testing cell . . . . .	.60
3.13	HBT mesa surface profile . . . . .	.61
3.14	Base-emitter junction diode I-V . . . . .	.62
3.15	Base-collector junction diode I-V . . . . .	.62
3.16	HBT common emitter I-V . . . . .	.64
3.17	HBT common base I-V . . . . .	.65
3.18	HBT $BV_{cb0}$ measurement . . . . .	.65
3.19	HBT $\beta_{dc}$ against $I_c$ . . . . .	.66
4.1	Surface band diagrams . . . . .	.73
4.2	Current gain of an HBT passivated with $(NH_4)_2S$ . . . . .	.83
4.3	Deterioration of the $(NH_4)_2S$ passivation effects on an HBT. . . . .	.84
4.4	Current gain of an HBT passivated with $H_2S$ . . . . .	.85
4.5	Deterioration of the $H_2S$ passivation effects on an HBT . . . . .	.86
4.6	Reverse leakage current before and after $Ar^+$ treatment . . . . .	.88
4.7	Current gain before and after $Ar^+$ treatment. . . . .	.88
5.1	A typical hysteresis loop . . . . .	.92
5.2	Placement of magnetic structures . . . . .	.98
5.3	Effect of 3-D magnetic structure . . . . .	.99
5.4	Design flow for simulation of magnetic structures . . . . .	100
5.5	Magnetic structure simulation . . . . .	101
5.6	Plot of magnetic structure simulation results. . . . .	101
5.7	Magnetic structure material simulations. . . . .	103
5.8	Perpendicular field component over the base area (perpendicular field) . . . . .	104
5.9	Parallel field component over the base area (perpendicular field) . . . . .	105
5.10	Perpendicular field component over the base area (parallel field) . . . . .	107
5.11	Parallel field component over the base area (parallel field) . . . . .	107
5.12	A test 3-D magnetic structure . . . . .	109
5.13	SEM of 3-D magnetic structure integrated onto an HBT . . . . .	109
5.14	Surface profile of 3-D magnetic structure integrated onto an HBT . . . . .	110

6.1	Magnetic field experimental setup . . . . .	112
6.2	Common-base current measurement configuration . . . . .	113
6.3	LabVIEW program process flow . . . . .	114
6.4	Electromagnet supply output . . . . .	115
6.5	Electromagnet calibration data and polynomial fit . . . . .	116
6.6	Electromagnet calibration fit oscillation test . . . . .	116
6.7	Electromagnet rotation calibration . . . . .	118
6.8	Emitter configuration of an LA-HBT . . . . .	119
6.9	Emitter configuration of an MEF-HBT . . . . .	119
6.10	Magnetotransport mobility for an LA-HBT . . . . .	120
6.11	Magnetotransport dependence on $I_e$ . . . . .	121
6.12	An LA-HBT in a parallel magnetic field . . . . .	122
6.13	An LA-HBT in a perpendicular magnetic field . . . . .	122
6.14	Noise measurement for an LA-HBT . . . . .	123
6.15	Applied field angle response of an LA-HBT . . . . .	124
6.16	Curves fitted to the magnetic field response of an LA-HBT . . . . .	125
6.17	An MEF-HBT in a parallel magnetic field . . . . .	125
6.18	An MEF-HBT in a perpendicular magnetic field . . . . .	126
6.19	Applied field angle response of an MEF-HBT . . . . .	126
6.20	Curves fitted to the magnetic field response of an MEF-HBT . . . . .	127
6.21	Device to device variation . . . . .	128
6.22	Response of an HBT to variation of $V_{cb}$ . . . . .	128
6.23	Response of an HBT to variation of $I_e$ for $\theta = 90^\circ$ . . . . .	129
6.24	Response of an HBT to variation of $I_e$ for $\theta = 0$ . . . . .	130
6.25	Magnetic field response of an MEF-HBT for all angles . . . . .	131
6.26	Magnetic field angle response of an MEF-HBT under optimum bias . . . . .	132
6.27	Base current against temperature . . . . .	133
6.28	Magnetic response at different temperatures . . . . .	134
7.1	Response of an HBT to parallel magnetic field before and after argon treatment . . . . .	138
7.2	Response of an HBT to parallel magnetic field before and after passivation . . . . .	139
7.3	A bipolar transistor differential pair amplifier . . . . .	140

7.4	Magnetic response of an HBT with and without magnetic structures . . .	141
7.5	Increase in response of an MEF–HBT with integrated magnetic structures .	141
7.6	Magnetic field angle response of an HBT with magnetic structures under optimum bias . . . . .	142
7.7	Angle response of an HBT with and without magnetic structures . . . .	143
7.8	An HBT ring oscillator circuit . . . . .	143
7.9	Perpendicular magnetic field response and fitted curve . . . . .	145
7.10	Magnetic field response for all angles and fitted curves . . . . .	146
7.11	Polynomial coefficients for an MEF–HBT . . . . .	147
7.12	Polynomial coefficients for an MEF–HBT with integrated 3–D magnetic structures. . . . .	147

# 1 Introduction

Sensors for magnetic fields have many existing and potential future applications. Small solid state sensors are continuing to improve the performance of systems into which they are embedded. This work shows that it is possible to utilise the basic technology of the indium phosphide (InP) heterojunction bipolar transistor (HBT) and couple it with high magnetic permeability thin film materials to build a magnetic field sensor. There is an existing and growing market for such devices in motion sensing, such as rotary motion sensors, and pattern sensing, as in magnetic card readers, as well as in other applications.

There follows in this chapter a discussion of the context of the work, including HBT technologies and previous work on the physical phenomena that allowed magnetic field transduction. The second chapter deals with the underlying concepts of bipolar transistor operation and the third describes the fabrication procedures employed and the results of HBT electrical characterisation. The fourth and fifth chapters detail some theory and the experimental work which was carried out to research ways of enhancing the operation of the magnetic field sensors, with surface modification treatments (Chapter 4) and integration of 3-dimensional magnetic structures (Chapter 5). The two following chapters contain the experimental results of the measurement of response to magnetic field, firstly of the native HBT in Chapter 6 and then of the surface treated, integrated, HBT magnetic field sensor in Chapter 7. The final chapter contains some summary and a discussion of future work that might be conducted.

## 1.1 History

Bardeen and Brattain invented the transistor in 1948. Made from a small block of germanium, it was posited as a scalable and reliable replacement for the vacuum tubes in use at the time[1]. The germanium was prepared in such a way that it was bulk doped n-type. The authors theorised that p-type surface states at the collector and emitter point contacts lead to minority carrier current transport through the bulk, which, in their experimental arrangement, constituted the base. Both the collector-base and emitter-base junctions were observed to form a diode, or rectifier. Thus the modern electronic

era was born. By the dawn of the twenty-first century, annual transistor production was of the order of  $10^{17}$ [2].

The same year transistors were invented,<sup>1</sup> the concept of a wider bandgap emitter–base junction in a transistor was proposed by Shockley in a US Patent: “a device...in which one of the separated zones is of a semiconductive material having a wider energy gap than that of the material in the other zones” [3]. However, the technology—in terms of the ability to grow complex, lattice matched layer structures—did not exist to take advantage of the proposed benefits of heterostructures until the nineteen-seventies[4, 5].

Only at that time could the theoretical predictions of a marked increase in  $\beta_{dc}$  values be realised (studies have achieved DC current gains of the order  $10^5$ [6]). Along with increased gain, a decrease in base resistance and a smaller base–emitter capacitance was possible through higher dopant concentrations in the base and lower concentrations in the emitter. These devices employed liquid phase epitaxy (LPE) to grow the epilayer structures[7, 8]. Early research showed that the low density of interface recombination sites in epitaxially grown GaAs–AlGaAs heterojunctions made it the ideal material system in which to fabricate heterojunction bipolar transistors (HBTs). It was also noted, as device fabrication began to be realised, that HBTs held benefits in terms of higher power output capabilities[9]. It was predicted at that point (by the then–future Nobel Laureate Herbert Kroemer) that the use of HBTs would become more widespread, and that, as the cost of manufacture dropped, the number of applications where HBTs were not used would also fall[10]. Kroemer suggested that in the microwave industry, the incumbent FET technology would eventually be superseded by RF HBT devices, a claim borne out by the fabrication of HBTs with operating frequencies over 500 GHz in recent years[11, 12]. The advent of the growth technologies *molecular beam epitaxy* (MBE) and *metal organic chemical vapour deposition* (MOCVD) caused research in the field to increase markedly[13]. MBE was developed at the end of the sixties to study surface kinetics, but within ten years was one of the most versatile tools in device fabrication[14]. MOCVD–grown HBTs were reported by 1979[15].

The majority of the focus of HBT research since this milestone has been on optimisation for high speed applications, outwith the scope of this project, however, a brief discussion of this important topic can be found below.

---

<sup>1</sup>The patent in question was actually filed in 1948, although it wasn’t issued until 1951.

## 1.2 The InP Material System

When MBE technology advanced sufficiently to make HBT fabrication a realistic possibility it was the III–V material system that was the first choice. Not only is MBE growth more easily achieved with III–Vs[16] but the potential performance increases were also very significant.

Indium phosphide substrates (and hence any epiwafers produced in the InP material system) are more expensive than those of gallium arsenide and much more expensive than silicon. Since GaAs-based materials were the original and established technology for fabricating III–V HBTs and HBT-based circuits, the suitability of InP had to be proven. The wafer size of InP production is also smaller than GaAs with 4 inch wafers being the norm (GaAs wafers are usually 6 inches or larger). Gallium arsenide has also been grown on silicon wafers with an eye on the integration of heterostructure and CMOS devices and also cost reduction[17].

One of the main advantages offered by InGaAs/InP and the associated InAlAs/InGaAs heterostructures is the potential speed increases offered by the higher electron velocities therein. Electron mobility is high under equilibrium conditions and the saturation velocity at high fields is also large[18]. Although ballistic transport is possible through the base of InGaAs/InP HBTs, it is only predicted to be the case for base lengths of  $\sim 10$  nm[19]. In the case of real devices which have bases longer than this, the main form of transport is diffusive, although the carriers are more energetic than thermalised electrons and are strongly susceptible to scattering. The emitter injection efficiency of InGaAs/InP HBTs is very high. The maximum current gain of abrupt emitter–base junctions and those with undoped InGaAs spacers has been shown theoretically to be  $\approx 10^5$  with base dopant levels of up to  $1 \times 10^{20} \text{ cm}^{-3}$ . Experimental results which don't match up to this are due to base recombination currents[20]. Recombination at the InGaAs surface is significantly lower than in GaAs ( $1 \times 10^3 \text{ cm s}^{-1}$  c.f.  $1 \times 10^6 \text{ cm s}^{-1}$ ). This also makes device (emitter) scaling easier.

These factors are, in part, offset by the lower breakdown voltages caused by the smaller bandgap in InGaAs compared to GaAs[21]. Since it has a low thermal conductivity, the InGaAs collector leads to high thermal resistance as well as low breakdown voltages[22]. Gallium arsenide wafers are also both mechanically and thermally more stable. The small bandgap of InGaAs makes it an ideal material for the base of an HBT: formation of low resistance contacts is readily achievable and doping need not be high, thus reducing recombination. Or, alternatively, high dopant concentrations can be employed to reduce sheet resistance without greatly affecting contact formation. The

Physical quantity	In <sub>0.53</sub> Ga <sub>0.47</sub> As	GaAs	Si
$E_g$ / eV	0.75 (direct)	1.42 (direct)	1.12 (indirect)
$\mu_n$ / cm <sup>2</sup> V <sup>-1</sup> s <sup>-1</sup>	7000	4000	800
$m_e^*$ /m <sub>0</sub>	0.041	0.067	0.26
$E_{\Gamma-L}$ / eV	0.55	0.28	—
$v_{\text{sat}}$ / cm s <sup>-1</sup>	7 x 10 <sup>6</sup>	8 x 10 <sup>6</sup>	8 x 10 <sup>6</sup>
$s$ / cm s <sup>-1</sup>	1 x 10 <sup>3</sup>	1 x 10 <sup>6</sup>	1 x 10 <sup>3</sup>
$k_{\text{th}}$ /Wcm <sup>-1</sup> K <sup>-1</sup> (substrate)	0.68	0.46	1.5

**Table 1.1:** Properties of common semiconductor material systems (at room temperature). Electron mobility values are given for moderately doped ( $N_D = 1 \times 10^{17} \text{ cm}^{-3}$ ) n-type material and the substrate material quoted for the In<sub>0.53</sub>Ga<sub>0.47</sub>As thermal conductivity is InP. (Adapted from [23].)

small bandgap also reduces the required forward voltage for switching in digital applications and hence the power consumption[18]. The high substrate thermal conductivity would help reduce self-heating in high speed circuits (see Table 1.1) and the fraction of the bandgap offset which forms an offset in the valence bands between the (wide gap) emitter and the base is also in its favour (see Table 2.1 in §2).

The energy of the direct bandgap of InGaAs is perfectly suited for the radiation in the range of 1.3 – 1.5  $\mu\text{m}$  used in optical fibres for communications and in optoelectronic integrated circuits (OEICs). This means that a photon which is emitted or absorbed does not need momentum to be transferred to or from the lattice in order that the total momentum of the event is conserved. Also, the favourable band line-up in InP-system heterojunctions can be used to impart a high kinetic energy to electrons entering the base which will reduce the base transit time and serve to increase the maximum frequency of operation[18].

### 1.3 Advantages of HBTs

#### Advantages over Silicon BJTs

In a BJT a proportion of holes will be back injected into the emitter from the base due to the forward bias of the emitter-base junction. These holes contribute a component of the base current,  $I_b$  which is deleterious to device performance as it reduces emitter injection efficiency[24]. By employing a heterojunction it is possible to deliberately introduce conditions under forward bias which promote the injection of minority carriers into the base while retarding the back injection of majority carriers with a potential barrier (particularly in the  $Npn$  regime). For an  $Npn$  HBT this requires a larger bandgap dis-

continuity in the valence band than the conduction band. Both the  $\text{Al}_{0.3}\text{Ga}_{0.7}\text{As}/\text{GaAs}$  and  $\text{In}_{0.53}\text{Ga}_{0.47}\text{As}/\text{InP}$  lattice-matched regimes (amongst others) provide this. High dopant concentrations in the emitter are thereby no longer necessary to limit back injection in the emitter-base junction.

Having relaxed constraints on dopant concentration it is then possible to design emitter, base and collector doping to minimise parasitics. The base doping is increased as far as possible; concentrations of  $1 \times 10^{20} \text{cm}^{-3}$  have been demonstrated in InGaAs[25]. This decreases the parasitic base resistance,  $R_b$ . Emitter doping is reduced, which in turn reduces minority carrier storage and hence the emitter-base capacitance,  $C_{be}$ .

Higher saturation velocities and higher electron mobilities are available in III-V materials than in silicon so base transit times are smaller (see Table 1.1). This leads to devices with faster switching times and higher maximum frequencies of operation. The semi-insulating III-V substrates also reduce the parasitic capacitances of bond pads and on-wafer interconnects[26].

However, silicon holds advantages in the available wafer size and cost, planar (implant) fabrication technologies and the quality of the native oxide-semiconductor surface interface.

### **Bipolar versus Field-effect Devices**

Although planar III-V FET devices may be considered to be simpler in design, the scaling required to reduce gate dimensions to the 50 nm dimensions demonstrated in this department[27] necessitates very costly lithographical tools to pattern the lateral structures. They also incorporate complex epitaxial layer structures, albeit with a lower overall MBE growth thickness requirement. Bipolar heterostructure devices have vertical structures which can be grown simply by using MBE or (MO)CVD to achieve similar dimensions. They can be processed in a more cost-effective manner using photolithography. This relatively large feature size may be something of an encumbrance when it comes to system-level integration but is a positive feature when it comes to power handling characteristics. The whole area of the emitter will conduct and large current densities can be achieved through the device. The heat generated in power applications is efficiently dissipated by the high thermal conductivity of the substrate material, particularly in the InP regime[26]. While CMOS is the natural choice for large scale integrated circuits (ICs), bipolar devices are to be found in many specialist applications, including high speed circuits, power amplifiers and precision analogue or mixed signal components[2].

Characteristics such as the turn-on voltage of HBT devices on a wafer are governed by the built-in potential at junction boundaries and hence, in turn, by the dopant con-

centrations of the bulk regions and the bandgap line-up of the heterointerface. This can lead to an excellent degree of uniformity of devices across the wafer and allows fabrication of paired or differential devices.

## 1.4 High Frequency HBTs

To maximise the potential of the heterostructure bipolar regime there are some considerations to incorporate into the technology. The intrinsic speed of a device is determined by the epilayer structure. Subsequent processing determines the lateral extent and the associated parasitics[28]. The device design must minimise the separation of base contacts and the edge of the emitter mesa to minimise the base access resistance. The area of the base-collector junction should also be minimised as the extrinsic base (the region of the base which is not directly underneath the emitter mesa) and collector regions contribute to a parasitic capacitance[18]. HBTs based on III-V materials are limited by the parasitic capacitance of the base-collector junction which has a larger relative effect as the emitter size is scaled down[29]. The short base length which is advantageous for high frequency operation comes with a requirement for shallow base contacts. This causes a high base resistance so the minimum necessary dimensions of the base contacts becomes a factor. Thin base layers also bring a high base-collector capacitance and a low punchthrough voltage. These reduce the maximum frequency of operation and operating voltage range.

Control over semiconductor material composition offers another degree of freedom in device design. Quasi-electric fields can be created to exert forces on the charge carriers[13]. However, the conduction band discontinuity will tend to cancel the improvement in the ratio  $\Delta E_v/\Delta E_c$  so integral to the HBT. This discontinuity can be eliminated by appropriately grading the composition of the emitter-base junction. Digital applications benefit from the low turn on voltage which results from this although ballistic electron transport in the base no longer occurs. The electron quasi-ballistic range in III-V materials is of the order of a few hundred Angstroms. This is longer in InP- than GaAs-based transistors[30]. Recombination and minority carrier storage in the vicinity of the graded region tends to increase[31]. Gradual changes in semiconductor composition can be achieved by growing short period superlattices in which the composition is alternated over a few monolayers. It is also possible by compositionally grading the base to produce an effective electric field for minority electrons which accelerates the electrons towards the collector[31].

By employing a wide bandgap collector it is possible to increase the base-collector breakdown voltage caused by impact ionisation in the collector[32] (in a similar way, the emitter-base heterojunction reduces the number of holes injected into the emitter).

Compositional grading can eliminate the discontinuity in the conduction band that would act as an impediment to electron flow[31].

The applications driving HBT research are wideband high resolution ADCs and DACs, along with 40 and 160 GBs<sup>-1</sup> digital communications. Monolithic millimetre-wave integrated circuits (MMICs) are another area where HBTs are proving useful in building transmitters, receivers and preamps for radio frequency (RF) applications with the end goal of useful gain over the full 3 - 300 GHz RF range[33]. The desirable higher bitrates in digital applications require collector thickness to be reduced (to reduce switching time) which in turn means higher current densities and higher temperatures due to the extra dissipated power[22]. Screening of field in the space-charge region of the base-collector junction (the Kirk effect) by electrons sets an upper limit to the current densities that are available. HBTs are also often used as ultra-responsive photodetectors in data transmission applications[34].

Selective regrowth of the emitter region has been incorporated and allows a further degree of freedom to design devices which minimise the various parasitics inhibiting high frequency operation[35]. A transferred substrate process allows complete elimination of extrinsic parasitic capacitances since both junction etches are self-aligned[36]. The emitter mesa and the base and collector mesa (device isolation mesa) are first etched and contacts are made to the emitter using an airbridge. The devices are then encapsulated, planarised, flipped and finally bonded to a carrier wafer. The substrate can be etched back to reveal the collector and contacts formed. This technology has matured in recent years to allow high yield, high frequency circuits to be realised[37].

Recent advances in HBT technology have been made in InP/GaAsSb/InP double heterostructure devices[38]. These offer an excellent alternative material to the InP/InGaAs/InP scheme because the valence band offset is very large while the conduction band offset is small. This allows for an abrupt collector-base junction which does not suffer due to a conduction band spike. Electrons are instead launched into the collector with high velocities. The lattice matched GaAs<sub>0.5</sub>Sb<sub>0.5</sub> layer can be grown on InP with MOVPE. Furthermore, studies have been conducted into using a metamorphic buffer to incorporate InP-based HBT devices onto GaAs wafers (so-called MHBTs)[39]. While this holds many advantages in terms of large scale production, cost and ease of processing the performance of devices has been shown to be dependent on the quality of the metamorphic barrier layer growth[40].

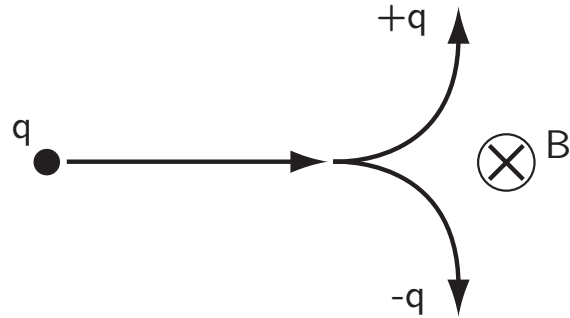


**Figure 1.1:** The Lorentz force on a charged particle moving in a magnetic field is perpendicular to both the field and the direction of travel. Positively charged particles obey a right-hand rule.

## 1.5 Sensor Technologies

The compass was the first magnetosensor. In 1820 Oersted observed that a magnetic needle was deflected in the presence of a current carrying wire while in the same period Faraday was completing his work on magnetic induction which ultimately led to *Faraday's Law*. This paved the way for Edwin Hall to discover the famous effect whereby a lateral voltage is produced in a gold plate conducting current in an orthogonal magnetic field in 1879. The so-called Hall voltage  $V_H$  was proportional to the applied field such that  $V_H \propto BI$ . The force on the charge carriers exerted by the magnetic field is orthogonal to the directions of travel and the field, i.e.

$$\mathbf{F} = q\mathbf{v} \times \mathbf{B}, \quad (1.1)$$

often called the *Lorentz force* after the Dutch Nobel Prize winning physicist. In a transistor the charge carrier is an electron (or a hole) and the drift or diffusion velocities are considered, as appropriate.

The Hall effect is essential in characterising material (particularly semiconductor) transport and mobility properties in the form of Hall bars[41]. First demonstrated in semiconducting germanium as a small and reliable magnetic field meter in 1948[42], Hall bars then progressed to be integrated into CMOS for on-chip sensing of Hall signal[43] twenty years ago.

Since then the increase in III-V and complex heterostructure band engineering for high speed and optoelectronic devices has brought its own challenges in Hall effect material characterisation[44, 45] and heterostructure III-V Hall bar sensors have found many and varied uses[46]. It is worth noting, however, that little work has been carried out

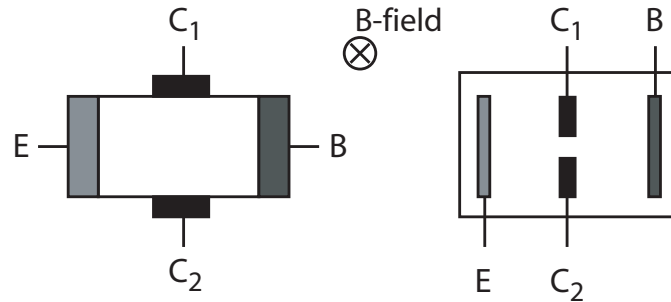


**Figure 1.2:** Typical arrangements of the emitter (E), base (B, B<sub>i</sub>) and collector (C<sub>i</sub>) contacts in planar silicon BJT orthogonal field technologies using the Hall effect for magnetic transduction. The device (a) is fabricated from a block of silicon, much like a Hall bar. The device (b) has a planar design in silicon, similar to a standard Si BJT. (Adapted from [41, 50].)

to integrate magnetic field sensors into HBT technologies or the epilayer structure of wafers typical to HBT fabrication. Hall sensors, although linear in response, have a low transduction efficiency and a highly temperature dependent offset[47]. Advanced materials and layer structures such as GaAs based quantum well superlattices have led to Hall bar magnetic field sensors with sensitivities of  $18 \text{ VT}^{-1}$  able to detect fields well below  $1 \text{ nT}$ [48]. The ability only to resolve out-of-plane field component was circumvented in Hall sensors by utilising ion implantation to isolate the current and voltage contacts in a planar device instead of requiring that they be on different facets of a sensing ‘block’[49]. No significant loss of sensitivity was measured using this technique.

Suggested in a patent by Hudson in 1969[51] the original bipolar magnetic transistor (BMT) employed a dual collector structure to detect non-equilibrium current flow. Figure 1.2 shows the layout of two typical BMTs and Figure 1.1 the field effect on the carriers. Several effects have been reported to allow the detection of magnetic fields with a BMT: Lorentz deflection of carriers as they transit the device, Hall effect in each of the device regions, modulation of emitter injection and modulation of carrier concentrations; all of which are due to the action of the Lorentz force[41, 43]. Figure 1.2(a) shows a BMT in which the Hall effect dominates and Figure 1.2(b) a device in which emitter injections dominates.

These multiple effects which are difficult to isolate for independent study make determining the magnetoresponse of a transistor a complex problem involving the chemical and metallurgical aspects of the device formation, the spatial distribution of doping impurities and defects in the crystal lattice as well as their interaction[47]. However, simulation of device operation has been reported and seen to be in agreement with experimental

Type	Output	Sensitivity/ %T <sup>-1</sup>	Equivalent noise/T	Linear range/T	Reference
<b>Orthogonal field BMT sensor</b>					
npn	differ.	56	$5 \times 10^{-5}$	$\pm 0.2$	[53]
pnp	differ.	7	$2 \times 10^{-5}$	$\pm 0.3$	[54]
pnp	differ.	0.6	—	$\pm 1$	[55]
<b>Parallel field BMT sensor</b>					
npn	differ.	5	$1 \times 10^{-5}$	$\pm 1$	[56]
npn	differ.	3050	—	$\pm 0.03$	[57]
npn	single	3000	—	—	[58]

**Table 1.2:** Figures of merit for several silicon bipolar magnetotransistors whose layouts are given in Figure 1.2. All of the sensors use carrier deflection as the transduction mechanism except for [56] which utilises emitter injection modulation. (Adapted from [47].)

results[52].

Magnetic field sensors integrated into electronic circuits have found uses in process control, automotive control, avionics, scientific instrumentation, nondestructive testing, biomedicine and consumer electronics and for contactless switches in the home and office, and position sensors in brushless motors[52, 59]. The properties of some BMTs are given in Table 1.2.

In a BMT where emitter injection modulation dominates, the applied magnetic field causes a voltage variation along the base–emitter junction and results in nonuniform carrier injection into the base[50]. This is detectable as unequal currents at the collector electrodes. BMTs are fabricated out of non–magnetic materials so that the magnetic field influences only the charge carriers as they travel through the device. Thus modulation of the current output can be viewed as a result of the effect of the field. With appropriate circuit integration, the current modulation in such a transistor can effect a change in output that can easily exceed that of a Hall sensor or magnetodiode[47]. BMTs can also resolve applied field direction.

Pure Lorentz deflection of minority carriers in the base and majority carriers in the collector is a mechanism for detecting magnetic field in a device with long unconfined base region. This is because there is no possibility of a Hall field in the base and field strength is determined by the relative sizes of the currents in two or more spatially separated collector contacts. Another mechanism is using a Hall field created in the base by the majority carriers under the influence of the magnetic field. Thirdly, at high levels of emitter injection the magnetic field can cause an asymmetrical carrier distribution in the

base depending on to which side the Lorentz force deflects the carriers and on the surface recombination rates at these locations[47].

Thus it can be seen that there exists a range of mature technologies in the fields of heterojunction bipolar transistors and in bipolar magnetic sensors. Having explored these technologies in this introductory chapter, a discussion of the background theory now follows.

## 2 The Bipolar Junction Transistor

This chapter contains a discussion of the physical and electrical considerations of bipolar transistor operation. It starts with the component part, the p–n junction diode, both at equilibrium and its characteristics under the different bias conditions. The current components of the BJT are analysed along with their physical origin. The chapter goes on to look at heterojunctions and heterojunction bipolar transistors.

A brief discussion of the Hall effect in semiconductors precedes the section on the theory proposed in studies to date of the effects of magnetic field on HBTs. The final section outlines of some figures of merit for transistor magnetic sensors.

### 2.1 P–n Junctions

A p–n step homojunction is a metallurgical junction of a single (compound or elemental) semiconductor that has different dopant types on each side. Considered below is a one-dimensional step junction with uniformly doped p– and n– regions and perfect ohmic contacts to each far from the junction itself.

In considering a one-dimensional device similar to that shown in Figure 2.1(b) some basic physical relationships can be established. If it is uniformly doped to a concentration  $N_A$  and  $N_D$  in the p–type and n–type regions, respectively. Since the junction is described as *metallurgical* it is well defined and abrupt at  $x = 0$ . A system of this type is often referred to as a p–n junction diode.

#### Thermal Equilibrium

Under the equilibrium conditions of no thermal gradient, no applied bias ( $V_A = 0$ ) no incident light and no applied electric or magnetic fields the carrier concentration in the region of the junction will be different to the dopant concentrations. Diffusion of majority carriers across the junction will occur since there is a relatively small concentration of (thermally excited) minority carriers on both sides. This effect can be described energetically by the necessity of alignment of the Fermi levels on each side of the junction: since the Fermi level is higher in the n–type than in the p–type some electrons must flow

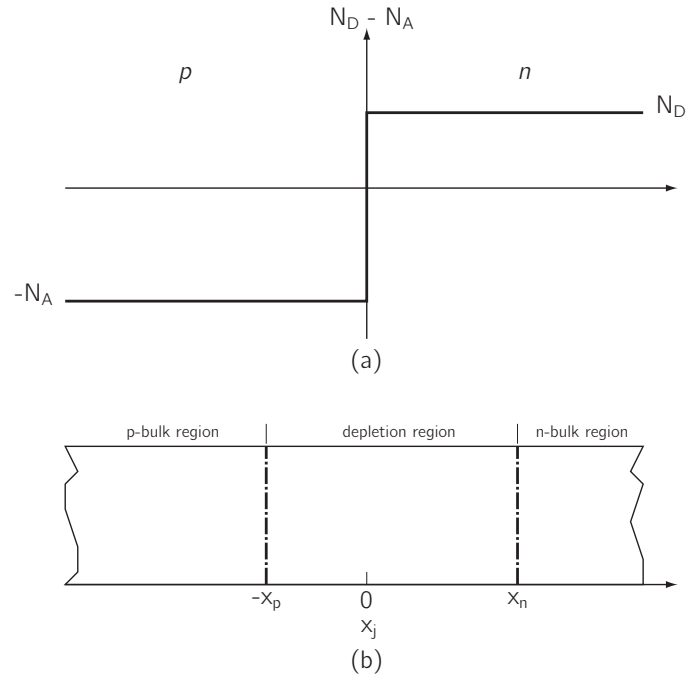


**Figure 2.1:** Dopant concentration (a) and schematic (b) of a 1–dimensional p–n junction. (Adapted from [60].)

out of the n–type semiconductor. An example of carrier concentration at a p–n junction is shown in Figure 2.2(a). A region of charged dopant ions is then left unquenched which retards further diffusion and there is a *space–charge region* on either side of the junction. This net charge density per unit length by Gauss’s law results in an electric field which in turn leads to a potential difference as shown in Figure 2.2(b–c).

The electric field  $\mathcal{E}$  ( $\text{Vcm}^{-1}$ ) is given by

$$\mathcal{E}(x) = \frac{1}{K_s \varepsilon_0} \int_{-\infty}^x \rho(x) dx \quad (2.1)$$

where  $K_s$  is the relative dielectric constant of the semiconductor and  $\varepsilon_0 = 8.854 \text{ F cm}^{-1}$  is the permittivity of free space. The net charge density  $\rho(x)$  ( $\text{C cm}^{-1}$ ) is

$$\rho(x) = q(p - n + N_D - N_A) \quad (2.2)$$

The space–charge region shown in Figure 2.2 is called the *depletion region* because the majority carrier concentration on each side has been depleted. Since

$$\mathcal{E} = -\nabla V(x) \quad (2.3)$$

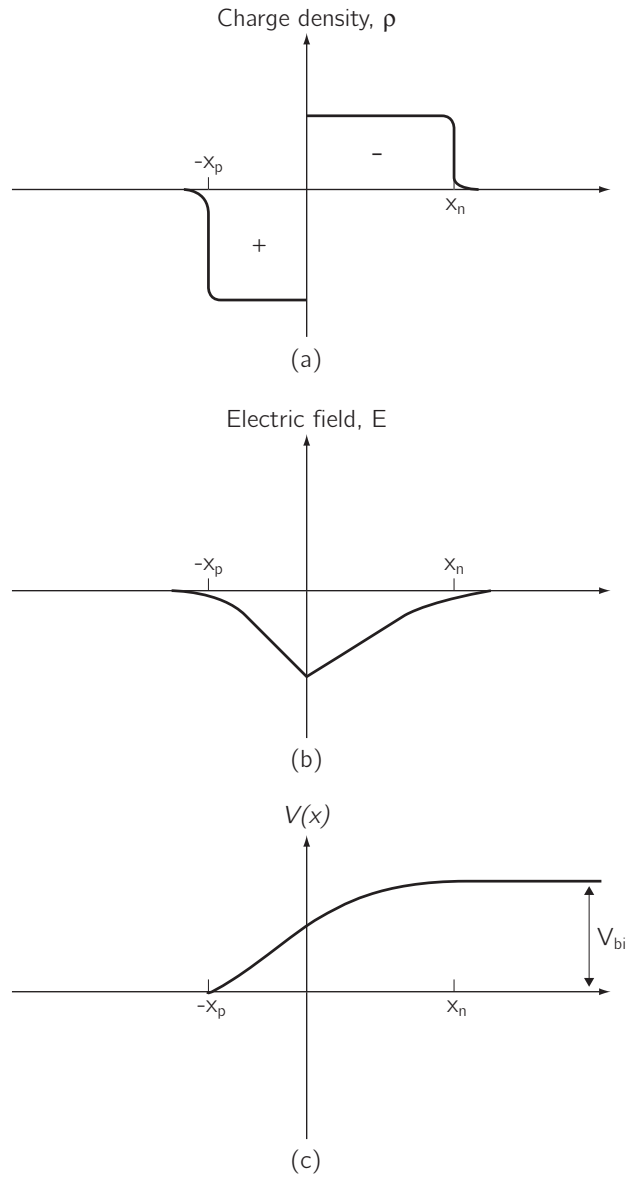


**Figure 2.2:** Charge density (a), electric field (b) and potential (c) for a 1-D p-n junction. (Adapted from [60].)

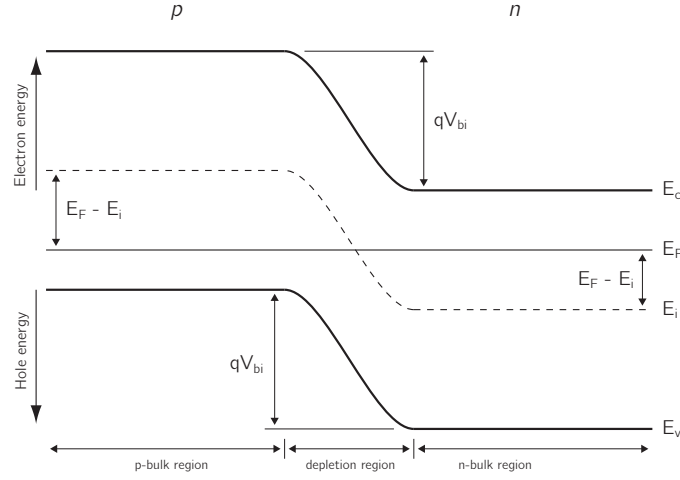


**Figure 2.3:** Energy bands of a 1-D p–n junction. (Adapted from [60].)

the electric field gives rise to a potential gradient according to

$$V(x) = - \int_{-\infty}^x \mathcal{E}(x) dx \quad (2.4)$$

where  $V(-\infty) = 0$ . Figure 2.3 shows the energy bands for the junction with the relative positions calculated from the fact that the Fermi level  $E_F$  must be constant throughout at thermal equilibrium.

The energy gap  $E_g$  is also fixed everywhere in a homojunction and in the bulk materials the conduction band minimum  $E_c$  and the valence band maximum  $E_v$  are fixed with respect to the Fermi level. From these constraints *band bending* such as that shown in Figure 2.3 arises. From the definition of the Fermi level

$$E_F - E_i = kT \ln [n_n/n_i] = kT \ln [N_D/n_i] \quad N_D \gg N_A, n_i \quad (2.5)$$

$$E_i - E_F = kT \ln [p_p/n_i] = kT \ln [N_A/n_i] \quad N_A \gg N_D, n_i \quad (2.6)$$

where Boltzmann's constant  $k = 1.381 \times 10^{-23} \text{JK}^{-1}$ . The built in potential can be shown to be

$$V_{bi} = \frac{kT}{q} \ln \left[ \frac{n_n p_p}{n_i^2} \right]. \quad (2.7)$$

Furthermore, by considering zero net current flow in thermal equilibrium, i.e.

$$J_N = J_{N|\text{drift}} + J_{N|\text{diffusion}} = q\mu_n n \mathcal{E} + qD_N \frac{dn}{dx} = 0, \quad (2.8)$$

it is possible to derive the equivalent result,

$$V_{bi} = \frac{kT}{q} \ln \left[ \frac{N_D N_A}{n_i^2} \right]. \quad (2.9)$$

In (2.8)  $\mu_n$  and  $D_N$  are the electron mobility and diffusion coefficient in the n–type material, respectively. The potential hill gives rise to the drift ( $J_{N,P|drift}$ ) of minority carriers and the density gradient gives rise to the diffusion ( $J_{N,P|diffusion}$ ) of majority carriers across the junction.

The width,  $W$ , of the depletion region is given under equilibrium conditions by  $x_n + x_p$  where the relation

$$x_p = \left[ \frac{N_D}{N_A} \right] x_n \quad (2.10)$$

holds and implies that the depletion region extends further into the more lightly doped region. The width will decrease under forward bias and increase under reverse bias according to the relation

$$W = \left[ \frac{2K_S \epsilon_0}{q} (V_{bi} - V_A) \left( \frac{N_A + N_D}{N_A N_D} \right) \right]^{1/2} \quad (2.11)$$

where  $W$  is the total depletion region width and  $K_S$  is the relative dielectric constant of the semiconductor material.

### Forward Bias

In applying a forward bias to a p–n junction diode (that is a positive bias to the p–type side, with respect to the n–type side) the difference in potential over the junction is reduced to  $q(V_{bi} - V_A)$ . This occurs since energy  $E$  (eV) is proportional to potential according to

$$E = -qV \quad (2.12)$$

and referring to (2.4) and Figure 2.2 it can be seen that the n–type bulk material under thermal equilibrium is at a *higher* potential than the p–type.

Figure 2.4 exemplifies the physical situation of a diode under forward bias. As the potential barrier for the minority carriers is lowered they will diffuse across the junction, according to the density gradient and diffusion coefficient. (It is worthwhile to note the Einstein relationship for the diffusion coefficient  $D$  ( $\text{cm}^2 \text{s}^{-1}$ ),

$$D_{N,P} = \frac{\mu_{n,p} kT}{q}, \quad (2.13)$$

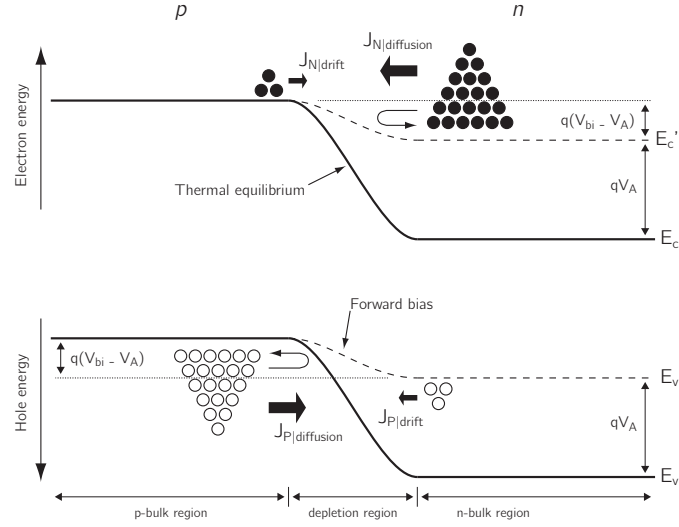


**Figure 2.4:** A p–n junction under forward bias. (Adapted from [60].)

where the coefficient for holes and electrons will be different in both n– and p–type materials.) In thermal equilibrium the drift and diffusion currents (for both electrons and holes) are equal and opposite. The increase in diffusion under forward bias is not countered by any increase in drift as drift is limited by minority carrier generation in the p–type region near the junction. The majority carrier occupancy levels are determined by the product of the Fermi function  $f(E)$  and the density of states  $g(E)$  given by

$$f(E) = \frac{1}{1 + e^{(E-E_F)/kT}} \quad (2.14)$$

and

$$g_c(E) = \frac{m_n^* \sqrt{2m_n^*(E_c - E)}}{\pi^2 \hbar^3} \quad E \geq E_c \quad (2.15)$$

$$g_v(E) = \frac{m_p^* \sqrt{2m_p^*(E - E_v)}}{\pi^2 \hbar^3} \quad E \leq E_v \quad (2.16)$$

where  $g_c(E)$  and  $g_v(E)$  are the conduction and valence band densities of states, respectively. The product leads to a carrier distribution that decreases exponentially with increasing energy (for electrons, decreasing energy for holes) and so, as the forward bias increases until it is equal to  $V_{bi}$ , the forward current will also increase exponentially. In fact the *ideal diode equation* (or sometimes the Shockley diode equation) gives the diode

current to be

$$I = I_0(e^{qV_A/kT} - 1) \quad (2.17)$$

where the magnitude of the reverse saturation current (see below) is

$$I_0 = qA \left[ \frac{D_N}{L_N} \frac{n_i^2}{N_A} + \frac{D_P}{L_P} \frac{n_i^2}{N_D} \right]. \quad (2.18)$$

In (2.18)  $A$  ( $\text{cm}^2$ ) is the junction area,  $L_{NP}$  ( $\text{cm}$ ) is the *minority carrier diffusion length* and is equal to  $\sqrt{D_{NP}\tau_{np}}$  with  $\tau_{np}$  (s) the average time to recombination of a minority carrier. The ideal diode equation is derived using the assumption that the net recombination and generation<sup>1</sup> in the depletion region is zero.

### Reverse Bias

In applying a reverse bias to a p–n junction diode (that is a positive bias to the n–type side, with respect to the p–type side) the difference in potential over the junction is increased to  $q(V_{bi} - V_A)$ . The diffusion of majority carriers is reduced as fewer have the energy required to traverse the potential barrier as shown in Figure 2.5. The drift current of minority carriers is unchanged from its small, generation–limited thermal equilibrium value.

Since the electron current is from left to right and the hole current is from right to left the reverse bias saturation current is negative as well as small and quickly becomes saturated under increasing reverse bias.

Figure 2.6(a) shows a typical (ideal) diode current–voltage characteristic and (b) shows the real case.

### Diode Breakdown Mechanisms

If the electric field in the depletion region is high it will accelerate drifting electrons to a large velocity. At a certain critical value of electric field  $\mathcal{E}_{cr}$  the average velocity will be high enough that each collision of electron into a lattice atom will create an electron–hole pair. These will then be accelerated by the electric field and will create more electron–hole pairs, and so on. This is *avalanche breakdown* and leads to an exponentially increasing reverse current with applied reverse bias. *Zener breakdown* occurs when a reverse bias brings the top of the valence band in the p–type material below the bottom of the conduction band in the n–type material. If the barrier is thin enough ( $< 100\text{\AA}$ ) electrons

<sup>1</sup>i.e. electrons being thermally excited from the valence band into the conduction band, creating an electron hole pair.

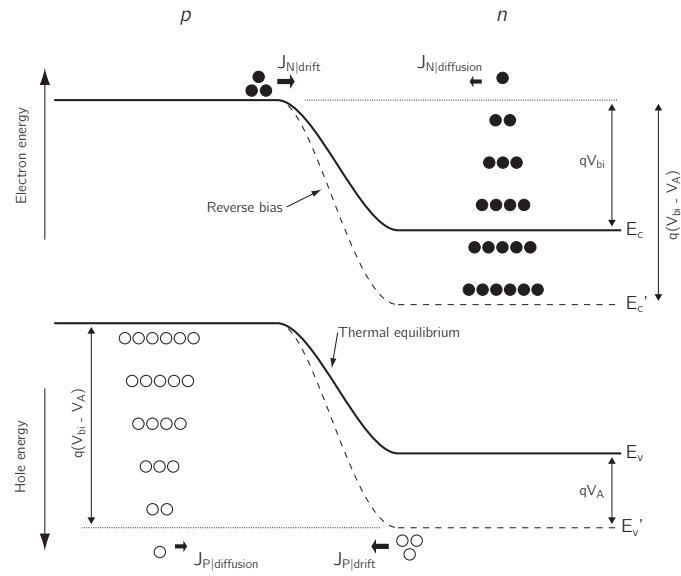


Figure 2.5: A p-n junction under reverse bias. (Adapted from [60].)

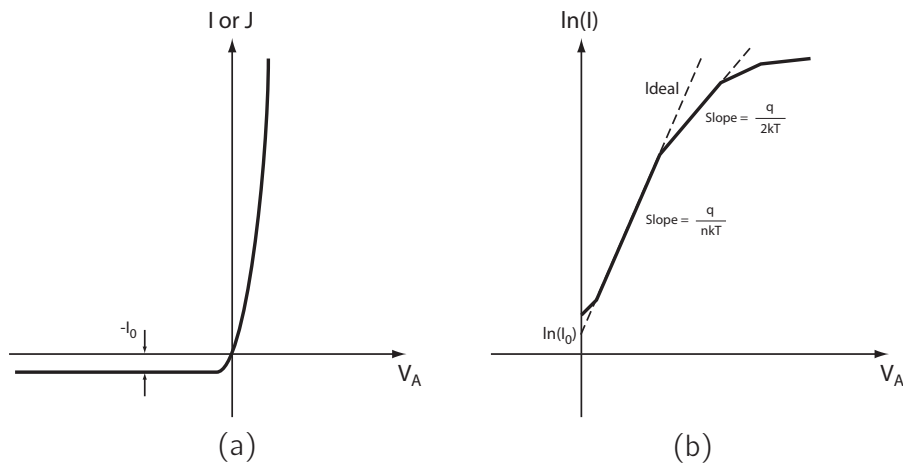


Figure 2.6: Current against applied bias for a p-n junction diode in the ideal (a) and non-ideal (b) cases. (Adapted from [60].)

can tunnel from the highly populated p–type side to the relatively empty n–type side. As the bias increases still further more occupied states will have the opportunity to tunnel across.

### Recombination–Generation in the Depletion Region

The ideal diode equation is derived using an assumption that the net recombination and generation in the depletion region is zero. In practice, however, this is not the case; under reverse bias conditions generation dominates since carrier concentrations therein are less than at equilibrium. Any electrons or holes generated in this way will be accelerated by the electric field and will add to the respective drift current, hence increasing the reverse saturation current. It is approximately constant throughout the depletion region and its contribution increases monotonically with the depletion width. Conversely, at small values of forward bias, the excess of both holes and electrons in the depletion region leads to an increase in recombination<sup>2</sup> which will reduce the forward current.

## 2.2 Bipolar Junction Transistors

A bipolar junction transistor (BJT) consists of two p–n homojunctions fabricated so that the central region is shared between both junctions. Since the electron mobility in semiconductors is higher, npn is the prevalent system (rather than pnp) in circuit applications.

The region of p–type semiconductor, sandwiched between two n-type regions, is the *base* and is short compared to its *minority carrier diffusion length*. The other regions, the *emitter* and the *collector*, are so named because of the functions they perform (see below). The emitter has a much larger dopant concentration than the base, this is signalled by the ‘+’ in  $n^+pn^3$ . In a BJT the *active region* has a forward bias in the emitter–base (E–B) junction and a reverse bias in the collector–base (C–B) junction. The forward bias in the E–B junction leads to a decrease in the barrier height which the majority electrons in the (very heavily doped) emitter must surmount to get to the base. Thus electrons are injected into the base. As the base length is shorter than the diffusion length for electrons in the p–type material, few electrons will recombine with a hole here. Most will diffuse across the base and be accelerated down the potential hill into the collector. Hence the decreasing dopant concentration from emitter to base is primarily to restrict back injection from base to emitter.

<sup>2</sup>Electrons can drop from the conduction band to fill a hole in the valence band. This often happens via an intermediate midgap (impurity) state.

<sup>3</sup>In fact, the ‘+’ means that the material is *degenerate*, i.e. its (dopant concentration dependent) Fermi level is within  $\sim 3kT$  of relevant band edge, here  $E_c$

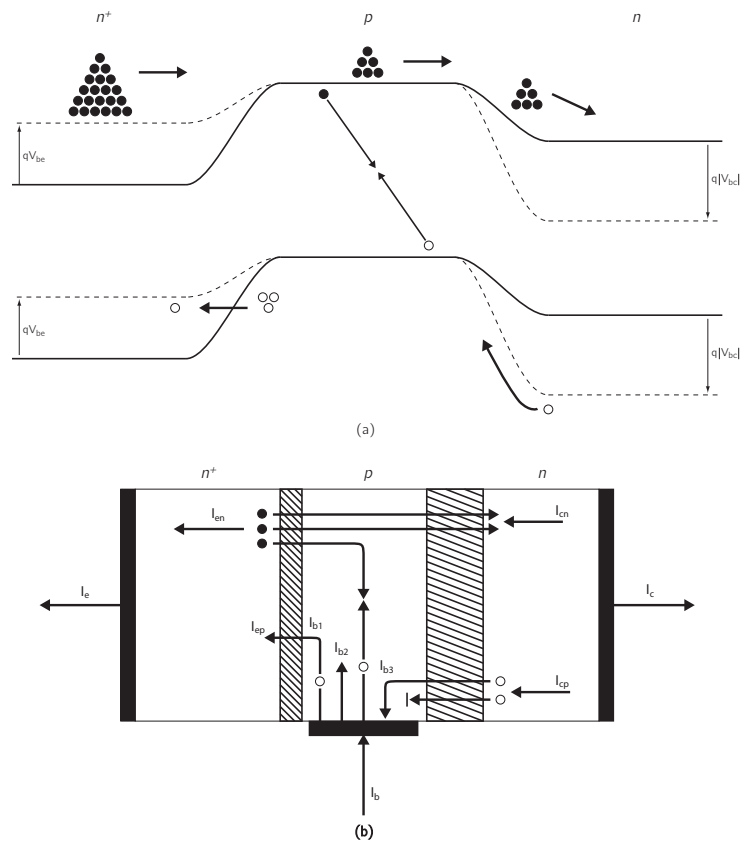


**Figure 2.7:** Energy bands (a) and schematic showing the current components (b) of a 1-D bipolar junction transistor. (Adapted from [24].)

Electrons drifting into the collector from the base will have an excess kinetic energy equivalent to the difference between the conduction band edge in the base and that in the collector. These will scatter off the crystal lattice ions and this deceleration mechanism results in the generation of lattice phonons and causes heating.

Figure 2.7(b) shows the current components in a BJT. In the emitter  $I_{en}$  is the component from majority electrons diffusing into the base and  $I_{ep}$  is the component from back injected holes from the base. In the collector  $I_{cn}$  is the component from electrons drifting down the potential hill from the base and  $I_{cp}$  is the component from minority holes drifting up the potential hill into the base.

The base current components labelled on the diagram:  $I_{b1}$  is the current arising from holes back injected into the emitter and is equivalent to  $I_{ep}$ .  $I_{b2}$  is the current that must enter the base (from the external circuit) to compensate for holes that recombine with electrons injected from the emitter.  $I_{b3}$  is the base current arising from minority holes that are generated within one diffusion length of the C–B depletion region edge and drift down the potential hill into the base, it is equivalent to  $I_{cp}$ .

The equations for the currents at the metal contact to each region are, at the emitter contact

$$I_e = I_{en} + I_{ep}, \quad (2.19)$$

at the collector contact

$$I_c = I_{cn} + I_{cp} \quad (2.20)$$

and at the base contact

$$I_b = I_e + I_c = I_{b1} + I_{b2} + I_{b3}. \quad (2.21)$$

For a bipolar transistor, the ratio of the electrons leaving the base to the electrons entering the base is termed the *base transport factor*. The base transport factor,  $\alpha_T$ , should be as close to one as possible, it is largely affected by the thickness of the base, as well as its dopant concentration.

$$\alpha_T = \frac{I_{cn}}{I_{en}} \quad (2.22)$$

It is also useful to define the ratio of the emitter injected electron current to the total emitter current as the *emitter injection efficiency*,  $\gamma$ ,

$$\gamma = \frac{I_{en}}{I_e} = \frac{I_{en}}{I_{en} + I_{ep}} \quad (2.23)$$

This is also ideally very close to one.

The *dc alpha factor*, or  $\alpha_{dc}$ , is given by the ratio of the terms defined in 2.19 and

2.20:

$$\alpha_{dc} = \frac{I_c}{I_e} = \frac{I_{cn} + I_{cp}}{I_{en} + I_{ep}}, \quad (2.24)$$

i.e., the ratio of collector to emitter currents. Since, while the E–B junction is forward biased and the C–B junction is reverse biased,  $I_{cn} \gg I_{cp}$ , this simplifies to

$$\alpha_{dc} = \frac{I_{cn}}{I_{en} + I_{ep}} \quad (2.25)$$

and hence

$$\alpha_{dc} = \gamma\alpha_T. \quad (2.26)$$

The other current ratio of interest is defined as  $\beta_{dc}$ ,

$$\beta_{dc} = \frac{I_c}{I_b} = \frac{I_{cn} + I_{cp}}{I_{b1} + I_{b2} + I_{b3}}. \quad (2.27)$$

And from Equation 2.24,

$$\beta_{dc} = \frac{I_c}{I_b} = \frac{I_c}{I_e - I_c} = \frac{\alpha_{dc}}{1 - \alpha_{dc}} \quad (2.28)$$

The figure  $\beta_{dc}$  is a useful current gain parameter with which to characterise a device[24]. It is the ratio of the DC collector current to the DC base current, in a transistor operating in the active region. The theoretical maximum value of  $\beta_{max}$  is given by the case of negligible recombination currents,

$$\beta_{max} = \frac{I_{cn}}{I_{b1}} = \frac{I_{en}}{I_{ep}}. \quad (2.29)$$

From Figure 2.7 the energy barrier for electrons is  $E_n$  and for holes  $E_p$ . If the doping levels in the emitter and base are  $N_e$  and  $N_b$ , respectively, then the injection current densities at the E–B junction are

$$J_n = N_e \nu_{nb} \exp \left[ \frac{-E_n}{kT} \right] \quad (2.30a)$$

$$J_p = N_b \nu_{pe} \exp \left[ \frac{-E_p}{kT} \right] \quad (2.30b)$$

where  $\nu_{nb}$  and  $\nu_{pe}$  are material dependant quantities termed the effective velocities of electrons in the base and holes in the emitter, respectively. If there has been no bandgap

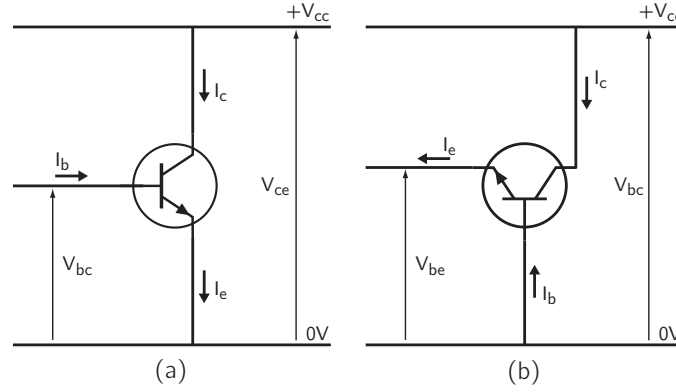


**Figure 2.8:** Common emitter (a) and common base (b) configurations for an npn bipolar transistor.

narrowing due to degeneracy then  $E_n$  and  $E_p$  can be considered equal, hence

$$\beta_{max} \approx \frac{N_e \nu_{nb}}{N_b \nu_{pe}} \quad (2.31)$$

As discussed above, to ensure a high current gain in a *homojunction* bipolar transistor the dopant levels in the emitter must be significantly higher than that of the base. This is not necessarily the case in a *heterojunction* bipolar transistor, as will be seen below.

### 2.2.1 Ideal Operational Characteristics

In circuit applications BJTs are often used in the *common-emitter* configuration as shown in Figure 2.8(a) or in the *common-base* configuration as shown in Figure 2.8(b).

For an ideal pnp bipolar transistor it can be shown by solving the minority carrier diffusion equations that

$$I_e = qAn_i^2 \left[ \frac{D_e}{L_e N_e} + \frac{D_b}{WN_b} \right] (e^{qV_{be}/kT} - 1) - qAn_i^2 \left[ \frac{D_b}{WN_b} \right] (e^{qV_{cb}/kT} - 1) \quad (2.32)$$

where  $L_e$  is the minority carrier diffusion length in the emitter,  $L_e$  is the minority carrier diffusion constants in the emitter and  $N_e$ ,  $N_b$  are the emitter and base dopant densities. The length of the neutral base region is  $W$  (this is the distance the minority carriers must traverse to be collected) and the intrinsic device area is  $A$ . (For a full treatment of the ideal bipolar transistor see, for example, [24].) The collector current can be given as

$$I_c = qAn_i^2 \left[ \frac{D_b}{WN_b} \right] (e^{qV_{be}/kT} - 1) - qAn_i^2 \left[ \frac{D_c}{L_c N_c} + \frac{D_b}{WN_b} \right] (e^{qV_{cb}/kT} - 1) \quad (2.33)$$

where  $L_c$ ,  $D_c$  and  $N_c$  are for the collector. The base current can then be calculated from Kirchoff's Current Law as

$$I_b = qAn_i^2 \frac{D_e}{L_e N_e} (e^{qV_{be}/kT} - 1) + qAn_i^2 \frac{D_c}{L_c N_c} (e^{qV_{cb}/kT} - 1). \quad (2.34)$$

In the *active region* of operation there is a forward bias on the base–emitter junction and a reverse bias on the base–collector junction. This gives

$$\exp\left(\frac{qV_{cb}}{kT}\right) \ll 1 \quad (2.35)$$

and

$$\exp\left(\frac{qV_{be}}{kT}\right) \gg 1 \quad (2.36)$$

for biases of a few tenths of a Volt since  $q/kT$  at room temperature. This leads to the current components in the active region

$$I_e \cong qAn_i^2 \left[ \frac{D_e}{L_e N_e} + \frac{D_b}{WN_b} \right] e^{qV_{be}/kT}, \quad (2.37)$$

$$I_c \cong qAn_i^2 \frac{D_b}{WN_b} e^{qV_{be}/kT} \quad (2.38)$$

and

$$I_b \cong qAn_i^2 \frac{D_e}{L_e N_e} e^{qV_{be}/kT}. \quad (2.39)$$

Thus, given sufficient reverse bias on the base–collector junction, the current in the active region is governed by the forward bias on the base–emitter junction.

Other modes of operation of a BJT are the saturation, cut–off and inverted regions. In the saturation region both junctions are forward biased so injected majority carriers from the collector reduce the emitter current and many more majority carriers from the base are injected into the collector. This latter effect serves to increase the base current. In the cut–off region both the junctions are reverse biased. In this case only thermally generated carriers in the vicinity of the space–charge region are available and will drift into the base.

The reverse saturation current in the base–collector junction is  $I_{cb0}$ . This is measured with the emitter open–circuited ( $I_e = 0$ ). The current flowing from the emitter to the collector with the base open–circuited is  $I_{ce0}$ .

If the base–collector junction is forward biased either inverted active or inverted saturation operation occurs, depending on whether the emitter–base region is reverse or

forward biased. Figures of merit for this region can be defined as  $\gamma_R$ ,  $\alpha_{dcR}$  and  $\beta_{dcR}$  and are lower than in normal operation[24].

The common base, active region gain<sup>4</sup> is determined by  $I_c/I_e$ , i.e.  $\alpha_{dc}$ , and can be shown[24] to be

$$\alpha_{dc} = \frac{1}{1 + \frac{D_e N_b W}{D_b N_e L_E}} \quad (2.40)$$

which sets limits for the design of high gain devices, for example  $W \ll L_e$ . The common emitter current gain is given by  $I_c/I_b$  and can be shown to be

$$\beta_{dc} = \frac{D_b N_e L_e}{D_e N_b W}. \quad (2.41)$$

Thus by increasing the emitter doping over the base doping and reducing the base region dimension a high gain can be achieved.

### 2.2.2 Deviations from Ideal

The ideal current output determined by the equations given above is not observed in real devices. Several physical processes account for this. The ideal case does not account for recombination in the base region. A quasi-ideal solution can be derived from assuming a low rate of base recombination and a linear fall-off in minority carrier concentration in the base[24] in a device with  $W \simeq 0.1L_b$  or less (valid for most real devices). This gives a base current of

$$I_b = qAn_i^2 \left[ \frac{D_e}{L_e N_e} \times \frac{W}{2L_b} \right] (e^{qV_{be}/kT} - 1) + qAn_i^2 \left[ \frac{D_c}{L_c N_c} \times \frac{W}{2L_b} \right] (e^{qV_{cb}/kT} - 1) \quad (2.42)$$

which gives an increase in the base current proportional to  $W/2L_b$ .

Another effect seen in real devices is *base width modulation*, where the applied bias on the junction changes their depletion width according to (2.11). With the small base widths used by necessity in real devices, the changes in  $W$  caused by this effect have a noticeable effect on the output characteristics. The effects of base width modulation on the common emitter output characteristics are shown in Figure 2.9. In the real case, the output current increases with increasing bias. This effect, called the *Early effect* is pronounced in this configuration. In the active region, as described by (2.37), (2.38) and (2.39), a constant base current implies constant  $V_{be}$ . However, the collector current of

<sup>4</sup>The base transport factor for an ideal device is unity, so according to (2.26), we have simply  $\alpha_{dc} = \gamma$  with  $\gamma$  the emitter injection efficiency.

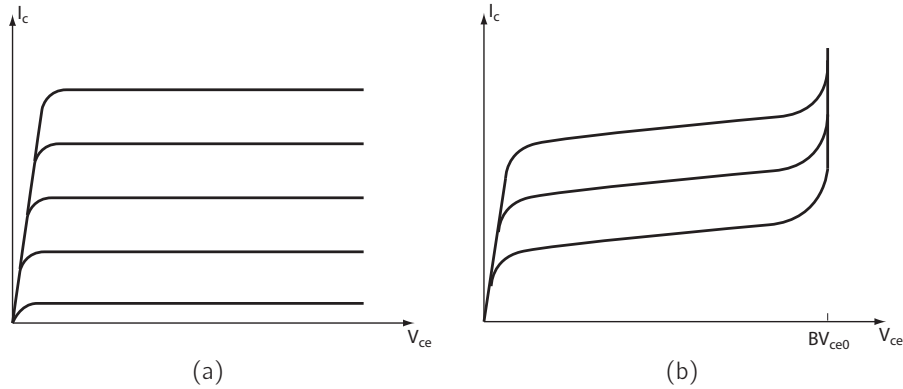


**Figure 2.9:** A representation of ideal (a) and real (b) BJT common base output characteristics. (Adapted from [24].)

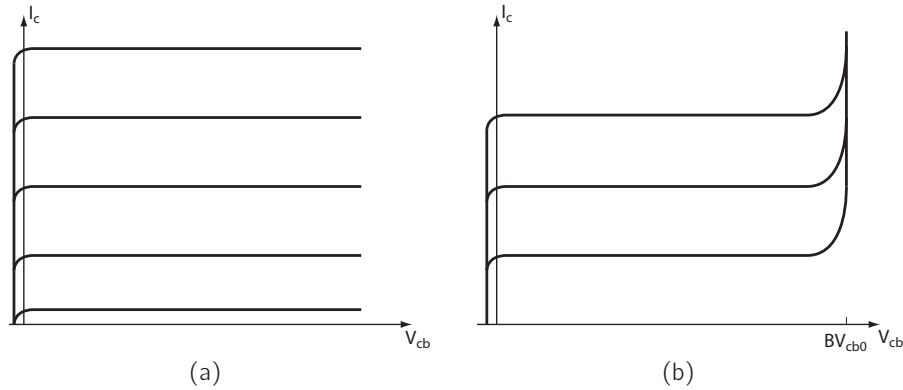


**Figure 2.10:** A representation of ideal (a) and real (b) BJT common base output characteristics. (Adapted from [24].)

(2.38), repeated here

$$I_c \cong qAn_i^2 \frac{D_b}{WN_b} e^{qV_{be}/kT}, \tag{2.43}$$

for a fixed  $V_{be}$  but increasing  $V_{cb}$  will see a decreasing value of  $W$  and hence  $I_c$  will increase.

Figure 2.10 is a representation of ideal (a) and real (b) device common base I–V characteristics. This can be rationalised as a decrease in effective base width which was seen above to lead to a higher device gain. For a given value of  $I_e$  the increasing reverse bias at the base–collector junction increases the depletion region there. This effect is ameliorated in the common base configuration as the fixed value of  $I_e$  requires that  $V_{be}$  decreases with  $W$ , thus less carriers are injected and  $I_c$  cannot rise.

Further increases in  $I_c$  are caused by carriers generated in the base–collector space–

charge region[24]. This extra current un-accounted for in the discussions above leads to a greater slope in the common emitter output I–V characteristic.

If the base width modulation effect leads to a zero base width then the emitter and collector regions are electrostatically coupled. This is called *punch-through*. Increasing the reverse bias on the base–collector junction past the punch-through point will cause the potential hill at the base–emitter junction to decrease[24]. This leads to an exponential increase in  $I_c$  for small change in applied voltage.

Another high current effect is *avalanching*, where the large base–collector junction reverse bias imparts enough energy into the carriers which flow through it that they ionise atoms in the collector on collision. These ionisations create electron–hole pairs and a large current flows through the junction. The high current characteristics in BJTs are caused by whichever effect occurs at the lowest voltage. The *collector-to-base breakdown voltage*  $BV_{cb0}$  is the point of rapidly increasing current in the common base configuration with  $I_e = 0$  (open circuited). The *collector-to-emitter breakdown voltage*  $BV_{ce0}$  is the point of rapidly increasing current in the common emitter configuration with  $I_b = 0$ . It can be seen in Figure 2.10 and Figure 2.9 that there is some avalanching throughout the active region of the common emitter configuration as majority carriers are created in the junction and drift into the emitter as minority carriers. This causes an increase in forward injection from emitter to base. The numerical value of  $BV_{ce0}$  is less than that of  $BV_{cb0}$ . A resistance placed between the base and emitter would reduce this effect by “absorbing” some of the avalanching carriers.

It is also the case that the voltages applied to the device are not the voltages at the device junctions. There is a finite resistance between the metal contact and the bulk material as the electrons must pass through a non-zero potential barrier dependent on the physical properties of the metal and the bulk material and the interface formed between the two. Thus a voltage drop occurs attributable to the contacts. A further resistance is introduced by the bulk material as the carriers must traverse through this from the contacts to the intrinsic device region (or in the reverse direction). This has a large effect on the emitter as  $I_e$  is exponentially dependent on the forward bias.

A forward biased diode will have excess recombination in its depletion region[24]. A reverse biased diode will have excess generation in its recombination region. The generation in the reverse biased diode will provide extra carriers for injection into the base and then back injection into the emitter. This will increase both  $I_{cb0}$  and  $I_{ce0}$  from ideal. The recombination current in the emitter–base junction will have a more noticeable effect on the device current gain  $\beta_{dc}$  at lower values of  $I_c$  and will be overcome at higher levels of injection.

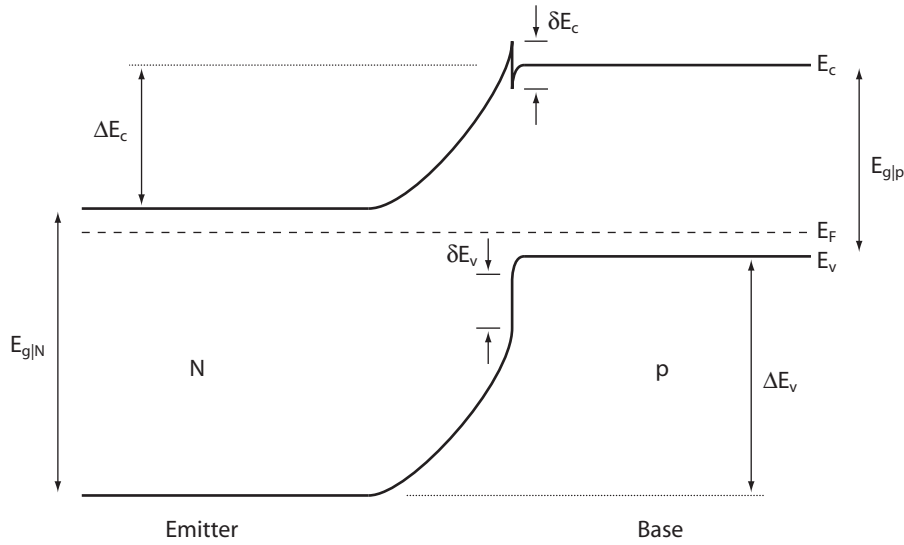


**Figure 2.11:** An example of the band structure of the emitter–base junction of a hetero-junction bipolar transistor.

## 2.3 Heterojunctions

If the two sides of the p–n junction are made from different semiconductor materials it is said to be a *heterojunction*. Different materials will not necessarily have the same value of  $E_g$ , the bandgap, nor work function,  $\phi$ , electron affinity  $\chi$  or dielectric constant,  $\epsilon_r$ . The work function,  $\phi$ , of a solid state material is the difference in energy between that of an electron at infinity (with respect to the material surface), at rest in a vacuum and the Fermi level of the material surface:

$$\phi = E_{vac} - E_F. \quad (2.44)$$

Similarly the electron affinity is defined as

$$\chi = E_{vac} - E_c, \quad (2.45)$$

the energy required to remove an electron from the edge of the conduction band to the vacuum level. The position of the Fermi levels with respect to the band edges in any given material system will depend on the dopant type and concentration (and hence so will the work function). With epitaxial growth it is possible to make the change between materials within one or two atomic layers.

Figure 2.11 represents the band structure of the two materials of a p–N hetero-

Physical quantity	InP/ In <sub>0.53</sub> Ga <sub>0.47</sub> As	Al <sub>0.3</sub> Ga <sub>0.7</sub> As/ GaAs	Si/Si <sub>0.8</sub> Ge <sub>0.2</sub>
$\Delta E_g$ /eV	0.60	0.37	Unstrained:0.078 Strained:0.165
$\Delta E_c$ /eV	0.23	0.24	
$\Delta E_v$ /eV	0.37	0.13	

**Table 2.1:** Bandgap offsets of selected heterojunctions at room temperature. (Adapted from [23].)

junction<sup>5</sup>. At the interface of an abrupt heterojunction there is a change in the crystal potential and electronic structure[61, 62]. Chemical bonds form between the adjacent atoms of the different materials and surface dipoles then arise. The chemistry of the junction determines the ratio of  $\Delta E_c$  to  $\Delta E_b$  where and their sum is equal to the difference in bandgap,  $\Delta E_g$ . Table 2.1 shows the band offsets in several common heterogeneous material systems. Figure 2.11 is representative of the band structure of the junctions described in Table 2.1. The spike in the conduction band is a feature of heterojunctions of this type and is attributable to the chemical bond interface dipoles. Careful design and growth of compositionally graded junctions can eliminate the spike which is a barrier to electron injection across the junction (although it also finds uses as a means to ‘launch’ electrons into the base with excess kinetic energy).

## 2.4 Heterojunction Bipolar Transistors

Heterojunctions have applications in many areas of semiconductor device engineering; however, in terms of the improvement of bipolar junction transistor performance by incorporating heterostructures the most important of these is the restricting of base–emitter back injection by the large valence band offset  $\Delta E_v$  (in an npn device).

Further consideration of (2.29) and (2.30) for an HBT gives

$$\beta_{max} = \frac{N_e \nu_{nb}}{N_b \nu_{pe}} \exp \left[ \frac{\Delta E_v}{kT} \right]. \quad (2.46)$$

which is the maximum value of current gain achievable considering the typical HBT band structure shown in Figure 2.11, discounting effects not directly related to the band line–up.

<sup>5</sup>It is customary to represent the larger bandgap material in a heterojunction with a capital P or N, whichever is appropriate. Further, a heterojunction between two materials with differing dopant types, as in this case, is said to be *anisotype*

Similarly to the discussion in §2.2.1 above, for an npn transistor it is possible to show from the minority carrier diffusion equations that

$$I_{bp} = \frac{qAD_{pe}}{W_e} \frac{n_{ie}^2}{N_e} \exp\left(\frac{qV_{be}}{kT}\right) \quad (2.47)$$

and

$$I_c = \frac{qAD_{nb}}{W_b} \frac{n_{ib}^2}{N_b} \exp\left(\frac{qV_{be}}{kT}\right) \quad (2.48)$$

where  $D_{pe}$ ,  $D_{nb}$ ,  $W_e$ ,  $W_b$  are the minority hole diffusion constant in the emitter, the minority electron diffusion coefficient in the base, the emitter thickness and the base thickness, respectively. The back-injection current  $I_{bp}$  is the dominant component of the base current in silicon BJTs[23]. If the diffusion constants are taken to be approximately equal, as well as the physical lengths, a higher doping is required in the emitter than in the base to achieve a high gain. However, a high base doping allows a transistor to have low base resistance which is useful for a higher power gain and a low emitter doping reduces the base-emitter junction capacitance which is useful for high frequency performance[23]. High base doping reduces the base access resistance  $R_b$ . Increased dopant concentration in the base also reduces the width of the base-collector depletion region in the base which defers punch-through breakdown to a larger bias.

In considering (2.9), (2.47) and (2.48), for an HBT with no conduction band spike there is

$$\frac{I_c}{I_{bp}} = \frac{D_{nb}W_eN_e}{D_{pe}W_bN_b} \frac{n_{ib}^2}{n_{ie}^2} = \frac{D_{nb}W_eN_e}{D_{pe}W_bN_b} \exp\left(\frac{\Delta E_g}{kT}\right), \quad (2.49)$$

which is equivalent to (2.46). For an abrupt HBT this becomes

$$\frac{I_c}{I_{bp}} = \frac{D_{nb}W_eN_e}{D_{pe}W_bN_b} \exp\left(\frac{\Delta E_v}{kT}\right). \quad (2.50)$$

In both cases gain is possible regardless of the relative dopant concentrations in the base and emitter.

Hence, HBTs fabricated in a combinatory material system that has a large valence band offset can exhibit significant increases in  $\beta_{max}$  over homojunction devices.

Furthermore, the conduction band spike can serve to impart extra kinetic energy to electrons diffusing from emitter into base and allow minority carrier velocities in the base higher than thermal values[20]. The base transit time is reduced and the device can operate faster (i.e. at higher frequencies).

Some holes will be back injected into the emitter from the base, due to the forward bias of the emitter-base junction. This is  $I_{bp}$ , a component of the base current,  $I_b$ . Since

many HBTs are not planar technologies like silicon BJTs there must be a mesa structure. The intrinsic device region is located under the area of the emitter–base region in such a device. The exposed extrinsic base surface then adds a surface recombination current component to the base current,  $I_{b,\text{surf}}$ . This has particular relevance to the topic of this thesis. The physical processes involved in this are discussed further in Chapter 4. Other components of the base current are the interface recombination current at the base contact,  $I_{b,\text{cont}}$ , the bulk recombination current in the base,  $I_{b,\text{bulk}}$ , and the space–charge recombination current in the emitter–base junction depletion region,  $I_{b,\text{scr}}$ [23]. Due to the inherently statistical nature of recombination currents, and the fact they can be a limiting factor on device performance (see below), they are a significant contributor to device noise in an HBT.

Surface recombination in the depleted base region of the emitter–base junction will reduce the base transport factor,  $\alpha_T$ . Since InGaAs has a *surface recombination velocity* (a form of recombination rate, see Chapter 4) three orders of magnitude smaller than GaAs it is a better choice of material for the base of an HBT. The surface recombination current contribution to the base current,  $I_{b,\text{surf}}$  is a function of the emitter perimeter to area ratio and so has a larger relative affect in smaller devices. Thus smaller devices can be achieved in InGaAs/InP allowing for lower current operation and reducing parasitic capacitances. The noise created by recombination events is also reduced.

The recombination velocity of metal–semiconductor junctions is estimated to be  $2 \times 10^7 \text{ cm s}^{-1}$ [23]. While this is considerably higher than even an un–passivated GaAs surface the contribution of this to overall base current is much smaller, since the contacts are likely to be fabricated in a location removed from the intrinsic device area. The excess carrier concentration decreases rapidly with distance from the emitter–base junction.

The bulk recombination current  $I_{b,\text{bulk}}$  is determined by the recombination rates per unit volume of the three major recombinative processes. Radiative recombination (rate,  $U_{\text{rad}}$ ) is the process by which an electron and hole pair recombine directly with energy and momentum conserved through the emission of a photon. This is far more common in materials with direct bandgaps (e.g. III–V semiconductors) than indirect bandgaps (e.g. silicon). Shockley–Read–Hall (SRH) recombination (rate,  $U_{\text{SRH}}$ ) is the process by which an electron jumps from the conduction to valence bands via an intermediary state within the bandgap arising from a discontinuity or impurity in the lattice. The energy and momentum are conserved by the creation of a phonon. Auger recombination (rate,  $U_A$ ) is the process by which an electron recombines and transfers its energy to other electrons in the conduction band. This is most common in situations like the base of an Npn HBT where dopant concentrations are very high. Expressions for these recombination rates

can be given as

$$U_{\text{rad}} = \frac{\Delta n}{\tau_{\text{rad}}}, \quad (2.51)$$

$$U_{\text{SRH}} = \frac{\Delta n}{\tau_{\text{SRH}}} \quad (2.52)$$

and

$$U_{\text{A}} = \frac{\Delta n}{\tau_{\text{A}}}, \quad (2.53)$$

where  $\tau_{\text{rad}}$ ,  $\tau_{\text{SRH}}$  and  $\tau_{\text{A}}$  are the effective lifetimes of the three processes and  $\Delta n$  is the excess carrier concentration. Thus an effective electron minority carrier lifetime in the base  $\tau_{\text{n}}$  can be defined in the equation for the total recombination rate

$$U = U_{\text{rad}} + U_{\text{SRH}} + U_{\text{A}} = \frac{\Delta n}{\tau_{\text{n}}} \quad (2.54)$$

and from (2.51), (2.52) and (2.53)

$$\tau_{\text{n}} = \left( \frac{1}{\tau_{\text{rad}}} + \frac{1}{\tau_{\text{SRH}}} + \frac{1}{\tau_{\text{A}}} \right)^{-1}. \quad (2.55)$$

This can be considered the average time between electron recombination events in the bulk device. If  $I_{\text{b,bulk}}$  is the dominant component of  $I_{\text{b}}$  then it is possible to write

$$\beta = \frac{I_{\text{c}}}{I_{\text{b,bulk}}} = \frac{\tau_{\text{n}}}{\tau_{\text{b}}} \quad (2.56)$$

where  $\tau_{\text{b}}$  is the minority carrier transit time across the base. Typical values of  $\tau_{\text{n}}$  and  $\tau_{\text{b}}$  for an AlGaAs/GaAs HBT are of the order of 1 ns and 0.01 ns, respectively[23].

## 2.5 The Hall Effect in Semiconductors

The Lorentz force was discussed in Chapter 1. This phenomenon can be used to great advantage in semiconductor materials to measure the carrier concentration. The resistivity  $\rho$  is given by

$$\mathcal{E} = \rho J, \quad (2.57)$$

the reciprocal, conductivity, is  $\sigma = 1/\rho$ , and also

$$\nu_d = \mu_{\text{n,p}} \mathcal{E}, \quad (2.58)$$

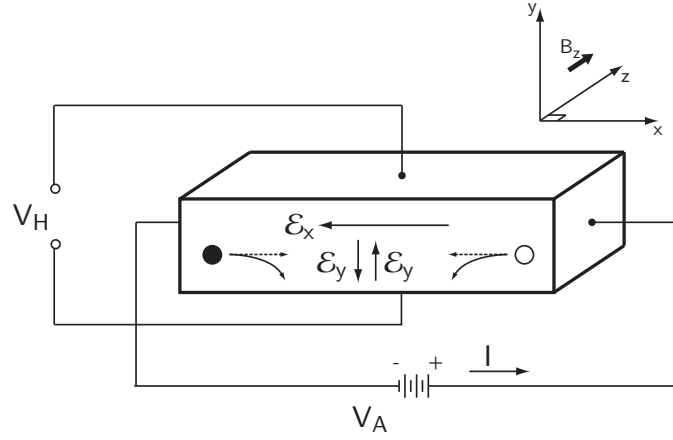


**Figure 2.12:** Hall effect in an n-type semiconductor (adapted from [63])

$$J = nq\nu_d \quad (2.59)$$

where  $\nu_d$  is the *drift velocity*,  $\mathcal{E}$  is the electric field and  $J$  is the current density. It can then be shown that

$$\rho = \frac{1}{\sigma} = \frac{1}{q(\mu_n n + \mu_p p)} \quad (2.60)$$

Thus, if  $n \gg p$ ,

$$\rho \simeq \frac{1}{q\mu_n n}. \quad (2.61)$$

A typical setup for measuring mobility is shown in Figure 2.12. The bias applied to the block of n-type semiconductor material causes an electric field along the x-direction,  $\mathcal{E}_x$ . The external magnetic field applied to the block along the z-axis,  $B_z$ , causes a component of electric field  $\mathcal{E}_y$  as the electrons collect at the bottom side of the block. This electric field is the Hall field and it exactly balances the Lorentz force (according to  $F = q\mathcal{E}$ )[63]. Thus

$$\mathcal{E}_y = (V_H/W) = R_H J_x B_z \quad (2.62)$$

where  $V_H$  is the Hall voltage and  $R_H$  is the (material dependent) Hall coefficient. The Hall mobility is defined as the product of the Hall coefficient and the conductivity,

$$\mu_H = |\sigma R_H|. \quad (2.63)$$

## 2.6 Figures of Merit for Transistor Magnetic Sensors

The critical figure of merit for all sensors is the *transduction efficiency*. In a BMT this is the magnetosensitivity,  $S$ . Defined as the ratio of the change in output signal to the change in applied field, this gives

$$S_A^I = \left| \frac{\partial I_c(B)}{\partial B} \right| \quad [AT^{-1}] \quad (2.64)$$

for the *absolute* current magnetosensitivity and

$$S_R^I = \left| \frac{1}{I_c(0)} \frac{\partial I_c(B)}{\partial B} \right| \quad [T^{-1}] \quad (2.65)$$

for the *relative* current sensitivity at fields  $B \rightarrow 0$ . The voltage sensitivities are dependent on the values of the collector resistors such that  $S_{(A,R)}^V = R_C S_{(A,R)}^I$  [VT<sup>-1</sup>] although a high output resistance would render voltage and current sensitivities numerically equivalent. The minimum field detectable by a BMT is determined by the device noise power spectral density. The magnetic field which is equivalent to the noise in the frequency range  $\Delta f$  is

$$B_{eq} = N/S \quad (2.66)$$

where  $N$  is the current or voltage noise and  $S$  is the relevant magnetosensitivity[47]. At this point the signal-to-noise ratio is unity. Another figure of merit is the *offset*. This is the static output current when the applied field is zero.

In this work the change in  $\beta_{dc}$  was used in analogy to earlier work[64] instead of  $I_c$ . This is equivalent to a sensitivity in  $I_c$ , since  $I_c$  is linearly proportional to  $\beta_{dc}$ .

The *dynamic range* of a sensor is a measure of the smallest unit that can be detected compared to the largest. In this work the signal-to-noise ratio was calculated as a measure of this. This is given by

$$\text{SNR(dB)} = 20 \log_{10} \left( \frac{A_{\text{signal}}}{A_{\text{noise}}} \right) \quad (2.67)$$

where  $A_{\text{signal}}$  is the amplitude of the maximum transduction (the maximum relative change in normalised  $\beta_{dc}$ ) and  $A_{\text{noise}}$  is the equivalent amplitude of the noise.

## 2.7 Charge Transport and Magnetic Field

The uses of Hall bars to study material properties has already been mentioned[44, 45]. Magnetotransport is also often used to study charge transport phenomena in semicon-

ductors, such as boundary scattering[65], as well as spin-based effects[66]. In early work the effects of magnetic field on current transport in HBTs were used to confirm the results of a hot electron spectroscopy technique in AlGaAs/GaAs[67, 68]. Further studies into the electron effective mass in InP/InGaAs HBTs at liquid helium temperatures (4.2 K) were also carried out using magnetic techniques[69].

A study was conducted on the effects of applied magnetic field on the current transport properties of InAlAs/InGaAs HBTs[64]. It was noted that there is a distinction between nonequilibrium transport of electrons with excess kinetic energy through the base (where the base width is less than the nonequilibrium electron mean free path) and drift-diffusion transport where carriers scatter as they traverse the base. With a series of small emitter width devices with multiple base widths it was shown that as a magnetic field applied perpendicular to the main current transport direction (i.e. the direction normal to the semiconductor surface) is increased the current gain of the device decreases. This can be attributed to the increased path length caused by Lorentz deflection of the carriers in the base. All electrons travelling through the base were accelerated in a circular path in the  $x$ - $z$  plane of the device, as shown in Figure 2.13. The current transport regime was thus changed from quasi-ballistic to drift-diffusion and recombination rates increased by applying a field of up to 8 T. This had a deleterious effect on the current gain of the device.

The cyclotron radius for an electron moving in a magnetic field is given by

$$r = m^*v/eB_{\perp} \quad (2.68)$$

where  $m^*$  is the electron effective mass,  $v$  is its velocity and  $B_{\perp}$  is the applied field perpendicular to the direction of motion. If either the field was increased or the base length sufficiently increased that the cyclotron radius became comparable with the base length, the carriers could then only exit the base by scattering events and the current gain dropped to almost zero. To produce this effect with a hot electron ( $v = 10^8 \text{ cm s}^{-1}$  and  $m^* = 0.041m_0$ ) in a device of base length 50 nm a field of 4 T was applied. A related decrease in average excess kinetic energy caused by increased scattering was also seen to increase the transistor breakdown voltage as fewer had energy above the threshold for impact ionisation.

Furthermore, a field applied parallel to the direction of current transport was seen to improve current gain. Recombination in the extrinsic base is a source of base current which is detrimental to transistor current gain and electrons which scatter in the intrinsic device may then travel out of it. It was suggested that the scattering angle was offset

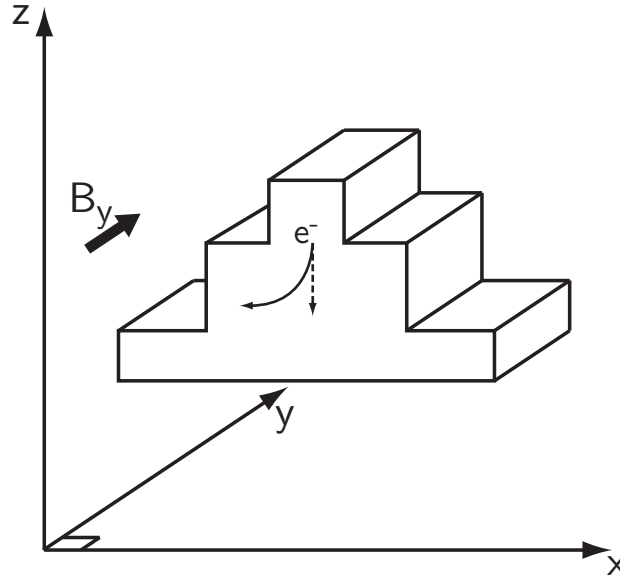


**Figure 2.13:** Electrons in an HBT accelerated in a circular path by an applied magnetic field perpendicular to the normal.

by the parallel magnetic field. It kept the electrons in a smaller volume because of the helical path ensuing from the new (post-scatter) perpendicular component of the velocity. Thus electrons that would normally have scattered into the extrinsic device region and recombined were collected. All of the experiments described above were carried out at a temperature of 4.2 K[64].

The mobility of minority electrons in the base of an InGaAs/InP HBT was also studied using the effects of a perpendicular applied magnetic field[70, 71]. Magnetotransport in a npn HBT is described by the modified drift-diffusion equations

$$\mathbf{J}_e = qD_e\nabla n - \mu_e\mathbf{J}_e \times \mathbf{B} + q\mu_en\mathbf{E} \quad (2.69a)$$

$$\mathbf{J}_h = -qD_h\nabla p + \mu_h\mathbf{J}_h \times \mathbf{B} + q\mu_hp\mathbf{E} \quad (2.69b)$$

(see also (2.8), the 1-dimensional equivalent) where  $\mathbf{J}_e$ ,  $\mathbf{J}_h$ ,  $D_e$ ,  $\mu_e$ ,  $D_h$  and  $\mu_h$  are the electron and hole current densities, the electron diffusion constant and mobility and the hole diffusion constant and mobility, respectively,  $n$  is the electron minority carrier concentration,  $p$  is the hole majority carrier concentration and  $q$  is the electronic charge. The vector magnetic field  $\mathbf{B}$  was applied along the x-direction and  $\mathbf{E}$  is the electric field.

In a base without any confinement in the lateral directions and a length which was long compared to the momentum relaxation mean free path (in this case, 400 nm) it was shown that the current density in the  $z$ -direction  $J_{ez}$  is

$$J_{ez} = q \frac{D_e + (\mu_e n / \mu_h p) D_h}{1 + \mu_e^2 B^2} \frac{\partial n}{\partial z} = q D^*(B) \frac{\partial n}{\partial z}. \quad (2.70)$$

This is equivalent to the diffusion current without magnetic field but with a field dependent diffusion constant. Assuming that the emitter injection efficiency is high in an InP/InGaAs HBT (which the authors had shown in earlier work[20]) and that the base current is predominantly due to recombination, it was shown that

$$\frac{\Delta I_b(B)}{I_b(B=0)} = \mu'^2 B^2 \quad (2.71)$$

where  $\Delta I_b(B)$  is the change in base current induced by the magnetic field,  $I_b(B=0)$  is the base current when the applied field is zero and  $\mu'$  is the magnetotransport mobility of electrons in the base. Thus the gradient of a plot of the normalised change in base current against applied field strength gave the minority carrier mobility. An experiment was carried out with an InP/InGaAs HBT with a 400 nm base length with a magnetic field of up to 0.6 T. The obtained value of  $3300 \text{ cm}^2 \text{ V}^{-1} \text{ s}^{-1}$  for  $N_A = 3.1 \times 10^{19} \text{ cm}^{-3}$  agreed well with results from the standard zero field time of flight technique which would predict a result of just under  $3300 \text{ cm}^2 \text{ V}^{-1} \text{ s}^{-1}$ [72] suggesting that the magnetotransport mobility and electron minority carrier mobility were numerically similar.

This technique was used successfully to determine the minority carrier mobility in  $p^+$ GaAs doped with carbon at different concentrations and to compare the results with theoretically calculated values[73]. Furthermore, given the relation

$$\beta = \frac{\tau_n}{\tau_b} = \left( \frac{2\mu_e k T}{e W_b^2} \right) \tau_n \quad (2.72)$$

where  $\beta$  is the DC current gain,  $\tau_n$  is the minority electron lifetime in the base,  $\tau_b$  is the base transit time,  $k$  is Boltzmann's constant,  $T$  is the absolute temperature and  $W_b$  is the base length, it was possible to calculate the minority lifetime. Results agreed well with values calculated by other means[74]. The mobility and lifetime measurements were used to characterise  $\text{Ga}_{0.52}\text{In}_{0.48}\text{P}/\text{Al}_x\text{Ga}_{1-x}\text{As}/\text{Ga}_{0.52}\text{In}_{0.48}\text{P}$  DHBT devices in comparison with a more typical  $\text{AlGaInP}/\text{GaAs}/\text{GaInP}$  DHBT structure[75]. The technique was also used to measure the increase in bulk recombination (from the decrease in minority carrier lifetime) in a carbon doped GaAs base layer annealed at  $600^\circ\text{C}$  for various times[76].

Significant reductions in device performance were observed.

Studies into the surface recombination properties of AlGaAs/GaAs HBTs were conducted by probing the devices with a magnetic field applied along the normal of the wafer surface (i.e. parallel to the primary direction of electron flow)[77]. This allowed for direct measurement of the surface recombination in as-fabricated devices. From the continuity equations for a transistor in a magnetic field[78], for an HBT with a parallel field (oriented along the  $z$ -direction) there is a diffusion equation

$$\frac{D_e}{1 + (\mu_e B_z)^2} \left( \frac{\partial^2 n}{\partial x^2} + \frac{\partial^2 n}{\partial y^2} \right) + D_e \frac{\partial^2 n}{\partial z^2} - \frac{n}{\tau_e} = 0. \quad (2.73)$$

Thus the diffusion constant along the  $x$ - and  $y$ -directions was reduced by the applied magnetic field. For a device in which the emitter width in the  $y$ -direction is large

$$\frac{\partial^2 n}{\partial \tilde{x}^2} + \frac{\partial^2 n}{\partial z^2} - \frac{n}{D_e \tau_e} = 0, \quad (2.74)$$

where  $D$  is the diffusion constant (at  $B = 0$ ) and

$$\tilde{x} = \sqrt{1 + (\mu_e B_z)^2} x \quad (2.75)$$

which is the effective scaling of the  $x$ -axis due to the effect of the applied field,  $B_z$ . The current density in the  $x$ -direction, that is the current component which flows from the intrinsic base to the extrinsic base, is

$$J_x = \frac{e D_e}{\sqrt{1 + (\mu_e^2 B^2)}} \frac{\partial n}{\partial \tilde{x}}. \quad (2.76)$$

An AlGaAs/GaAs HBT was fabricated and the response to parallel applied magnetic field was measured. In the accompanying experiments the current gain of the device was seen to increase with increasing field in the  $z$ -direction and decrease with increasing field applied in the  $x$ -direction. Using an analytical model based on (2.74)–(2.76) and the procedure outlined in previous studies[20] to obtain the mobility and the carrier lifetime it was possible to determine a surface recombination velocity from the change in current gain with applied field strength. The minority carrier lifetime and velocity of surface recombination events were found to be 40 ps and  $1 \times 10^7 \text{ cm s}^{-1}$ , respectively. Magnetic fields of up to 5 T were employed to observe these effects.

Analytical descriptions of the diode, the bipolar transistor and the heterojunction

bipolar transistor have been produced in this chapter. Furthermore, some consideration has been given to the factors which cause non-ideal response in the measurement of real devices. The effect of the magnetic force on charge carriers has been described for a Hall bar and studies into the effect in HBTs have also been related. In addition, the figures of merit for magnetic sensors have been introduced.

## 3 HBT Fabrication

This chapter details the fabrication of the InP/InGaAs single heterojunction bipolar transistors (SHBTs) that were used to detect magnetic field. The wafer structure and band diagram is discussed in reference to the high frequency devices for which it was designed. After this there is a general discussion of the fabrication processes used during the course of the project.

The results of the ohmic contact optimisation are presented before the HBT fabrication process flow is given. The design considerations for the device and wafer layouts are considered. Presented at the end are the in-line and end-of-line testing schemes for the fabricated HBTs and some results typical of the fabricated devices.

### 3.1 Wafer Epilayer Structure

The epilayer structure for the wafers used in the project, grown by metal organic vapour phase epitaxy (MOVPE) for the fabrication of Npn InP/InGaAs single heterojunction bipolar transistors are shown in Table 3.1. The topmost layer is the emitter cap which provides a very low Schottky barrier for fabricating metal contacts to the emitter with an ohmic response, utilising the smaller bandgap of InGaAs and very high dopant concentration. The second, more lightly doped cap layer decreases the access resistance of the emitter by providing a smaller potential barrier step between upper cap layer and emitter layer. The top layer of InP is highly doped to provide large numbers of electrons for injection into the base. A secondary benefit may be bandgap narrowing which allows for a slight potential barrier reduction between the layer and the layer above. The lower layer of InP is more lightly doped to reduce charge storage which leads to intrinsic base-emitter junction capacitances. Extraneous device capacitances and resistances (parasitics) are detrimental to high frequency device performance. As this project was undertaken to prove the operation of a magnetic field sensor which could be integrated into high speed circuitry with somewhat higher demands on native device performance, the wafers were designed with this in mind.

The undoped InGaAs spacer layer is to reduce the possibility of diffusion of the base

**Table 3.1:** Layer structure for InGaAs/InP HBT wafers. The wafers were grown from Fe doped, semi-insulating, (100) oriented InP substrates using MOVPE by the EPSRC National Centre for III-V Technologies at the University of Sheffield.

Layer	Dopant Concentration/cm <sup>-3</sup>	Thickness/Å	Type
n-In <sub>0.53</sub> Ga <sub>0.47</sub> As	3 x 10 <sup>19</sup> :Si	750	Cap
n-In <sub>0.53</sub> Ga <sub>0.47</sub> As	2 x 10 <sup>19</sup> :Si	2500	Cap
n-InP	1 x 10 <sup>19</sup> :Si	800	Emitter
n-InP	3 x 10 <sup>17</sup> :Si	2500	Emitter
i-In <sub>0.53</sub> Ga <sub>0.47</sub> As	—	50	Spacer
p-In <sub>0.53</sub> Ga <sub>0.47</sub> As	> 1 x 10 <sup>19</sup> :Zn	750	Base
n-In <sub>0.53</sub> Ga <sub>0.47</sub> As	2 x 10 <sup>16</sup> :Si	3000	Collector
n-InP	1 x 10 <sup>16</sup> :Si	300	Etch Stop
n-In <sub>0.53</sub> Ga <sub>0.47</sub> As	3 x 10 <sup>19</sup> :Si	4000	Sub-collector
n-InP	1 x 10 <sup>19</sup> :Si	2000	Buffer

dopant into the emitter region and may become p-type during the growth process. This effective series resistance between the emitter and the base can also increase the emitter to collector breakdown voltage,  $BV_{ce0}$ , (see §2). Zinc, the p-type dopant for base layer is a mobile species in III-V materials[79, 80]. The base is doped as highly as possible, which with the technologies employed by the wafer grower, the EPSRC National Centre for III-V Technologies at the University of Sheffield, was at a concentration of  $1 \times 10^{19} \text{ cm}^{-3}$ . The base layer thickness should be less than a tenth of the diffusion length of minority carriers in the base (see §2), which for MOVPE InGaAs:Zn with dopant concentration  $1 \times 10^{19}$  is  $\sim 2 \mu\text{m}$ [81]. The thinner the base, the higher is  $\alpha_T$ . A higher dopant concentration also affects  $\alpha_T$  by increasing the recombination and scattering rates in the base. In RF devices maximum frequency of operation improvements can be realised both by scaling the base thickness and reducing the base resistance.

The upper collector layer is lightly doped InGaAs as there is no requirement for high carrier concentration. Thus the base-emitter capacitance is reduced. High concentrations of carriers are unnecessary in the collector because the carriers are accelerated from the base. The collector region will also be the dielectric in a capacitor between the base metal contacts and the highly doped sub-collector so excess carriers are undesirable. A secondary benefit of this is the absence of any bandgap narrowing in the collector. The breakdown voltages caused by ionisation discussed in §2 are determined by the bandgap of the collector, amongst other parameters. The sub-collector layer is highly doped for

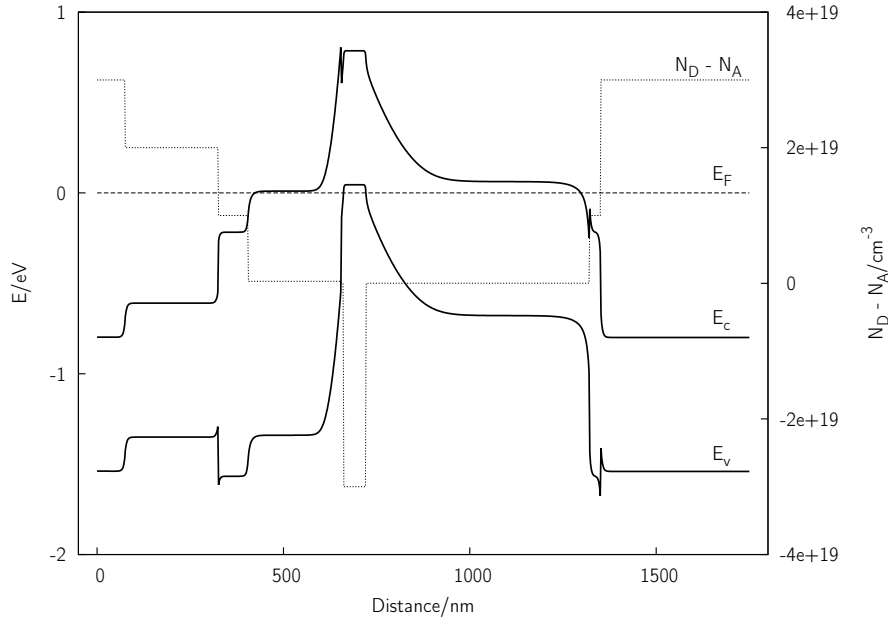


**Figure 3.1:** Band diagram of the HBT layer structure shown in 3.1 as calculated using Schrödinger–Poisson self-consistent modelling.

the same reason as the emitter cap, to facilitate the formation of ohmic contacts. To improve the quality of the active device layers grown on the InP substrate a 2000 nm buffer layer of InP is grown using the same growth conditions as the uppermost layers.

Figure 3.1 displays the band structure of the epilayers described above. A numerical modelling program for the self-consistent Schrödinger–Poisson equations was used to generate the data for the layer structure[82]. Written by Gregory Snider[83] the freeware simulation program *1DPoisson* allows for various compound and elemental material systems, including ternaries with arbitrary alloy composition fractions. Much of the data in the materials specification file used by the 1DPoisson program was provided by Karol Kalna and others of the Device Modelling Group of the Department Electronics and Electrical Engineering. For the material system of this project some of the physical parameters were accessible from the ternary data for InGaAs on GaAs as provided in the materials file with the composition fraction  $x = 0.53$ . The conduction band offset of lattice-matched  $\text{In}_{0.53}\text{Ga}_{0.47}\text{As}$  on InP ( $\Delta E_c = -0.250 \text{ eV}$ ) was obtained from the relevant literature[84].

## 3.2 Fabrication Processes

Semiconductor device fabrication involves combinations of several basic techniques, or variations on those techniques. The most important of such techniques is that of lithography as this is where device geometries are defined for both metallisation and etching (which are themselves further processes), amongst other things. Now follows a description of each process used in fabricating the large area HBTs used as the basis for the project.

### 3.2.1 Sample Preparation

The relatively high cost of InP wafers with their requirement for multiple epilayers was the main factor in determining that small sample pieces should be used for the project. Coupled with the ability to complete more design iterations with more, smaller samples, an optimum size of 10 mm x 10 mm was chosen. This allowed for fourteen pieces from a single 50 mm diameter wafer, plus some spare pieces for etch tests, etc. The wafer was scribed using a diamond-tipped scribing tool (rather than a pen) to keep the size and shape regular.

An ultrasonic cleaning bath was used to clean the samples through the mechanism of cavitation. The small bubbles formed in the surface collapse at high speed providing a physical mechanism for particulate and contaminant removal[85]. With its very high solvency[86], acetone is the ideal solvent with which to clean organic contaminants from semiconductor substrates. It is an organic solvent (propanone,  $\text{CH}_3\text{COCH}_3$ ) and hence will not react with any of the materials used in III–V device fabrication. Since acetone may leave a residue when it evaporates, a transfer to isopropyl alcohol (IPA or propan-2-ol,  $\text{C}_3\text{H}_8\text{O}$ )—similarly unreactive—was performed while limiting any opportunity for evaporation. Further ultrasonic bathing in IPA and then a reverse osmosis (RO) water rinse to remove any polar contaminants completed the procedure.

### 3.2.2 Lithography

The procedure for applying patterning a semiconductor wafer (or part-wafer sample) is similar for both photo- and electron beam (ebeam) lithography. After cleaning, a polymer based resist is applied to the sample. The sample, which is attached to a spinner in a laminar air flow (LAF) cabinet by means of a vacuum, is then rapidly accelerated to a given rotational speed for a pre-determined time. The thickness of the now uniform layer of resist is determined by spin speed and the fluid properties of the resist[87]. For small, rectangular samples, the discontinuous nature of the edges (particularly at the corners) causes an increase in surface tension and hence there collects a thicker layer of

resist. This *edge bead* generally renders the outer regions of the piece of semiconductor unusable.

Following on from the spinning of resist, a pattern must be written into it using a lithography tool. The pattern is then developed using a solvent to selectively remove either the exposed (positive tone) or un-exposed (negative tone) areas of the thin film. A CAD application (here *L-Edit*, Tanner Research, Inc., California, USA) is used to design the desired pattern. After rinsing away the solvent, any residual resist scum in the developed areas can be removed using a barrel asher. This generates a low power oxygen plasma in a barrel shaped chamber. The reactive oxygen ions etch the resist at a rate insignificant to the remaining film but which cleans off the scum. (See §4 for a further discussion on plasma processing.)

### Electron Beam Lithography

Electron beam lithography creates a pattern in resist with a focussed electron beam using a source of electrons (the electron gun), an accelerating voltage and a system of lenses, together with x- and y-deflection coils. The sample itself is clamped to a moving stage with stepper motors (again for both x- and y-directions) and an attached back-scatter detector for detecting alignment marks (see below). All of these are contained in a vacuum chamber in an ebeam tool. In the initial stages of the project a Leica Electron Beam Pattern Generator 5 (EBPG5) was used for the procedure although later a newer Leica VB6 Ultra High Resolution Extremely Wide Field (UHR EWF) tool was employed in the James Watt Nanofabrication Centre (JWNC) at the University of Glasgow.

After creating a pattern file in the CAD software proprietary format, it was exported in the universal GDSII format. Another commercial application, *CATS* (Synopsys Inc., California, USA) then fractured the pattern into trapezia, as the format required by the ebeam tool. Registration of the fractured pattern with a given sample size, dose, beam size and resolution was handled by *Belle*, a bespoke software tool developed at the University of Glasgow. It was also possible to align subsequent layers to the first metallisation layer, provided appropriate metal markers were deposited in the first instance. This procedure was also handled by *Belle* and utilised the ebeam tool's back-scatter detector to locate the original markers. The *Belle* file contained information about the relative position of, and allowed accurate registration of, the new pattern to the original metal layer.

For this project the ebeam resist of choice was poly-methyl methacrylate (PMMA) which is available in different molecular weights and can be made in arbitrary solutions with o-xylene (C<sub>8</sub>H<sub>10</sub>) to obtain differing viscosities. Once spun, the thin film must be

baked to evaporate the solvent. When exposed to a calibrated dose of electrons (measured in  $\mu\text{C cm}^{-2}$ ) the long chains of the polymer are broken. This allows the exposed regions to be selectively developed by immersion in a solvent that preferentially dissolves the short chain molecules. For PMMA, the developer is a solution of 4-methyl pentan-2-one (methyl isobutyl ketone or MIBK,  $\text{C}_6\text{H}_{12}\text{O}$ ) and IPA. To facilitate consistent and effective metal lift-off with PMMA two layers are spun and baked consecutively. The lower layer is a higher concentration, lower molecular weight resist solution. This makes it both thicker and more sensitive to ebeam dose. The upper layer is then both thinner and less sensitive. The result is that for a given dose the lateral dimensions of the exposed region of the lower layer will be larger than those of the upper region and the lower region will be thicker than the upper. This gives the familiar lip and undercut of the resist lift-off profile.

The resist profile is dependent on a combination of concentration and spin speed (i.e. resist thickness), molecular weight (sensitivity to dose), ebeam dose, developer dilution and development time.

### Photolithography

Photolithography creates a pattern in resist using ultraviolet (UV) light. The polymer in (positive tone) photoresists is broken down by the UV photons. Once the thin film has been spun onto a wafer, a pre-patterned mask is placed over the sample. When the sample is correctly aligned to the pattern on the mask, the sample is brought into contact<sup>1</sup> with the mask and a UV lamp illuminates only those parts where the mask is transparent. Thus a pattern of exposed and un-exposed areas is transferred to the resist. The procedure was carried out on a Karl Süss MA6 mask aligner housed in the JWNC.

The masks required for patterning the resist were made using the ebeam tool described above. Technical staff were responsible for the processing of masks beyond the CAD design and ebeam job submission. The process consisted of patterning a quartz mask with chrome on one surface and ebeam resist on top of the chrome. The chrome was then etched away using a chemical wet etch and then the remaining resist removed in a barrel asher leaving the original pattern transferred into the chrome. Multiple copies of the chrome master could then be made using a photolithography technique and ferric oxide (iron oxide,  $\text{Fe}_2\text{O}_3$ ) coated quartz plates (ferric oxide being opaque to UV light).

The resist used for this project was Shipley S1818. This is a positive tone resist which is photosensitive from 350 nm to 450 nm[88]. The thickness could be controlled

---

<sup>1</sup>This is not always true, as there exist enhanced resolution techniques which can involve further lensing or immersion.

by the spin speed. Since the proximity of the ferric oxide of mask to the surface of the resist was paramount for faithful reproduction of the pattern in the resist (due both to the divergence of the non-collimated light source and the fringing effects of Fresnel interference at the edges of the pattern's shapes) the edge bead thickness had to be kept to a minimum. Two methods employed to achieve this were to ensure as large an acceleration up to the desired spin speed as possible and to remove as much excess resist as possible with careful pipetting. The solvent in the resist was driven out using a hotplate. After exposure to UV light at 365 nm for a calibrated time the exposed resist was then developed using Shipley Microposit Developer Concentrate (a metal ion containing developer).

Obtaining a lift-off profile in photoresist was attempted in two different ways. Originally a lift-off resist was spun onto the sample before the photoresist. This resist (Microchem LOR-10A) was not photosensitive and an undercut could be developed in it once the S1818 had been exposed, developed and then cured in an oven. This technique, however, produces the edge bead thickness of two distinct resist layers and leads to poor pattern reproduction. Instead a soak in chlorobenzene ( $C_6H_5Cl$ ) immediately after exposure was employed. This caused a hardening of the upper layer of the *un-exposed* polymer. Once developed the resist profile exhibited a lip of hardened polymer and an undercut created by an increased development time.

### 3.2.3 Metallisation

Depositing metal onto semiconductor wafers or samples can be carried out in several different ways including thermal or electron beam evaporation and sputtering. Electron beam evaporation was the method employed in this project, using both a Plassys MEB 450 Electron Beam Evaporator (*Plassys I*) and a Plassys MEB 550S (*Plassys II*). Firstly a sample appropriately processed was clamped to the holder specific to the evaporation tool required. Once loaded upside down into the vented loadlock and then pumped down to the process pressure (in all cases below  $2 \times 10^{-6}$  Torr) the desired metal (according to the recipe chosen on the PC control software) was selected and its crucible was heated past melting point by a beam of electrons. Once a steady deposition rate had been attained, the shutter that blanks the holder and sample was opened. The metal evaporated up onto the wafer where it condenses. Metal is thus deposited on the wafer regions without resist (as defined by lithography and then development), where it should adhere. The resist covered regions were not metallised as the lift-off profile allowed for the resist to be easily and consistently dissolved in acetone, removing the unwanted metal.

Plassys I is an older model with a base pressure of  $1 \times 10^{-7}$  Torr maintained by a

diffusion pump where Plassys II has a lower base pressure by a factor of 10, as generated by its cryogenic vacuum pump. The metals available for deposition by evaporation were Al, Au, Ge, Ni, Pd, Pt, Ti and NiCr.

The JWNC facility also houses a modified thermal evaporator into which small boats of any metal can be placed. These boats are then evaporated using resistive heating with a manually controlled applied voltage. Although this method was tried for other metals, it was found to be comparatively unreliable and inconsistent.

Since the metal contacts to the semiconductor in this project were all intended to have an optimised resistance a de-oxidation step was performed before metal deposition. The native oxide layer which can be found on the surface of III-V semiconductors presents a barrier to electrons as they pass from metal to semiconductor and should be removed. A standard process of a short dip in a dilute solution of hydrochloric acid (HCl) in RO water was employed for this purpose[89].

To facilitate the bonding of wires (see below) to access the device, bond pads were also deposited. These consisted of an adhesion layer of 50 nm of Ti and then 300 nm of Au.

### 3.2.4 Etching

III-V semiconductors can be etched using either dry or wet etching. Dry etching uses a plasma to remove any material that is un-masked<sup>2</sup>. Ions in the plasma are accelerated towards the surface using the DC self-bias in the system or, in the case of remote plasmas, by an applied bias to the sample and platen. A full description of plasma processing is given in Chapter 4. Dry etch processes are a combination of a physical process, whereby the actual bombardment of the semiconductor by ions etches the semiconductor away, and a reactive process, where the chemical reactivity of the ion removes the material at the surface. Depending on the process conditions, the plasma constituents and the material, one process may dominate. The particles that are etched away are prevented from redeposition by the low process pressure in the chamber. Dry etching can be isotropic or anisotropic and varyingly crystallographic, depending on the chemistry and plasma chamber conditions. Most commonly they are directional and can be used to fabricate nearly vertical sidewalls over large  $\sim 2\ \mu\text{m}$  scales, with high aspect ratios[90].

Wet etching III-V materials involves liquid chemical etchants, usually acid solutions in water. An *oxidising agent* creates an oxide layer at the material surface and then a *complexing agent* removes the oxide in a reduction reaction[91]. Oxides of GaAs derived alloys are amphoteric, meaning that either a base or an acid can be used to remove

---

<sup>2</sup>Masking can be achieved using a plasma resistant resist or with a deposited and patterned dielectric.

them[92]. Once the oxide has been formed it is dissolved by the complexing agent in a continuous process and the ratio can be adjusted to give the desired dissolution rate. It should be noted that an oxide layer measuring  $\sim 5$  nm remains on the surface after removal from the etchant[92]. The favoured crystallographic directions and the resulting etch profiles have been investigated in InGaAs[93] and InP[94]. An important consideration when employing a wet etch process is then that the sample surface must see constantly replenished etchant to avoid a diffusion-rate limited etch. Agitation of the sample in the etchant is a must. Wet etching was preferred for this project because of a desire both to eliminate as far as possible any damage to the mesa surfaces as may be caused by the physical element of dry etching processes and for selectivity between the  $\text{In}_{0.53}\text{Ga}_{0.47}\text{As}$  and InP epilayers. Dry etch chemistries that selectively etch between indium containing alloys are not common[95].

The selectivity needed to consistently and accurately achieve the correct etch depth in the InP/ $\text{In}_{0.53}\text{Ga}_{0.47}\text{As}$  HBT structure given in Table 3.1 was available with a orthophosphoric acid ( $\text{H}_3\text{PO}_4$ ), hydrogen peroxide ( $\text{H}_2\text{O}_2$ ) and water etchant for InGaAs and an orthophosphoric acid and hydrochloric acid etchant for InP. High selectivities have been reported for both[96].

### 3.2.5 Thin Film Deposition

Chemical vapour deposition (CVD) is a process by which a solid material can be deposited on the surface of a semiconductor. Reactant gases (precursors) are flowed into a reaction chamber which contains the (heated) semiconductor substrate and a chemical reaction takes place at the surface. The product of this reaction is a solid material which is useful for fabricating semiconductor devices, most commonly silicon dioxide ( $\text{SiO}_2$ ) or silicon nitride ( $\text{Si}_3\text{N}_4$  or  $\text{SiN}_x$ ) which are desired for their dielectric, resistive and passivating properties. Films deposited in this way are highly conformal over varying device topography. The different types of CVD employed in research into semiconductor devices include low pressure CVD (LP-CVD), which takes place in a reaction chamber in which the process pressure is low, ultra high vacuum CVD (UHV-CVD) and plasma enhanced CVD (PE-CVD), where the precursors are excited into a plasma in the chamber to assist the reaction.

For the purposes of this project, an insulating layer of  $\text{Si}_3\text{N}_4$  was used to access the device from the bond pads. The dry etch facility in the James Watt Nanofabrication Centre operates an Oxford Instruments Plasmalab System 100 ICP180  $\text{Si}_3\text{N}_4$  ICP-CVD system. ICP-CVD is inductively coupled plasma CVD. A dense, remote plasma was generated in the chamber using a coil with an RF power supply. The reaction of precursor

gases to form silicon nitride is given in (3.1).



This can lead to the incorporation of hydrogen into the dielectric[97] which is detrimental to device performance by causing extraneous surface traps[98]. A low hydrogen-content, room temperature  $\text{Si}_3\text{N}_4$  ICP-CVD deposition process had been developed by Zhou and co-workers at the University of Glasgow[99]. Whereas high temperature processes (e.g. PE-CVD) cause any resist on the sample to deform, low temperature deposition of  $\text{Si}_3\text{N}_4$  allowed for patterning using standard lithographical lift-off techniques. Since the deposition process is highly conformal, lift-off without a very large lower resist layer is prone to failure or at least inconsistency. Large lower layers are simple to achieve in photoresist, such as the process described above, but difficult in ebeam resists. The solution to this problem was found to be the spinning of a further layer of resist after the  $\text{Si}_3\text{N}_4$  was deposited. If this was baked in an oven at  $120^\circ\text{C}$  for 30 min there was an increase in the stress in the  $\text{Si}_3\text{N}_4$  film. Where there was resist both above and below the dielectric layer the stress caused it to crack. This cracking did not occur where the dielectric was deposited on the exposed semiconductor. The cracks facilitated consistent lift-off for films up to 250 nm in thickness. This process, developed in the department for other purposes, was further optimised in the completion of this work.

### 3.2.6 Bonding

Once fabricated, a semiconductor device must either have its operational parameters analysed (see below) or be incorporated into an external circuit. The normal method of building an external circuit in low volumes is using a lithographically defined, copper tracked printed circuit board (PCB) such as those made in the Electronics Workshop in the Department of Electronics and Electrical Engineering. To attach a device (or a set of devices) to the PCB it must first be fixed to a chip carrier (package) with an adhesive such as superglue or silver-DAG. The chip carrier can then either be soldered onto the PCB or inserted into a socket that is soldered onto the PCB. To connect terminals of a device to the leads of a chip carrier a wire bonding process is employed. A thin ( $20\ \mu\text{m}$ ) gold wire is welded onto a gold pad on the package using a combination of heat and ultrasonic energy. This *thermosonic* bonding involves a hard metal wedge with a hole from the back through to the base into which the wire is fed from a small drum and, ultimately, a clamp. A small tail of wire allows for the first bond to be made to the package by the wedge, which presses the wire down and applies the heat and ultrasound. This is known as bonding in the reverse direction. The forward direction can also be employed and, in

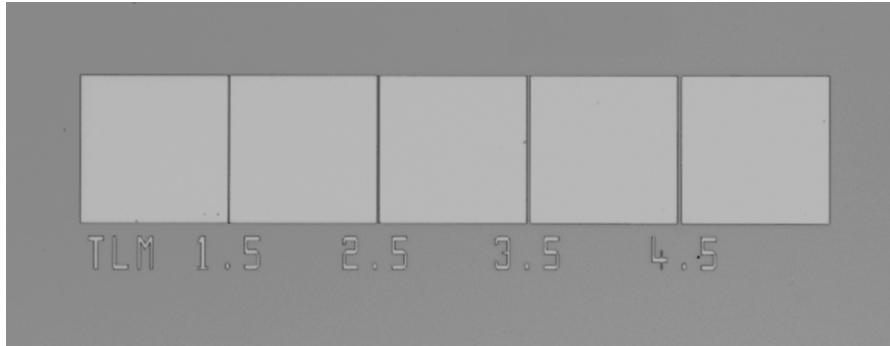


**Figure 3.2:** An optical micrograph of an ohmic contact TLM metallisation. The contacts pads measured  $150\ \mu\text{m} \times 150\ \mu\text{m}$ .

fact, is less prone to short-circuiting at the device pads[100]. The motion of the wedge as it withdraws from the first bond and the package is moved underneath it creates a loop of wire between the contacts. To break the wire after the bonding is complete the clamp closes and the wedge withdraws.

The bonding required for this project was carried out on a K&S Micro-Swiss thermosonic wire bonder. For much of the device testing and measurement where external circuits were necessary an 18-pin ceramic leadless chip carrier (LCC) was a satisfactory package. This allowed the use of a PCB socket to attach to the circuit.

### 3.3 Ohmic Contacts

Optimisation of the ohmic contacts to the device took place by first defining the metal pattern required using ebeam lithography. For the n-InGaAs layers the patterns could be defined on the emitter cap alone as this had the same alloy and dopant concentration as the sub-collector (where the collector ohmic contacts would be deposited). For the p-InGaAs base it was necessary to first etch down to the base layer. This was done using exactly the same etch that would define the emitter mesa (see below). The contact scheme used for the n-type material was Au/Ge based as used, for example, in [101] but optimised in the Department to Au/Ge/Au/Ge/Au/Ni/Au. Germanium is an n-type dopant in InGaAs. Figure 3.2 shows the ohmic metal transmission line measurement (TLM) metallisation as used to calculate the specific contact resistance  $R_c$  of both n-type and p-type contacts. Figure 3.3 shows the pattern used to measure the leakage current  $I_l$  due to diffusion of the p-type contacts through the thin base layer into the collector.

Anneal tests were carried out in a rapid thermal annealer (RTA). This process involved using an *Jipelec*, Jet First Processor RTA to quickly heat the sample to a given temperature for 60 s in an inert nitrogen environment. In annealing, the individual layers

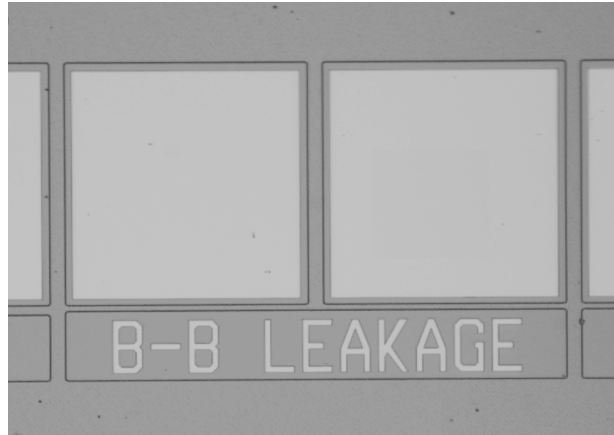


**Figure 3.3:** An optical micrograph of the p-type contact leakage current measurement patterns. The contacts pads measured  $150\ \mu\text{m} \times 150\ \mu\text{m}$  and their separation was  $20\ \mu\text{m}$ .

of the contact alloy together and diffuse into the semiconductor, creating a low specific resistance contact.

The p-type contact metallisation is more demanding in an HBT. No dopant is used since the thin base could easily be shorted by dopant diffusion into the collector. Several contact schemes have been studied, including Mn/Au/Ti/Au and Ti/Pt/Au[102, 103]. The lowest contact resistance and least diffusion were found to be in Ti/Pt/Au where Ti is used for its adhesive properties and Pt acts as a diffusion barrier. Anneal tests were run on the p-type material for this metallisation scheme, as deposited using Plassys II.

The results of the anneal tests for the n- and p-type materials are shown in Figures 3.4 and 3.5, respectively. For a complete discussion of the method for extracting contact resistance from a TLM pattern see, for example [91]. The leakage currents in between the two isolated p-type contact structures were calculated using a four probe technique where a voltage was applied between the two contacts and the current which flowed was then measured at a particular bias, in this case, 1 V. The results are shown in Figure 3.6.

The performance of the n-type contacts, while showing a minimum  $R_c$  at an anneal temperature of  $280\ ^\circ\text{C}$ , was relatively independent of the temperature for all temperatures of  $400\ ^\circ\text{C}$  and below. There is a large increase in the contact resistance at the  $440\ ^\circ\text{C}$  data point. This was caused by the physical decomposition of the stack of metals. The high temperature was likely to cause one or more of the metals to react with the InGaAs[104]. The intermixing which occurs in this case cause compounds such as InAu to form[105]. These compounds create a highly resistive barrier at the surface.

The p-type contact resistances showed a minimum at  $240\ ^\circ\text{C}$  and increase with higher

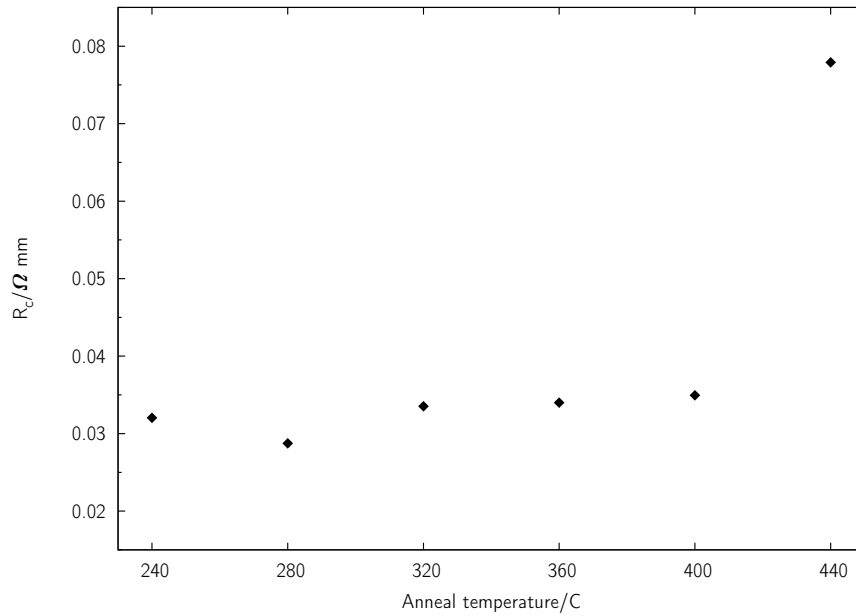


**Figure 3.4:** Specific contact resistance against anneal temperature for the n-type ohmic contact metallisation to InGaAs.

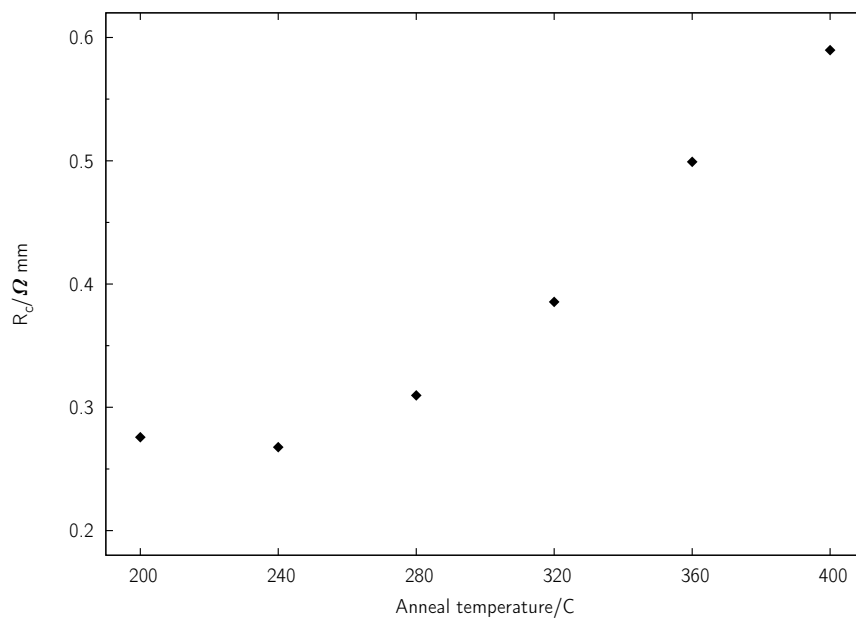


**Figure 3.5:** Specific contact resistance against anneal temperature for the p-type ohmic contact metallisation to InGaAs.

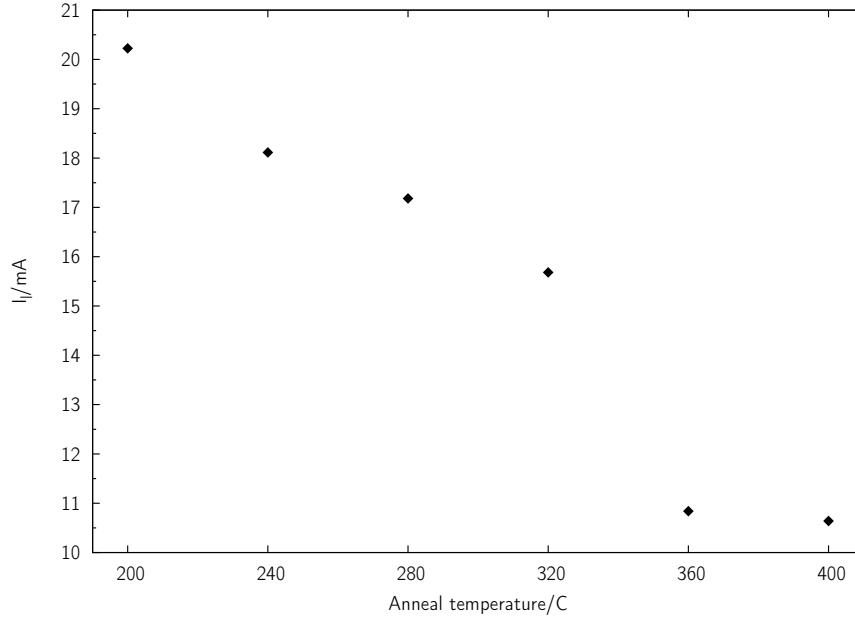


**Figure 3.6:** Leakage current at  $V_A = 1$  V against anneal temperature for the isolated p-type ohmic contact metallisation to InGaAs.

temperatures. The contact resistance showed an a decrease at moderate annealing temperatures and a subsequent increase as the temperatures were increased towards  $400^\circ\text{C}$  consistent with previous studies[103]. In order to minimise the contact resistance, there is an optimum depth of interfacial reaction (and intermixing of the component elements). This depth varies with annealing temperature.

The non-annealed contact resistance was  $0.31\ \Omega\text{mm}$  so only anneal temperatures of  $280^\circ\text{C}$  and below showed an improvement. The leakage currents showed a marked drop at an aneal temperature of  $360^\circ\text{C}$ . This may have been due to the high temperature annealing some of the defects in the base layer which could serve as current paths for leakage currents into the collector. Similarly, the longer diffusion lengths of the alloying process at higher temperature may have allowed some of the metal species to interact with the defects in a way which reduced the unwanted carrier flow. The non-annealed value of  $I_l$  was  $16.5\ \text{mA}$  so there was only an improvement for anneal temperatures of over  $280^\circ\text{C}$ .

Since the n-type contact resistance was both low and temperature insensitive, the choice of anneal temperature was made with a trade-off between p-type contact resistance and leakage current. By calculating the product of the two dependent variables and selecting the minimum, the optimum temperature was determined to be  $280^\circ\text{C}$ . An-

nealing of both types of contact was carried out in a single step once all the metals had been deposited.

### 3.4 HBT Process Flow

This section describes the entire fabrication process for the large area HBTs used in this project. Although the initial process development took place in both the Ultra-small Structures Laboratory (USSL) and the departmental clean room in the Department, the main body of the research was carried out in the James Watt Nanofabrication Centre, a new interdisciplinary research facility run by the Department of Electronics and Electrical Engineering at the University of Glasgow. The centre houses a class 1000 cleanroom with 32 laminar air flow cabinets (class 100) and a full compliment of processing and analysis tools, including those mentioned above.

Before each step in the process the sample was thoroughly cleaned. This process consisted of 5 min in an ultrasonic bath in a beaker (plastic, as glass was found to transfer too much of the ultrasonic power to the sample and could cause it to fracture) containing first acetone and then IPA. Care was taken when transferring from one solution to the other that no opportunity arose for the sample to dry and any particulate in the solution to adhere to its surface. A rigorous RO water rinse was then carried out for 2 min, in the beaker and then directly under the running tap. Failure to complete an adequate rinse in RO water would have a deleterious effect on the adhesion of metal and dielectric to the semiconductor.

The first stage of fabrication was to define the emitter metal layer using ebeam lithography. This was the stage where accurate pattern transfer was most important as the photolithography and ebeam markers (see Figure 3.7) must be accurately reproduced to ensure that the alignment of subsequent layers is correct. A faithful reproduction of the size and shape of the alignment markers for both ebeam and photolithography was important for later steps, so the accuracy of the ebeam process was preferred for this step. The resolution of the electron beam exposure employed for the patterning was 25 nm with a beam diameter of  $\sim 33$  nm. Care was taken at this stage to mitigate any stitching errors[106] arising from tilt in the sample during pattern writing, by cleaning any traces of resist residing on the back surface after spinning. These could lead to the alignment markers being misplaced with respect to the centre of the pattern.

Following the lithography, a de-oxidation of the semiconductor surface was carried out. The emitter metal was then deposited using one of the evaporation tools discussed above.

Photolithography was then used to define the emitter mesa structure. As this step re-

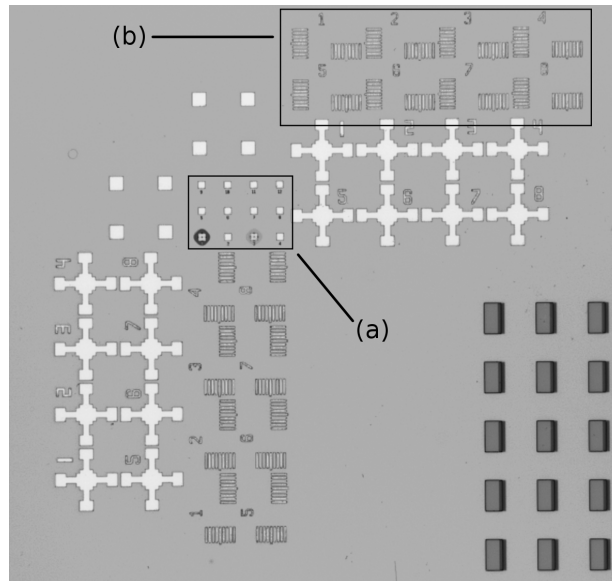


**Figure 3.7:** An optical micrograph showing ebeam lithography and photolithography alignment markers. The ebeam alignment used twelve squares of metal (a), one at each corner of the pattern, and photolithography used a set of Vernier marks (b) at each corner. It was possible to align eight subsequent layers to the first with these photolithography marks and 12 with the ebeam markers.

quired etching, the resist was used as a mask to protect regions where no etching should take place, for example around the alignment markers and other assorted identifying marks of the pattern. The emitter metal was covered for most of the device designs to maintain a separation between the edge of the etched mesa and the edge of the metal. One of the later design iterations used the emitter metal as the mask for the etch, however. The etchants prefer one crystal direction over the others[93, 107] so an anisotropic, crystallographic etch profile was achieved. This etch to the base layer required that the InGaAs emitter cap be etched first, using a 1:1:100  $\text{H}_2\text{O}_2:\text{H}_3\text{PO}_4:\text{H}_2\text{O}$  etchant which etched at a rate of  $\sim 35 \text{ nm min}^{-1}$ . Here  $\text{H}_2\text{O}_2$  was the oxidising agent and  $\text{H}_3\text{PO}_4$  the complexing agent.

After etching through the InGaAs emitter cap, the selectivity of the etchant on InP meant that it must be changed for another to remove the InP emitter. The etchant used for InP was 1:3  $\text{HCl}:\text{H}_3\text{PO}_4$ . This etched at a rate of  $\sim 100 \text{ nm min}^{-1}$ .

The next step was to use photolithography to define the base metal pattern. After defining this pattern metal could be evaporated and then the base mesa was defined. The etch process for the base mesa was similar to that of the emitter. The InGaAs collector was first etched to the InP etch stop layer and then the etch stop was removed.

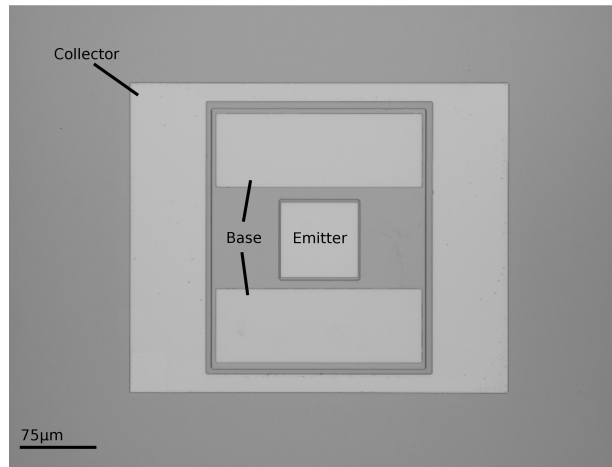


**Figure 3.8:** An optical micrograph of the metal contacts for the emitter, base and collector and the mesa structure of the active device region. The central emitter mesa measures  $75\ \mu\text{m} \times 75\ \mu\text{m}$ .

A further short etch into the InGaAs sub-collector was carried out. The collector metal pattern was defined using photolithography and then the metallisation was carried out. Figure 3.8 shows the mesa and contact metallisation of the devices.

At this stage it was possible to anneal the ohmic contacts to improve the contact resistance. The full procedure is discussed in §3.3.

Initially, wire bonding onto the ohmic contacts was attempted. The size of the contacts was found to be restrictive, however, and the adhesion wasn't always sufficient to support this technique. To this end bond pads were accommodated into the design and process flow. Two methods were considered to achieve this. The first was that the whole mesa be isolated by etching down to the non-conducting InP buffer layer and depositing the bond pads there. The second was to depositing an insulating layer on the collector and then depositing the bond pads on top. Since it was desirable to leave the surface of the devices exposed, a common RF device procedure[18] of spinning on a thick, planarising, dielectric layer such as polyimide was not useful. For both techniques, in order to access the inner contacts (emitter, base) either an insulating layer must be deposited or airbridges constructed. The most straightforward solution was to deposit an insulating layer of 250 nm room temperature  $\text{Si}_3\text{N}_4$  (which could be patterned using lithography) on to the collector and then the bond pads were deposited on top of the  $\text{Si}_3\text{N}_4$ . Tracks were deposited from the bond pad to the device terminal.

The finished devices are shown in Figure 3.9. The full fabrication process is given in the Appendix, complete with all resist processing parameters, etch times, etc.

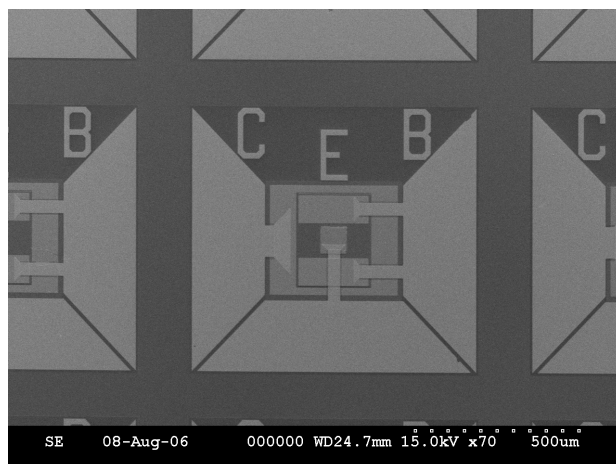


**Figure 3.9:** A scanning electron micrograph of a large area HBT fabricated in InGaAs/InP complete with Si<sub>3</sub>N<sub>4</sub> bond pad insulation and bond pads.

After cleaving and bonding the devices were ready to be used in conjunction with an external circuit. Figure 3.10 shows a set of devices affixed and bonded to an 18-pin leadless ceramic chip-carrier (LCC) as used for testing. Three wire bonds are made to each device to access the terminals.

### 3.5 Design Considerations

When creating the original CAD designs and transferring these into photolithography masks for processing there was latitude at the beginning of the project to tailor geometry and device scale not only to the application but also for ease of fabrication, testing and post-processing. The devices went through several design iterations during the natural progression of the project and as experience was accumulated through repeated fabrication and testing. Figure 3.11 shows the layout of the devices of the final iteration (fabricated devices are shown in Figure 3.9).

The first decision made was one of size. The emitter was chosen to be 75  $\mu\text{m}$  x 75  $\mu\text{m}$  to facilitate wire bonding without bond pads (although this was discovered to be unreliable). Space was deliberately left on two opposite sides of the emitter to incorporate magnetic elements at a later stage. Following on from this the base metal contacts were made to be large. No p-type dopant was available for metal contacts to InGaAs so a large metallised area was designed to reduce contact resistance.

The bond pads were designed around making the whole device square, to tile an array across a square sample easily and the insulation tracks were made to keep as much of the device surface accessible as possible.

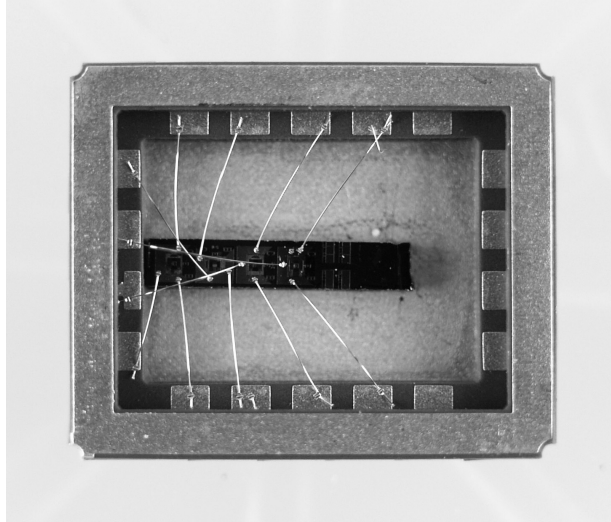


**Figure 3.10:** Four HBTs bonded into a ceramic LCC. (Image taken by Mr Peter McKenna of the Department of Electronics and Electrical Engineering.)

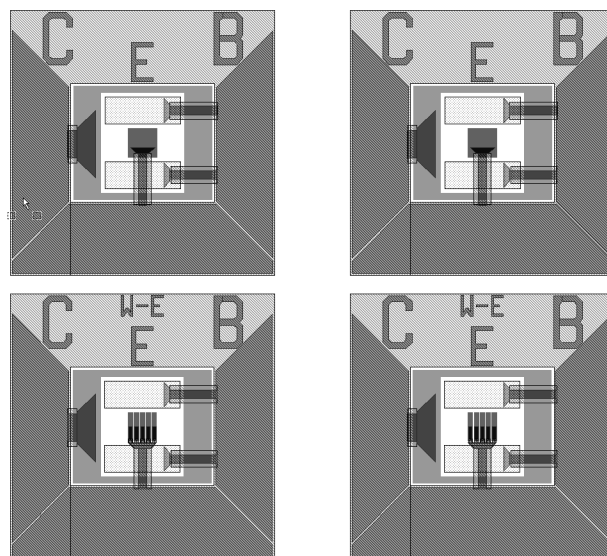


**Figure 3.11:** A section of the layout file for HBT devices. The upper two devices are large area HBTs. The lower two devices are multiple emitter finger devices.

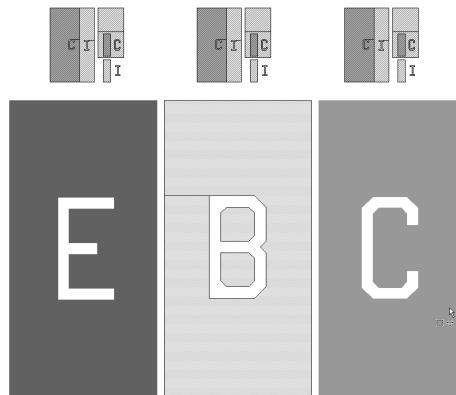


**Figure 3.12:** The layout of the design file used to fabricate in-line test structures for HBT fabrication. The emitter, base and collector are indicated with ‘E’, ‘B’ and ‘C’, patterned in the metal pads, for ease of identification.

Since the optimisation of native device performance was not a major goal of this project there was little need to alter the design of the active device region from the first iteration to the last, although some changes in the emitter design are discussed in Chapter 6 to improve the sensitivity to magnetic field.

## 3.6 Device Testing

### 3.6.1 In-line Testing

To properly monitor the success of the various process steps some in-line testing was carried out. This is on-wafer testing during the fabrication process, as opposed to end-of-line testing (see below).

Figure 3.12 shows the in-line testing cell included in the designs for the masks, etc.. There is a very large HBT onto which it is straightforward to place probes (see below) and various masked regions which result in replication of the mesa etch depths.

As the metal deposition process is monitored by the evaporator during deposition, secondary testing is not carried out. It is also difficult to verify the presence of the correct constituents once further layers have been deposited on top, although the overall height can be measured. Once the emitter mesa has been defined, however, it is possible to use either an atomic force microscope (AFM) or a surface profilometer (the model of the profilometer in JWNC is a *Veeco Dektak 6m* and it is generally referred to as the Dektak) to ensure the correct depth has been achieved.

The Dektak uses a diamond tipped probe to carry out contact profilometry whereby it

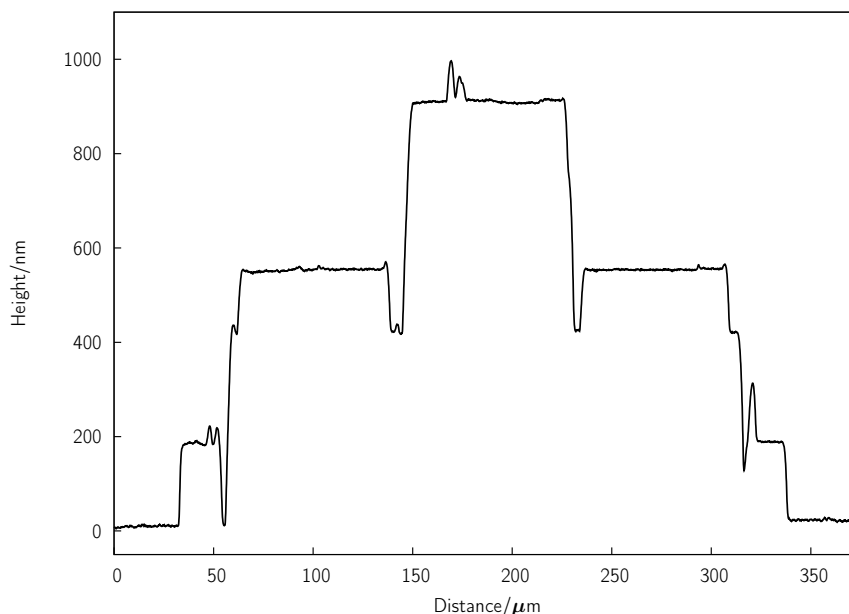
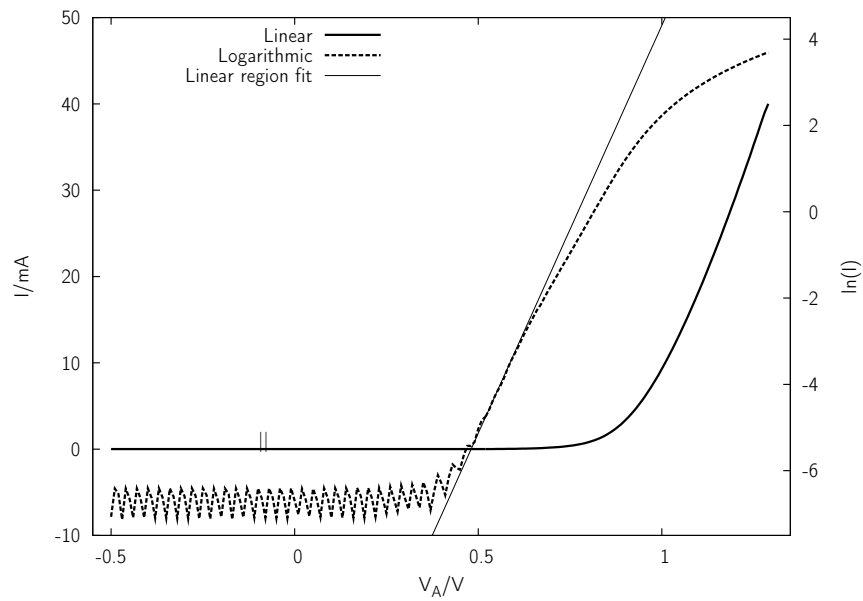


**Figure 3.13:** A surface profilometer scan over the mesa of an HBT.

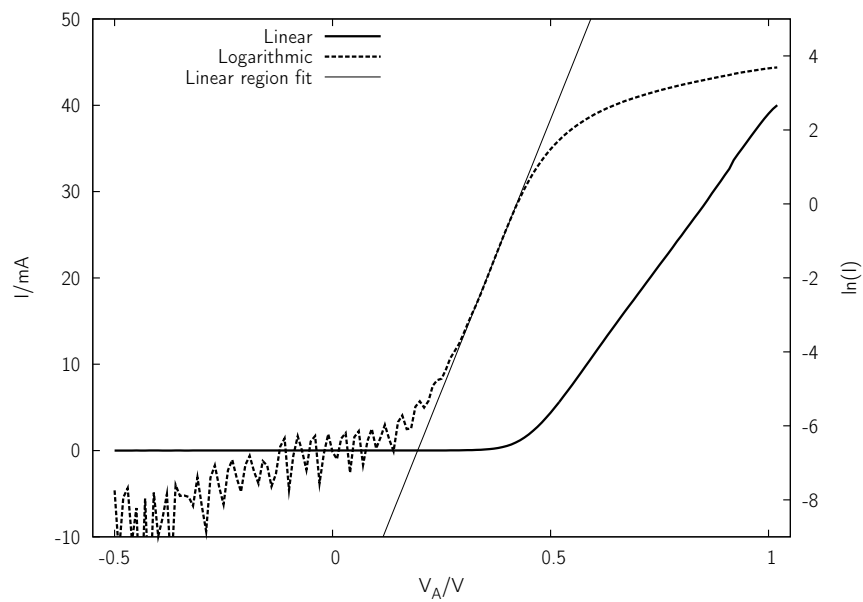
scans across a surface and measures vertical displacement with the results displayed on a PC. A single line scan was used to measure the depth of the etch to base and compared to the wafer specification. For a more accurate measure of the etch depth or the thickness of the metal contact the AFM was used. The AFM was also useful when calculating etch rates where a better resolution was required while the Dektak is more robust and needs less setting up. The contact profilometer is quicker and can measure much larger height differences ( $65\ \mu\text{m}$  c.f.  $1 - 2\ \mu\text{m}$  for the AFM). The AFM in JWNC is a *Digital Instruments Dimension 3100 AFM*. Atomic force microscopy works by reflecting a laser beam from the top of the cantilever on the probe onto an array of four photodiodes. The stage is controlled by stepper motors and moves the sample so that the tip of probe is scanned over the sample according to the parameters set in the computer controlled interface. The deflection of the tip as it moves over the topography of the sample is calculated from the deflection of the reflected laser beam.

Figure 3.13 shows a Dektak scan over a device mesa.

Once the base metal had been deposited it was possible to measure the base-emitter diode I-V characteristics using a probe station and a semiconductor parameter analyser (SPA). A probe station consists of a stage, microscope and light source and a scaffold on which sit up to four adjustable probe mounts with tungsten probes on the end of their arms. The probes are fine tipped with diameters that could range from  $0.1\ \mu\text{m}$  to  $100\ \mu\text{m}$



**Figure 3.14:** Current against forward applied voltage for the base-emitter junction diode of a typical InP/InGaAs SHBT



**Figure 3.15:** Current against forward applied voltage for the base-collector junction diode of a typical InP/InGaAs SHBT

Wafer	Ideality factor	
	B-E	B-C
MR2242	2.44	2.45
MR2244	1.49	1.29
TS0093	2.17	1.33
TS0117	2.06	1.36

**Table 3.2:** The base-emitter (B-E) and base-collector (B-C) diode ideality factors for the four InP/InGaAs SHBT epi-wafers used during the project.

(and beyond) at the end. The probes can be raised or lowered onto the metal contacts of a semiconductor sample on the stage, thus making electrical contact to the device. An SPA connects to the probes and via its display allows for various bias conditions and current sources to be applied to the device and for the resulting voltage or resulting current to be measured. Using the various settings of an SPA such as an HP4155B it is possible to measure any of the DC electrical parameters of a device.

Figure 3.14 shows a typical I-V characteristics of the emitter-base diode.

The base mesa etch can be measured in the same manner as the emitter mesa and using a test structure from the in-line test cell. After the collector metal had been deposited it was possible to measure the I-V characteristics of the base-collector diode. Figure 3.15 shows a typical measurement. The diode ideality factor for both of these junctions gave an indication of the success of the epilayer growth stage in terms of the quality of metallurgical junction. For a well-formed abrupt heterojunction the diode ideality factor should be unity plus a small positive factor which is dependent on the material on each side[23]. When the ideality factor is near two it indicates a high level of recombination at the junction. The ideality factors for both junctions is given for four of the wafers used in the project in Table 3.2. The two letter prefix denotes the MOCVD reactor used for the growth process. Fabrication began with wafer MR2242 and each wafer was used up before moving on to the next. The work in the final two chapters relating to HBT sensors was carried out on wafer TS0117.

Figure 3.16 shows the common-emitter I-V characteristics of an HBT. This was used to test for transistor action in the device after the deposition of the collector metal. A device which was functioning correctly showed the quasi-saturation of  $I_c$  typical of all bipolar transistors.

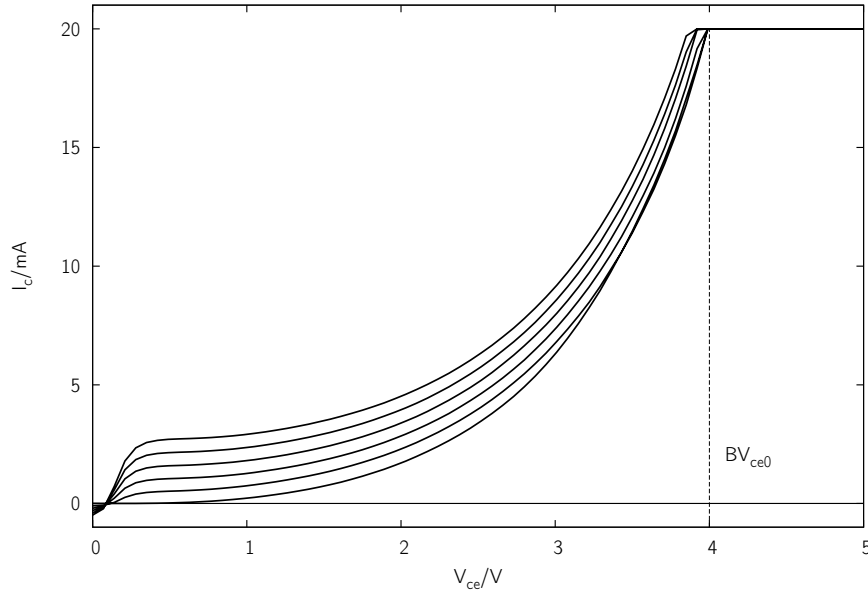


**Figure 3.16:** Collector current against collector–emitter bias for a typical InP/InGaAs SHBT. The base current was varied from 0 to 500  $\mu\text{A}$  in 100  $\mu\text{A}$  steps.

### 3.6.2 End-of-line Testing

Once the bond pad metal was deposited the fabrication process could be considered finished. This allowed end-of-line testing to be carried out.

The common emitter and common base I–V characteristics of a typical device are shown in Figures 3.16 and 3.17, respectively. The devices under test were sensitive to current spikes caused by breakdown. Figure 3.18 shows a single measurement sweep to determine  $BV_{cb0}$ , carried out individually to avoid irrecoverable device failure..

Further to the HBT I–V characteristics discussed above, the DC current gain  $\beta_{dc}$  was measured as a function of the collector current,  $I_c$ . Figure 3.19 shows the results of this measurement.

The DC current gain was to be used to measure the transduction of applied magnetic field in the HBTs, as well as to measure the efficacy of several surface treatments. To this end, the device to device variation of the current gain was measured across a sample on which fabrication had been completed. The values are shown in Table 3.3. The average value is 12.02 with a standard error of 0.22 or 1.8%.

Analysis of the common–emitter characteristics allowed for the extraction of values for  $I_{ce0}$  and  $BV_{ce0}$  while  $\alpha_{dc}$ ,  $I_{cb0}$  and  $BV_{cb0}$  values were obtained from the common–base characteristics.

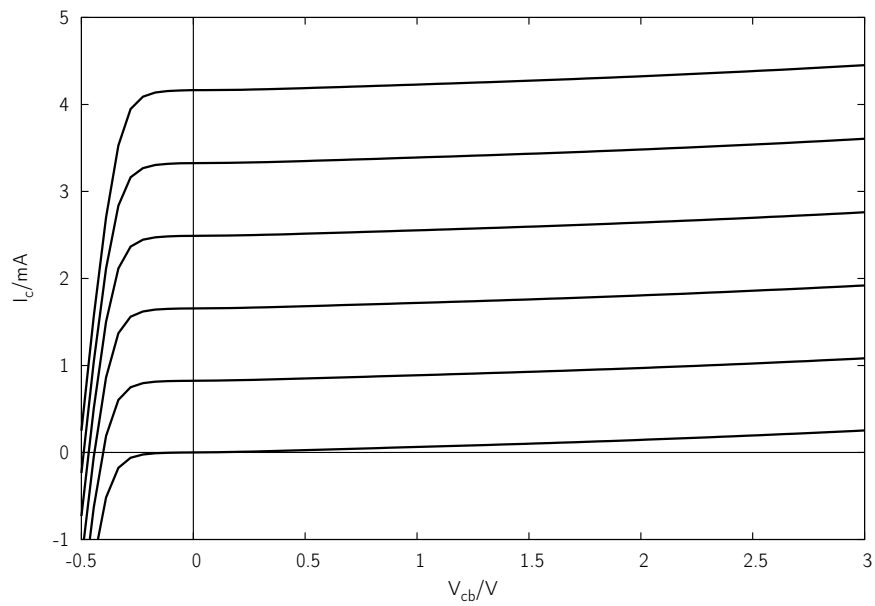


**Figure 3.17:** Collector current against collector–base bias for a typical InP/InGaAs SHBT. The emitter current was varied from 0 to 5 mA in 1 mA steps.

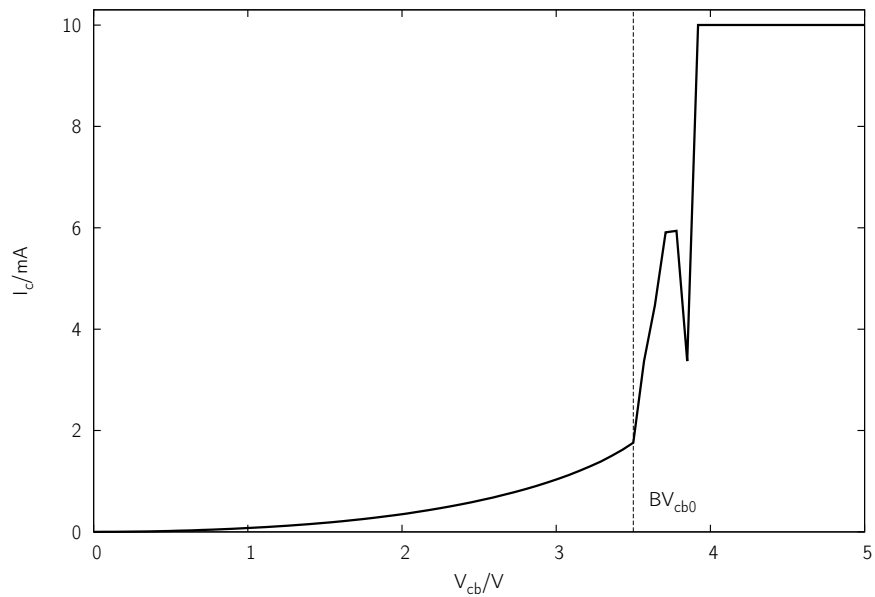


**Figure 3.18:** Collector current against collector–base bias for a typical InP/InGaAs SHBT, showing  $BV_{cb0}$ . The base current was fixed at 0 for this measurement.

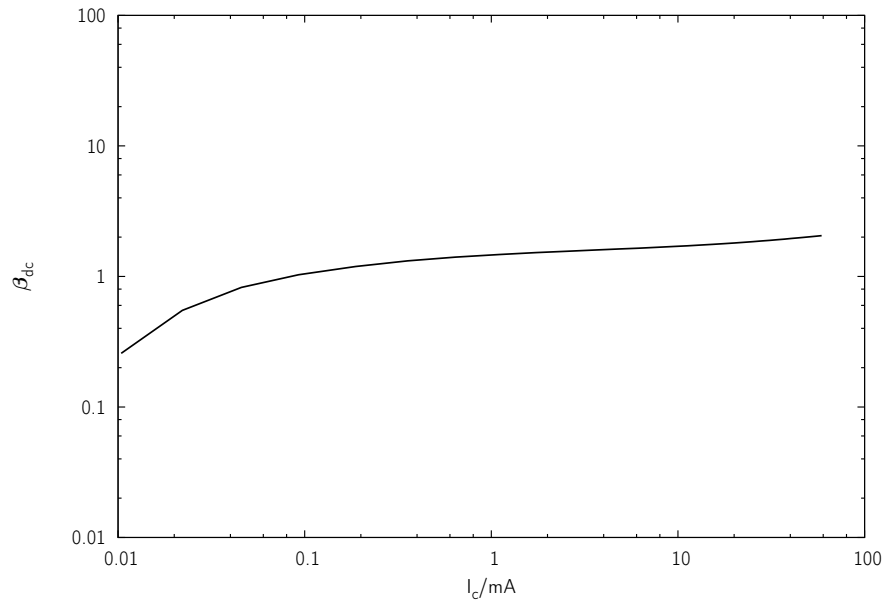


**Figure 3.19:** DC current gain,  $\beta_{dc}$ , against collector current,  $I_c$ , for a typical HBT.

Device	$\beta_{dc}$
2A	12.8
2B	11.6
2C	12.3
4A	10.3
6D	12.1
6E	12.0
7F	12.1
7H	12.5
8A	12.2
8C	12.0

**Table 3.3:** DC current gain for several InP/InGaAs SHBTs on a sample, fabricated from wafer MR2254.

Device Parameter	Value
B–E diode ideality factor	2.06
B–C diode ideality factor	1.32
$\beta_{dc}$ at $I_c = 50$ mA	7.50
$BV_{ce0}$	4.0 V
$BV_{cb0}$	3.6 V

**Table 3.4:** Values for each of the common device parameters of an InP/InGaAs single heterojunction bipolar transistor fabricated from wafer TS0117.

Table 3.4 gives values for each of these parameters for a device fabricated from wafer TS0117, a full DC electrical characterisation.

The general fabrication principles as well as the specifics of HBT fabrication as applied to the work on this project have been discussed. The process flow and design considerations for the InP/InGaAs SHBTs were presented.

Work was undertaken to optimise the ohmic contact recipes used by varying the alloying temperature. An optimum temperature for rapid thermal annealing of 280 °C was determined.

The procedure for device testing was also detailed. In determining the p–n junction diode ideality factors, an insight into the quality of the material growth is available. The values measured for all the wafers used in the project were high compared to the literature, where ideality factors of 1.1[108] and 1.2[109] have been shown for the base–emitter junction of InP/InGaAs SHBTs over wide ranges of bias. This may have an effect on the ability of the devices to sense magnetic field, since poor quality interfaces will contain traps and recombination–generation sites which will produce statistical noise. This noise may drown out small changes in magnetic field and will affect the signal–to–noise ratio of the sensor. The values for  $\beta_{dc}$  were also considerably lower than those reported in single heterojunction devices as early as 1988[110], though it should be noted that demands on current gain are not necessarily high. For most applications a DC current gain of around 20 is sufficient[111]. Since the transduction magnitude will be measured using  $\beta_{dc}$ , a smaller current gain may lead to a lower value at which field can be measured before the sensor saturates. While the device to device variation would have to be closely controlled in sensors which were being mass–produced, the system of normalisation used in the later stages of this project should limit the effects of this on the validity of the results.

While high breakdown voltages are important for RF and microwave power applications[111],

the of operational biases used in this study were small. However,  $BV_{ce0}$  values of over 5 V and  $BV_{cb0}$  of over 11 V are possible in InP/InGaAs SHBTs[112]. Collector to emitter breakdown voltages of 7 V can be realised in InP/InGaAs/InP DHBTs[113].

# 4 Semiconductor Surface Effects and Crystal Defects

This chapter explains the theoretical background behind interface effects observed at semiconductor surfaces. The origins of surface space-charge and surface states are discussed and then equilibrium and non-equilibrium conditions at the surface are introduced.

Following this, plasma processing is discussed and plasma-induced surface damage is considered and then the topic of passivation is covered.

There is a brief discussion of some of the lattice defects in common in bulk semiconductors and then the experimental results of plasma processing and passivation are presented.

## 4.1 Semiconductor Surfaces

The derivation presented below loosely follows an argument which is available in more detail in [114]

### 4.1.1 Work Function

Similarly to p-n interfaces and heterojunctions, semiconductor surfaces (semiconductor-air interfaces, semiconductor-oxide interfaces, semiconductor-metal interfaces) may give rise to space-charge regions<sup>1</sup>[114]. This is a distinguishing feature of semiconductors over metals. A net excess of charge will give rise to an electric field and hence a potential, in accordance with Gauss's law, and will induce band bending. In many cases the Fermi level of the semiconductor surface will be fixed with respect to the top of the valence band,  $E_v$ , regardless of the dopant levels in the bulk material and this is referred to as *Fermi level pinning*.

A key parameter in the discussion of surfaces of solid state materials is the work

---

<sup>1</sup>Non-degenerately doped semiconductors exhibit this property due to the low carrier densities therein.

function,  $\phi$ , as defined in §2 as the difference in energy between that of an electron at infinity, at rest in a vacuum and the Fermi level of the material surface:

$$\phi = E_{vac} - E_F. \quad (4.1)$$

Other relevant quantities include the electron affinity  $\chi = E_{vac} - E_{cs}$  and the ionisation energy  $I = E_{vac} - E_{vs}$  where  $E_{cs}$  and  $E_{vs}$  are the conduction and valence band edges at the surface respectively. Hence the work function can be written

$$\phi = I - (E_F - E_{vs}). \quad (4.2)$$

#### 4.1.2 Surface Space-Charge

The change in potential resulting from the lattice discontinuity at the surface of semiconductors may lead to a space-charge layer at equilibrium conditions. In order to analyse this the electrostatic potential in the material must be defined and Poisson's equation solved for the system. The position-dependent electrostatic potential is given by

$$V(z) = \frac{1}{q} [E_{vb} - E_v(z)] = \frac{1}{q} [E_{cb} - E_c(z)] \quad (4.3)$$

where  $z$  is the direction perpendicular to the plane of the interface and increases with increasing distance into the semiconductor. Here  $E_{vb}$  and  $E_{cb}$  refer to the bulk values for the energy of the valence band maximum and conduction band minimum respectively (as opposed to  $E_{vs}$  and  $E_{cs}$ , same at surface). This is for a simple one-dimensional system for a semi-infinite semiconductor (in  $x$  and  $y$ ) where  $V(z) \rightarrow 0$  in the bulk (i.e. for large  $z$ ) and edge effects are not considered. When  $V(z) < 0$  there is an excess of positive charge and the bands bend up; conversely, downward bending results from a positive potential due to excess negative charge.

The surface bending can be described by

$$qV = E_{vb} - E_{vs} = E_{cb} - E_{cs} \quad (4.4)$$

The space charge per unit volume,  $\rho(z)$ , is given by the sum of carriers and dopant ions

$$\rho(z) = q [N_d^+ - N_a^- + p(z) - n(z)] \quad (4.5)$$

and it is related to the potential by the Poisson equation

$$d^2V/dz^2 = -\rho(z)/\epsilon_b\epsilon_0 \quad (4.6)$$

where  $\varepsilon_b$  and  $\varepsilon_0$  are the relative dielectric constant of the bulk semiconductor and the permittivity of free space respectively. By application of the density of states function and the Fermi–Dirac distribution function to the conduction band electrons for a non-degenerately doped semiconductor<sup>2</sup> the electron density can be shown to be

$$n = N_c \exp [-(E_c - E_F) / k_B T] \quad (4.7)$$

and for the bulk semiconductor

$$n_b = N_c \exp [-(E_{cb} - E_F) / k_B T] = n_i \exp [-(E_{ib} - E_F) / k_B T] \quad (4.8)$$

where  $n_i$  is the intrinsic carrier concentration in the bulk,  $E_{ib}$  is the intrinsic Fermi level and  $N_c$  is the effective density of states in the conduction band and has its usual definition as found, for example, in[115]. A similar result can be obtained for holes in the valence band. Combining above equations (4.4), (4.7) and (4.8) for a semiconductor in the exhaustion range (where all donors and acceptors are ionized) the electron and hole densities can be shown to be

$$n(z) = n_b e^{v(z)} = n_i e^{u(z)} \quad (4.9a)$$

$$p(z) = p_b e^{-v(z)} = p_i e^{-u(z)} \quad (4.9b)$$

using the following two reductions

$$v \equiv qV / k_B T = (E_{ib} - E_i) / k_B T \quad (4.10)$$

(note the relation between 4.10 and the band bending given in 4.4) and

$$u \equiv (E_F - E_i) / k_B T. \quad (4.11)$$

Poisson's equation then gives

$$dv/dz = \mp F / L_D \quad (4.12)$$

or,

$$z / L_D = \int_{v_s}^v (\mp F)^{-1} dv \quad (4.13)$$

---

<sup>2</sup>i.e. a semiconductor to which Maxwell–Boltzmann statistics can be applied.

where

$$F(u_b, v) = \sqrt{2} [\cosh(u_b + v) / \cosh u_b - v \cdot \tanh u_b - 1]^{1/2}. \quad (4.14)$$

with the extrinsic Debye length, the depth to which the external field penetrates before it is screened by charge carriers,

$$L_D^2 = \varepsilon_b \varepsilon_0 k_B T / q^2 (n_b + p_b). \quad (4.15)$$

Applying Gauss's law to the total charge per unit area at the surface, the space-charge density  $Q_{sc}$ , gives

$$Q_{sc} = \varepsilon_b \varepsilon_0 \mathcal{E}_s = \varepsilon_b \varepsilon_0 \left. \frac{dV}{dz} \right|_{z=0} \quad (4.16)$$

and incorporating (4.10), (4.15) and (4.12) gives

$$Q_{sc} = \mp q(n_b + p_b)L_D F_s. \quad (4.17)$$

In (4.17) the negative sign refers to the case where  $v > 0$  and the positive sign refers to  $v < 0$ ;  $F_s$  is the space charge function  $F(v_s)$  and  $\mathcal{E}_s$  is the electric field strength, both at the surface. Since  $u_b$  is an expression of the shift of the bulk Fermi level from the intrinsic value it describes the dopant concentration, where  $u > 0$  implies n-type and  $u < 0$  implies p-type ( $u = 0$  is the intrinsic semiconductor). Three separate regimes emerge from analysis of (4.17) for an n-type semiconductor,  $v_s > 0$ ,  $-2u_b < v_s < 0$  and  $v_s < -2u_b$ ; in addition,  $v_s = 0$  is the specific case for flat bands (i.e. no surface space-charge).

For positive values of  $v_s$  the bands bend down ( $E_{ib} > E_{is}$ ) and the conduction band edge approaches the Fermi level. This leads to an increase in electron concentration at the surface and is hence called an *accumulation layer*. The electron concentration increases as  $F(v_s)$  becomes more negative.

In the regime where  $-2u_b < v_s < 0$  the reverse applies: the upward bending of the bands increases the gap between the Fermi level and the conduction band minimum and depletes the majority carrier (electron) concentration at the surface. This is a *depletion layer* and its width can be shown to be

$$z_{dep} = L_D (2|v_s|)^{1/2} = \pm Q_{sc} / qN_{d,a} \quad (4.18)$$

At  $v_s \approx -2u_b$ ,  $|E_{cb} - E_F| = |E_{vs} - E_F|$  and so the concentration of majority and minority carriers is equal. Hence for  $v_s < -2u_b$  the minority carrier concentration increases with space-charge function and an *inversion layer* is formed. The mobile carriers at the

surface of an n-doped semiconductor with an inversion layer would thus be holes. A depletion layer will also be present between the inversion layer and the bulk.

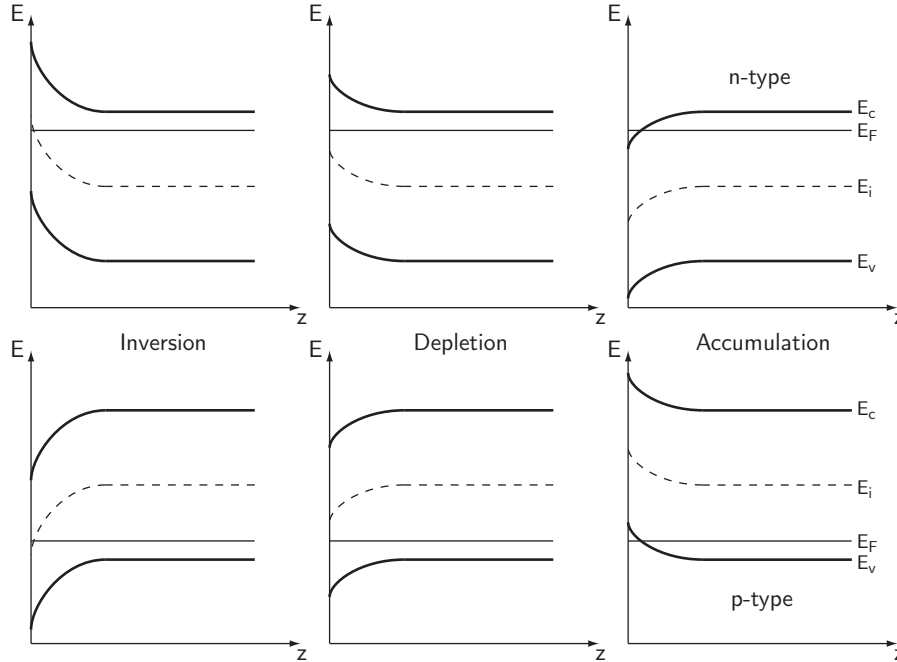


**Figure 4.1:** Inversion, depletion and accumulation band diagrams for n- and p-type semiconductors. (Adapted from [114]).

As a further note, it is worth pointing out that inversion and accumulation layers are created by potential wells at the surface of the semiconductor and as such are confined to a two-dimensional region parallel to the surface. The width of the space-charge layer,  $L_{sc}$ , can be shown to be

$$L_{sc} = \frac{|v_s|}{F_s} L_D \quad (4.19)$$

In many cases  $L_D$  for the system will be comparable to—or even less than—the de Broglie wavelength of the carrier. This leads to quantum size effects in the  $z$ -direction which will create non-classical carrier distributions in  $z$  in the space-charge region.

### 4.1.3 Surface States

The existence of mid-gap states that occur purely because the lattice is not continuous was first theorised by Shockley[116], amongst others, in the 1930s. He showed how the surface states arise from the complex band structure of the lattice. As the lattice parameter is varied from a finite value to infinity the well-defined levels split and leave a pair of states in the gap. These “virtual gap states” arise from solving Schrödinger’s

equation for the lattice and have a wavefunction that decays exponentially into both  $z$  and  $-z$ . They are similar to those which occur at metal–semiconductor interfaces (metal induced gap states) and cause the deviation of Schottky barrier heights from theoretical values<sup>3</sup>.

Further gap states are introduced when an adatom forms a chemical bond with an atom in the lattice. This can be considered to take place between the adatom and its nearest neighbour alone and as such the interaction can be treated as an isolated, heteropolar molecule. By utilising the fact that covalent bonds are partially ionic adatoms, these can be considered to introduce surface dipoles as well as creating gap states exponentially decaying into both vacuum and solid in an analogous manner to the above. The direction of the dipole moment is dependent on the character of the wavefunction tail, either donor– or acceptor–like<sup>4</sup>. This can be analysed using the normal electronegativity method for covalent bonding.

In the bulk region of elemental group–IV semiconductors and that of III–V and II–VI compound semiconductors the crystal lattices are tetrahedrally coordinated. In binary compound semiconductors with the zincblende lattice structure (e.g. GaAs or InP) each atom forms four covalent bonds with its four nearest neighbours. At the  $\{110\}$  surface of such a lattice each atom has only three neighbours and hence has one unsaturated or dangling bond comprised of an electron[114]. The anion (e.g. Ga) and cation (e.g. As) dangling bonds have different binding energies; the anion dangling bonds are more tightly bound than the cation dangling bonds. Furthermore, since the anion dangling bonds are below the valence band maximum it is energetically favourable for those to fill with electrons from the cation. This charge redistribution leads to a reorganisation of the structure of both the bonds at the surface and the atoms' bonds with the second monolayer further into the semiconductor. The relaxation of the crystal thus introduces a surface strain which will offset the energy gain from the charge redistribution and cause changes to the lattice parameter and bonding angle at the surface. As will be seen later, the addition of extra atoms or molecules to the surface by chemical treatment can redress this effect and partially return the semiconductor properties at the surface to those in the bulk.

---

<sup>3</sup>In fact, the metal–induced gap states are regarded as the primary factor in determining barrier heights[114].

<sup>4</sup>If the surface state is exactly at the branch point of the virtual gap states of the complex band structure, as described in[116], no dipole moment would be observed.

#### 4.1.4 Equilibrium and Non-equilibrium Surface Carrier Conditions

##### Equilibrium Carrier Conditions

In order to maintain surface charge neutrality the condition

$$Q_{ss} + Q_{sc} = 0, \quad (4.20)$$

must be met where  $Q_{ss}$  and  $Q_{sc}$  are the net charge in surface states and the space charge per unit area respectively. The surface states take on an acceptor- or donor-like character and, depending on their position with respect to the Fermi level, become charged as such. As discussed in §4.1.2 above, this potential caused by the surface charge will cause a space-charge region immediately below the surface and band bending will result.

If, for example, acceptor-type midgap states exist at a semiconductor surface, what are the band bending conditions for charge neutrality? In a p-type semiconductor where the acceptor surface states are above the Fermi level no band bending occurs since the surface states do not become occupied. These states are neutral and need no compensation by space charge. In this case downward band bending would mean the presence of negative charge carriers which would violate charge neutrality, similarly with upward band bending and an accumulation layer. When the bands bend in the presence of excess charge the mid gap states will also move with respect to the Fermi level. This becomes important when considering the same situation in n-doped material: mid gap acceptor-like states will be below the Fermi level, will become full and lead to an excess negative charge at the surface. To offset this, there must be a region of positive space charge. As the surface states move closer to the Fermi level because of the upward band bending some of the states become unoccupied. An equilibrium is reached and charge neutrality is obtained.

The same argument can be applied to the donor-like surface states with the result that downward band bending will be observed in the p-type semiconductor and flat bands in the n-type.

If both acceptor- and donor-like mid gap states exist at the surface then the situation where no band bending results does not occur; depletion layers will form to maintain charge neutrality. Donor-type states in the valence band and acceptor-type states in the conduction band do not cause any band bending.

### Non-equilibrium Carrier Conditions

Electron–hole pairs are created in a semiconductor when photons of energy greater than the bandgap are incident on the surface. This effect is larger at the surface than in the bulk. Because of the band bending this injection of bipolar charge will be accelerated in  $z$ , but in opposite directions and the flattening of the bands that results is called the *surface photovoltage*. Because of this the carrier density in the space–charge region under incident light will deviate from thermal equilibrium values but (4.20) is not violated since equal numbers of electrons and holes are generated. No surface photovoltage is expected for a surface with flat bands. A further effect to consider in this system is the Demer effect: the difference in mobilities between holes and electrons leads, by Einstein’s relationship

$$D_{p,n} = (k_B T/q)\mu_{p,n}, \quad (4.21)$$

to a difference in diffusion coefficients,  $D_{p,n}$ . Hence there must exist a small internal electric field to maintain the total current flow to the surface at zero. This field, known as  $\mathcal{E}_D$  is usually negligible compared to the surface photovoltage.

From this it is possible to pursue an argument describing the excess surface charge using the *Shockley–Read–Hall* recombination model[117] applied to surface states. One useful definition from the calculation is that of *surface recombination velocity*,  $s$ ,

$$s \equiv U_s/\Delta p_s \quad (4.22)$$

where  $U_s = U_{cs} = U_{vs}$  is the recombination rate per unit area which is equal to that of electrons and holes and  $\Delta p_s$  is the carrier excess at the surface (given charge neutrality this is equal for electrons and holes).

### Carrier Transport at Semiconductor Surfaces

Carrier transport parallel to the surface can occur if there exists a surface excess of carriers in the semiconductor. Quantities  $\Delta N$  and  $\Delta P$  are the number of mobile holes and electrons per unit surface area such that

$$\Delta N = \int_0^\infty [n(z) - n_b] dz \quad (4.23)$$

and

$$\Delta P = \int_0^\infty [p(z) - p_b] dz \quad (4.24)$$

Accumulation and inversion layers lead to an increase in surface conductance due to

the increase in mobile carriers compared to the bulk while depletion layers tend to lead to a decrease. The change in conductance parallel to the surface is given by

$$\Delta\rho = q(\mu_{ns}\Delta N + \mu_{ps}\Delta P) \quad (4.25)$$

where  $\mu_{ns}$  and  $\mu_{ps}$  are the surface mobilities of electrons and holes, respectively, and it can also be shown that the minimum value of surface conductance occurs for a band bending of

$$v_s^{\min} = -2u_b + \ln(\mu_{ps}/\mu_{ns}). \quad (4.26)$$

A simple model of the mobility of excess surface charge can be created by assuming diffuse scattering at the surface and specular scattering at the inner boundary. Diffuse scattering events cause a statistical re-orientation of velocity according to Maxwell–Boltzmann statistics and these events hence cause a reduction in mobility. The space–charge region relaxation time is then

$$\tau_s \approx L_{sc}/\bar{c}_z \quad (4.27)$$

where  $\bar{c}_z$  is the average (Maxwell–Boltzmann) velocity normal to the surface and  $\tau_s$  is taken as the time from specular scattering event at the inner boundary to diffuse scattering at the surface.

One–dimensionally, the mean free path in the bulk  $\Lambda_b$  is related to the bulk relaxation time  $\tau_b$  by

$$\Lambda_b = \bar{c}_z \cdot \tau_b \quad (4.28)$$

and combining the two (independent) rates to give an effective collision rate  $\tau_{\text{eff}}$

$$1/\tau_{\text{eff}} = 1/\tau_b + 1/\tau_s \quad (4.29)$$

The relaxation–time approximation of mobility gives the ratio of surface to bulk mobilities as

$$\mu_s/\mu_b = (1 + \Lambda_b/L_{sc})^{-1} \quad (4.30)$$

although for a full treatment, which requires solving the Boltzmann transport equation (see, for example, [118]), the result is

$$\mu_s/\mu_b = 1 - (1 - r)M_s\Lambda_b/L_D. \quad (4.31)$$

Here  $r$  is the fraction of scattering events that are specular and  $M_s \equiv M(u_b, v_s)$  is the

mobility function which accounts for the space-charge region carrier type.

These details had a bearing on the effects of deliberately inducing damage to the surface of a semiconductor. Below is detailed an experiment where the surface transport properties were changed in the p-InGaAs base layer of an HBT and the electrical characteristics of the base-emitter junction monitored.

## 4.2 Plasma Processing

Many different processes involve exposing the surface of a semiconductor to ionised species. These processes are as diverse as reactive ion etching[90, 95], ion implantation[119, 120] and surface cleaning[121].

Reactive ion etching (RIE) is a common tool used for processing semiconductors, especially where the device is fabricated subtractively. As discussed in Chapter 3 it carries advantages and disadvantages over wet etching, such as its anisotropy and its resulting poorer surface quality. The starting point for RIE is a plasma, a ‘gas’<sup>5</sup> containing positive particles (positive ions) and negative particles (electrons or negative ions) in a vacuum chamber that also contains the substrate to be processed. This plasma is created from a gas or mixture of gases at low pressure by ionising excitation (usually RF radiation) coupled into the plasma and because a plasma is not a system at equilibrium this energy must be continuously fed in to maintain it in balance with the energy loss due to particle recombination. Also, since the electromagnetic excitation is coupled to the plasma by accelerating electrons, the effective electron temperature (20 000K to 100 000K) will exceed the effective ion temperature (300K to 20 000K) when considering velocity distributions[122].

The fact that the electrons are hotter will lead to any isolated object in the plasma rapidly gaining a negative charge from collecting many more fast electrons than slower, heavier positive particles. The ensuing potential difference between the substrate and the plasma will have several effects. Firstly, a steady state will be reached where only as many electrons as positive ions are aggregated by the substrate. Secondly, the repulsive action of the negative potential will result in a *plasma sheath*, a dark region around the substrate where no electrons reside and hence no light is emitted by recombination. Lastly, and most importantly from a device fabrication point of view, the accelerating potential for positive ions serves to collimate the heavy ions and facilitates the anisotropy and high aspect ratio etches that are a common feature of RIE. The *sheath potential*, as it is known, is a function of the electron temperature and the mass ratio of the electron

---

<sup>5</sup>Plasma is more regularly considered to be a fourth phase of matter, although it is akin to a gaseous collection of charged and uncharged particles.

to the ion.

The sheath potential is a source of *DC self-bias* but it is useful to control the ion energy with applied bias separately to the RF excitation for finer control over etch rate and bombardment damage. To achieve this an external contact is added to the substrate of the sample in the plasma chamber. Through this contact, coupled by a capacitor, a bias is applied to the substrate. It is important to note that the ion current at the device is limited not by the accelerating sheath potential (which in fact has a short penetration distance due to the small —electronic— Debye length in the plasma) but by the ion flux. An AC source coupled by a capacitor is connected to the external contact and the potential of the wafer varies with the source. The ion flux does not increase to compensate for the electron flux into the substrate in the positive half-cycle, however, so the average wafer bias becomes more negative. The steady state is that for which the total ion flux over the cycle is equal to the electron flux over the positive half-cycle. The DC bias magnitude is related to the AC bias magnitude and for large AC bias is approximately half.

### Plasma-Induced Surface Damage

Studies into the damage caused by the ion bombardment of GaAs[123] and InP[124, 125] have shown that there is an energy threshold for ion energies below which damage free plasma processes are possible. This is particularly important in alloyed III-V semiconductor materials since the high temperature anneals used to recover damaged surfaces in, for example, silicon are not feasible.

A defect density of  $10^{12} - 10^{13} \text{ cm}^{-2}$  on a semiconductor surface will significantly affect its electrical characteristics. This can be characterised by measuring (or inferring) the number of charges per unit surface area (i.e.  $Q_{sc}/q$ ) produced by a plasma process. This number density may understate the actual number of surface states as it will not account for donor-acceptor compensation (see above) or defect states with energy levels outside the band gap.

Using spectroscopy techniques, defect centres have been resolved within the band gap for both GaAs[123] and InP[124, 125]. These states will cause the Fermi level to be pulled down in n-type material and pulled up in p-type material with respect to the valence band maximum at the surface. Thus an accumulation of surface charge is created at the surface.

## 4.3 Passivation of Semiconductor Surfaces

When defining a large vertical mesa in, for example, an HBT, a considerable surface area is exposed to the environment. Semiconductor surfaces produce gap states and

(particularly in III–V compound semiconductors) oxidise readily. Semiconductor–oxide interfaces are another source of gap states. Gap states increase recombination rates, and hence degrade injection efficiencies and device performance. Carrier concentrations at the surface are also affected (see §4.1.3). In an HBT the base surface recombination current  $I_{b,\text{surf}}$  is the component of the base current,  $I_b$ , due to the recombination of minority carriers (i.e. electrons) in the base, at the exposed surface. Its magnitude is dependent on the available surface area to recombine, so has a proportionally larger effect on smaller devices[9]. Furthermore,  $I_{b,\text{surf}}$  is dependent on the surface recombination velocity,  $s$ , which is a characteristic value of material and surface processing, amongst other things. Larger values of  $I_{b,\text{surf}}$  will tend to increase  $I_b$  and decrease  $I_c$  and  $\beta_{\text{dc}}$ .

One of the most flexible and efficient methods of passivating the surface of a III–V semiconductor is chalcogenide passivation[126–131]. Sulphide– (or selenide–) containing solutions are used as a treatment agent, the device is exposed to sulphide ions in a solution and a chemical reaction takes place at the surface. The treatment first results in the removal of the native oxide layer of the material[132]. Electrons are then removed from the semiconductor into the solution (i.e. there is oxidation) as bonding takes place between the sulphur and semiconductor atoms. The resultant sulphidising of the semiconductor surfaces leads to a change in the electrical properties at the surface and a decrease in surface recombination sites.

The initial electronic structure of the semiconductor and the energy state of the sulphur ion (in solution) will have an effect on the efficiency of the sulphidising that takes place and the form of the semiconductor surface after treatment[131]. A chemical bond is created between the sulphur ion in the solution when it comes into contact with the surface and the surface semiconductor atoms in the crystal. This happens in the form of an interaction between the outer electron shell of the ( $\text{S}^{2-}$ ) sulphur ion and the valence electrons in the near-surface region of the material. If the separation is small enough the wave functions of the two overlap and a chemical bond will form in a way as to reduce the energy of the overall system. The sulphur atoms bridge the atoms on the semiconductor, thus saturating the dangling bonds. Implicit in this argument is the fact that the initial conditions of the sulphur ion in solution have an effect on the efficacy of the passivating process[131]. In GaAs systems, the result is a bridging of adjacent As atoms by either one or two S atoms[130], which leads to the growth of a surface terminating coating of  $\text{As}_x\text{S}_y$  approximately 1.5 monolayers thick[126]. This results in a dramatic reduction in surface recombination velocity.

Different solutions show different passivating characteristics. Alcoholic solutions of  $(\text{NH}_4)_2\text{S}$  and  $\text{Na}_2\text{S}$  and other solutions with high sulphur reactivity (e.g.  $\text{S}_2\text{Cl}_2 + \text{CCl}_4$ )

have been shown to be the most effective in reducing the surface barrier and increasing photoluminescent yield[131]. These effects result from a decrease in the number of surface states.

Although it is true that  $\langle 100 \rangle$  InGaAs has a low surface recombination velocity[9], surface recombination can indeed be considerably reduced by sulphide passivation[133]. Surfaces passivated in this way have been found to deteriorate over time, especially if they are exposed to light or oxygen[130]. To maintain the passivation effects surfaces can be covered with a film of  $\text{SiN}_x$  or  $\text{SiO}_2$ . In this way semi-permanent improvements of InGaAs/InP HBT current gain have been realised[133]. An alternative coating that has become widespread in its use is polyimide[134]. Polyimide holds significant advantages in that current gain is seen across a far wider range of collector currents, it degrades much more slowly and it can be spin-coated rather than requiring deposition.

Theoretical studies have suggested that passivation (of GaAs) with selenium rather than sulphur - still a very similar process - will degrade more slowly over time[130]. Selenium will bond to both Ga and As atoms at the crystal surface but this process requires there to be excess hydrogen present to be equally as effective as sulphur in reducing surface states.

Sulphur passivation treatment with ammonium sulphide solution ( $(\text{NH}_4)_2\text{S}$ ) has been shown to provide marked improvements on both InP[128] and GaAs[126] surface quality. Amongst other devices, the treatment has found use in improving the performance of AlGaAs/GaAs[135, 136] and InP/InGaAs[133, 137, 138] HBTs.

## 4.4 Lattice Defects

It has already been seen (§4.1.3) that lattice irregularities can cause mid-gap surface states and even Fermi level pinning. While the latter is not likely in the bulk there exist deep level traps caused by defects in a semiconductor crystal lattice.

### 4.4.1 Dislocations

Dislocations are often produced in a crystalline material during growth[139]. In the case of an epitaxially grown semiconductor wafer there are a number of sources for dislocations. These include relaxation of the heterostructure epi-layers and propagation of point defects on the seed crystal through the substrate crystal (and their subsequent propagation through the epi-layers as they are grown).

When the crystal solidifies any lattice disorder is frozen in. The two basic forms of crystal dislocation are the *edge* and *screw*[139]. An edge dislocation acts like an extra plane inserted on one side of the dislocation. A screw dislocation is more complex but

can be either right- or left-handed. Since the planes of crystals under stress will tend to slip over each other as they begin to yield it is easy to visualise how a decrease in dislocations can contribute greatly to the perceived strength of the crystal as a whole. Dislocations may even be described as boundaries between regions of the crystal, one of which has slipped by the dimension of one inter-atomic spacing with respect to the other. Due to energy considerations, dislocations of more than one atomic spacing will dissociate into multiple single spacing dislocations.

A dislocation line must terminate somewhere, be it at the surface, in a closed loop or in a loop comprising of multiple dislocations. Dislocations of opposite slip direction will attract one another and may annihilate if they are on the same slip plane, otherwise they will combine to form a line of lattice vacancies or interstitial atoms (see below). The combination of lattice vacancies and dislocation lines as they diffuse through the crystal will produce jogs (steps) in the dislocation. It is possible for dislocations to be immobile, however, which, along with some types of jogs can anchor other dislocations.

#### 4.4.2 Point Defects

Point defects are either extra atoms in the crystal not situated at a lattice site or lattice sites which contain no atom. While point defects such as lattice vacancies or interstitial atoms can be produced by the methods described above they are also a common, stable defect type. Although there is an associated energy of formation for a valence site, the entropy increase involved in disordering the lattice is large enough that the energy of the perfect crystal system is greater than that of the imperfect, disordered lattice (for finite temperatures)[139]. The formation of a valence site necessitates the co-production of an interstitial atom which has its own energy barrier. Phenomenologically, it is simple to envisage a crystal losing an atom from its surface and the vacancy being filled from below, and so on: with a surface present the formation of point defects can be considered to have very little potential barrier. In this sense there is an energy of vacancy migration and this is usually found to be less than the energy cost of forming the vacancy.

### 4.5 Experimental Results

After fabrication of HBTs several methods of investigating surface interactions were undertaken. These included surface passivation by ammonium sulphide,  $(\text{NH}_4)_2\text{S}$ , and by exposure to sulphur-containing gas (hydrogen sulphide,  $\text{H}_2\text{S}$ ) and surface bombardment with argon ions. The effect of surface passivation is to decrease the concentration of surface states, while ion bombardment will cause damage that will increase the concentration.

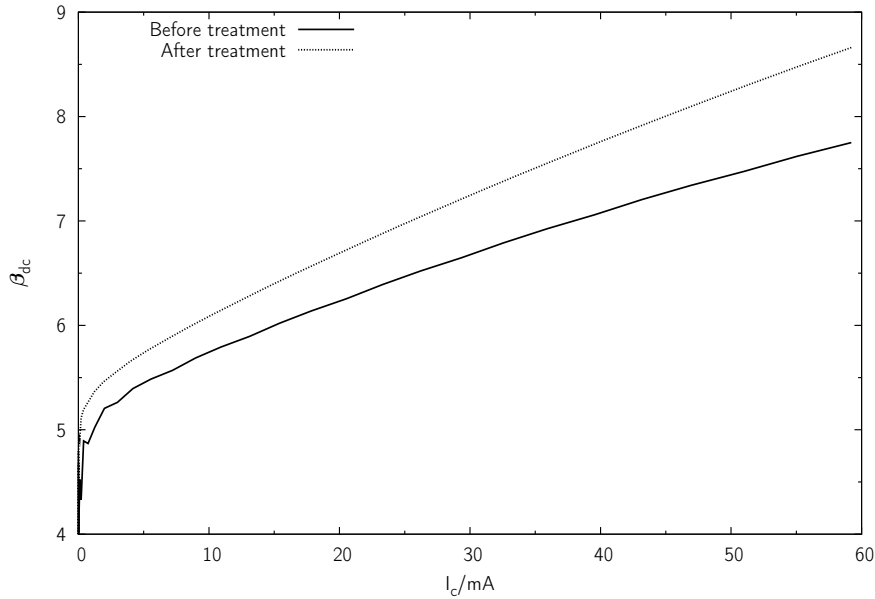


**Figure 4.2:** DC current gain against collector current for an InP/InGaAs HBT passivated with  $(\text{NH}_4)_2\text{S}$ .

#### 4.5.1 Ammonium Sulphide

A commercial ammonium sulphide solution at 40% concentration was decanted into a Petri dish at a sufficient volume (approximately 20 ml) to fully submerge the LCC and device. Immediately after de-oxidation (as described in Chapter 3), the device was placed in the sulphide solution, covered and left for 20 min at room temperature. Upon removal from the solution, the sample was rinsed in RO water and then in isopropyl alcohol. The sample was finally blown dry with  $\text{N}_2$ .

The DC current gain of the device before and after treatment in  $(\text{NH}_4)_2\text{S}$  is shown in Figure 4.2. A marked improvement in  $\beta_{dc}$  can be seen immediately after passivation.

As discussed in §4.3, the passivating layer will deteriorate over time. To this end, the effects of passivation with  $(\text{NH}_4)_2\text{S}$  were studied over time. Figure 4.3 shows the time-resolved effect of treatment on the current gain of the device over a period of 45 days. The partial return of  $\beta_{dc}$  to pre-treatment values can be explained by the desorption of sulphur atoms over time.

#### 4.5.2 Gas Phase Sulphur

A further means to modify the surface electronic characteristics of a device such as a III-V HBT is to expose it to a sulphur-containing gas, for example hydrogen sulphide,

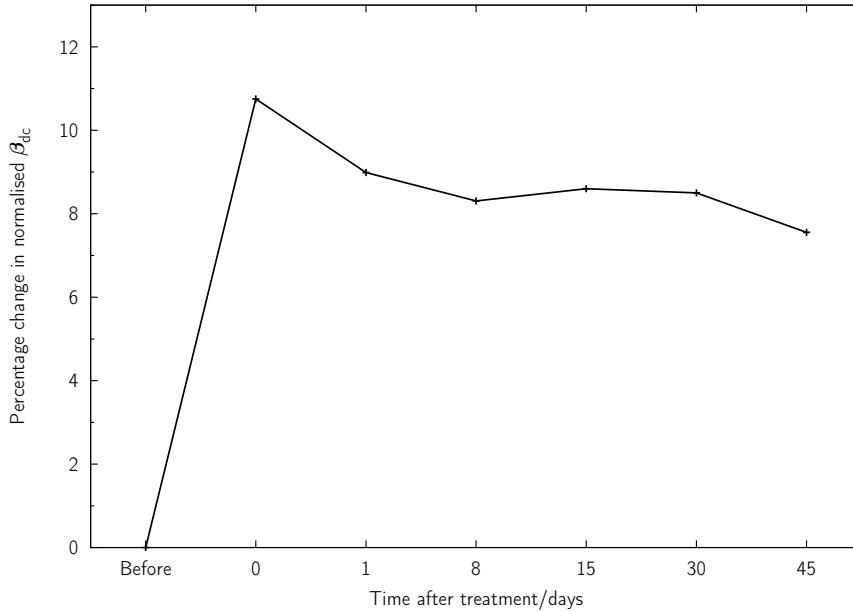


**Figure 4.3:** Time resolved plot of DC current gain for an InP/InGaAs HBT passivated with  $(\text{NH}_4)_2\text{S}$ . The current gain was measured at  $I_c = 50 \text{ mA}$ .

$\text{H}_2\text{S}$ . The mechanisms of adsorption and desorption in such a regime have been studied for GaAs[140, 141]. The effects are well-understood and multiple cycles of  $\text{H}_2\text{S}$  exposure can be seen to saturate the surface so that the majority of dangling bonds are passivated.

In order to produce hydrogen sulphide and to study its passivating effects, a few grams of crystalline sodium sulphide were added to 200 ml of RO water in a conical flask. A small volume (10 ml) of HCl was added to the solution. This starts an effervescent reaction, generating gaseous  $\text{H}_2\text{S}$ . The HBT to be treated was first de-oxidised in HCl solution order to remove any surface oxide and was then attached to a flat lid and placed at the mouth of the flask, which loosely sealed it. The device was exposed to the  $\text{H}_2\text{S}$  rich environment for 20 min following which it was rinsed in RO water and then in isopropyl alcohol. The sample was finally blown dry with  $\text{N}_2$ .

The DC current gain of the device before and after treatment in  $\text{H}_2\text{S}$  is shown in Figure 4.4. An improvement in  $\beta_{dc}$  can be seen immediately after passivation. This can be attributed to the dissociative bonding of SH and H species to the In, Ga and As dangling bonds[140, 141]. The base current is reduced as the surface of the extrinsic base region is passivated, which leads to a decrease in surface conduction and a reduction in recombination. This effect, here most pronounced at larger collector currents, deteriorated after one day in a sealed sample box at room temperature due to thermal desorption of the

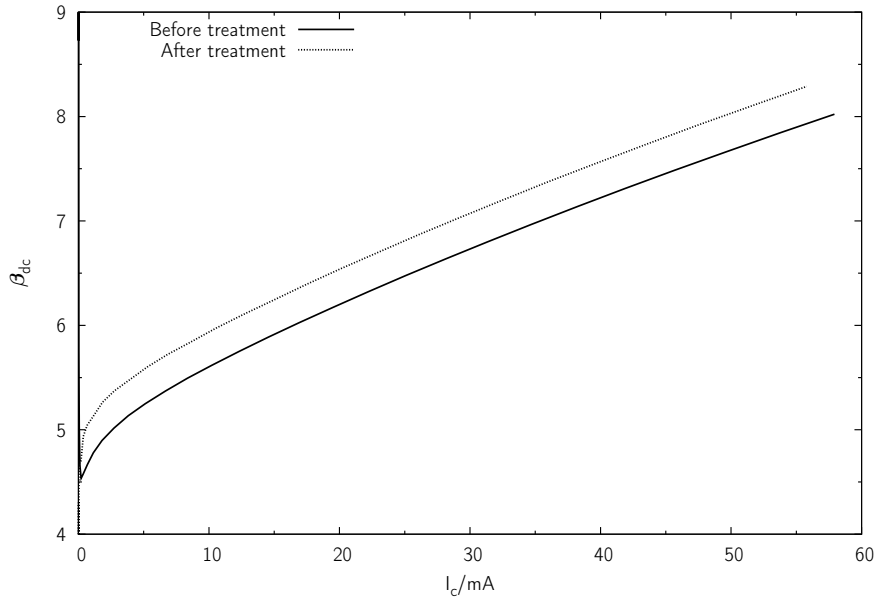


**Figure 4.4:** DC current gain against collector current for an InP/InGaAs HBT passivated with H<sub>2</sub>S.

passivating species. After a further week in the same conditions the treatment still had a beneficial effect on device performance.

The effects of passivation with (NH<sub>4</sub>)<sub>2</sub>S were studied over time. Figure 4.5 shows the time-resolved effect of treatment on the current gain of the device over a period of 45 days.

It is possible to conclude that the beneficial effects of passivation with ammonium sulphide solution are greater than that with gas phase hydrogen sulphide treatment: a numerical improvement in  $\beta_{dc}$  of 0.80 at  $I_c = 50$  mA compared with 0.35 for the H<sub>2</sub>S treatment. These correspond to fractional improvements of 11% and 5%, respectively, and can be explained by the different adsorption cross-sections of sulphur species from gas and liquid phase sources. It is generally understood that saturation sulphur coverage can be easily achieved with (NH<sub>4</sub>)<sub>2</sub>S liquid phase passivation[142] while multiple exposures are required to saturate the surface with H<sub>2</sub>S. It can be seen from Figures 4.2 and 4.4 that the improvement in current gain after (NH<sub>4</sub>)<sub>2</sub>S passivation was proportional to  $I_c$  but for the H<sub>2</sub>S passivation consisted of an additive component only. This can possibly be attributed to the saturation of the passivating effects of H<sub>2</sub>S at small  $I_c$ . Due to the complete coverage of the passivating layer in the (NH<sub>4</sub>)<sub>2</sub>S experiment, the improvement in current gain could still be proportional to the current distributed near the surface, which

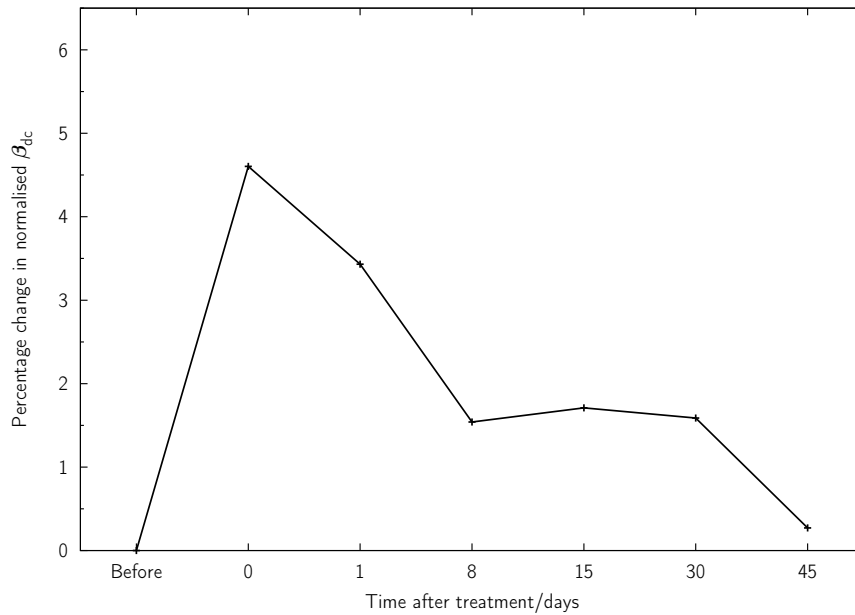


**Figure 4.5:** Time resolved plot of DC current gain for an InP/InGaAs HBT passivated with H<sub>2</sub>S. The current gain was measured at  $I_c = 50$  mA.

would in turn be proportional to the magnitude of the collector and emitter currents.

The clear difference in passivation efficacy from the two different types of treatments can be explained as follows. Sulphur atoms being less electronegative than oxygen atoms, H<sub>2</sub>S has a smaller dipole moment than H<sub>2</sub>O. Due to its large electric dipole moment, water can form extensive hydrogen bonded network structures and that explains why water exists as a liquid at room temperature but hydrogen sulphide is a gas. The small dipole moment of H<sub>2</sub>S is insufficient to distribute it on mixed ionic-covalent surfaces of compound semiconductors. In contrast, sulphide ions in solution carry a full unit negative charge of  $1.6 \times 10^{-19}$  C and are strongly attracted to In sites. This holds true for most narrow band gap semiconductors and thus we would see better passivation where sulphur species come as ions rather than weakly polarized H<sub>2</sub>S molecules. This is in spite of the fact that the concentration of H<sub>2</sub>S molecules in the gas phase is much higher than that of S<sup>2-</sup> ions in the liquid phase. Furthermore, the polar nature of semiconductor surfaces will affect the degree of passivation with non-polar surfaces less prone to sulphide passivation than polar surfaces.

After 45 days the improvement in current gain from treatment in H<sub>2</sub>S has effectively disappeared. This is supported by the thermal desorption arguments presented in the literature.

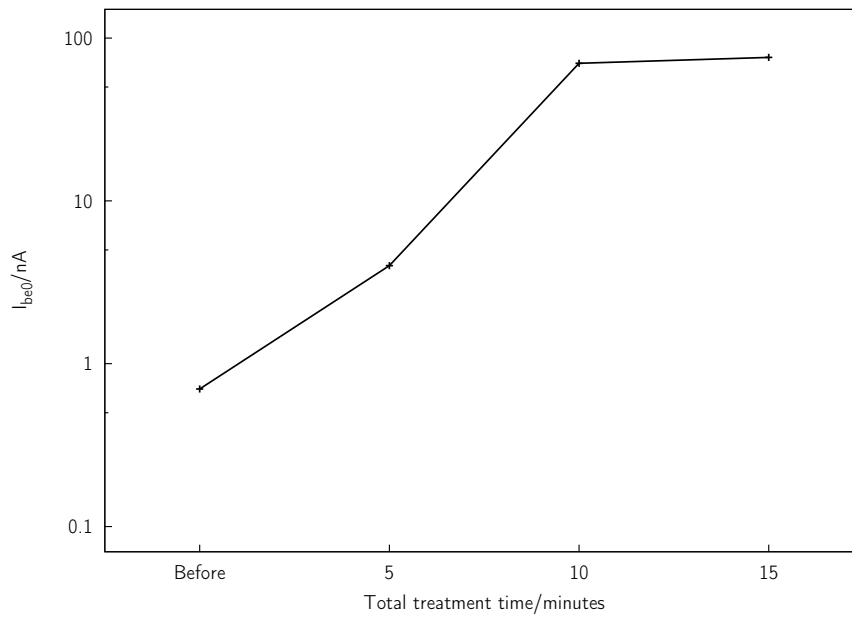
### 4.5.3 Ion Bombardment of Semiconductor Surface

In order to achieve the opposite effect to passivation some method of increasing the disorder of the surface of the HBTs had to be devised. In §4.2 there is a discussion of the effects of plasma ion bombardment on semiconductor surfaces.

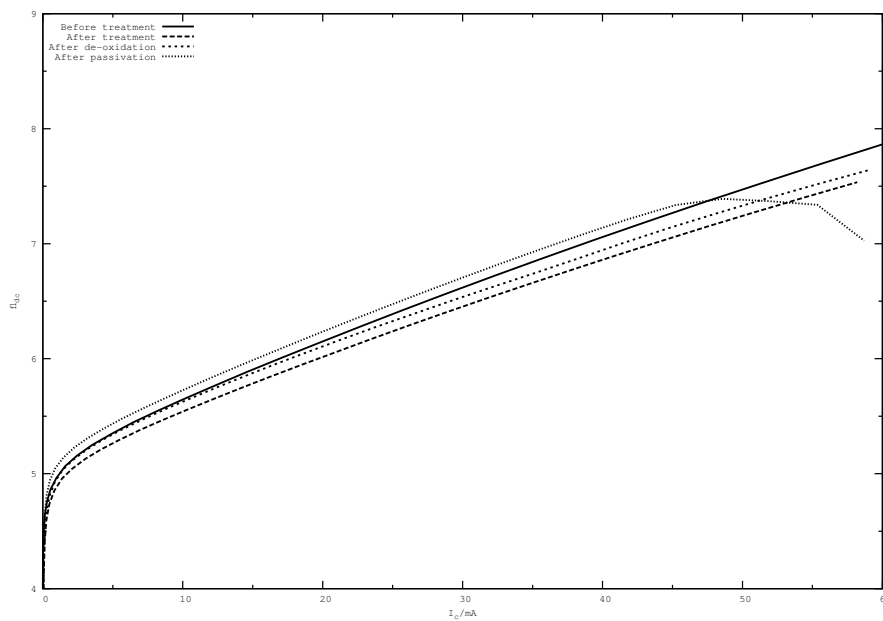
An Ar<sup>+</sup> treatment was developed using an STS Multiplex ICP dry etch machine for this purpose. Argon is commonly used as a pre-treatment in RIE processes to remove any deposits such as resist scum on surfaces that might hinder the etch chemistry; hence it was readily available. Two other major benefits of using an argon plasma are that it is unreactive, being one of the Group VIII inert gases and that it is a heavy gas (atomic number 18 c.f. oxygen, eight). The process involved creating an inductively coupled, remote argon plasma with an RF power of 200 W, a platen RF power of 5 W and an argon flow rate of 10 sccm. Using this equipment, the remote plasma required a voltage to be applied to the sample platen to accelerate the charged species towards the sample. By choosing a suitably low platen power, a low damage process was obtained. A sample masked with photoresist was exposed to the argon plasma for 60 min and subsequent measurement of the etch depth revealed the etch rate to be 0.3 nm min<sup>-1</sup>. After small piece sample loading the vacuum pump valve was fully opened to minimise the chamber pressure and hence redeposition of any material removed by sputtering. This resulted in a chamber pressure of <10 mTorr. The process was conducted at ambient temperature.

Figure 4.6 shows the effect of the Ar<sup>+</sup> treatment on the reverse leakage current of the emitter–base junction before argon treatment and the same device after successive 5 min treatments. An increase in the current can be attributed to an increase in surface conduction by accumulated surface charge caused by a deterioration of the condition of the semiconductor surface. A change of two orders of magnitude was observed after two 5 min exposures. There was only a small change after the third exposure, suggesting that the effect might have saturated.

The DC current gain of the device before and after Ar<sup>+</sup> for 10 min treatment is shown in Figure 4.7. The device was also re-measured after a further de-oxidisation in HCl and then after passivation in (NH<sub>4</sub>)<sub>2</sub>S (as described above). This was observed to restore device performance in the regions of lower collector current. It must be considered, however, that the device measurement taken before treatment incorporated the effects of a native oxide layer. These may have been deleterious to device performance and would not have been present immediately after the second de-oxidation. This could have falsely allowed the impression that the second de-oxidation restored device performance. Subsequent passivation of the sample then improved device performance. Such large gains in  $\beta_{dc}$  observed in Figure 4.2 were not seen which suggests that the argon bombardment



**Figure 4.6:** Reverse leakage current of an emitter–base junction of an InP/InGaAs HBT before and after successive 5 min exposures to  $Ar^+$  treatment



**Figure 4.7:** DC current gain against collector current of an InP/InGaAs HBT before and after a 10 min exposure to  $Ar^+$  treatment, after an HCl de-oxidation and after surface passivation in  $(NH_4)_2S$ .

caused some damage below the surface of the device.

In this chapter, as well as outlining some of the physical phenomena determining the electrical characteristics of semiconductor surfaces, the methodologies for using three different surface treatments to modify the surface of the extrinsic base region of HBTs have been given. Of the two passivating treatments, the ammonium sulphide process was shown to be the most effective, with the improvement in current gain proportional to the collector current throughout the measurement range. A maximum improvement of 11 % was realised with this technique. The treatment was also considerably more stable over time.

A novel process which was designed to damage the surface of the base layer was developed using argon ion bombardment. The effects of this process were measured firstly on the reverse leakage current of the emitter–base junction where a marked increase was observed for the first 10 min of treatment. After this the effect on the current gain was measured where a decrease of the order of 3 % was observed. Further investigation using alternative chemical treatments revealed the damage not to be constrained to the surface.

The development of these processes was undertaken with the aim of enabling the magnetic field response of an untreated HBT to be compared with that of an HBT with an ‘improved’ extrinsic base surface and one in which the surface had been ‘degraded’.

# 5 Magnetic Materials and Integrated Magnetic Structures

This chapter introduces the subject of magnetism and magnetic materials. The different classes of magnetic materials are discussed. The origins of the magnetic effects on a microscopic level are explained along with their application to the phenomenon of magnetic domains. A brief review is presented of the uses magnetic materials find in modern electronic technology.

The application of magnetic materials to this work is in the integration of 3-dimensional magnetic structures onto HBTs. The latter part of this chapter details how the structures were designed with the aid of simulation and numerical analysis and also how they were fabricated.

## 5.1 Magnetism

In discussing magnetic materials it is useful to define various quantities. As was stated in §1 (equation (1.1)), the force on charge carriers moving through a magnetic field is orthogonal to the directions of motion and field. The magnetic field  $\mathbf{B}$  (T) is created by the fundamental laws of electromagnetism. The magnetic field strength  $\mathbf{H}$  ( $\text{A m}^{-1}$ ) in a material is related to the magnetic field through the equation

$$\mathbf{H} = \frac{\mathbf{B}}{\mu} \quad (5.1)$$

where  $\mu$  is the *permeability* of the material. The permeability of free space  $\mu_0 = 4\pi \times 10^{-7} \text{ H m}^{-1}$  (where H, henries, is equivalent to  $\text{V s A}^{-1}$ ).

A magnetic dipole has a magnetic moment  $\mathbf{m}$  associated with it[143]. Thus the *magnetisation*  $\mathbf{M}$  can be defined such that

$$\mathbf{M} = \frac{\mathbf{m}}{V}, \quad (5.2)$$

i.e.  $\mathbf{M}$  is the magnetic moment per unit volume. The magnetisation and the magnetic field strength both contribute to the magnetic field in a material so

$$\mathbf{B} = \mu_0(\mathbf{H} + \mathbf{M}). \quad (5.3)$$

The magnetic field in a material without any external field can be given as  $\mathbf{B} = \mu_0\mathbf{M}$ . This is a result of the combination of the uncompensated electronic magnetic moments within the material (see §5.3.1). Saturation magnetisation is achieved when all the magnetic moments are aligned parallel to an applied external magnetic field.

In analogy to defining the permeability as

$$\mu = \frac{B}{H} \quad (5.4)$$

the *susceptibility* of a material can be defined thus

$$\chi = \frac{M}{H} \quad (5.5)$$

and is the degree of magnetisation of a material in an external magnetic field.

## 5.2 Classification of Magnetic Materials

Three main types of magnetic materials exist and can be classified according to their bulk susceptibility. The materials which first prompted inquiry into magnetic properties<sup>1</sup> were *ferromagnetic* with a high susceptibility in the order  $10^1$  to  $10^5$ [143].

The two other main categories of magnetic materials are *diamagnetic* and *paramagnetic*. Diamagnetic materials have a small negative susceptibility of the order  $-10^{-5}$ , so they oppose an applied magnetic field, and paramagnetic materials have a small positive susceptibility of the order  $10^{-3}$  to  $10^{-5}$  and they weakly reinforce the applied field.

All materials that are not ferromagnetic or paramagnetic display a diamagnetic characteristic. There are also less common sub-types of ferromagnetic ordering; these include ferrimagnetism and anti-ferromagnetism.

---

<sup>1</sup>An early record of awareness of magnetic materials comes from a dialogue of Plato's circa 400 B.C. although *lodestones* (naturally occurring permanent magnets) would certainly have piqued the curiosity of prehistoric and, particularly, iron age man[144].

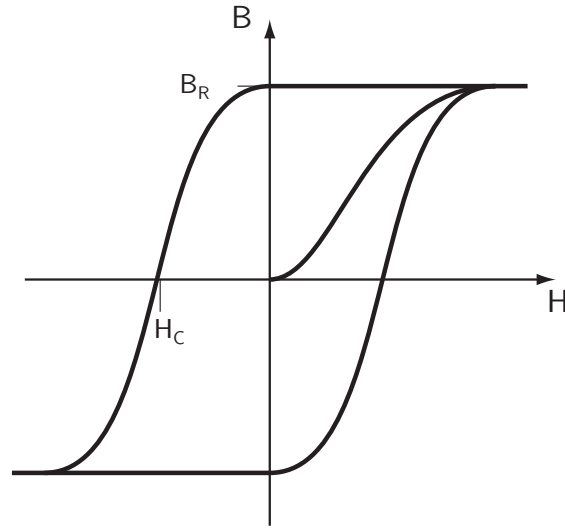


**Figure 5.1:** A typical hysteresis loop of a ferromagnetic material. The values for the remanent induction,  $B_R$ , and coercivity,  $H_C$ , are shown.

### 5.2.1 Ferromagnetism

Ferromagnets have a high relative permeability, given by  $\mu_r$  in

$$\mu = \mu_0 \mu_r. \quad (5.6)$$

Since large magnetic inductions can then be generated from small applied fields, ferromagnetic materials (such as iron and nickel) have many practical applications as a means of concentrating magnetic flux. Ferromagnets can also retain their magnetisation after the external field has been removed.

A plot of magnetic field against magnetic field strength for a ferromagnet where the applied field is increased from zero to the point of saturation magnetisation in the material, then decreased to saturation magnetisation in the opposite direction and then increased to the original saturation point gives what is known as a hysteresis loop. An example of a hysteresis loop is shown in Figure 5.1. Saturation magnetisation is achieved when all the microscopic magnetic moments in the material have aligned in the direction of the applied field. The *remanent induction*  $\mathbf{B}_R$  of the bulk material is the induction remaining after the applied field has been reduced to zero. This relates to the *remanent magnetisation*  $\mathbf{M}_R$  by

$$\mathbf{B}_R = \mu_0 \mathbf{M}_R. \quad (5.7)$$

The *remanence* is the value of either  $\mathbf{B}_R$  or  $\mathbf{M}_R$  in the specific case where the material

has first been magnetised to saturation. It can be seen from the hysteresis loop that the magnetic flux can be reduced to zero by the application of a non-zero field. This field is applied in the reverse direction to the magnetising field and is called the *coercive field* and in the specific case of reducing the induction to zero from saturation is the *coercivity*,  $H_C$ . Remanance and coercivity are products of a persistence of the order introduced by the applied field. At a suitably high temperature the thermal energy of the individual atoms (with their associated magnetic moments) ensures that the order is not maintained. This temperature is called the *Curie temperature*.

### 5.2.2 Paramagnetism and Diamagnetism

#### Paramagnetism

While the effects of ferromagnetism can be attributed in part to the interaction between near neighbour atomic magnetic moments those of paramagnetism are due to magnetic moments which do not interact with those around it. It follows from this that ferromagnets above their Curie temperature act as paramagnets, where the thermal energy is greater than that of the interaction. It is often the result of an unpaired electron spin or an electronic magnetic moment highly localised near the nucleus and effectively shielded by other electrons. A typical characteristic of some paramagnetic materials is the dependence of susceptibility on temperature in what is known as the Curie law

$$\chi = \frac{C}{T} \quad (5.8)$$

where  $T$  is the temperature and  $C$  is the Curie constant. This does not hold for all paramagnets: some exhibit a temperature independent susceptibility which arises from a conduction band electronic magnetic moment model.

#### Diamagnetism

A material can consist of atoms with no net magnetic moment should it have filled electron shells and hence no uncompensated electronic magnetic moments (see §5.3.1). These materials can not then exhibit ferro- or paramagnetism. The magnetic field induced in a diamagnetic material, as described by Lenz's Law, must oppose the applied magnetic field. These leads to a small, negative, temperature independent susceptibility determined by, among other factors, the number of electrons per atom and the root mean square atomic radius.

Where Faraday's law states that a voltage (magnetically) induced in an electrical circuit is proportional to the rate of change of magnetic flux through the circuit, Lenz's law states that the induced voltage is in a direction which opposes the changing flux that

produces it. Lenz's law is a consequence of conservation of energy. These are given by

$$V = -N \frac{d\Phi}{dt} \quad (5.9)$$

where  $\Phi$  is the magnetic flux passing through a coil of  $N$  turns and  $d\Phi/dt$  is the rate of change of flux.

## 5.3 Origins of Magnetic Effects

### 5.3.1 Microscopic Magnetism

Electrons are the principle cause of an atom's magnetic moment. Classically this can be considered a product of orbiting electrons as a charge in motion inducing magnetic field. There are two contributors to the electron magnetic moment, orbital magnetic moment and spin magnetic moment. Classically, the orbital magnetic moment  $\mathbf{m}_o$  is given by

$$\mathbf{m}_o = - \left( \frac{e}{2m_e} \right) \mathbf{p}_o \quad (5.10)$$

where  $\mathbf{p}_o$  is the orbital angular momentum,  $e$  is the electronic charge and  $m_e$  is the mass of an electron.

This classical approach breaks down for electron spins due to the tangential velocities as calculated using the Bohr magneton. (The Bohr magneton is the magnetic dipole moment of an electron in a hydrogen atom and is so-called because of the Bohr model of the atom.) As is to be expected, the quantum description of electronic magnetic moment does not allow all values of  $p_o$  and  $p_s$ . Bohr's theory of the atom introduces a principle quantum number,  $n$ , that relates to the energy  $E_n$  of an electron orbiting an atom, given by the equation

$$E_n = - \frac{Z^2 m_e e^4}{8n^2 h^2 \epsilon_0^2} \quad \text{where } n = 1, 2, 3, \dots \quad (5.11)$$

Here  $Z$  is the atomic number and  $\epsilon_0$  is the permittivity of free space. The allowed energy levels for electrons orbiting in atoms predicted by (5.11) are degenerate. The orbital angular momentum quantum number  $l$  is used to measure this. It can take value  $l = 0, 1, 2, 3, \dots, (n - 1)$  and relates to the eccentricity of the electron orbit and also to the orbital angular momentum by

$$\mathbf{p}_o = l \left( \frac{h}{2\pi} \right) \quad (5.12)$$

where  $h$ , Planck's constant, is  $h = 6.626 \times 10^{-34}$  J s. Two further quantum numbers are defined, the spin quantum number  $s$ , which has a value of  $1/2$  for an electron, with spin

angular momentum given by

$$\mathbf{p}_s = \mathbf{s} \left( \frac{h}{2\pi} \right), \quad (5.13)$$

and the total angular momentum quantum number  $j$ , which has a value of  $l + s$ , the vector sum.

The orientation of the spin and orbital angular momentum vectors when subjected to an applied magnetic field is also quantised with respect to the  $z$  axis of the coordinate system and this gives rise to the quantum numbers  $m_l$  and  $m_s$ . The probabilistic wave functions which arise from the combinations of these quantum numbers (under the restrictions of the Pauli exclusion principle) in turn give rise to the well recognised electron orbital distributions ( $1s$ ,  $2p$ ,  $3d$ , etc.) and determine the bonding properties of the atom.

Just as the magnetic moment of the electron is determined by its angular momentum, the magnetic moment of the atom is determined by the vector sum of the angular momenta of its electrons. This is calculated either from the sum of  $j$  for each electron, giving  $J$ , or from the vector sum of  $L$  and  $S$ , the individual sums of  $l$  and  $s$ . The two do not give the same numerical answer if the spin and orbit magnetic moments are coupled. It is the interaction of overlapping electron orbits in solids (the so-called *exchange interaction*) and their effect on the magnetic moments of adjacent atoms that give rise to the order which is observed macroscopically as magnetism in materials (see [143] for a complete description).

### 5.3.2 Magnetic Domains

If the magnetisation of a paramagnet or a ferromagnet is zero it is not unreasonable to assume random distribution of atomic magnetic moments. While this is true of paramagnetic materials, it is not the case with ferromagnets as localised regions of order exist within the material[143]. These regions of aligned magnetic moments are called *domains*. In a demagnetised state these domains have a moment that is random and not aligned to any direction so that the net magnetisation is zero. The bulk properties of ferromagnetic materials can be explained by invoking this, the *Weiss domain theory*. The atomic moments of  $10^{12}$  to  $10^{18}$  atoms are aligned in parallel and although some crystallographic directions are preferred (the 'magnetic easy axes'), the direction of magnetisation is random. The theory added a mean field term to the classical Boltzmann statistical thermodynamics used to explain paramagnetism by Langevin[143]. The mean field interatomic interaction causes adjacent atoms to align because the energy of the (multi-particle) system is then lower. It follows from this that a single large domain would be the lowest energy state for any given ferromagnetic structure. In fact the energy is minimised by multiple small domains with two factors in consideration, maintaining

the magnetic flux within the material (i.e. providing for closing of the flux loops within the material), and the energy of the domain walls themselves.

The existence of domains leads to discrete changes in magnetic induction caused when two or more domains merge together (magnetisation) or when a domain splits into smaller domains (demagnetisation). This is known as the *Barkhausen effect* and was one of the first, albeit indirect, observations of magnetic domains.

## 5.4 Applications of Magnetic Materials

The applications in which magnetic materials are employed are wide and varied. Ferromagnets can be further classified by their coercivity, whereby those with a high coercivity are classed as *hard* and those with a low coercivity classed as *soft*. In general terms, a material with a coercivity above  $10 \text{ kA m}^{-1}$  is a hard magnetic material and below that is soft. Certain iron alloys such as Nd-Fe-B and ferro-platinum are hard materials while iron, nickel and some of their alloys specially designed for the purpose (such as permalloy, Ni-Fe-Mo or Ni-Fe-Cu-Mo) are soft[143].

Soft magnetic materials have applications in electromagnets, motors, transformers and relays where the ability to reverse the induction (or switch the direction) is important. A high relative permeability is essential for electromagnets so that large inductances can be generated while low conductivity steels are used for transformer cores to reduce eddy currents. A relay requires low remanance as well as coercivity and is usually made of unalloyed iron, Fe-Si or Fe-Ni.

Permanent magnets are made from hard magnetic materials. These are often made from ferrites which can be also either hard or soft. Hard ferrites such as those made with barium or strontium are found in motors, generators and loudspeakers, amongst other things. Soft ferrites have a high electrical resistivity which can be important in high frequency applications[143].

One of the most high profile uses of magnetic materials is in magnetic recording media and magnetic storage media. While this was originally in the form of magnetic tape (for data and audio) modern storage media are almost exclusively magnetic disks in hard disk drives. These require a high remanance and coercivity to ensure that the storage *bit* is not demagnetised and data lost. The disks are usually made from aluminium and coated in glass, with the medium itself a thin film of a cobalt based alloy in the form of crystallites with a grain size under 10 nm and a magnetic easy axis in the plane of the film[145]. The individual bits must be written over several hundred grains in order that the randomly aligned anisotropy can be overcome. More recently Co-Cr films have been used to manufacture perpendicular recording media which allows for a much higher data

density[146].

Another technology that employs magnetic materials that of magnetic random access memory (MRAM), touted as an alternative to static RAM implemented in CMOS for ICs[147]. MRAM offers several advantages including non-volatility, speed of access and lifetime. It uses a device called a *magnetic tunnel junction* (MTJ) which consists of a thin dielectric tunnel sandwiched between two layers of ferromagnetic material, one of which is permanently magnetised in a specific direction and the other of which can be aligned either parallel or anti-parallel[148]. Much research towards using the magnetic tunnel junction as a randomly accessible storage bit in high bandwidth computing applications has been done by IBM and others recently[149].

Another route to MRAM could be to use *domain wall traps* in which thin films of a high permeability material such as permalloy are patterned into specific geometries. These geometries are designed so that the domain walls are trapped in one of two stable positions and can be moved reproducibly between them by the application of a small external field[150].

In this work, magnetic materials were used for another purpose. As will be described, 3-dimensional structures fabricated in high permeability, soft magnetic materials were designed to be incorporated into the device to improve the magnetic field response of an HBT, to make a novel integrated HBT magnetic field sensor.

## 5.5 Design of 3-D Structures

Techniques to increase the transduction effects of the native device were required to enable fabrication of a magnetic field sensor using an epilayer structure optimised for high speed HBT applications. One such technique employed was to integrate three-dimensional magnetic structures onto the extrinsic base region of the HBTs. In doing this it was possible through appropriate design to focus the magnetic field into the base region (where the physical processes of transduction took place) to increase the sensitivity of the sensor. A secondary benefit may have been in partially shielding the emitter from magnetic field so that electrons were affected less by the magnetic field prior to injection into the base.

The design of the magnetic structures would determine the efficacy of the shielding and focussing effects. Thus a procedure of simulation and analysis was undertaken. To optimise the design of the structures the simulations were carried out on a 2-D software modelling tool called *Vizimag* (written by J. Beeteson). This allowed the field shaping effect of various designs of magnetic element (fabricated in a ferromagnetic material) in a uniform external field to be studied. Figure 5.2 shows the intended placement of the

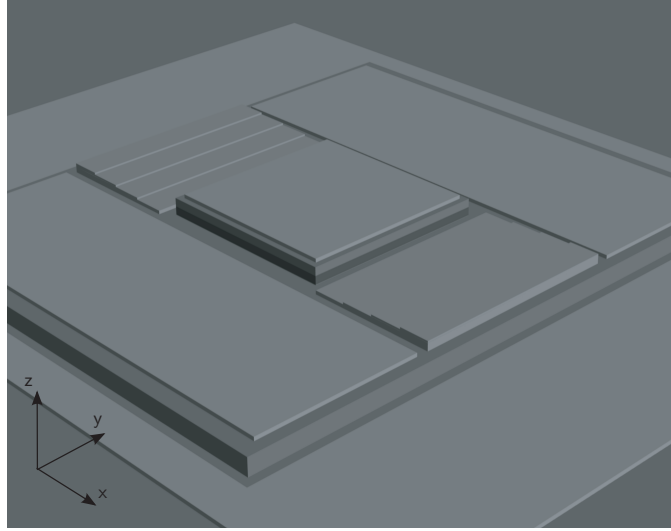


**Figure 5.2:** Three dimensional model of the mesa of the integrated device. The magnetic structures are placed on the extrinsic base surface. The  $z$ -axis scale is magnified ten times.

structure on the device. The plane in which the magnetic field should be altered by the structures was the plane in which the simulations were conducted and equates to the  $x$ - $z$  plane of the device in Figure 5.2. The  $x$ - $y$  plane is the plane of the semiconductor surface, as shown in the figure, and the  $z$ -direction is normal to this surface, increasing out of the semiconductor. This is shown schematically in Figure 5.3 where the focussing magnetic field lines into the base and relative shielding of the emitter is depicted. In this case the field is applied perpendicular to the  $z$ -direction. The  $z$ -direction is the primary direction of electron velocity as the electron density gradient is aligned along the axis. It is also the normal to the plane of the epiwafer surface. In further discussions of magnetic field the angle in which the external field is applied is given with respect to this direction, hence the field applied in Figure 5.3 is said to be applied in the *perpendicular* direction.

### 5.5.1 Cross-sectional Design

Figure 5.4 shows the iterative design stages. The arbitrary starting point for the simulations was a single block of ferromagnetic material. This was the reference against which to compare the more complex designs. A control simulation without magnetic structure was also executed. The footprint of the block would be some  $55\ \mu\text{m}$  by  $90\ \mu\text{m}$  reflecting the size of the extrinsic base ledge and the  $75\ \mu\text{m}$  emitter  $y$ -dimension (see 5.2). The height ( $z$ -dimension) of the structure would be comparable to that of the emitter,  $600\ \text{nm}$ .

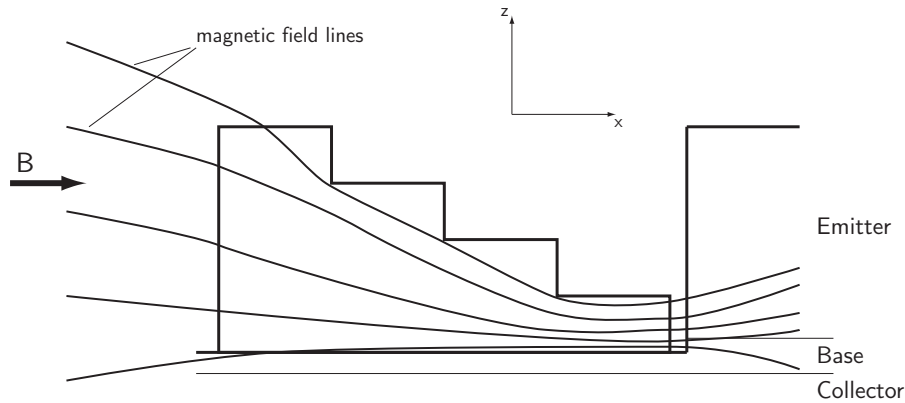


**Figure 5.3:** A schematic of the effect of integrating a magnetic structure onto the base of an HBT. The upper regions of the emitter mesa are shielded from the magnetic field which is focussed in the the base region.

The route taken from there was to break the symmetry in the  $z$ -direction. In order to measure the effect of the magnetic structure a line was taken through the cross-section for each simulation and the magnetic field in each element plotted along the line. The line was co-located with the approximate edge of the emitter mesa on the device. The field lines were observed to relax more with increasing distance from the right hand edge of the structure. This made it important to locate the structures as close to the side of the emitter mesa as possible. A plot of all the designs was then able to show which was the most effective at focussing the field. The structures in branch (1) of the simulations were chosen to have no symmetries at all and in branch (2) some of the structures have a  $180^\circ$  rotational symmetry.

The simulations were carried out with a mesh size of  $400 \times 400$  where the  $x$ -axis scale was 1:2 and the  $y$ -axis scale was 1:250. The large scale in the  $y$ -direction was necessitated by the large aspect ratio in the structures discussed above. The applied field was 0.615 T reflecting the maximum field of the experimental test apparatus. The relative permeability of the structures was set initially at that of nickel ( $\mu_r \simeq 100$ ) and then when the optimum design was achieved a comparison with other materials was conducted. In order to gauge the efficacy of the different structures the applied field was aligned along the  $x$ -axis. Figure 5.5 shows a simulation setup and its results including flux contours and field lines.

Figure 5.6 shows the plot of the simulation output for several design candidates. The positions of the upper surface and the bottom of the base layer are indicated as well as the control simulation which contained no magnetic structures.

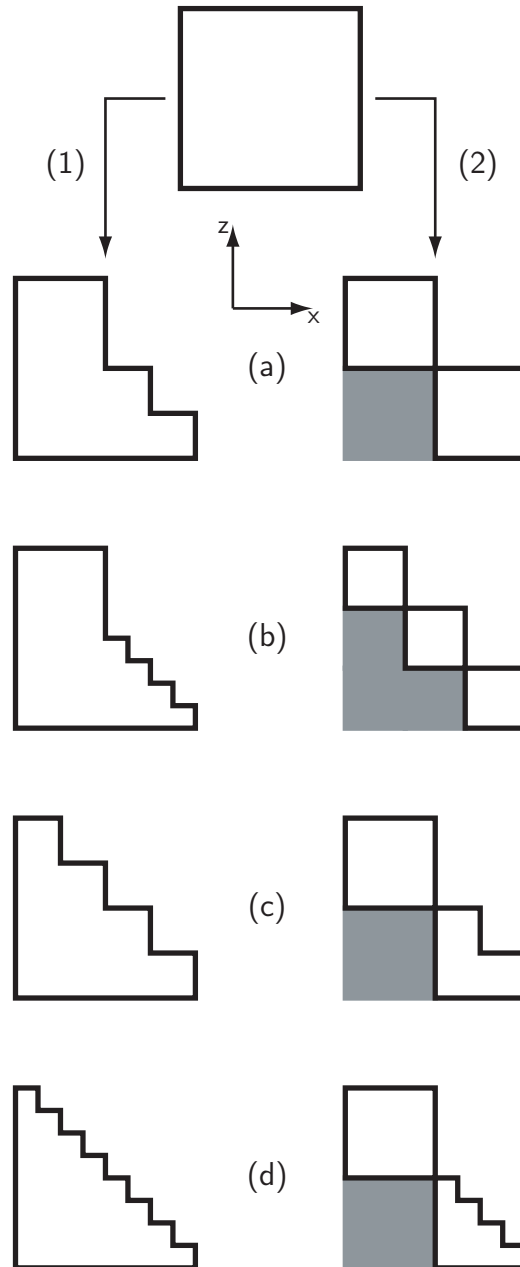


**Figure 5.4:** Iterative design flow for simulations of magnetic structures. Simulations were carried out on different  $x$ - $z$  cross-sections of the 3-D structures. Branch (1) involved breaking the symmetry in the  $y$ -direction and branch (2) was to break the rotational symmetry. The grey regions indicate the location of a silicon nitride scaffold.

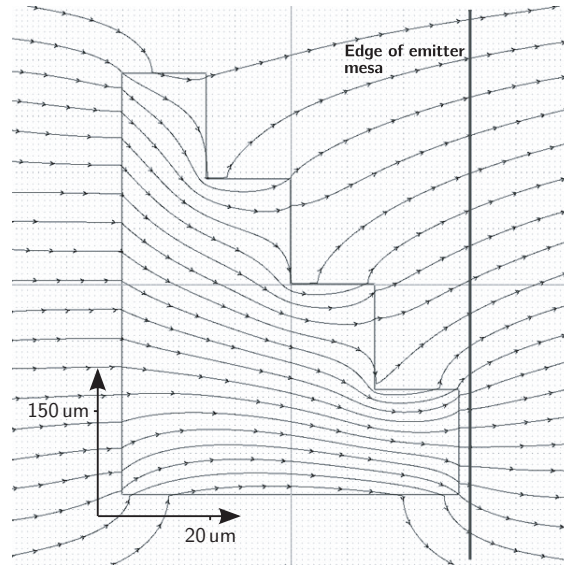


**Figure 5.5:** Vizimag 2-D magnetic element simulation of a typical iterative step. A vertical line has been added to indicate where the emitter mesa is positioned (according to the design file). This is the line along which the data was extracted for analysis and plotted in Figure 5.6.

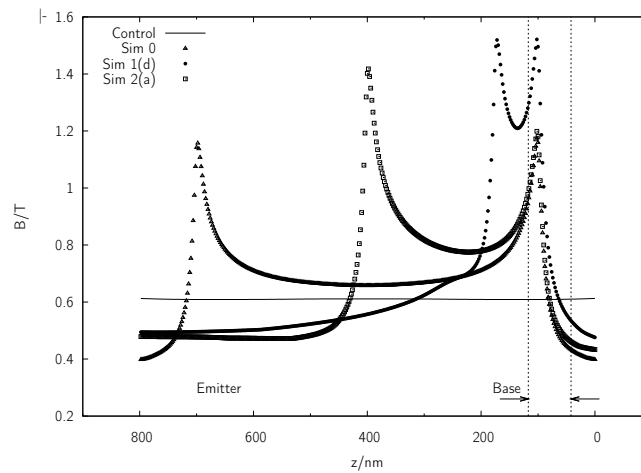


**Figure 5.6:** Position along the  $z$ -axis against magnetic field strength for several magnetic structure designs. The top and bottom of the base layer indicated with dashed lines. Also shown is the control plot.

Design	Integrated flux density/T-nm
Control	92.6
0	109.0
1(a)	126.7
1(b)	138.4
1(c)	127.2
1(d)	140.7
2(a)	112.8
2(b)	117.0
2(c)	123.2
2(d)	135.0

**Table 5.1:** The results of the simulation of each magnetic structure design, as determined by the value of the magnetic flux integrated over the width of the base.

Table 5.1 shows the values of the magnetic induction for each simulation, integrated over part length of the line which describes the edge of the emitter (the part which constitutes the base length). The integrated values of *total magnetic flux density* are quoted in Tesla nanometres. The design which best focusses the magnetic field into the base region is 1(d).

### 5.5.2 Material Choice

The magnetic material chosen for the 3-D magnetic structures would be dependent on availability, compatibility with current InP HBT fabrication processes and, primarily, efficacy at focussing the field in the base region. Once the optimum design for the structure had been determined it was possible to simulate the effect of using materials with higher relative permeabilities. Figure 5.7 shows the plots for nickel ( $\mu_r \simeq 100$ ), permalloy ( $\mu_r \simeq 8000$ ) and  $\mu$ -metal ( $\mu_r \simeq 20000$ ). Little difference is observed between the three plots.

The numerical integration described above was also carried out for the simulation of the three different materials. The results are shown in Table 5.2. The magnetic flux focussing effect is seen to be far more strongly dependent on the topography of the magnetic structure than on the magnetic material from which it is fabricated.

### 5.5.3 Base Volume Analysis

Placing a magnetic structure in close proximity to the intrinsic base would not only increase the magnetic flux in the base in the direction it was applied, the focussing would also cause an increase in the component of the field parallel to the normal of the wafer surface. To analyse this from the simulations it was necessary to extract the field

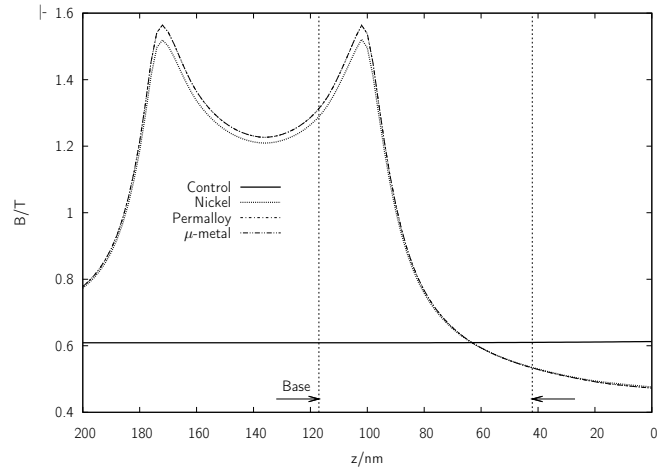


**Figure 5.7:** Position along the  $z$ -axis against magnetic field strength for three different magnetic materials designs. Also shown is the control plot.

Material	$\mu_r$	Integrated flux intensity/T-nm
Control	0	92.61
Nickel	100	140.72
Permalloy	8000	142.94
$\mu$ -metal	20000	142.95

**Table 5.2:** The results of the simulation of magnetic structure design 1(d) with materials of differing relative permeability. The value of the magnetic flux integrated over the width of the base is shown.

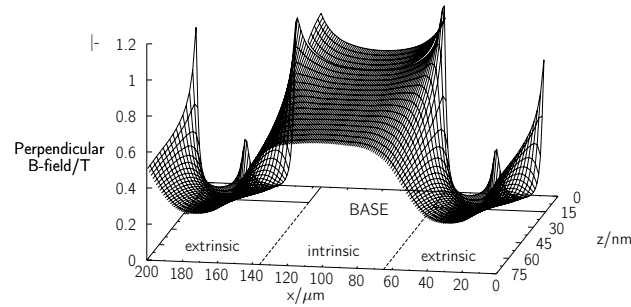


**Figure 5.8:** Magnitude of the magnetic field component perpendicular to the normal over the  $x$ - $z$  cross-sectional area of the base. An external field applied perpendicular to the normal and 3-D magnetic structures are present. The intrinsic base is demarcated by lines.

magnitude and directional data from each mesh element that constituted the  $x$ - $z$  cross-sectional area of the base (hence this was actually a ‘base area analysis’ but was assumed to be effectively constant across the whole extent in the  $y$ -direction). Simulations were carried out with applied magnetic field perpendicular and parallel to the normal and with the mesh extending over the whole region of interest, i.e. the emitter, the base and the two magnetic structures on either side. In this simulation the mesh size was  $200 \times 200$ , the  $x$ -axis scale 1:1 and the  $z$ -axis scale 1:250. The results for both simulations also calculated and plotted in turn for both directional components are given in §5.5.3 and §5.5.3.

### Perpendicular Applied Field

The plots of magnetic field strength for the base area are shown in Figures 5.8 and 5.9 for the field component perpendicular and parallel to the normal, respectively, in the case of an applied field perpendicular to the normal. Because there are two counteracting physical processes the effect of which is dependent on the magnitude of the field in each of these directions a numerical integration was performed over the base area for both.

In the case of the field perpendicular to the normal it was shown in [77] by solving the equations of state that the majority of the current transport is within the intrinsic base region. It is then reasonable to assume that the physical process governed by the field in this direction (described in Chapter 2) is dependent only on the integral of the magnetic field component in this region. The effect of the field parallel to the normal

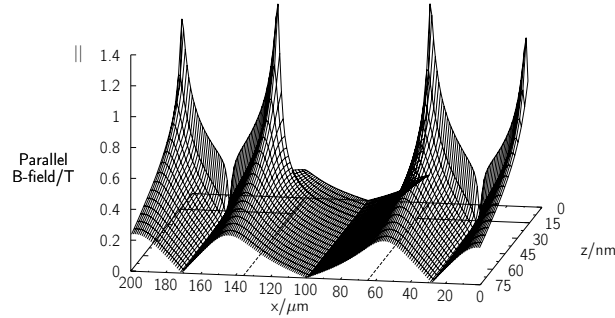


**Figure 5.9:** Magnitude of the magnetic field component parallel to the normal over the  $x$ - $z$  cross-sectional area of the base. An external field applied perpendicular to the normal and 3-D magnetic structures are present. The intrinsic base is demarcated by lines.

(of reducing the recombination rate by accelerating scattered electrons in a helical path) could be considered to have an effect through the whole, or part of, the extrinsic base region. The contribution of the parallel field to transport in the device would then be a figure somewhere between the total magnetic flux intensity in the intrinsic region and the total magnetic flux intensity of the whole (extrinsic and intrinsic) base. The parallel field effect applies only to electrons which have velocities which are not aligned along the direction of the carrier density gradient. Generally, this will only apply to electrons which have scattered. The perpendicular field effect applies to all electrons travelling in the primary diffusion direction. The maxima of magnetic field strength correspond to the locations of the corners of the 3-D magnetic element, where the focussing effect is strongest.

The total flux densities are shown in Table 5.3 along with the total flux density in the direction perpendicular to the normal of the control simulation. The total flux density parallel to the normal of the control simulation is zero. It can be observed from the data that the enhancement of the field applied in the perpendicular direction (of  $\sim 0.8 \text{ T}\mu\text{m}^2$ ) is somewhat offset by the increased flux density parallel to the normal. This is especially true of the regions immediately flanking the intrinsic base area, through which any potential recombining electrons must pass.

The relative strengths of the effects were then to be evaluated in isolation in a device without magnetic structures. If the effect of the parallel field was active over a portion

Field component	Base region	Total flux density/ $T\mu\text{m}^2$
Control (perp.)	Intrinsic	3.899
Perpendicular	Intrinsic	4.672
Parallel	Intrinsic	0.648
Parallel	Intrinsic + Extrinsic	3.009

**Table 5.3:** Total magnetic flux density for the x–z cross-sectional area of the base for a field applied perpendicular to the normal. The flux density in the intrinsic base of the control simulation is also shown.

of the extrinsic base and the sensitivity of the device to the two counteracting processes similar it was possible that any gains from incorporating 3-dimensional magnetic structures onto the base ledge would cancel each other. It should be noted that the effect of the parallel field, while decreasing the scattering volume, will also increase the length of an electron's path before being collected and so will increase the effective base length and the probability of recombination.

### Parallel Applied Field

The plots of magnetic field strength for the base area are shown in Figures 5.10 and 5.11 for the field component perpendicular and parallel to the normal, respectively in the case of an applied field perpendicular to the normal. There is a concentration of the parallel field component in the extrinsic base due to the focussing effect of the magnetic structures. An increase in the perpendicular component can also be observed at the edge of the intrinsic base region.

There is an increase (from zero) in the perpendicular field component in the intrinsic base in this case. The parallel field component is also increased in the extrinsic base. The total flux densities are shown in Table 5.4 along with the total flux density in the direction parallel to the normal of the control simulation. The total flux density perpendicular to the normal of the control simulation is zero. There is a slight increase in the parallel field component over the whole base but a decrease in the intrinsic base. More significant is likely to be the increase (from zero) in the perpendicular component in the intrinsic base.

## 5.6 Fabrication of 3-D Magnetic Structures

A fabrication process was required that could support each of the different designs in the simulation set. In order to fabricate the designs in branch (2) of the magnetic structure simulations (see Figure 5.4) not only could different depths of metal be needed but also a scaffold of non-magnetic material would be incorporated. This scaffold would provide

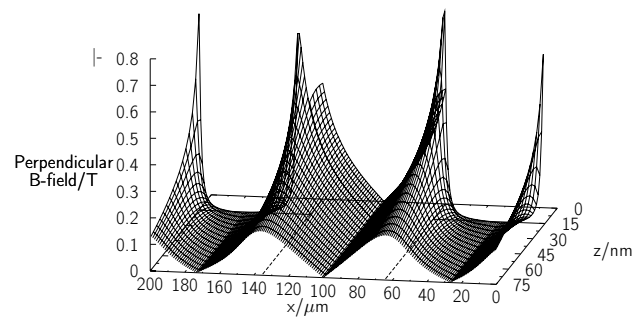


**Figure 5.10:** Magnitude of the magnetic field component perpendicular to the normal over the  $x$ - $z$  cross-sectional area of the base. An external field applied parallel to the normal and 3-D magnetic structures are present.

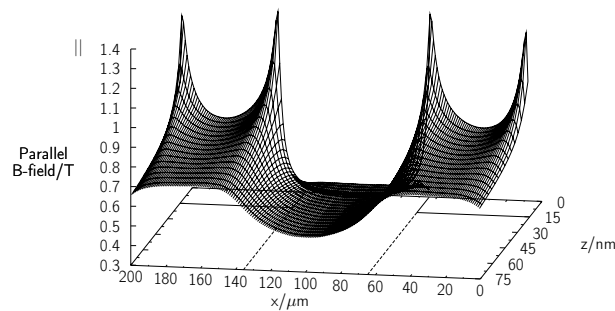


**Figure 5.11:** Magnitude of the magnetic field component parallel to the normal over the  $x$ - $z$  cross-sectional area of the base. An external field applied parallel to the normal and 3-D magnetic structures are present.

Field component	Base region	Total flux density/ $T\mu\text{m}^2$
Control (parallel)	Intrinsic	3.895
Control (parallel)	Intrinsic + Extrinsic	9.238
Perpendicular	Intrinsic	0.840
Parallel	Intrinsic	2.875
Parallel	Intrinsic + Extrinsic	9.358

**Table 5.4:** Total magnetic flux density for the x-z cross-sectional area of the base for a field applied parallel to the normal. The flux density in the intrinsic base of the control simulation is also shown.

a means to manufacture the asymmetric structures shown in the diagram.

The geometry of the metallisations was achieved through lithographical techniques. In the initial development ebeam lithography was used but once a final design was chosen a photolithography mask was made. Photolithography is cheaper, simpler and faster. The most readily available method to make the scaffold was a dielectric, deposited with CVD. This is generally a high temperature process and so incompatible with lithography. Patterning must be carried out using a lithography step and an etch after deposition, which can be time consuming. The room temperature SiN process discussed in Chapter 3 was considered the ideal solution as a single lithography and lift-off step would suffice for each layer. Arbitrary scaffold geometries could then be constructed, at various thicknesses, limited only by the consistency of lift-off as the thickness of the dielectric increased towards the thickness of the lower resist layer. Silicon nitride thicknesses of up to 250 nm have been lifted off successfully.

Figure 5.12 shows one such device, fabricated from  $\text{Si}_3\text{N}_4$  and nickel. As has been seen above, the permeability of the material was relatively unimportant. Nickel has a relative permeability of around 100 and was readily available to deposit using either of the metal evaporation tools in JWNC.

The evidence of the simulations suggests that the more smoothly stepped the metallisation layers of the magnetic structure, the better the focussing effects. A compromise had to be made, however, between fabrication time and efficacy. A four layer structure, similar to design 1(c), was fabricated as the optimal solution. Figure 5.13 shows a scanning electron micrograph of the integrated device and Figure 5.14 shows the profile of the emitter mesa with the four layer structures on each side.

After discussing the background of magnetic materials and their applications, this chapter detailed the design process for the 3-dimensional magnetic structures which

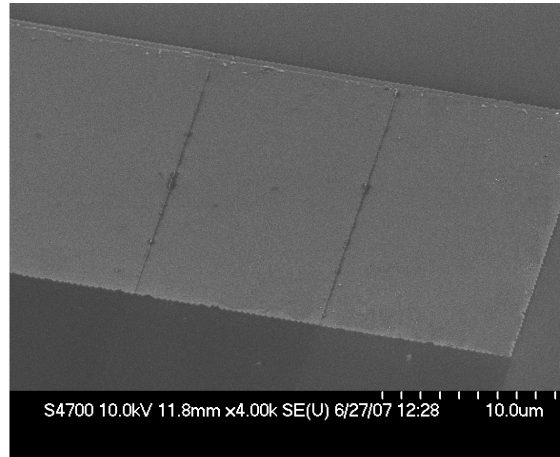


**Figure 5.12:** An SEM image of a 3-dimensional magnetic structure, complete with SiN scaffold.

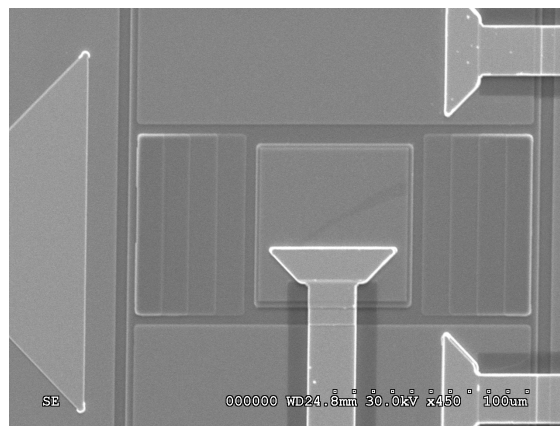


**Figure 5.13:** An SEM image of a 3-dimensional magnetic structure, integrated onto an HBT.

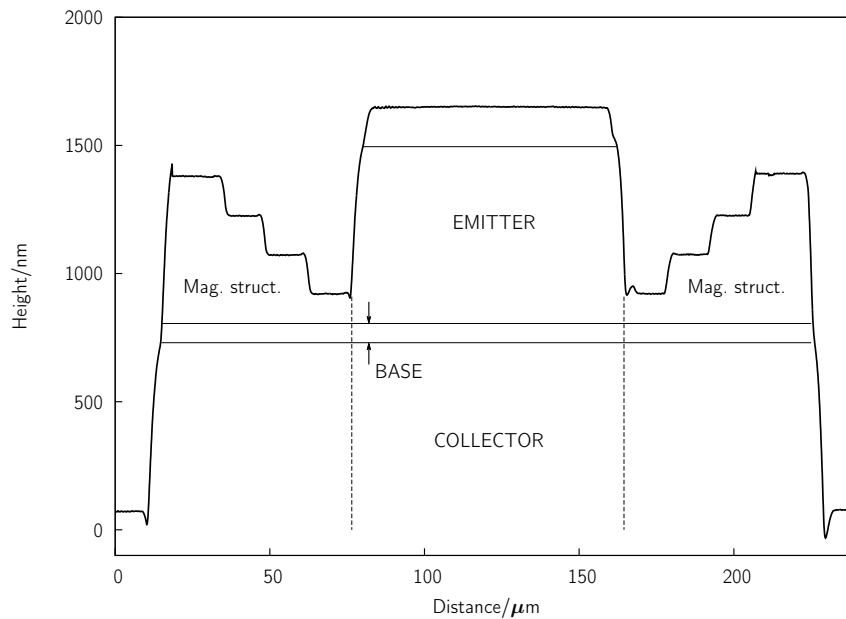


**Figure 5.14:** A Dektak surface profilometer scan of a 3-dimensional magnetic structure, integrated onto the mesa of an HBT.

were to be integrated onto the extrinsic base region of the HBT magnetic field sensor. Firstly, the cross-sectional design was optimised given the initial design parameters. An evenly stepped structure was found to be the most effective in focussing the force in to the base. A full analysis of the effect of such a structure on the magnetic response of an HBT was carried out, with reference to the increase in stray field effects. These would cause a response of the device in which the parallel and perpendicular field components were intermixed. The overall increase in the perpendicular component of a magnetic field applied in the perpendicular direction of around 20% was offset by an increase in the parallel field component.

For magnetic field applied in the parallel direction there is a small increase in the parallel field component across the whole base region, although there is an increase of the perpendicular component from zero, which will counteract this effect.

The fabrication process was designed and the optimal 3-dimensional magnetic structures were integrated onto the device. These were simple four step structures fabricated in four metal lift-off steps.

# 6 Effects of Applied Magnetic Field on HBTs

This chapter discusses the investigation of the response of as-fabricated HBTs in an external applied magnetic field. An investigation of the transport properties of the devices was carried out to confirm the findings of previous studies as well as to verify the experimental procedure. Further low temperature measurements have also been carried out. A discussion of the experimental setup precedes that of the response of an unmodified device to magnetic field applied parallel and perpendicular to the wafer growth (and primary current) direction. A sweep of the angles between parallel and perpendicular directions then highlights the angle response of the transistor.

Amongst other findings the existence of appropriate effects on carrier transport for sensing of magnetic field using the particular band structure of the devices at a measurable level is demonstrated. A discussion of the noise inherent in the devices is also contained below, since the signal to noise ratio of a sensor is determined in part by this metric.

## 6.1 Experimental Setup

The magnetic field experiments were carried out in the Department of Physics at the University of Glasgow. A *Newport* Electromagnet Type E electromagnet was used to provide a uniform and highly directional field. The HBT was mounted in an 18-pin ceramic leadless chip carrier (LCC) which was inserted into the PCB socket designed to accept the 18-pin LCC. The socket itself was attached to an arm of a jig which allowed it to be inserted from above directly between the two poles of the magnet. Connections were wired from the pins of the socket, through the arm of the jig to BNC connectors at the head of the jig. Thus the appropriate bias and sense connections could be made to the device under test. Figure 6.1 shows the arrangement of the equipment.

In keeping with the previous work on the effects of magnetic field on the transport properties of HBTs[64, 70, 71, 73, 75, 77, 151] devices were biased in a common-base

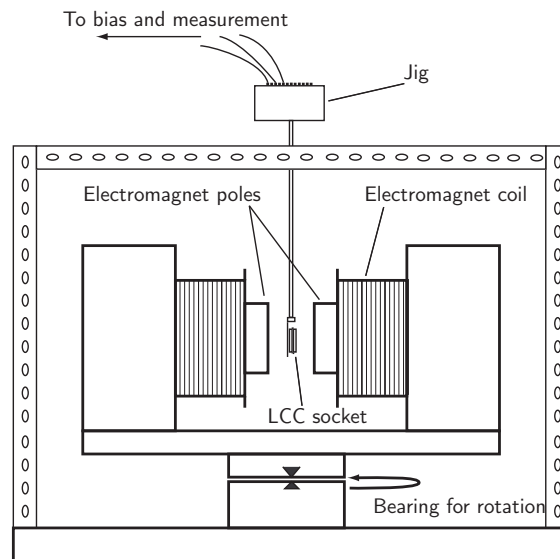


**Figure 6.1:** The experimental setup for applying an external magnetic field to an HBT. Shown is the jig and LCC socket, as well as the electromagnet and connections.

configuration. This is advantageous in such an experiment because it is the base current  $I_b$  that is of interest. Changes in  $I_b$  could not be inferred from, for example, the collector current in a common-emitter configuration, since  $I_b$  is held constant. Also, measuring small changes in a small current directly is experimentally expedient. Thus the devices were biased in the configuration shown in Figure 6.2 using an HP 3245A Dual Channel Universal Supply. The power supply provided seven voltage ranges between  $\pm 1$  V and  $\pm 10$  V with a 12-bit resolution and a  $100 \mu\text{s}$  settling time and four current ranges with the same resolution between 0.1 mA and 100 mA. In practice, the device could be incorporated into a circuit designed so that the small changes in currents caused by the transduction mechanisms would be converted into, for example, a potential difference or a shift in oscillatory frequency. Potential circuit applications are discussed in Chapter 7. A constant (reverse) voltage was applied to the base-collector junction and a constant current to the emitter. The base current was measured using a Keithley 2000 6.5 Digit Multimeter (resolution 10 nA at 10 mA scale) reading the current over a period of ten power line cycles (PLC) and averaging a further ten of these readings for measuring the response to applied magnetic field and reading over one PLC without any averaging for noise measurements. Reading errors in the multimeter were observed to be insignificant when compared to the random error, which was created by the noise in the system. The magnetic induction,  $B$ , was varied by varying the current supplied to the electromagnet

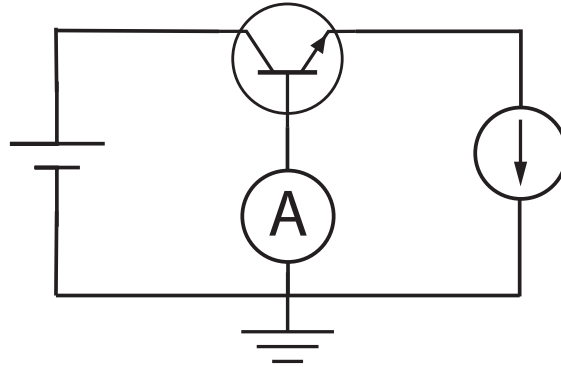


**Figure 6.2:** The common–base configuration as used to bias the HBT under test and to measure the base current.

coils by an 8A constant current source<sup>1</sup>. The output was controlled by an HP 59501B Power Supply Programmer. The direction of the field was varied by rotating the electromagnet on its vertical axis. The electromagnet assembly incorporated a mechanism for doing this and angle gradations were marked on the base at the appropriate points. The gradations allowed for the accurate reading of angle to approximately  $\pm 0.1^\circ$  of rotation.

Applying the appropriate bias conditions, sweeping the magnetic field, the timing of the measurements and the formatting and storage of the data were all carried out within the *National Instruments* LabVIEW environment. This allows for straightforward interfacing with each of the control and measurement systems. The experimental routines were designed to be completely automated. A simplified process flow for the main LabVIEW program which was written to carry out the measurements is shown in Figure 6.3.

The appropriate figures for analysing the devices under test are the relative change in  $I_b$ , i.e.  $(I_b(\mathbf{B}) - I_{b0}) / I_{b0}$  where  $I_{b0} \equiv I_b(0)$  and the relative change in DC current gain, i.e.  $\beta / \beta_0$  where  $\beta \equiv \beta_{dc}(\mathbf{B})$  and  $\beta_0 \equiv \beta_{dc}(0)$ . As the electromagnet was constructed from a core of ferromagnetic material with a non–zero remanence the magnetic field intensity at zero supply current was also non–zero. This necessitated that  $I_{b0}$  was measured with the device outwith the influence of the electromagnet. Furthermore,  $I_b$  was observed to decrease in magnitude for the first  $\sim 120$  seconds after bias had been applied before reaching a stable value. Hence a wait of 180 seconds was incorporated into the LabVIEW

<sup>1</sup>Strictly this is in vector form,  $\mathbf{B}$ , but the direction of the field from the magnet was assumed to be known and constant. This was a valid assumption as the two poles were flat and parallel and they were also large (approximately two orders of magnitude larger) both in comparison to their separation and to the size of the device, situated close to the central axis.

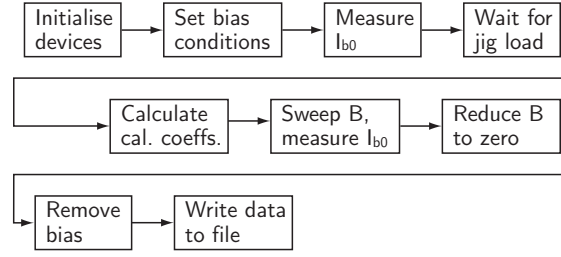


**Figure 6.3:** A simplified process flow for the main LabVIEW program that controlled the HBT bias and the sweep of the magnetic field intensity.

code which biased the devices. The common-base equivalent current gain was calculated by combining (2.21) and (2.27) to give

$$\beta_{dc} = \frac{I_c}{I_b} = \frac{I_e - I_b}{I_b} \quad (6.1)$$

where  $I_e = I_{en} + I_{ep}$  is the current applied to the emitter by the HP 3245A.

In order to measure the temperature dependence of magnetic field applied parallel to current flow on the DC current gain of an HBT the device was placed in a custom-made cryostat. This was attached to an arm that allowed it to be swung into a position where the device was centrally located between the the two poles of the electromagnet. Since the cryostat was designed to measure temperature dependent Hall voltages (with a field applied parallel to the normal) there was no ability to vary the angle using the bearing which allowed rotation of the electromagnet.

The cryostat was cooled using a *CTI-Cryogenics* 8200 Compressor, a self-contained helium cooling system, and the temperature stabilised using a resistive heater in the cryostat which was controlled by an *Oxford* Intelligent Temperature Controller 502. Specially written LabVIEW code allowed the temperature to be stabilised at points between 10 K and 300 K.

## 6.2 Calibrating the Applied Magnetic Field Intensity

The interface to the HP 59501B allowed for an integer number of (arbitrary) current units between zero and 999 to be specified to control the output of the supply to the electromagnet. Assuming a linear relationship between programmer output and supply output this corresponds to 8 mA for each current unit. The relationship between current control units and the supply current (as given by the digital indicator on the front panel of the supply) is shown in Figure 6.4. It takes a linear form.

It was then necessary to calibrate the current control units with the magnetic field

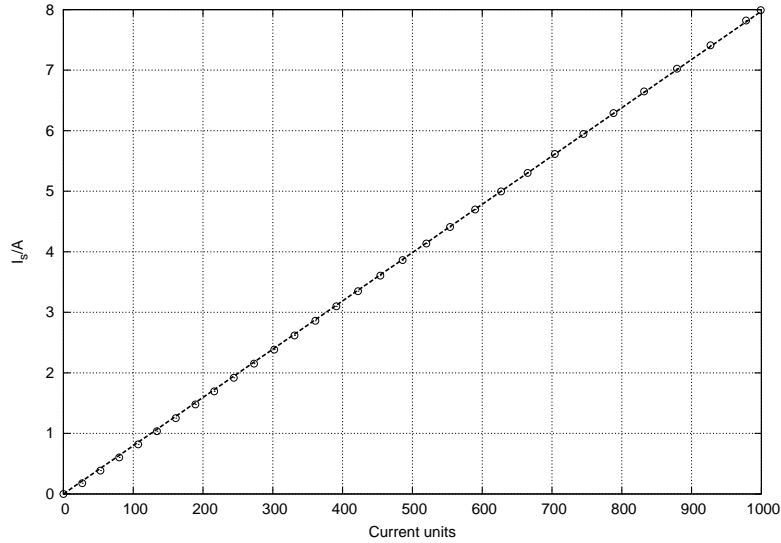


**Figure 6.4:** Electromagnet supply current,  $I_s$ , vs. the number of current control units specified to the HP 59501B Power Supply Programmer. A linear relationship can be observed in the fit where the gradient is 0.00797 A.

intensity between the poles of the electromagnet. A Bell Instruments 620 Gaussmeter was positioned in the centre of the poles and its exact placement adjusted until the maximum reading was obtained. Multiple readings were taken at known values of the current control units and the field intensity measured. This was carried out for both the forward and backward current sweep directions, in order to obtain the hysteresis loop of the electromagnet. The values were then incorporated into a LabVIEW program where a built-in function calculated the coefficients of an  $n^{\text{th}}$  order polynomial regression fit. The program was designed to analyse the proximity to the measured data of the field intensity predicted by the fitted curve and also to plot the first derivative of the fitted curve to ensure a constant gradient. This was required because higher order polynomial fits are susceptible to oscillations between fitted points. An  $11^{\text{th}}$  order polynomial was chosen as it had a maximum error at any fitted point of 0.6% and no extraneous oscillations. The calibration data was supplied to the main LabVIEW bias and sweep program in a text file and the coefficients of the polynomial calculated before the sweep. The requisite number of current control units was then calculated for any given value of  $B$  provided the direction of the sweep was known. (It should be noted that the reverse calibration was only valid if a forward sweep to maximum field was completed immediately beforehand.) Figure 6.5 shows the calibration curves fitted to the data points and Figure 6.6 shows the gradient of the fitted curve as an oscillation test.

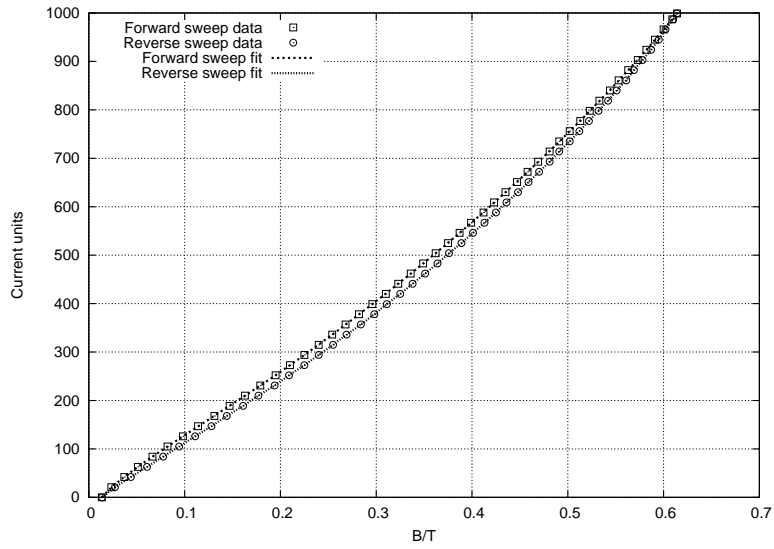


**Figure 6.5:** The calibration data and 11<sup>th</sup> order polynomial regression fit for forward and reverse sweeps of the electromagnet.

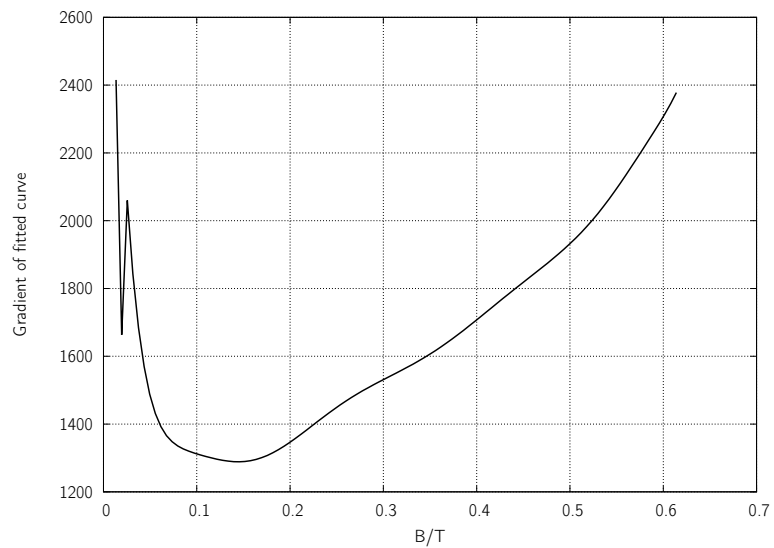


**Figure 6.6:** The first derivative of the polynomial regression fit for the forward sweep of the electromagnet. No oscillations are observed between the data points.

Current units	Sweep number, B/T				Change/%		
	First	Second	Third	Fourth	1 – 2	2 – 3	3 – 4
0	0.01309	0.01302	0.01303	0.01302	0.488	0.020	0.079
111	0.08862	0.08905	0.08911	0.08909	0.487	0.061	0.024
222	0.16771	0.16802	0.16802	0.16800	0.185	0.004	0.014
333	0.24563	0.24583	0.24584	0.24580	0.083	0.004	0.017
444	0.33390	0.33411	0.33414	0.33409	0.062	0.010	0.017
555	0.40321	0.40339	0.40339	0.40334	0.043	0.001	0.012
666	0.46745	0.46759	0.46754	0.46753	0.029	0.010	0.002
777	0.52690	0.52703	0.52696	0.52694	0.024	0.012	0.004
888	0.58147	0.58158	0.58151	0.58150	0.018	0.011	0.002
999	0.63083	0.63090	0.63083	0.63082	0.012	0.011	0.003
				Max	0.488	0.061	0.079

**Table 6.1:** The relative change (in percent) of the magnetic field intensity of the electromagnet between the first consecutive sweeps after several days without use.

It was also considered that the magnetic field intensity may not be constant, depending on the usage history of the electromagnet. To test this assumption, the gaussmeter was used to measure the electromagnet field in consecutive sweeps after several days without use. The results are shown in Table 6.1. These data show that the field changes by a maximum of  $\sim 0.5\%$  between the first and second sweep but this change reduced by an order of magnitude between the second and third sweeps to  $\sim 0.06\%$ . Thus the field could be considered stable by the second sweep and it was considered sufficient to do a single ‘reset’ sweep before carrying out any experiments on a given day.

Finally the angle between the plane of the base of the LCC and the central axis had to be determined once the jig had been inserted into the test position. It was assumed that the plane of the device wafer surface would always be parallel to the plane of the LCC base. To ensure that this was a reasonable assumption care was taken when fixing a sample to the LCC that the adhesive was of low viscosity and applied in as thin a layer as possible. Either liquid (not gel) ‘super glue’ or silver DAG was used for this purpose. Using a previously fabricated Hall bar (published in earlier work at the University of Glasgow [45]) in an identical LCC in the socket with the jig in the test position, it was possible to rotate the electromagnet on its bearing around the nominal zero position. The Hall voltage was measured at each point and plotted against the angle. A curve of the form  $a \cos(b\theta + c) + d$  was fitted to the points since the component of B parallel to the plane of the wafer was  $B \cos\theta$ . The data and the fitted curve are shown in Figure 6.7. Thus when the jig was in the test position the angle of zero rotation of the LCC with

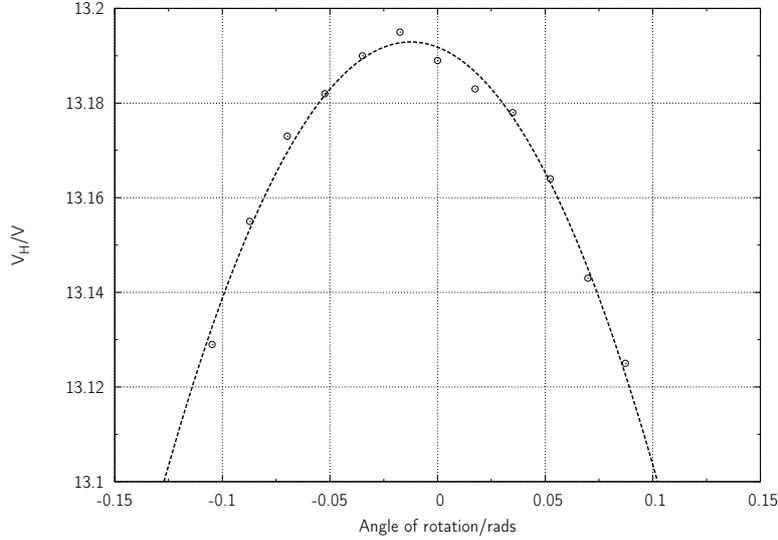


**Figure 6.7:** The calibration data and cosine regression fit for the angle of the LCC with respect to the electromagnet rotation.

respect to the the gradations on the electromagnet base was determined to be  $359.3^\circ$ .

## 6.3 Experimental Results

### 6.3.1 Measurement of Mobility

As discussed in Chapter 2 it is possible to measure an electron minority carrier mobility  $\mu'_e$  in the base from a field applied in the plane of the wafer. This mobility is obtained from

$$\frac{I_b(B) - I_{b0}}{I_{b0}} = \frac{\Delta I_b}{I_{b0}} = \mu_e'^2 B^2 \quad (6.2)$$

i.e. the gradient of the plot of  $\Delta I_b/I_{b0}$  against  $B^2$  is the square of the mobility. This plot is shown for a large area (LA-) HBT (as described in Chapter 3) in Figure 6.10.

The magnetic field intensity was varied from 0.0135 T (the zero supply current magnetic field intensity) to 0.615 T (maximum field) with the device positioned between the poles of the electromagnet and biased with  $V_{cb} = 1.5$  V and  $I_e = 1$  mA. The change in base current was recorded. The dependent variable is zero at zero field so a line of the form  $y = mx$  could be fitted to the data. In practice, however, the noise induced variation in  $I_b$  can lead to a non-zero  $y$ -axis intercept. In order that this should not introduce an error to the calculated value for  $\mu'_e$  a line of the form  $y = mx + c$  was fitted instead. The plot shows a gradient of 0.051 which corresponds to a mobility of  $2260 \text{ cm}^2 \text{ V}^{-1} \text{ s}^{-1}$ . This is lower than reported values using the same technique[70] and using the zero-

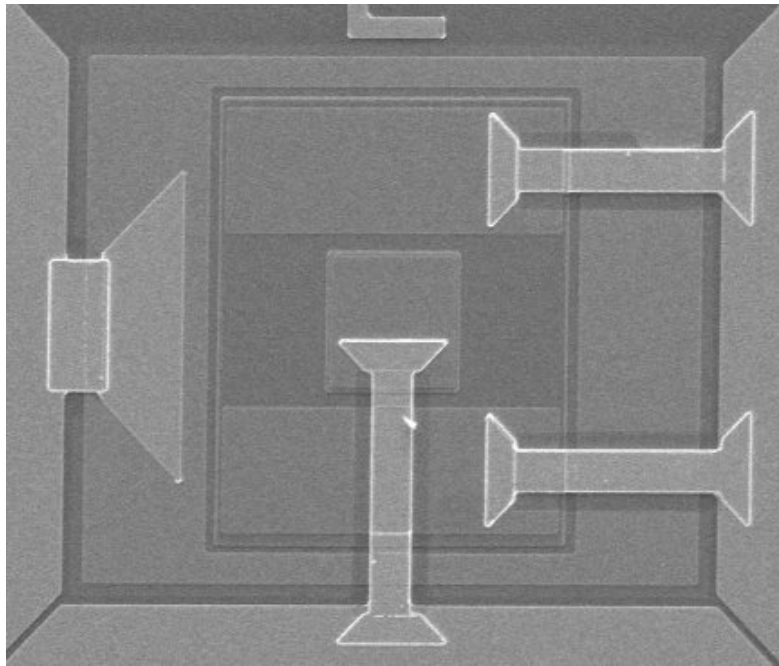


**Figure 6.8:** The emitter of an LA-HBT was a  $75\ \mu\text{m} \times 75\ \mu\text{m}$  square.

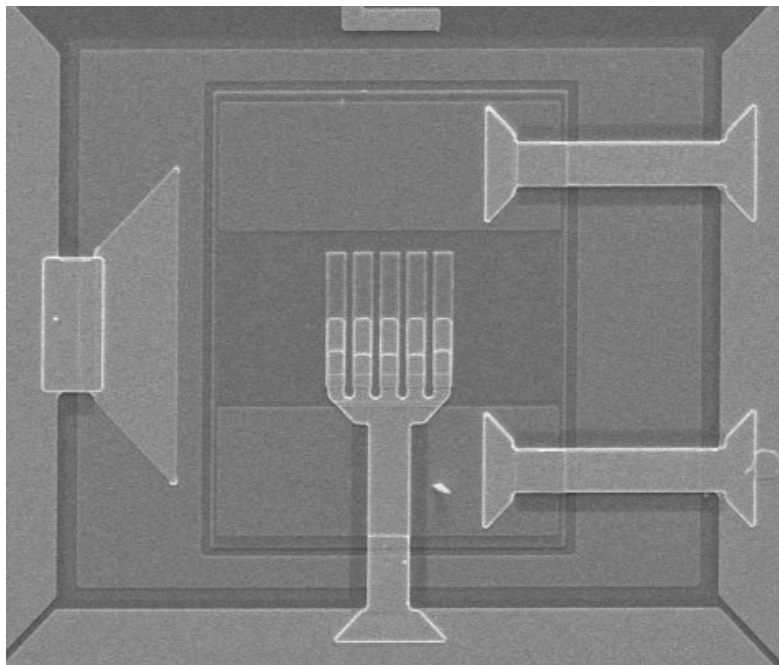


**Figure 6.9:** The emitter of an MEF-HBT consisted of five  $12\ \mu\text{m} \times 75\ \mu\text{m}$  'fingers'.

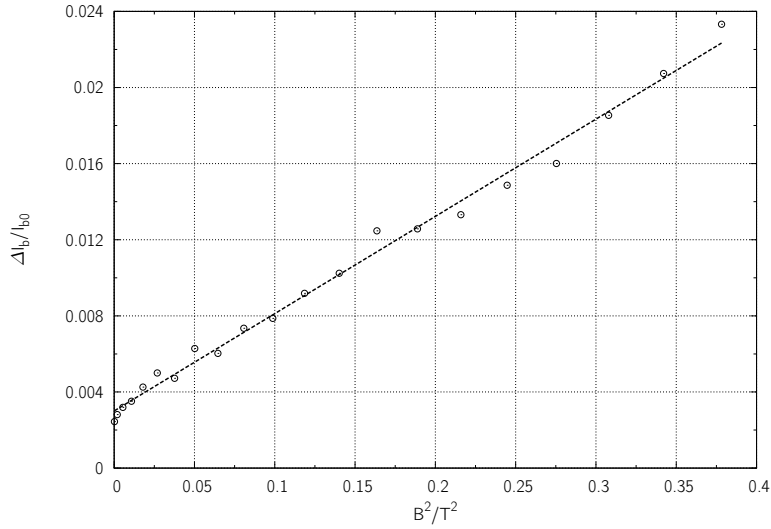


**Figure 6.10:** The change in relative base current  $\Delta I_b/I_{b0}$  against  $B^2$  for an LA-HBT is linear at high fields. The gradient of the line of best fit is the square of the magnetotransport mobility.

field time of flight technique[72] which reported values of  $2900 \text{ cm}^2 \text{ V}^{-1} \text{ s}^{-1}$  for p-InGaAs doped to  $9 \times 10^{18} \text{ cm}^{-3}$ . (Base layer doping for the HBTs was  $1 \times 10^{19} \text{ cm}^{-3}$ ). A multiple emitter finger (MEF-) HBT biased under the same conditions also gave a mobility of  $2260 \text{ cm}^2 \text{ V}^{-1} \text{ s}^{-1}$ . The effect of varying  $I_e$  on the values of  $\mu'_e$  obtained in such a device is shown in Figure 6.11. The emitter configuraion of an LA-HBT is shown in Figure 6.8. An MEF-HBT is shown in Figure 6.9.

Values of  $\mu'_e$  of 2260, 1970 and  $1840 \text{ cm}^2 \text{ V}^{-1} \text{ s}^{-1}$  were found for emitter currents of 1, 5 and 10 mA, respectively. This suggests a decreasing mobility with increasing emitter current. This could be explained with reference to (2.61) which can be written as

$$\sigma_b \simeq qn\mu'_e \quad (6.3)$$

where  $\sigma_b$  is the base conductivity. This conductivity will be strongly dependent on the effective length of base and the dopant concentration in the base. By increasing the emitter current (which involves increasing the junction forward bias) the value of  $n$  in (6.3) increases. The depletion width of the E-B junction also decreases due to the change in bias conditions. Thus the base conductivity may be decreased requiring an effective decrease in mobility. This result also contradicts earlier work [70] where the mobility is claimed to be independent of emitter current. The low values of  $\mu'_e$  in these devices are indicative of the poor quality of the epitaxial layers highlighted through other

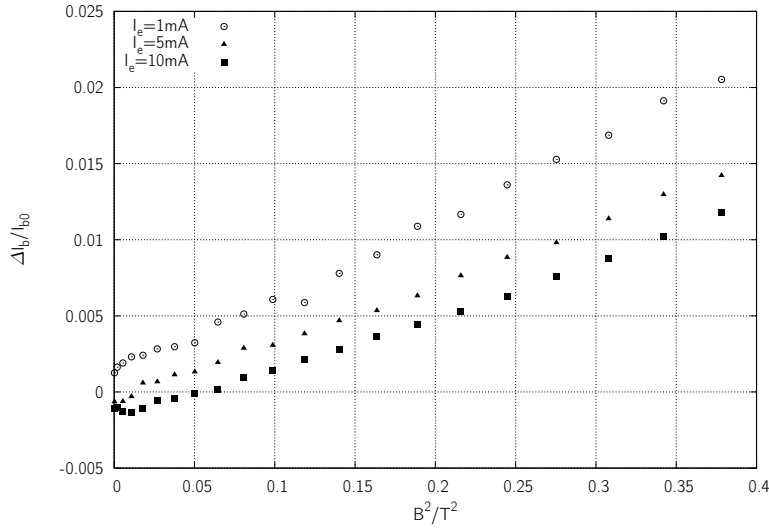


**Figure 6.11:** The variation of magnetotransport mobility with  $I_e$  in an MEF-HBT.

characterisations (Chapter 3 and Chapter 4), most notably the low values of  $\beta_{dc}$  and  $\alpha_{dc}$  and the high values of the junction diode ideality factors.

### 6.3.2 An LA-HBT in Magnetic Field

The response of a large area HBT to parallel and perpendicular magnetic fields are shown in Figures 6.12 and 6.13.

The device was biased with  $V_{cb} = 1.5\text{ V}$  and  $I_e = 1\text{ mA}$ . The normalised current gain ( $\beta/\beta_0$ ) has been plotted against magnetic field intensity. A noise figure for the device has also been obtained by biasing the device in exactly the same manner as during the magnetic field measurements but outwith the influence of the electromagnet, which was also turned off. Multiple values of  $I_b$  were then measured over time, with regular intervals of 100 ms and the bias maintained between readings. This plot is shown in Figure 6.14 and the calculated r.m.s. noise<sup>2</sup> of  $0.102\ \mu\text{A}$  has been applied to the normalised current gain in Figures 6.12 and 6.13. The noise figure could not be solely attributed to the intrinsic noise of the HBT, there is a contribution from the measurement apparatus, from, for example, the impedance of the access cabling and variations in the output of the current and voltage supplies. Variations in the magnetic field during the experiment would not be accounted for using this method. A measurable response can be seen in Figure 6.13 but any change in  $\beta$  in Figure 6.12 is completely obscured by the noise.

<sup>2</sup>This is the standard deviation of the  $I_b$  noise data around about the arithmetic mean for that data.

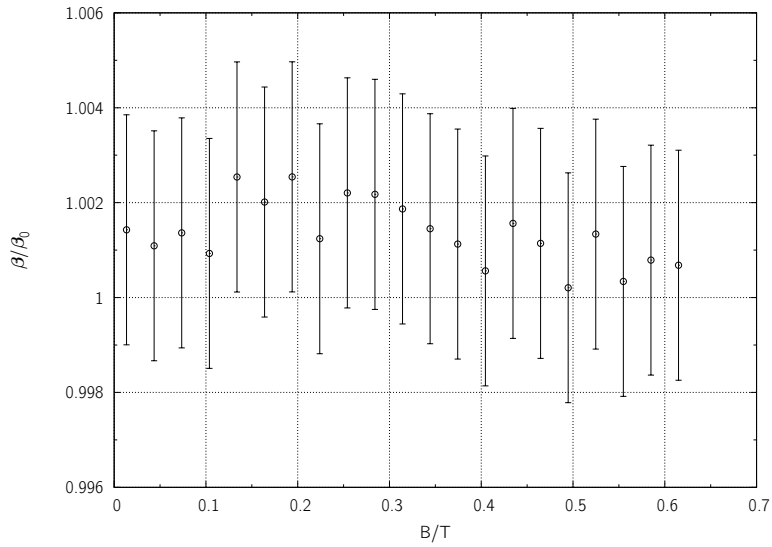


**Figure 6.12:** Normalised common-base current gain for an LA-HBT with the magnetic field applied parallel to the normal of the semiconductor wafer.

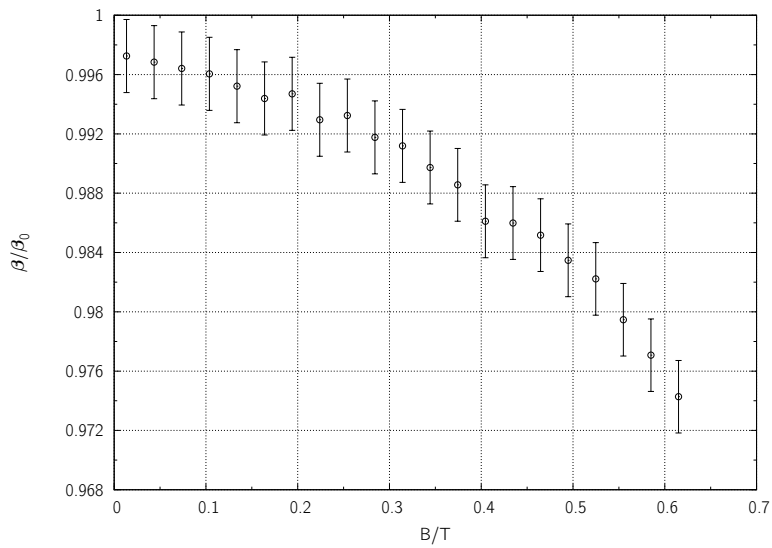


**Figure 6.13:** Normalised common-base current gain for an MEF-HBT with the magnetic field applied perpendicular to the normal of the semiconductor wafer.

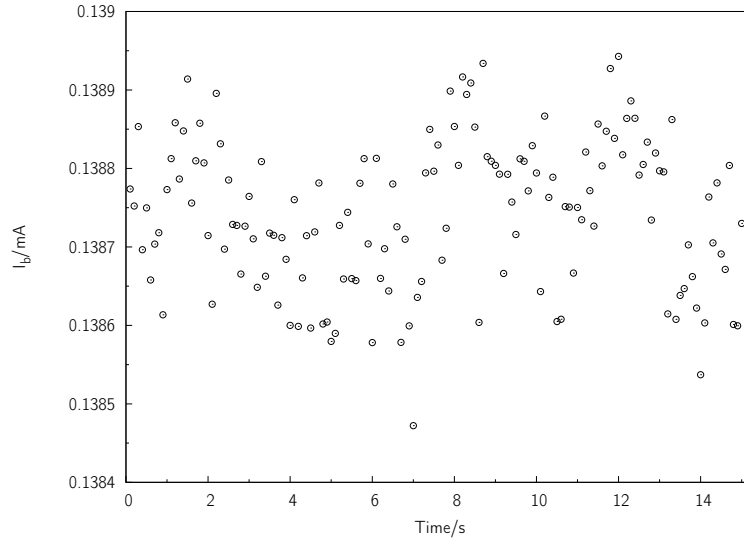


**Figure 6.14:** Base current against time measurement to determine the r.m.s. noise amplitude of an LA-HBT where multiple readings of  $I_b$  were taken at intervals of 100 ms and then the standard deviation of the data from the arithmetic mean calculated.

The change in response of the device as the angle of the applied magnetic field to the normal of the wafer ( $\theta$ ) was varied is shown in Figure 6.15. A variation of change in current gain can be seen as the angle changes. The magnetic field intensity in the plane of the wafer (i.e. the perpendicular direction) is  $B \sin \theta$ . Since in this configuration there is no observed effect on current gain at  $\theta = 0$  it is likely that the change in magnitude of the response varies with  $B \sin \theta$ . In this case it was expedient to assume that the value of  $I_b(B)$  at the minimum field of the magnet (0.0135 T) was equivalent to the zero-field value,  $I_{b0}$ . While this was not necessarily the case it lent itself to a more meaningful comparison between different plots. As there was no method of measuring the zero field value *in situ* the random noise in the data was such that despite the best efforts to compensate there was always a significant discontinuity between  $B = 0$  T and  $B = 0.0135$  T. These data are described as *re-normalised* hereafter.

Figure 6.16 shows the re-normalised current gain plotted against  $\theta$  and also a plot of the function  $a \sin \theta$  for  $B = 0.615$  T for each angle, with the constant  $a$  determined by regression fit. The quality of the fit gives an indication of the interaction between the processes governing the response to parallel and orthogonal field directions. A better fit is given by removing the requirement that the period of the fitted curve be  $360^\circ$ . This is correct because the measured effect on the scalar base current would have been similar for

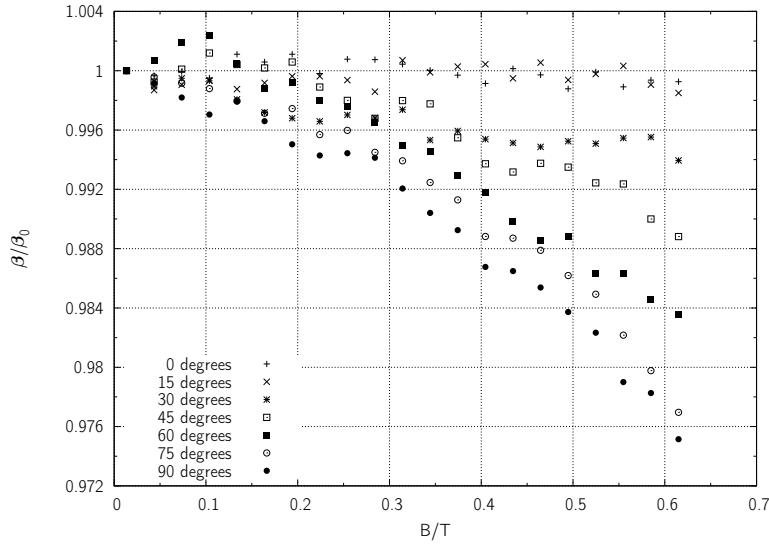


**Figure 6.15:** Re-normalised plots of current gain against applied magnetic field for field directions between zero and  $90^\circ$  for an LA-HBT.

$-\theta$  as for  $+\theta$  and so the period (ignoring interaction between the two different physical processes at  $\theta = 0$  and  $\theta = 90^\circ$ ) is likely to be  $180^\circ$ . The second plot is a regression fit of the form  $b \cos(c\theta + d) + e$  which can be observed to fit the data more accurately with  $c \sim 2$ .

### 6.3.3 An MEF-HBT in Magnetic Field

The response of a large area HBT to parallel and perpendicular magnetic fields are shown in Figures 6.17 and 6.18.

The device was biased with  $V_{cb} = 1.5$  V and  $I_e = 1$  mA. The normalised current gain ( $\beta/\beta_0$ ) has been plotted against magnetic field intensity. A noise figure for the device has also been obtained by biasing the device outwith any magnetic fields and measuring multiple values of  $I_b$  over time. The calculated r.m.s. noise of  $0.076 \mu\text{A}$  has been applied to the normalised current gain in Figures 6.17 and 6.18. A measureable response can be seen in Figure 6.18 but any change in  $\beta$  in Figure 6.17 is completely obscured by the noise.

The change in response of the device as the angle of the applied magnetic field to the normal of the wafer ( $\theta$ ) was varied is shown in Figure 6.19. A similar response to that of an LA-HBT can be observed.

Figure 6.20 shows the normalised current gain plotted against  $\theta$  and also a plot of the function  $a \sin \theta$  for  $B = 0.615$  T for each angle. Similarly to the LA-HBT there is a

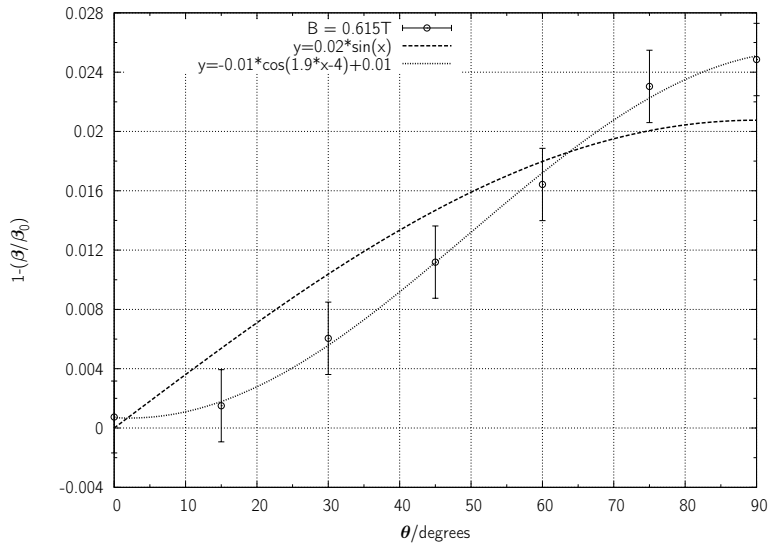


**Figure 6.16:** Response of an LA-HBT to an applied magnetic field of 0.615 T for field directions between zero and 90°.

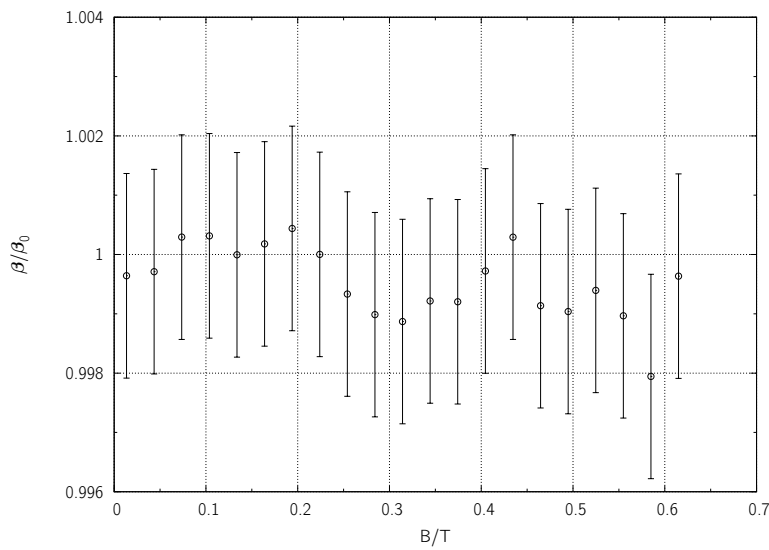


**Figure 6.17:** Normalised common-base current gain for an MEF-HBT with the magnetic field applied parallel to the normal of the semiconductor wafer.

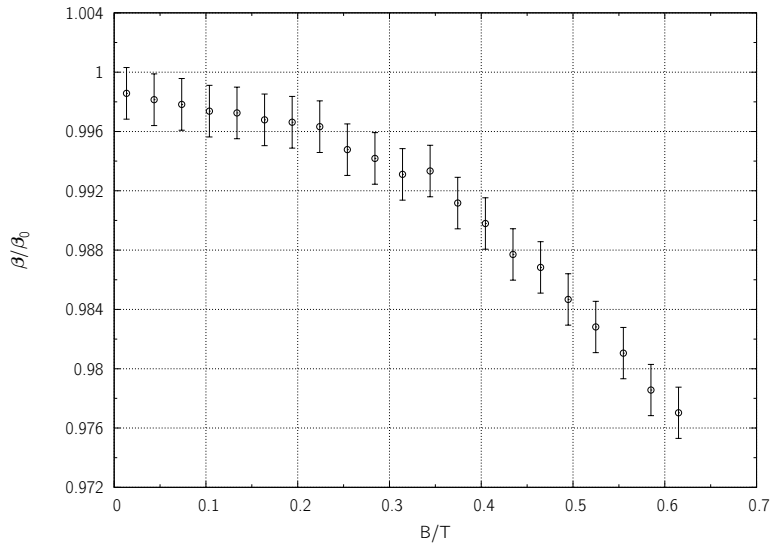


**Figure 6.18:** Normalised common-base current gain for an MEF-HBT with the magnetic field applied perpendicular to the normal of the semiconductor wafer.

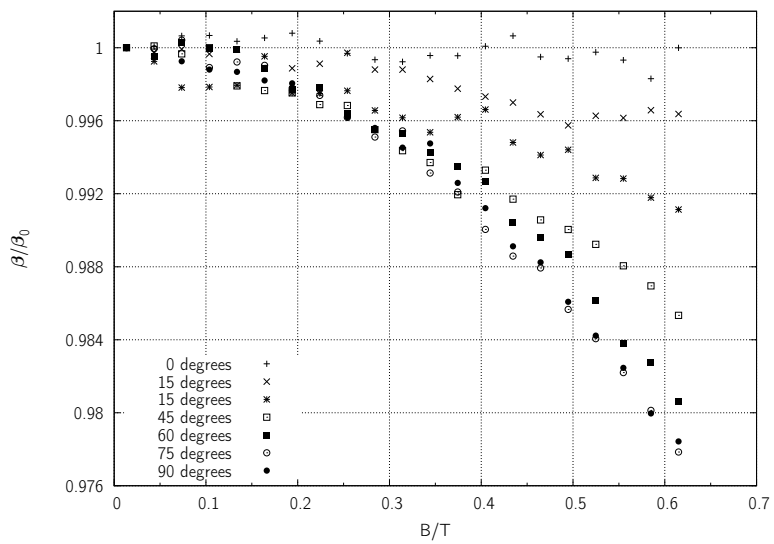


**Figure 6.19:** Re-normalised plots of current gain against applied magnetic field for field directions between zero and  $90^\circ$  for an MEF-HBT.

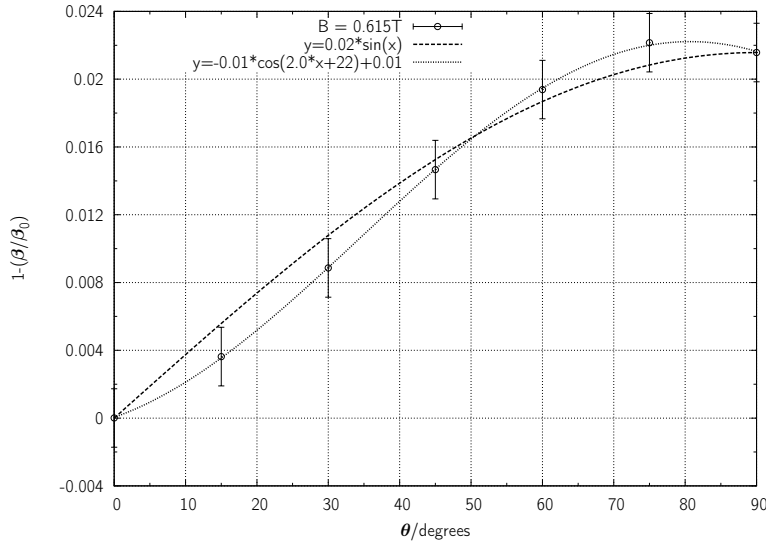


**Figure 6.20:** Response of an MEF-HBT to an applied magnetic field of 0.615 T for field directions between zero and  $90^\circ$ .

minimum close to  $\theta = 0$  and a maximum at  $\theta = 90^\circ$ . A curve of the form  $\cos 2\theta$  is the most appropriate.

The noise figure was observed to decrease between LA- and MEF-HBTs with typical values given above of 0.102 and  $0.076 \mu\text{A}$ , respectively. This suggested that the emitter-base heterojunction noise dominated over the surface recombination noise since the junction noise could be expected to vary with junction area (smaller in an MEF-HBT) and surface recombination noise with perimeter to area ratio (larger in an MEF-HBT). The device-to-device variation is shown in Figure 6.21. The response of both devices is the same, within the bounds of the error defined by the device noise.

### 6.3.4 Effect of Bias Conditions

The value of  $V_{cb}$ , the reverse bias on the base-collector junction, affects the width of the depletion region at the junctions according to (2.11). It has been seen in earlier reported results[64] that the base width has a rôle to play in the magnetic response of the device. The depletion width is a contributing factor to the base width over which an electron must travel before being swept into the collector by the field in the space-charge region. The effect of magnetic field on current gain was measured at  $V_{cb}$  values of 0.25, 1.0, 1.5, 2.0 and 2.5 V with a constant emitter current of 1 mA.

The data in Figure 6.22 shows that the signal was more susceptible to noise at higher bias voltages. There will be a higher probability of an electron undergoing punchthrough

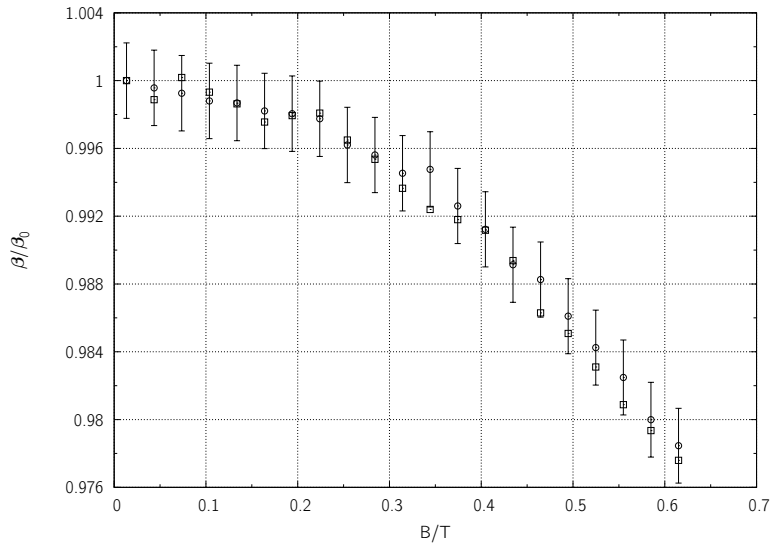


**Figure 6.21:** Response of two different MEF-HBTs to an applied magnetic field of direction  $90^\circ$ .

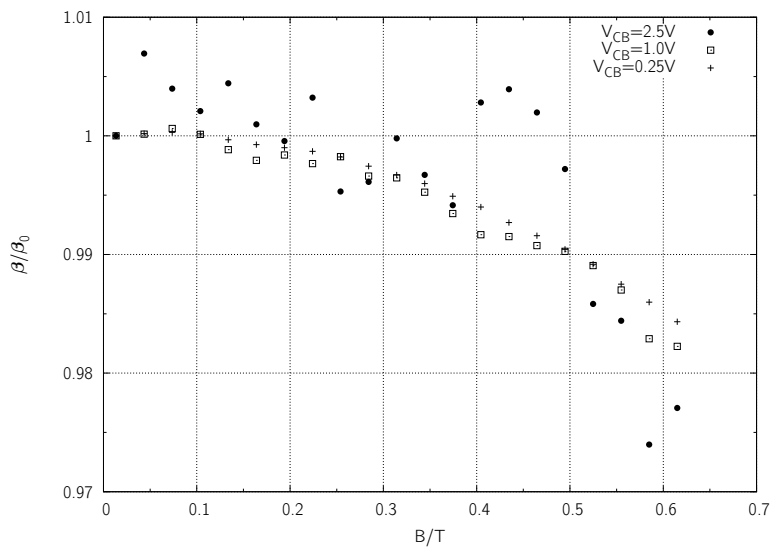


**Figure 6.22:** The normalised current gain against  $V_{cb}$  for an MEF-HBT, measured at  $\theta = 90^\circ$ .

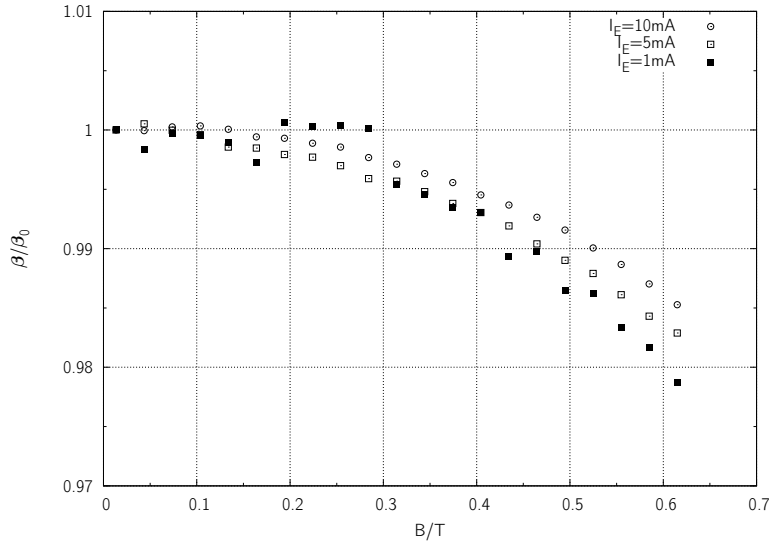


**Figure 6.23:** The normalised current gain against  $I_e$  for an MEF-HBT, measured at  $\theta = 90^\circ$  and  $V_{cb} = 1.5$  V.

breakdown and traversing the base ballistically as the barrier size has been reduced. This will create shot noise in the signal. Although decreasing the bias was not observed to significantly increase the sensitivity by increasing the effective base width, it has increased the signal to noise ratio of the device by decreasing the noise. The base of the HBT is already thin, and the high dopant concentrations meant would restrict the variations in base thickness.

The effect of changing  $I_e$  on device response to perpendicular magnetic field was also measured. The results of applying  $I_e$  values of 1, 5 and 10 mA with a constant  $V_{cb}$  of 1.5 V with a perpendicular magnetic field are shown in Figure 6.23.

Inspection of the plotted data reveals that the device is considerably less noisy with increasing  $I_e$ . This indicates that the noise sources are saturated and have a lesser effect on the overall current transport as the input current is increased. There is also an increase in shot noise at low values of  $I_e$ , where the measured value of  $I_b$  is seen to jump between consecutive readings.

The effect of changing  $I_e$  on device response to parallel magnetic field was also measured. The results of applying  $I_e$  values of 1, 5 and 10 mA with a constant  $V_{cb}$  of 1.5 V with a parallel magnetic field are shown in Figure 6.24. For comparison a control plot of current gain against  $B$  for a device measured outside the influence of the electromagnet but under all the same conditions otherwise is shown.

Similar results obtained in earlier work[64, 77] have shown the type of trend visible

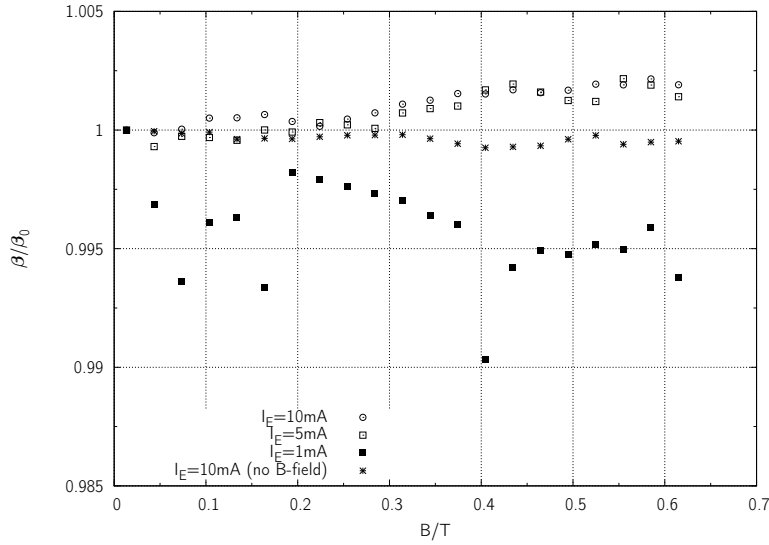


**Figure 6.24:** The normalised current gain against the magnetic field for different values of  $I_e$  for an MEF-HBT, measured at  $\theta = 0$  and  $V_{cb} = 1.5$  V.

in the  $I_e = 10$  mA and  $I_e = 5$  mA plots. The pattern of reduced recombination with increasing field reported in those works is observed. A slight device fade over the period of the measurement can also be seen in the control plot and this will have detracted from the measured response of the device to magnetic field. It is evident from the plots that the effect on  $I_b$  of reducing the surface recombination is small compared to the magnitude of the noise processes for  $I_e = 1$  mA but is detectable for the higher  $I_e$  values.

The DC r.m.s. noise is shown for each of the bias points described above in Table 6.2. The data show that the device noise levels were strongly affected by the base-collector junction bias over the whole range: an order of magnitude increase in the noise came with an order of magnitude increase in  $V_{cb}$ . The percentage noise value decreases by a factor of five with a similar increase in  $I_e$  although any further gains with increasing emitter current are minimal.

### An HBT Sensor under Optimal Bias

The response of an MEF-HBT biased under optimal conditions of applied magnetic field is shown in Figure 6.25. Compared to the response of the device bias with a larger  $V_{cb}$  and a smaller  $I_e$  (shown in Figure 6.19) it is observed to be less noisy. The low angle data are more clearly defined at the response to field applied at  $90^\circ$  is larger than that at  $75^\circ$ . The error bars on the  $90^\circ$  plot are calculated from the D.C. r.m.s. noise for the device which is  $0.15 \mu\text{A}$ .

$V_{cb}/V$	$I_e/mA$	$I_b \text{ Noise}/mA$	$I_b \text{ Noise}/\%$
0.25	1	$3.04 \times 10^{-5}$	0.02
1.0	1	$1.11 \times 10^{-4}$	0.08
1.5	1	$1.77 \times 10^{-4}$	0.15
2.0	1	$3.06 \times 10^{-4}$	0.30
2.5	1	$2.96 \times 10^{-4}$	0.36
1.5	5	$2.50 \times 10^{-4}$	0.03
1.5	10	$2.50 \times 10^{-4}$	0.02

**Table 6.2:** The DC r.m.s. noise amplitude for each different bias point at which the magnetic field response was measured.

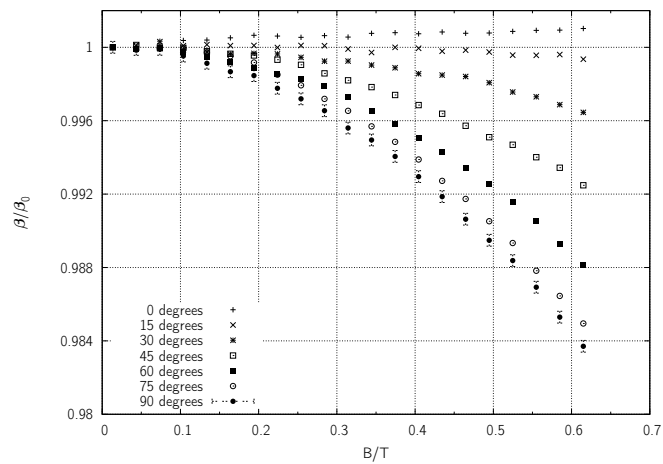


**Figure 6.25:** Re-normalised plots of current gain against applied magnetic field for field directions between 0 and 90° for an MEF-HBT under optimal bias conditions of  $I_e = 10 \text{ mA}$  and  $V_{cb} = 1 \text{ V}$ .

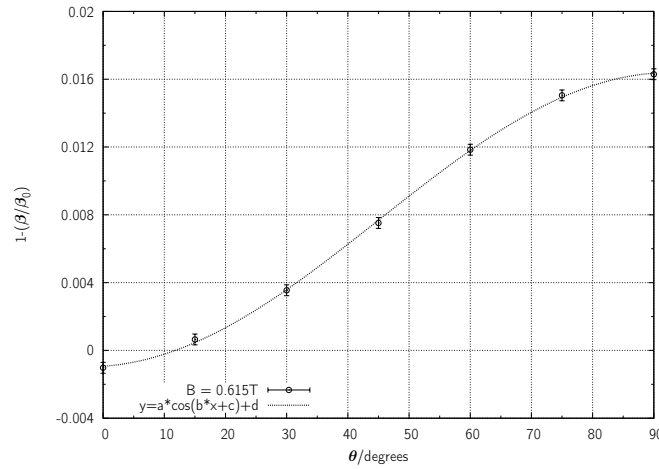


**Figure 6.26:** Response of an MEF–HBT under optimum bias to an applied magnetic field of 0.615 T for field directions between zero and 90°.

Figure 6.26 shows the re-normalised current gain plotted against  $\theta$  and also a plot of the function  $a \cos(b\theta + c) + d$  for  $B = 0.615$  T. For this plot  $b = 1.88$ , suggesting a period of around 180°, as expected, and the x-axis translation  $c = -0.01^\circ$  suggests a minimum response very close to  $\theta = 0$ .

### 6.3.5 Low Temperature Parallel Field Dependence

The bonded device in the cryostat was cooled from room temperature. Since no study of the performance of the metal–semiconductor contacts at low temperatures had been made it was unclear whether the device would still function at arbitrarily low temperatures. In addition to this, different thermal expansion rates of the materials constituting the cryostat LCC mount, connections, etc., would not guarantee consistent operation over the full range of temperatures. Thus the base current was monitored as the device was cooled and an appropriate low temperature starting point was chosen. The values of  $I_b$  as the temperature changed are shown in Figure 6.27. Device (or contact) failure occurred in the region of 140 K so the measurements were started at 160 K. The increase in  $I_b$  at lower temperatures could be attributed to a degradation of the quality of the base contacts at lower temperatures resulting in a large increase in  $I_{b,cont}$ . The noise data are also plotted in Figure 6.27. A decrease in the noise can be observed from 300 K to 220 K. This could be attributed to a decrease in recombination–generation as there is less lattice scattering at lower temperatures. Thus the electrons spend, on average, less time in the base and are less likely to recombine. The increase in the noise at the lowest temperatures could be attributed to the increase in noise from the metal–semiconductor interface recombination

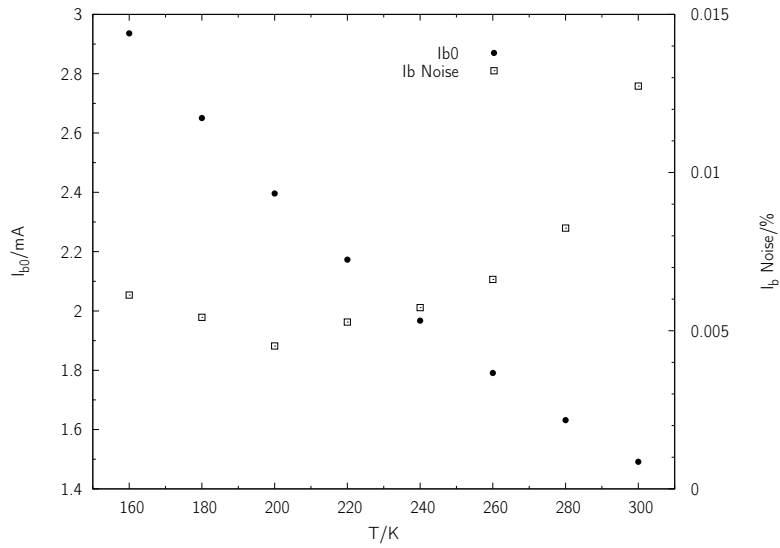


**Figure 6.27:** Measurements of  $I_b$  were taken as an MEF-HBT was cooled from room temperature.

events. However, it is also possible that the temperature dependent effects observed above are caused by changes in the experimental setup caused by the lowering temperatures.

The plot of the magnetic response to parallel field is shown for each temperature point in Figure 6.28.

The steps that were taken to make an appropriate experimental setup were described at the start of this chapter. A calibration curve was determined for the electromagnet in order that a specified magnetic field could be obtained by a known supply current. The first experiments to be carried out were to measure the minority carrier mobility in the p-InGaAs base of the HBTs. At  $2260 \text{ cm}^2 \text{ V}^{-1} \text{ s}^{-1}$  this was found to be lower than the values reported in the literature.

The response to magnetic field of two designs of HBT was measured, in terms of the change in current gain. The response to perpendicular applied field was measured, as was the response to parallel applied magnetic field, and then the angle dependence of the field response. A combined noise figure for the HBT and the experimental apparatus was determined and used to estimate the error on the sensor response. Since the magnitude of the transduction effect on the current was comparable the magnitude of the noise at arbitrary bias, a study into the effect of changing the bias conditions was carried out to determine the optimal values. These were found to be  $V_{cb} = 1 \text{ V}$  and  $I_e = 10 \text{ mA}$ .

Further measurements were carried out to determine the temperature dependence of

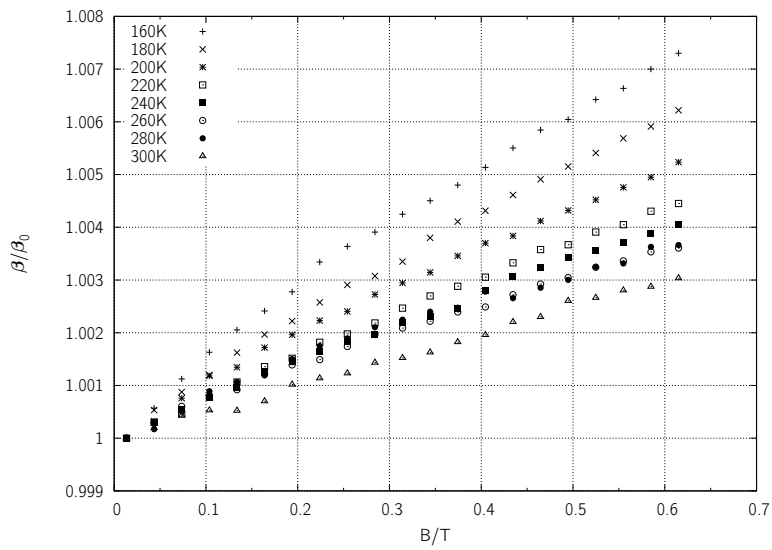


**Figure 6.28:** Normalised current gain against magnetic field intensity for an MEF-HBT at various temperatures.

the sensor's electrical characteristics and the magnetic field response. The magnitude of the base current increased monotonically with decreasing temperature and the measurement noise decreased as the temperature decreased to 200 K. The response of the HBT to magnetic field applied parallel to the normal increased as the temperature decreased to 160 K with a maximum change in normalised current gain of +0.007 compared to +0.003 at room temperature.

# 7 HBTs as Magnetic Field Sensors

This chapter describes how the details of research in the earlier discussion of the work have come together to create a working HBT magnetic field sensor with integrated 3-D magnetic structures. An analysis of the improvements in response to applied field with the structures incorporated is presented as well as the effect of two different surface treatments. A characterisation of the devices as sensors is also given.

## 7.1 HBT Sensitivity

The sensitivity of an HBT magnetic sensor is its transduction efficiency as described in (2.64) (absolute sensitivity) and (2.65) (relative sensitivity). These describe a device in the common-emitter configuration with  $I_c$  as the output current. To maintain consistency with earlier work this discussion will continue to use DC current gain,  $\beta_{dc}$ , as the transduction figure. This figure is directly proportional to  $I_c$  and inversely proportional to  $I_b$ . Thus the absolute magnetic field sensitivity is given by

$$S_A^B = \left| \frac{\partial \beta(B)}{\partial B} \right| \quad [\text{T}^{-1}] \quad (7.1)$$

Furthermore, the sensors were used to resolve the angle of the applied field for a given magnetic field strength. This gives rise to an absolute angle sensitivity for a known magnetic field where

$$S_A^\theta = \left| \frac{\partial \beta(B)}{\partial \theta} \right| \quad [\text{rad}^{-1}]. \quad (7.2)$$

The current gain magnetic field sensitivity for an MEF-HBT biased at the optimum conditions of  $I_e = 10 \text{ mA}$  and  $V_{cb} = 1 \text{ V}$  is given in Table 7.1. The response of the device to magnetic field can be seen in Figure 6.25. Since the device noise is demonstrably lower in r.m.s. amplitude for the MEF-HBT and the sensor response comparable in both device configurations, the MEF-HBT was used in the further studies presented in this chapter.

It can be observed from Table 7.1 that at higher fields the sensitivity increases steadily

$\theta/^\circ$	Sensitivity/ $T^{-1}$	
	at 0.044 T	0.615 T
0	0.003	0.017
15	0.013	0.049
30	0.012	0.083
45	0.025	0.188
60	0.020	0.221
75	0.025	0.296
90	0.022	0.313

**Table 7.1:** Current gain magnetic field sensitivity for an MEF-HBT.

$\theta/^\circ$	Sensitivity/ $\text{rad}^{-1}$	
	at 0.075 T	0.615 T
0	$5.2 \times 10^{-4}$	0.038
15	$8.7 \times 10^{-3}$	0.066
30	$1.5 \times 10^{-3}$	0.090
45	$8.6 \times 10^{-4}$	0.098
60	$1.3 \times 10^{-4}$	0.073
75	$1.2 \times 10^{-3}$	0.028
90	$1.2 \times 10^{-3}$	0.028

**Table 7.2:** Magnetic field angle sensitivity for an MEF-HBT.

as the angle increases. At low fields the sensitivity increases initially but levels out at around  $\theta = 45^\circ$ . This may be due to the interaction between the two opposite physical processes at work. Since the two effects are not independent, it is possible that the high angle sensitivity at low angles is related to the strength of the perpendicular field effect increasing rapidly from zero. The maximum quoted sensitivity of  $0.313 T^{-1}$  corresponds to an increase in  $I_b$  of  $2.0 \mu A$ .

The magnetic field angle sensitivity for an MEF-HBT biased at the optimum conditions of  $I_e = 10 \text{ mA}$  and  $V_{cb} = 1 \text{ V}$  is given in Table 7.2. The sensitivity to changes in angle at high field can be seen to increase up to a maximum at  $\theta = 45^\circ$  and then decrease at higher angles. These results are consistent with the curve that was fitted to the angle response data in Figure 6.20. The change in current gain is positive for increasing field at  $\theta = 0$  while it is negative for all other angles. At low fields this trend is not apparent which is due to the response being small compared to the noise.

The relative strengths of the parallel and perpendicular field effects can be also be

$\theta/^\circ$	$\Delta(\beta/\beta_0)$	
	at 0.044 T	0.615 T
0	$1.4 \times 10^{-5}$	$1.0 \times 10^{-3}$
90	$1.1 \times 10^{-4}$	$1.6 \times 10^{-2}$

**Table 7.3:** Total change affected in  $\beta/\beta_0$  for an MEF-HBT by a magnetic field applied parallel ( $\theta = 0$ ) and perpendicular ( $\theta = 90^\circ$ ) to the normal.

determined. Table 7.3 shows the change in  $\beta/\beta_0$  at high and low field. The perpendicular field effect is an order of magnitude larger than the parallel field effect. The parallel field effect may be less strong because, while it reduces the volume over which the charge carriers disperse, it also involves an increase in the effective path through the base for those electrons which scatter. The induced helical path is longer than the distance between the edges of the two space-charge regions. Thus these carriers have an increased chance of recombining in the bulk intrinsic base. Not only this, the effect is only experienced by carriers which have velocities with a perpendicular component, i.e. those that have scattered. The perpendicular field component is active on all carriers in the base, at all times.<sup>1</sup>

## 7.2 Surface Treated Sensors

It has been discussed in Chapter 2 and shown to hold true in these devices (Chapter 4) that the surface recombination velocity allows for the modification of the electrical properties by a magnetic field applied along the normal to the surface. In Chapter 4 several ways to modify the surface recombinative properties of the HBTs were discussed. To this end, the effects of two different surface treatments on the response of the devices were investigated. Figure 7.1 shows the responses of a device which has been treated with argon (as described in §4.5.3) to increase the surface recombination velocity before and after treatment. There was an increase in response to magnetic field throughout the applied field range with a maximum increase of  $\sim 0.0006$  at  $B = 0.615$  T.

Figure 7.2 shows the responses of a device which has been treated with ammonium sulphide (as described in §4.5.1) to decrease the surface recombination velocity before and after passivation. A decrease in sensitivity can be observed in the device, due to the reduction in the number of available surface recombination sites. A scattered electron was less likely to recombine instead of being collected so there was a smaller carrier

<sup>1</sup>Except for those whose velocity after a scattering event is exactly in line with the perpendicular magnetic field.

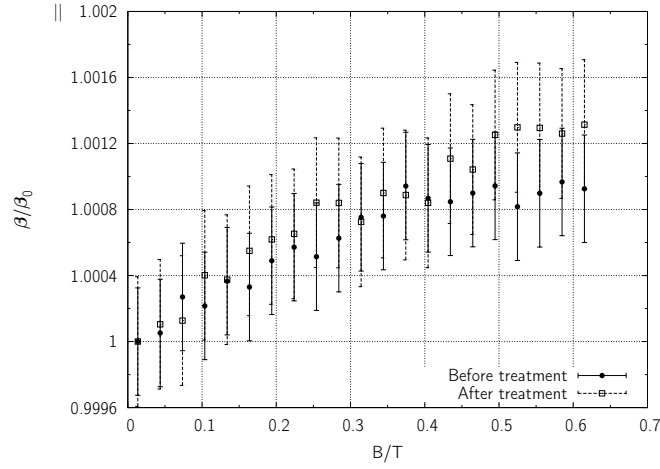


**Figure 7.1:** Response of an MEF-HBT to applied magnetic field parallel to the normal before and after argon surface treatment.

Treatment	Stage	$I_b$ Noise/mA	$I_b$ Noise/%
Argon	Before	$1.49 \times 10^{-4}$	0.011
Argon	After	$1.81 \times 10^{-4}$	0.013
Passivation	Before	$1.54 \times 10^{-4}$	0.011
Passivation	After	$1.19 \times 10^{-4}$	0.008

**Table 7.4:** D.C. r.m.s. noise for two MEF-HBTs, one before and after surface treatment with argon ions and another before and after passivation with ammonium sulphide.

population whose transport could be modified to produce the sensing effect. There is a decrease in response to magnetic field throughout the applied field range with a maximum decrease of  $\sim 0.0005$  at  $B = 0.615$  T

Since a portion of the intrinsic device noise must be due the recombination-generation noise at the surface the r.m.s. noise before and after each treatment was also measured. This is shown in Table 7.4. While the intrinsic device noise figure is similar for both devices before treatment there is an increase in the noise of the device treated with argon ions and a decrease in that which was treated with ammonium sulphide. The percentage changes in both were similar, a fact which corresponds to the similar changes in magnetic field response. It is unlikely, however, that extrinsic surface recombination accounts for all of the observed change, especially since there is still a measureable response to magnetic field in the device which has been passivated. Some recombination will occur in the extrinsic bulk base and this will also have an effect on response to applied field.

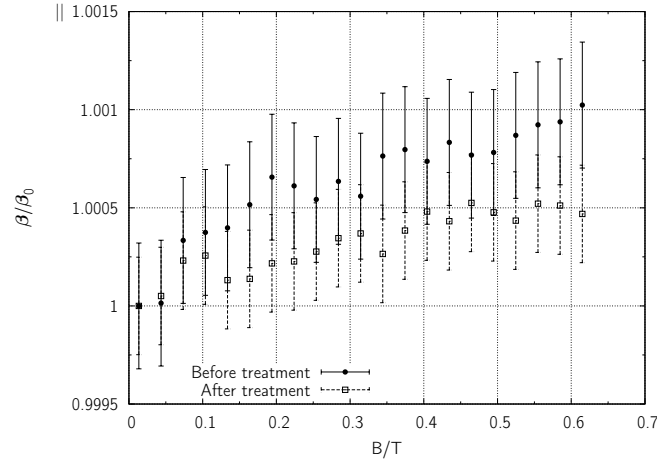


**Figure 7.2:** Response of an MEF-HBT to applied magnetic field along the normal before and after ammonium sulphide passivation.

The device response to magnetic field which was engineered to be different using the two distinct surface treatments could be applied to a circuit such as a *differential pair*. The output of such a circuit in the normal mode of operation is proportional to the (usually small) difference in voltage between the two inputs, i.e. the base contacts of the two matched transistors. However, if one transistor was a passivated HBT and the other was an argon treated HBT (as described above) and the base contacts were both grounded then an offset voltage proportional to the applied magnetic field strength parallel to the normal would be measured between the two collector contacts. The circuit configuration is shown in Figure 7.3.

### 7.3 Integrated Magnetic Structures

The magnetic structures designed and modelled in Chapter 5 were fabricated on the base ledge of the transistors. These served to increase the magnitude of the external magnetic field in the intrinsic base region and hence altered the response for a given field strength. For a typical MEF-HBT with integrated 3-dimensional magnetic structure the D.C. r.m.s. noise was  $0.13 \mu\text{A}$  which is lower than that for a device without structures ( $0.15 \mu\text{A}$ ). This may have been because of the difference in the interface at the intrinsic base surface where the magnetic structures were fabricated, either in the number of interface states or in the lifetime of the states. It was also the case that when the measurements were being taken with the integrated structures the value of  $I_b$  took longer to stabilise than without. This is also likely to be caused by the interface between semiconductor and metal. The results for a device with magnetic structures and one

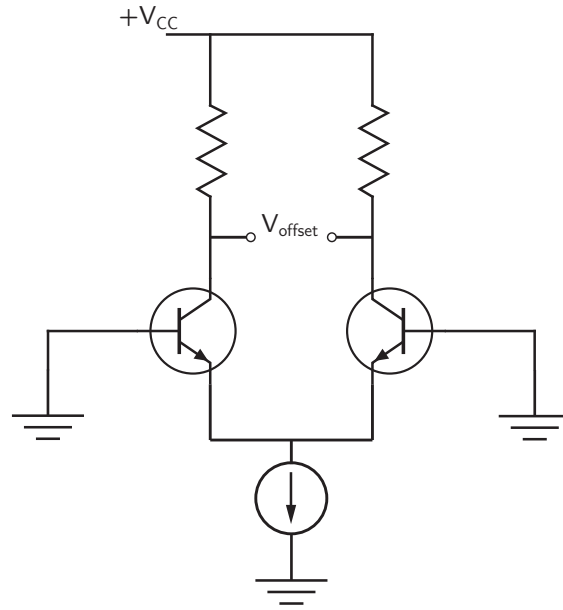
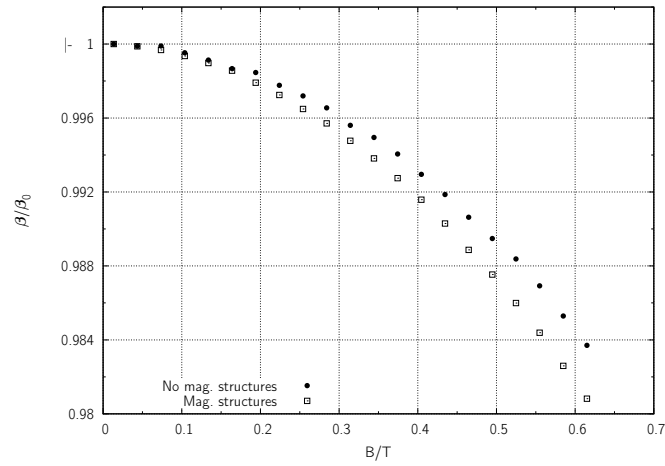


**Figure 7.3:** A typical differential pair amplifier consisting of two bipolar transistors. With the inputs grounded the offset voltage is the difference between the two collector voltages. (Adapted from [152].)

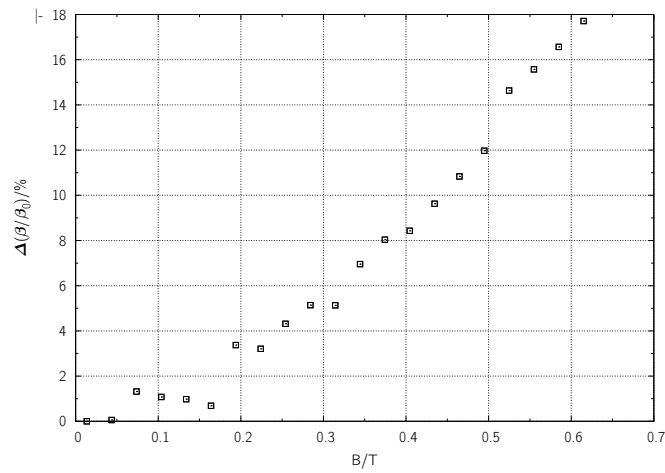
without where the field is applied perpendicular to the normal are shown in Figure 7.4. All the devices considered here were biased under the optimal conditions as described in §6.

Figure 7.5 shows the percentage increase in device response to magnetic field applied perpendicular to the normal of an MEF-HBT with integrated 3-dimensional magnetic structures compared to one without. An increase in sensitivity can be observed over the full field range, although it is particularly marked at higher fields. There is a direct proportionality at higher fields and there is a maximum increase of just under 18% at  $B = 0.615\text{T}$ . This correlates well with the numerical data from the simulations in §5 where there was an increase of 20% in the perpendicular total flux density. The discrepancy may be accounted for by the increase in the parallel field component caused by the focussing effects of the magnetic structures.

Figure 7.6 shows the re-normalised current gain plotted against  $\theta$  and also a plot of the function  $a \cos(b\theta + c) + d$  for  $B = 0.615\text{T}$ . For this plot  $b = 1.77$ , suggesting a period of greater than  $180^\circ$ . This does not make sense physically as the effect of magnetic field applied at  $+\theta$  should be identical to that applied at  $-\theta$  due to symmetry. It is reasonable to assume that the presence of the high permeability magnetic material on the extrinsic base interferes with the field to cause this. The x-axis translation of  $c = 34.6^\circ$  is also



**Figure 7.4:** Response to magnetic field applied perpendicular to the normal of an MEF-HBT with integrated magnetic structures and one without.



**Figure 7.5:** The percentage improvement in response to magnetic field applied perpendicular to the normal of an MEF-HBT with integrated magnetic structures over one without magnetic structures.

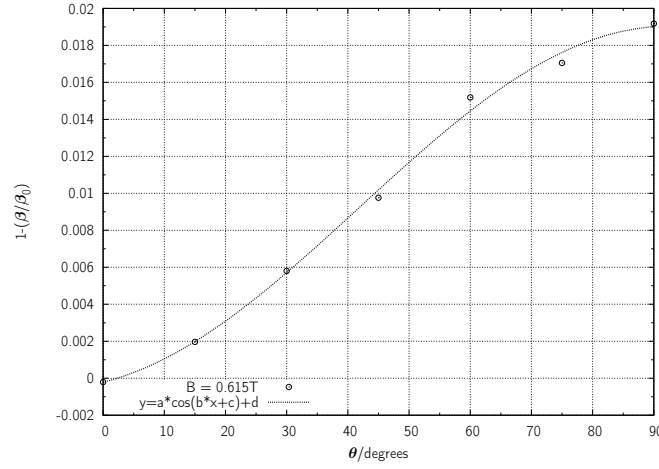


**Figure 7.6:** Response of an MEF-HBT with integrated magnetic structure under optimum bias to an applied magnetic field of 0.615 T for field directions between zero and 90°.

indicative of the same issue.

Similar to the discussion in §6 the effect of varying the angle of the applied field to the normal between zero and 90° is shown in Figure 7.7. The response of a device without integrated magnetic structures is also shown. The response to the field applied parallel to the normal ( $\theta = 0$ ) was smaller. This may have been because of the effects of the increased magnetic flux density component perpendicular to the normal discussed in §5. That there is any response at all could have been caused by an increase in surface states at the metal–semiconductor interface of the magnetic structures. The decrease in  $\beta_0$  from  $\sim 6$  in a device without structures biased at the optimal conditions to  $\sim 5.7$  in a device with structures is further evidence for this. At all other angles the response of the device is seen to increase with the integration of 3–dimensional magnetic structures.

The ability to selectively change the magnetic field response of individual devices is a technology that would lend itself well to inclusion in a differential circuit such as a *ring oscillator* (shown in Figure 7.8). Here small changes in the switching time of a single stage could be introduced by integrating magnetic structures onto it. Thus the oscillating frequency of the circuit, as governed by the equation

$$f_{\text{osc}} = \frac{1}{2nt_d} \quad (7.3)$$

where  $f_{\text{osc}}$  is the oscillation frequency of the ring oscillator circuit,  $n$  is the number of transistors and  $t_d$  is the switching delay time of the (slowest) device, would be altered

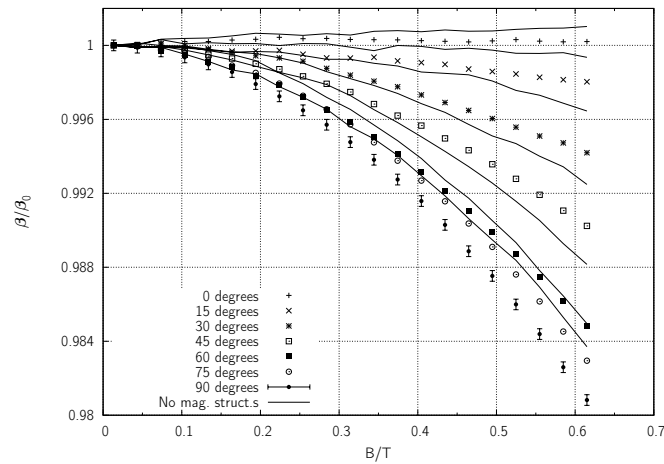


**Figure 7.7:** Angle response to magnetic field of an MEF-HBT with integrated magnetic structures and one without.

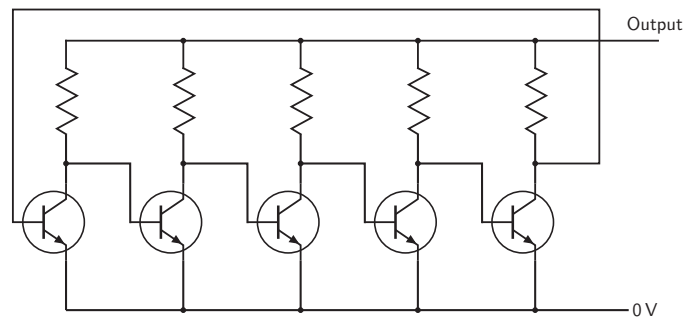


**Figure 7.8:** A typical ring oscillator circuit for npn HBTs. (Adapted from [153].)

by the increased magnetic field in the base region of the integrated device. In this way small changes in magnetic field can be converted into a phase difference compared to a reference oscillator (of the same total number of devices but with no integrated magnetic structures). Phase locking techniques would allow for very sensitive detection of perpendicular magnetic field with this setup.

## 7.4 Sensor Noise and Dynamic Range

The noise of the HBT sensors determined the minimum field which could be successfully detected. The field value which equates to a change in  $I_b$  (or  $\beta$ , or  $\beta/\beta_0$ ) given by the noise figure is the *equivalent noise*,  $B_{eq}$ . Since, as a general rule, the response of the devices was not linear, this figure of merit would be different for different parts of the response curve. For comparison with other devices the smallest available  $B_{eq}$  is shown

Device	$\theta/^\circ$	$B_{\text{eq}}/\text{T}$	
		Max	Min
MEF-HBT	0	0.257	0.018
MEF-HBT	45	0.031	0.004
MEF-HBT	90	0.017	0.002
Mag. struct.s	0	1.268	0.021
Mag. struct.s	45	0.043	0.003
Mag. struct.s	90	0.028	0.002

**Table 7.5:** Equivalent noise for various HBT magnetic sensors.

for various devices in Table 7.5. Because the strength of the response to magnetic field applied parallel to the normal is relatively small compared to the noise the variation between the maximum and minimum values of  $B_{\text{eq}}$  is quite large for this regime. (The values of  $B_{\text{eq}}$  were necessarily derived from the maximum and minimum gradients of the  $I_b$  response, and noisy data makes the variation between these irregular.) There is an order of magnitude difference both between the maximum and minimum effects and between the  $\theta = 0$  and  $\theta = 90^\circ$  regimes, data which correlates well with the relative strengths of the effects (see Table 7.3). That the values are larger than those seen for magnetotransistors in Table 1.2 is indicative of the difference in sensing mechanism and of the relatively large noise inherent in the devices caused by the quality of the epitaxial growth. The desire to integrate the sensors into layer structures compatible with high frequency devices (which feature short base lengths) also has an effect; greater sensitivity to magnetic field was reported with longer bases in [64].

The signal-to-noise ratio was discussed in §2. It is shown for several devices in Table 7.6 calculated from the device DC r.m.s. noise and the maximum measured response (i.e. at  $B = 0.615$  T) although it should be observed that the full range of the sensitivity of the device was not measured due to the maximum field restrictions of the test apparatus. There is every probability that increasing magnetic field to values of several Tesla, as shown in [64, 77], would still lead to a measureable magnetic response.

## 7.5 HBT Sensor Calibration

In order to successfully utilise one of the HBTs discussed above to sense magnetic field it must have a calibration curve which allows a magnetic field (or a magnetic field angle) to be calculated from a given change in DC current gain. Some discussion in §6 and in §7.3 above is given for dealing with the angle response of the devices which has been shown to be accurately represented by a cosine curve. Figure 7.9 shows the data measured for

Device	$\theta/^\circ$	SNR/dB
MEF-HBT	0	10.1
MEF-HBT	45	27.4
MEF-HBT	90	34.1
Mag. struct.s	0	4.5
Mag. struct.s	45	32.5
Mag. struct.s	90	36.4

**Table 7.6:** The signal-to-noise ratio for the various HBT magnetic sensors.

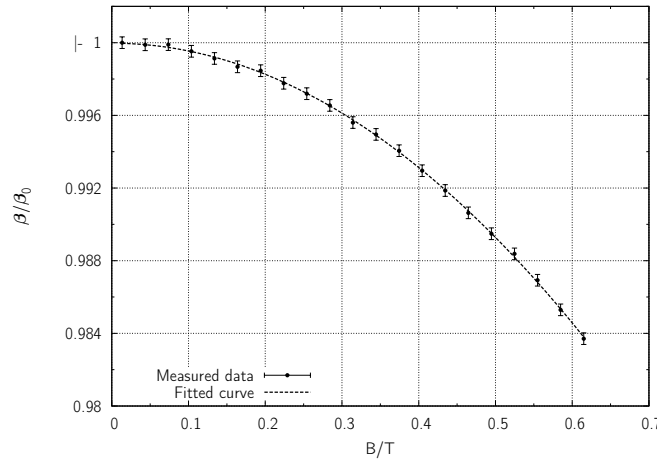


**Figure 7.9:** Response of an MEF-HBT to magnetic field applied perpendicular to the normal and the fitted curve.

the response of an MEF-HBT biased under optimal conditions to magnetic field applied perpendicular to the normal. A regression fit of the form  $y = ax^2 + c$  is also plotted since the change in  $I_b$  varies with  $B^2$  (see the equation (2.71) and [70, 71]).

At all other angles the field response was in part governed by the parallel field effect, except  $\theta = 0$  when it was wholly governed by the parallel field. It was suggested by the linearity of the parallel field response that a curve of the form  $y = ax^2 + bx + c$  might be appropriate for the rest of the angles and  $y = bx + c$  for  $\theta = 0$ . The results of the regression fits are shown in Figure 7.10. The  $y$ -intercept was forced to be unity.

The polynomial coefficients of the fitted curves could be expected to vary with  $\sin\theta$  for the ‘a’ coefficient and  $\cos\theta$  for the ‘b’ coefficient with only a multiplicative factor to set the scale. The ‘a’ and ‘b’ coefficients are plotted in Figure 7.11 and fitted with curves of the form  $y = c_1 \sin(d_1\theta + e_1) + f_1$  and  $y = c_2 \cos(d_2\theta + e_2) + f_2$ , respectively. The simple variation was not observed. This may be due to the interaction between the two

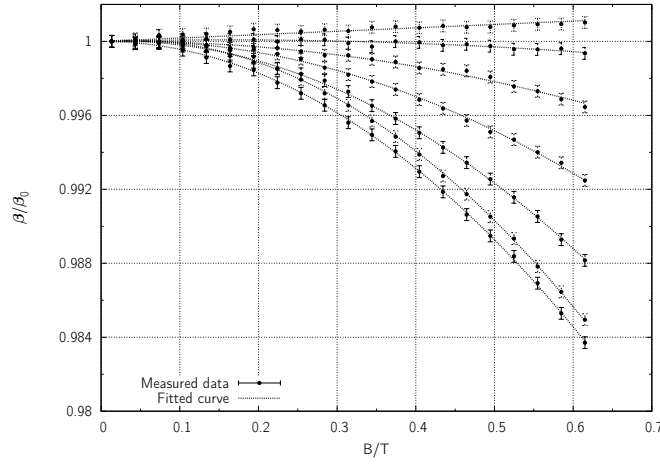


**Figure 7.10:** Response of an MEF-HBT to magnetic field and the fitted curves.

effects.

The same analysis for an MEF-HBT with integrated magnetic structures is shown in Figure 7.12. The dependence on the ‘b’ coefficient was less pronounced, suggesting that the parallel field effect was less prominent. There is further evidence for this in Figure 7.7 discussed above.

Thus it is possible to describe the HBT magnetic field sensors mathematically. For an MEF-HBT there is

$$\frac{\beta}{\beta_0} = a_1 B^2 + b_1 B \quad (7.4)$$

where

$$a_1 = 0.021 \sin(-2.62\theta + 125) - 0.024 \quad (7.5)$$

and

$$b_1 = -2.52 \cos(0.058\theta - 2) + 2.52. \quad (7.6)$$

And for an MEF-HBT with integrated 3-dimensional magnetic structures there is

$$\frac{\beta}{\beta_0} = a_2 B^2 + b_2 B \quad (7.7)$$

where

$$a_2 = 0.029 \sin(-1.6\theta + 63) - 0.023 \quad (7.8)$$

and

$$b_2 = -2.53 \cos(0.049\theta - 2) + 2.53. \quad (7.9)$$

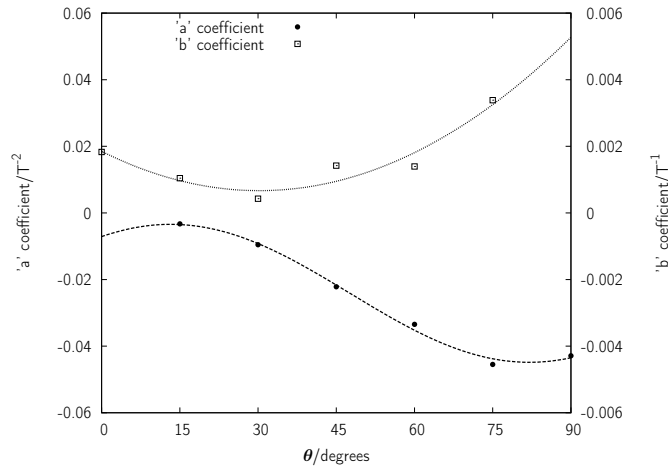


**Figure 7.11:** The coefficients of the polynomial fit to the magnetic field response against applied magnetic field angle for an MEF-HBT.

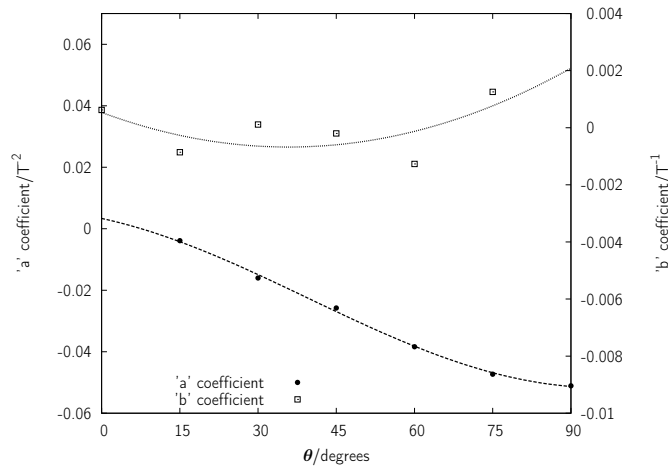


**Figure 7.12:** The coefficients of the polynomial fit to the magnetic field response against applied magnetic field angle for an MEF-HBT with integrated 3-D magnetic structures.

This would enable the sensors to be automatically calibrated, for example, by circuitry in the system into which they had been embedded. Numerical data could then be extracted for magnetic field amplitude, with a known field direction, or magnetic field direction, given a known field amplitude.

The sensitivities of HBTs as magnetic field sensors were presented at the beginning of this chapter. A maximum magnetic field sensitivity of  $0.313 \text{ T}^{-1}$  was observed in the native MEF-HBT and a maximum angle sensitivity of  $0.098 \text{ rad}^{-1}$  at  $45^\circ$ . It was also shown that the amplitude of the transduction effect is an order of magnitude larger for the perpendicular field effect than it is for the parallel field effect.

The surface modification treatments were applied to an HBT magnetic sensor. The argon treatment was shown to increase the relative change in current gain by 36% at  $B = 0.615 \text{ T}$ . The ammonium sulphide passivation treatment decreased the relative change in current gain by 50% at  $B = 0.615 \text{ T}$ . There was an increase in experimental noise measured in an MEF-HBT which had been treated with argon and a decrease in experimental noise measured in a device which had been passivated.

Integrating the 3-dimensional magnetic structures onto an HBT increased the response to perpendicular magnetic field by  $\sim 18\%$  at  $B = 0.615 \text{ T}$ . The sensor equivalent noise was thus reduced in an integrated device, both because of the greater sensitivity to magnetic field and also because the experimental noise was lower. A maximum signal-to-noise ratio of 36.4 dB was measured for the integrated sensor, compared to 34.1 dB for an MEF-HBT. A methodology for determining the appropriate coefficients for the sensor calibration curves was given and the curves were calculated for both of the sensor types.

## 8 Conclusions

It has been seen that there exists a range of mature technologies in the fields of heterojunction bipolar transistors and in bipolar magnetic sensors. The analytical descriptions of the diode, the bipolar transistor and the heterojunction bipolar transistor have been discussed and, furthermore, some consideration has been given to the factors which cause non-ideal response in the measurement of real devices. The effect of the magnetic force on charge carriers has been described for a Hall bar and studies into the effect in HBTs have also been related. In addition, the figures of merit for magnetic sensors were introduced.

The first experimental stage of the project was to fabricate InP/InGaAs single heterojunction bipolar transistors. The general fabrication principles as well as the specifics of HBT fabrication as applied to the work on this project were discussed. The process flow and design considerations for the InP/InGaAs SHBTs were presented. Work was undertaken to optimise the ohmic contact recipes used by varying the alloying temperature. An optimum temperature for rapid thermal annealing of 280 °C was determined. The procedure for device testing was also described. In determining the p-n junction diode ideality factors, an insight into the quality of the material growth is available. The values measured for all the wafers used in the project were high compared to the literature, where ideality factors of 1.1[108] and 1.2[109] have been shown for the base-emitter junction of InP/InGaAs SHBTs over wide ranges of bias. This may have had an effect on the ability of the devices to sense magnetic field, since poor quality interfaces will contain traps and recombination-generation sites which will produce statistical noise. This noise may drown out small changes in magnetic field and will affect the signal-to-noise ratio of the sensor. The values for  $\beta_{dc}$  were also considerably lower than those reported in single heterojunction devices as early as 1988[110], though it should be noted that demands on current gain are not necessarily high. For most applications a DC current gain of around 20 is sufficient[111]. Since the transduction magnitude will be measured using  $\beta_{dc}$ , a smaller current gain may lead to a lower value at which field can be measured before the sensor saturates. While the device to device variation would have to be closely controlled in sensors which were being mass-produced, the system of normalisation used in the later

stages of this project should limit the effects of this on the validity of the results. Although high breakdown voltages are important for RF and microwave power applications[111], the of operational biases used in this study were small. However,  $BV_{ce0}$  values of over 5 V and  $BV_{cb0}$  of over 11 V are possible in InP/InGaAs SHBTs[112]. Collector to emitter breakdown voltages of 7 V can be realised in InP/InGaAs/InP DHBTs[113].

The fabricated HBTs were then used for further experiments. As well as outlining some of the physical phenomena determining the electrical characteristics of semiconductor surfaces, the methodologies for using three different surface treatments to modify the surface of the extrinsic base region of HBTs were given. Of the two passivating treatments, the ammonium sulphide process was shown to be the most effective, with the improvement in current gain proportional to the collector current throughout the measurement range. A maximum improvement of 11 % was realised with this technique. The treatment was also considerably more stable over time. A novel process which was designed to damage the surface of the base layer was developed using argon ion bombardment. The effects of this process were measured firstly on the reverse leakage current of the emitter–base junction where a marked increase was observed for the first 10 min of treatment. After this the effect on the current gain was measured where a decrease of the order of 3 % was observed. Further investigation using alternative chemical treatments revealed the damage not to be constrained to the surface. The development of these processes was undertaken with the aim of enabling the magnetic field response of an untreated HBT to be compared with that of an HBT with an ‘improved’ extrinsic base surface and one in which the surface had been ‘degraded’.

To increase the response to applied magnetic field, 3–dimensional magnetic structures were to be integrated onto the extrinsic base region of the HBT magnetic field sensor. After discussing the background of magnetic materials and their applications, the design process for the 3–dimensional magnetic structures was described. Firstly, the cross–sectional design was optimised given the initial design parameters. An evenly stepped structure was found to be the most effective in focussing the force in to the base. A full analysis of the effect of such a structure on the magnetic response of an HBT was carried out, with reference to the increase in stray field effects. These would cause a response of the device in which the parallel and perpendicular field components were intermixed. The overall increase in the perpendicular component of a magnetic field applied in the perpendicular direction of around 20 % was offset by an increase in the parallel field component. For magnetic field applied in the parallel direction there is a small increase in the parallel field component across the whole base region, although there is an increase of the perpendicular component from zero, which will counteract this effect. The fab-

rication process was then designed and the optimal 3-dimensional magnetic structures were integrated onto the device. These were simple four step structures fabricated in four metal lift-off steps.

Since the technologies required to fabricate an integrated, surface treated HBT magnetic field sensor had been demonstrated, the steps that were taken to make an appropriate experimental setup were described. A calibration curve was determined for the electromagnet in order that a specified magnetic field could be obtained by a known supply current. The first experiments to be carried out were to measure the minority carrier mobility in the p-InGaAs base of the HBTs. At  $2260 \text{ cm}^2 \text{ V}^{-1} \text{ s}^{-1}$  this was found to be lower than the values reported in the literature. The response to magnetic field of two designs of HBT was measured, in terms of the change in current gain. The response to perpendicular applied field was measured, as was the response to parallel applied magnetic field, and then the angle dependence of the field response. A combined noise figure for the HBT and the experimental apparatus was determined and used to estimate the error on the sensor response. Since the magnitude of the transduction effect on the current was comparable the magnitude of the noise at arbitrary bias, a study into the effect of changing the bias conditions was carried out to determine the optimal values. These were found to be  $V_{cb} = 1 \text{ V}$  and  $I_e = 10 \text{ mA}$ . Further measurements were carried out to determine the temperature dependence of the sensor's electrical characteristics and the magnetic field response. The magnitude of the base current increased monotonically with decreasing temperature and the measurement noise decreased as the temperature decreased to 200 K. The response of the HBT to magnetic field applied parallel to the normal increased as the temperature decreased to 160 K with a maximum change in normalised current gain of +0.007 compared to +0.003 at room temperature.

A full characterisation of the sensors was then required, for integrated and surface treated devices. The sensitivities of HBTs as magnetic field sensors were presented. A maximum magnetic field sensitivity of  $0.313 \text{ T}^{-1}$  was observed in the native MEF-HBT and a maximum angle sensitivity of  $0.098 \text{ rad}^{-1}$  at  $45^\circ$ . It was also shown that the amplitude of the transduction effect is an order of magnitude larger for the perpendicular field effect than it is for the parallel field effect. The surface modification treatments were applied to an HBT magnetic sensor. The argon treatment was shown to increase the relative change in current gain by 36 % at  $B = 0.615 \text{ T}$ . The ammonium sulphide passivation treatment decreased the relative change in current gain by 50 % at  $B = 0.615 \text{ T}$ . There was an increase in experimental noise measured in an MEF-HBT which had been treated with argon and a decrease in experimental noise measured in a device which had been passivated. Integrating the 3-dimensional magnetic structures onto an HBT

increased the response to perpendicular magnetic field by  $\sim 18\%$  at  $B = 0.615$  T. The sensor equivalent noise was thus reduced in an integrated device, both because of the greater sensitivity to magnetic field and also because the experimental noise was lower. A maximum signal-to-noise ratio of 36.4 dB was measured for the integrated sensor, compared to 34.1 dB for an MEF-HBT. A methodology for determining the appropriate coefficients for the sensor calibration curves was given and the curves were calculated for both of the sensor types.

The first purposefully designed heterojunction bipolar transistor magnetic field sensor has been presented in this thesis. While the operation of such a device has been proven, the figures of merit are at least an order of magnitude poorer than incumbent silicon technologies. The novel work on surface treatment to alter the magnetic field response and the integration of 3-dimensional magnetic structures increased the transduction efficiency of the sensors but further work is required to reduce the equivalent noise and the signal-to-noise ratio, bringing the InGaAs/InP SHBT magnetic field sensor on a par with existing technologies.

The first development that should be undertaken is to improve the performance of the HBT that forms the basis of the sensor. Current gain could be increased by a factor of ten or more with higher quality material and, in particular, heterojunction interfaces. This would improve the intrinsic device noise and hence the signal-to-noise ratio.

If this was to be achieved then utilisation of the layer structure requirements of different HBT applications (e.g. digital circuits, RF circuits, high power circuits) in different material systems could be used to investigate the effects of changing the electron injection cross-section on the sensitivity to magnetic field. This would allow the comparison of sensors with highly non-equilibrium, diffusive and drift (using a base electric field) base transport regimes. Aggressively scaled devices in which surface recombination currents contributed the dominant proportion of base current could be used to increase the sensitivity and maximum field handling capabilities of a sensor designed for field applied parallel to current flow.

Scaled HBTs fabricated in high quality material schemes lend themselves well to high frequency operation. Another interesting study would be the ability, or otherwise, of the HBTs, when run at high frequencies, to continue to detect magnetic field and what effect the external field would have on operational characteristics.

Increasing the sensitivity of the sensor to fields applied perpendicular to the main current flow could be achieved by increasing the base length. This would have a deleterious effect on the transistors fabricated as the active components of the main circuitry on

any epiwafer, however. The current gain of all such devices would begin to suffer as the base length increased towards the minority carrier diffusion length therein. A trade-off would be made between the quality of the sensor and the appropriate operation of the circuitry. Integration of the sensor into a system on the same wafer would allow for automatic calibration of the device, temperature compensation, offset compensation and other methods of stabilising and improving sensor performance. The sensors could then be incorporated into circuits such as a differential pair or a ring oscillator. This would require an investigation into how to make the surface treatments permanent within the restrictions of HBT MMIC fabrication such as planarisation and encapsulation.

Different configurations of magnetic structure could also be integrated into the device. Building the structure without using the extrinsic base as a platform would allow for much more careful engineering of the field profile in the base, although it would add a considerable number of (non-subtractive) fabrication steps to the process. Furthermore, the use of higher magnetic permeability materials would provide an advantage. A temperature sensor could be constructed using gadolinium as the material for the magnetic structure. Since it has a Curie temperature of  $\sim 300$  K it loses its ferromagnetism at around room temperature. Fluctuations in temperature could thus be monitored by fluctuations in magnetic field induced current changes.

# Appendix

# Fabrication Process

## Sample cleaning process

Ultrasonic bath in acetone for 5 min.

Ultrasonic bath in acetone for 5 min.

Ultrasonic bath in acetone for 5 min.

Rinse in RO water.

Blow dry with N<sub>2</sub>.

## 1. Alignment marks and emitter contacts

Clean sample.

Spin 12% PMMA 2010 at 5000 rpm for 60 s.

Bake on hotplate at °C.

Spin 4% PMMA 2041 at 5000 rpm for 60 s.

Submit to Leica VB6 UHR EWF with a dose of  $320 \mu\text{Ccm}^{-2}$ , a beam current of 64 nA and a beam step size of 25 nm.

Develop with 2:1 MIBK:IPA for 60 s.

Rinse in IPA.

Blow dry with N<sub>2</sub>.

Ash at 40 W for 1 min.

De-oxidise in 4:1 H<sub>2</sub>O:HCl for 30 s.

Rinse in RO water.

Blow dry with N<sub>2</sub>.

Deposit n-type ohmic contact using electron beam metal evaporator.

Soak in acetone at 50 °C for 2 hours.

Transfer to IPA.

Blow dry with N<sub>2</sub>.

## **2. Emitter mesa**

Clean sample.

Spin Microposit S1818 resist at 4000 rpm for 30 s.

Bake on hotplate at 90 °C for 90 s.

Expose using MA6 for 5.0 s.

Develop with 1:1 Microposit Concentrate:H<sub>2</sub>O for 75 s.

Rinse in RO water.

Blow dry with N<sub>2</sub>.

Bake resist at 120 °C for 30 min.

De-oxidise in 4:1 H<sub>2</sub>O:HCl for 30 s.

Rinse in RO water.

Agitate in 1:1:40 H<sub>2</sub>O<sub>2</sub>:H<sub>3</sub>PO<sub>4</sub>:H<sub>2</sub>O for 10 min.

Rinse in RO water.

Agitate in 1:3 HCl:H<sub>3</sub>PO<sub>4</sub> for 45 s.

Rinse in RO water.

Agitate in 1:1:40 H<sub>2</sub>O<sub>2</sub>:H<sub>3</sub>PO<sub>4</sub>:H<sub>2</sub>O for 15 s.

Rinse in RO water.

Blow dry in N<sub>2</sub>.

## **3. Base contacts**

Clean sample.

Spin Microposit S1818 resist at 4000 rpm for 30 s.

Bake on hotplate at 90 °C for 90 s.

Expose using MA6 for 5.0 s.

Soak in chlorobenzene for 20 min.

Develop with 1:1 Microposit Concentrate:H<sub>2</sub>O for 150 s.

Rinse in RO water.

Blow dry with N<sub>2</sub>.

Ash at 40 W for 1 min.

De-oxidise in 4:1 H<sub>2</sub>O:HCl for 30 s.

Rinse in RO water.

Blow dry with N<sub>2</sub>.

Deposit p-type ohmic contact using electron beam metal evaporator.

Soak in acetone at 50 °C for 2 hours.

Transfer to IPA.

Blow dry with N<sub>2</sub>.

#### **4. Base and collector mesa**

Clean sample.

Spin Microposit S1818 resist at 4000 rpm for 30 s.

Bake on hotplate at 90 °C for 90 s.

Expose using MA6 for 5.0 s.

Develop with 1:1 Microposit Concentrate:H<sub>2</sub>O for 75 s.

Rinse in RO water.

Blow dry with N<sub>2</sub>.

Bake resist at 120 °C for 30 min.

De-oxidise in 4:1 H<sub>2</sub>O:HCl for 30 s.

Rinse in RO water.

Agitate in 1:1:40 H<sub>2</sub>O<sub>2</sub>:H<sub>3</sub>PO<sub>4</sub>:H<sub>2</sub>O for 19 min.

Rinse in RO water.

Agitate in 1:3 HCl:H<sub>3</sub>PO<sub>4</sub> for 45 s.

Rinse in RO water.

Agitate in 1:1:40 H<sub>2</sub>O<sub>2</sub>:H<sub>3</sub>PO<sub>4</sub>:H<sub>2</sub>O for 15 s.

Rinse in RO water.

Blow dry in N<sub>2</sub>.

## **5. Collector contacts**

Clean sample.

Spin Microposit S1818 resist at 4000 rpm for 30 s.

Bake on hotplate at 90 °C for 90 s.

Expose using MA6 for 5.0 s.

Soak in chlorobenzene for 20 min.

Develop with 1:1 Microposit Concentrate:H<sub>2</sub>O for 150 s.

Rinse in RO water.

Blow dry with N<sub>2</sub>.

Ash at 40 W for 1 min.

De-oxidise in 4:1 H<sub>2</sub>O:HCl for 30 s.

Rinse in RO water.

Blow dry with N<sub>2</sub>.

Deposit n-type ohmic contact using electron beam metal evaporator.

Soak in acetone at 50 °C for 2 hours.

Transfer to IPA.

Blow dry with N<sub>2</sub>.

Anneal at 240 °C for 60 s.

## **6. Insulation**

Clean sample.

Spin Microposit S1818 resist at 4000 rpm for 30 s.

Bake on hotplate at 90 °C for 90 s.

Expose using MA6 for 5.0 s.

Soak in chlorobenzene for 20 min.  
Develop with 1:1 Microposit Concentrate:H<sub>2</sub>O for 150 s.  
Rinse in RO water.  
Blow dry with N<sub>2</sub>.  
Ash at 40 W for 1 min.  
Deposit 200 nm of ICP-PECVD Si<sub>3</sub>N<sub>4</sub>.  
Soak in acetone at 50 °C for 4 hours.  
Ultrasonic acetone for 10 min.  
Transfer to IPA.  
Blow dry with N<sub>2</sub>.

## **7. Bond pads**

Clean sample.  
Spin Microposit S1818 resist at 4000 rpm for 30 s.  
Bake on hotplate at 90 °C for 90 s.  
Expose using MA6 for 5.0 s.  
Soak in chlorobenzene for 20 min.  
Develop with 1:1 Microposit Concentrate:H<sub>2</sub>O for 150 s.  
Rinse in RO water.  
Blow dry with N<sub>2</sub>.  
Ash at 40 W for 1 min.  
Deposit bond pad metal using electron beam metal evaporator.  
Soak in acetone at 50 °C for 2 hours.  
Transfer to IPA.  
Blow dry with N<sub>2</sub>.

## **8. 3-D magnetic structures**

Clean sample.

Spin Microposit S1818 resist at 4000 rpm for 30 s.  
Bake on hotplate at 90 °C for 90 s.  
Expose using MA6 for 5.0 s.  
Soak in chlorobenzene for 20 min.  
Develop with 1:1 Microposit Concentrate:H<sub>2</sub>O for 150 s.  
Rinse in RO water.  
Blow dry with N<sub>2</sub>.  
Ash at 40 W for 1 min.  
De-oxidise in 4:1 H<sub>2</sub>O:HCl for 30 s.  
Rinse in RO water.  
Blow dry with N<sub>2</sub>.  
Deposit bottom magnetic structure metallisation.  
Soak in acetone at 50 °C for 2 hours.  
Transfer to IPA.  
Blow dry with N<sub>2</sub>.  
\* Clean sample.  
Spin Microposit S1818 resist at 4000 rpm for 30 s.  
Bake on hotplate at 90 °C for 90 s.  
Expose using MA6 for 5.0 s.  
Soak in chlorobenzene for 20 min.  
Develop with 1:1 Microposit Concentrate:H<sub>2</sub>O for 150 s.  
Rinse in RO water.  
Blow dry with N<sub>2</sub>.  
Ash at 40 W for 1 min.  
Deposit upper magnetic structure metallisation .  
Soak in acetone at 50 °C for 2 hours.  
Transfer to IPA.  
Blow dry with N<sub>2</sub>. \*  
Repeat \* ... \* for two remaining magnetic structure metallisations.

# References

- [1] J. BARDEEN AND W. H. BRATTAIN (1948), *The Transistor, A Semi-Conductor Triode*, Physics Review Letters, **74**, 230.
- [2] P. M. ASBECK AND N. TOHRU (2001), *Bipolar Transistor Technology: Past and Future Directions*, IEEE Transactions on Electron Devices, **48**(11), 2455.
- [3] W. SHOCKLEY (1951), *No. 2,569,347*, US Patent.
- [4] A. CHO AND J. CASEY, H.C. (1974), *GaAs-Al<sub>x</sub>Ga<sub>1-x</sub>As double-heterostructure lasers prepared by molecular beam epitaxy*, Applied Physics Letters, **25**(5), 288.
- [5] H. KROEMER (1979), *Heterojunction Transistors*, Bulletin of the American Physical Society, **24**(3), 230.
- [6] T. OHISHI, Y. ABE, H. SUGIMOTO, K. OHTSUKA AND T. MATSUI (1990), *Ultra-high current gain InGaAsP/InP heterojunction bipolar transistor*, Electronics Letters, **26**(6), 392.
- [7] W. P. DUMKE, J. M. WOODALL AND V. L. RIDEOUT (1972), *GaAs-GaAlAs Heterojunction Transistor for High Frequency Operation*, Solid-State Electronics, **15**(12), 1339.
- [8] M. KONAGAI AND K. TAKAHASHI (1975), *(GaAl)As-GaAs heterojunction transistors with high injection efficiency*, Journal of Applied Physics, **46**(5), 2120.
- [9] W. LIU (1998), *Handbook of III-V Heterojunction Bipolar Transistors*, John Wiley and Sons, New York.
- [10] H. KROEMER (1978), *Current Problems in Heterojunction Devices and their Physics*, IEEE Transactions on Electron Devices, **25**(11), 1339.
- [11] W. HAFEZ AND M. FENG (2005), *Experimental demonstration of pseudomorphic heterojunction bipolar transistors with cutoff frequencies above 600 GHz*, Applied Physics Letters, **86**(152101), 1.
- [12] W. SNODGRASS, W. BING-RUEY, W. HAFEZ, K. Y. CHENG AND M. FENG (2006), *Performance enhancement of composition-graded-base type-II InP/GaAsSb double-heterojunction bipolar transistors with  $f_T > 500$  GHz*, Applied Physics Letters, **88**(22), 222101.

- [13] H. KROEMER (1982), *Heterostructure Bipolar Transistors and Integrated Circuits*, Proceedings of the IEEE, **70**(1), 13.
- [14] C. E. C. WOOD (1980), *Molecular Beam Epitaxy - A Review Of Recent Progress*, Annual Proceedings - Reliability Physics (Symposium), **1**, 101.
- [15] R. MILANO, T. WINDHORN, E. ANDERSON, G. STILLMAN, R. DUPUIS AND P. DAPKUS (1979), *Al<sub>0.5</sub>Ga<sub>0.5</sub>As-GaAs heterojunction phototransistors grown by metalorganic chemical vapor deposition*, Applied Physics Letters, **34**(9), 562.
- [16] N. MOLL (1985), *Heterojunction bipolar transistors – a review*, Cornell Conference on Advanced Concepts in High Speed Semiconductor Devices and Circuits, Ithaca, NY, USA, 35–44.
- [17] A. GEORGAKILAS, P. PANAYOTATOS, J. STOEMENOS, J.-L. MOURRAIN AND A. CHRISTOU (1992), *Achievements and limitations in optimized GaAs films grown on Si by molecular-beam epitaxy*, Journal of Applied Physics, **71**(6), 2679.
- [18] P. ASBECK, C. FARLEY, M. CHANG, K. WANG AND W. HO (1990), *InP-based heterojunction bipolar transistors: performance status and circuit applications*, 2nd International Conference on Indium Phosphide and Related Materials, Denver, USA, 2–5.
- [19] P. DODD AND M. LUNDSTROM (1992), *Minority electron transport in InP/InGaAs heterojunction bipolar transistors*, Applied Physics Letters, **61**(4), 465.
- [20] Y. BETSER AND D. RITTER (1995), *High emitter efficiency in InP/GaInAs HBT's with ultra high base doping levels*, Electron Device Letters, IEEE, **16**(3), 97.
- [21] F. FIEDLER, K. MAUSE, G. PITZ, D. FRITZSCHE, E. KUPHAL AND H. KRAUTLE (1992), *InP based HBTs-technology, performance and applications*, 4th International Conference on Indium Phosphide and Related Materials, Newport, USA, 404–409.
- [22] I. HARRISON, M. DAHLSTROM, S. KRISHNAN, Z. GRIFFITH, Y. KIM AND M. J. RODWELL (2004), *Thermal limitations of InP HBTs in 80- and 160-Gb ICs*, IEEE Transactions on Electron Devices, **51**(4), 529.
- [23] W. LIU (1999), *Fundamentals of III–V Devices: HBTs, MESFETs, and HFETs/HEMTs*, 1st edition, Wiley–Interscience, New York.
- [24] G. W. NEUDECK (1989), *Modular Series on Solid State Devices, Volume III: The Bipolar Junction Transistor*, Addison–Wesley, Reading, MA.
- [25] A.-H. XU, X.-J. CHEN, M. QI AND F.-Y. ZHU (2004), *Study on ultrahigh carbon-doped p-type InGaAs grown by gas source molecular beam epitaxy*, Journal of Functional Materials and Devices, **10**(4), 423.

- [26] J. PERKINS (1996), *Design and Fabrication Techniques for Indium Phosphide HBTs*, Ph.D. thesis, University of Leeds.
- [27] K. ELGAID, H. MCLELLAND, M. HOLLAND, D. MORAN, C. STANLEY AND I. THAYNE (2005), *50-nm T-gate metamorphic GaAs HEMTs with  $f_T$  of 440 GHz and noise figure of 0.7 dB at 26 GHz*, IEEE Electron Device Letters, **26**(11), 784.
- [28] M.-C. CHANG, P. ASBECK, K. WANG, G. SULLIVAN, N.-H. SHENG, J. HIGGINS AND D. MILLER (1987), *AlGaAs/GaAs heterojunction bipolar transistors fabricated using a self-aligned dual-lift-off process*, IEEE Electron Device Letters, **ED-8**(7), 303.
- [29] T. OKA, K. HIRATA, H. SUZUKI, K. OUCHI, H. UCHIYAMA, T. TANIGUCHI, K. MOCHIZUKI AND T. NAKAMURA (2001), *High-speed small-scale InGaP/GaAs HBT technology and its application to integrated circuits*, IEEE Transactions on Electron Devices, **8**(11), 2625.
- [30] T. ISHIBASHI (2001), *Nonequilibrium electron transport in HBTs*, IEEE Transactions on Electron Devices, **48**(11), 2595.
- [31] P. ASBECK (1989), *Heterojunction bipolar transistors: status and directions*, Proceedings of the 1989 Bipolar Circuits and Technology Meeting, Minneapolis, MN, USA, 65–9.
- [32] K. YANG, J. COWLES, J. EAST AND G. HADDAD (1995), *Theoretical and experimental DC characterization of InGaAs-based abrupt emitter HBT's*, IEEE Transactions on Electron Devices, **42**(6), 1047.
- [33] M. RODWELL, M. URTEAGA, T. MATHEW, D. SCOTT, D. MENSA, Q. LEE, J. GUTHRIE, Y. BETSER, S. MARTIN, R. SMITH, S. JAGANATHAN, S. KRISHNAN, S. LONG, R. PULLELA, B. AGARWAL, U. BHATTACHARYA, L. SAMOSKA AND M. DAHLSTROM (2001), *Submicron scaling of HBTs*, IEEE Transactions on Electron Devices, **48**(11), 2606.
- [34] T. CARRUTHERS, M. FRANKEL AND C. KYONO (1993), *Ultrafast photodetection with an AlInAs/GaInAs heterojunction bipolar transistor*, Applied Physics Letters, **63**(14), 1921.
- [35] S. PARK, T. CHIN, Q. LIU, S. FU, T. NAKAMURA, P. YU AND P. ASBECK (1998), *Submicron self-aligned HBT's by selective emitter regrowth*, IEEE Electron Device Letters, **19**(4), 118.
- [36] B. AGARWAL, D. MENSA, R. PULLELA, Q. LEE, U. BHATTACHARYA, L. SAMOSKA, J. GUTHRIE AND M. RODWELL (1997), *277-GHz  $f_{max}$  transferred-substrate heterojunction bipolar transistor*, IEEE Electron Device Letters, **18**(5), 228.

- [37] T. KRAEMER, F. LENK, A. MAASSDORF, H. WUERFL AND G. TRAENKLE (2007), *High yield transferred substrate InP DHBT*, 19th International Conference on Indium Phosphide and Related Materials, Matsue, Japan, 407–408.
- [38] C. BOLOGNESI, M. DVORAK, P. YEO, X. XU AND S. WATKINS (2001), *InP/GaAsSb/InP double HBTs: a new alternative for InP-based DHBTs*, IEEE Transactions on Electron Devices, **48**(11), 2631.
- [39] Z. GRIFFITH, M. J. W. RODWELL, X.-M. FANG, D. LOUBYCHEV, Y. WU, J. M. FASTENAU AND A. W. K. LIU (2005), *In<sub>0.53</sub>Ga<sub>0.47</sub>As/InP Type-I DHBTs having 450 GHz  $f_T$  and 490 GHz  $f_{max}$  with  $C_{cb}/I_c \approx 0.38$  ps/V*, Conference Digest — Device Research Conference, Santa Clara, USA, 265–266.
- [40] HONG YANG, HONG WANG AND K. RADHAKRISHNAN (2004), *Device stability of metamorphic InP/InGaAs heterojunction bipolar transistors by optical and electrical characterization*, 16th International Conference on Indium Phosphide and Related Materials, Kagoshima, Japan, 397–399.
- [41] C. ROUMENIN (1995), *Magnetic sensors continue to advance towards perfection*, Sensors and Actuators, A: Physical, **46**(1-3 pt 3), 273.
- [42] G. L. PEARSON (1948), *A magnetic field meter employing the Hall effect in germanium*, Review of Scientific Instruments, **19**, 263.
- [43] H. P. BALTES AND R. S. POPOVIC (1986), *Integrated semiconductor magnetic field sensors*, Proceedings of the IEEE, **74**(8), 1107.
- [44] S. GOZU, T. KITA, Y. SATO, S. YAMADA AND M. TOMIZAWA (2001), *Characterization of high indium content metamorphic InGaAs/InAlAs modulation-doped heterostructures*, Journal of Crystal Growth, **227–228**, 155.
- [45] G. W. PATERSON, J. A. WILSON, D. MORAN, R. HILL, A. R. LONG, I. THAYNE, M. PASSLACK AND R. DROOPAD (2006), *Gallium oxide (Ga<sub>2</sub>O<sub>3</sub>) on gallium arsenide - A low defect, high-K system for future devices*, Materials Science and Engineering B – Solid State Materials for Advanced Technology, **135**(3), 277.
- [46] Y. ABULAFIA, M. MCELFRESH, A. SHAULOV, Y. YESHURUN, Y. PALTIEL, D. MAJER, H. SHTRIKMAN AND E. ZELDOV (1998), *Measurement of the magnetic induction vector in superconductors using a double-layer Hall sensor array*, Applied Physics Letters, **72**(22), 2891.
- [47] C. ROUMENIN (1990), *Bipolar magnetotransistor sensors. An invited review*, Sensors and Actuators A, **24**(2), 83.
- [48] Y. SUGIYAMA, H. SOGA AND M. TACANO (1989), *Highly-sensitive Hall element with quantum-well superlattice structures*, Journal of Crystal Growth, **95**(1-4), 394.
- [49] R. POPOVIC (1984), *The vertical Hall-effect device*, IEEE Electron Device Letters, **5**(9), 357.

- [50] A. VINAL AND N. MASNARI (1984), *Operating principles of bipolar transistor magnetic sensors*, IEEE Transactions on Electron Devices, **ED-31**(10), 1486.
- [51] E. HUDSON (1969), *No. 2,569,347*, US Patent.
- [52] R. D. TIKHONOV (2005), *Response mechanism of the base-in-well bipolar magnetotransistor*, Russian Microelectronics, **34**(3), 160.
- [53] A. VINAL (1981), *A magnetic sensor utilizing an avalanching semiconductor device*, IBM Journal of Research and Development, **25**(2-3), 196.
- [54] L. DAVIES AND M. WELLS (1971), *Magneto-transistor incorporated in an integrated circuit*, Proceedings of the Institution of Radio and Electronics Engineers, Australia, **32**(6), 235.
- [55] G. REKALOVA, D. KOZLOV AND T. PERSIYANOV (1981), *Magnetic induction transducers based on silicon planar transistors*, IEEE Transactions on Magnetics, **17**(6), 3373.
- [56] V. ZIEREN AND B. DUYN DAM (1982), *Magnetic-field-sensitive multicollector n-p-n transistors*, IEEE Transactions on Electron Devices, **29**(1), 83.
- [57] L. RISTIC, T. SMY AND H. P. BALTES (1989), *Lateral magnetotransistor structure with a linear response to the magnetic field*, IEEE Transactions on Electron Devices, **36**(6), 1076.
- [58] R. POPOVIC AND H. BALTES (1983), *Dual-collector magnetotransistor optimized with respect to injection modulation*, Sensors and Actuators, **4**(2), 155.
- [59] Y. SUGIYAMA (1995), *Recent progress on magnetic sensors with nanostructures and applications*, Journal of Vacuum Science and Technology B: Microelectronics Processing and Phenomena, **13**(3), 1075.
- [60] R. F. PIERRET (1988), *Modular Series on Solid State Devices, Volume II: The PN Junction Diode*, Addison–Wesley, Reading, MA.
- [61] D. MORGAN AND R. WILLIAMS (editors) (1991), *Physics and technology of hetero-junction devices*, Materials and Devices Series, IET.
- [62] C. MATTHAI, J. BASS AND M. OLOUMI (1990), *Band offsets and electron localization in semiconductor interfaces and superlattices*, Journal of Vacuum Science and Technology B (Microelectronics Processing and Phenomena), **8**(4), 916.
- [63] S. SZE (1981), *Physics of Semiconductor Devices*, 2nd edition, John Wiley and Sons, London.
- [64] R. N. NOTTENBURG, A. F. J. LEVI, B. JALALI, D. SIVCO, D. A. HUMPHREY AND A. Y. CHO (1990), *Nonequilibrium electron transport in heterostructure bipolar transistors probed by magnetic field*, Applied Physics Letters, **56**(26), 2660.

- [65] F. RAHMAN, T. THORNTON, B. GALLAGHER AND R. STRADLING (1999), *Boundary scattering in wet-etched InAs/GaSb heterostructure wires: with and without magnetic field*, Semiconductor Science and Technology, **14**(5), 478.
- [66] V. KUBRAK, A. RUSHFORTH, A. NEUMANN, F. RAHMAN, B. GALLAGHER, P. MAIN, M. HENINI, C. MARROWS AND B. HICKEY (2000), *Transport of 2D electrons through magnetic barriers*, Physica E: Low-Dimensional Systems and Nanostructures, **7**(3), 997.
- [67] J. HAYES AND A. LEVI (1986), *Dynamics of extreme nonequilibrium electron transport in GaAs*, IEEE Journal of Quantum Electronics, **22**(9), 1744.
- [68] J. HAYES, A. LEVI, A. GOSSARD AND J. ENGLISH (1986), *Base transport dynamics in a heterojunction bipolar transistor*, Applied Physics Letters, **49**(21), 1481.
- [69] P. HOUSTON, Y. YANG, M. JOHNSON AND M. HOPKINSON (1994), *Magnetic field effects on InP/InGaAs quasiballistic heterojunction bipolar transistors*, Semiconductor Science and Technology, **9**(5), 1153.
- [70] Y. BETSER, D. RITTER, G. BAHIR, S. COHEN AND J. SPERLING (1995), *Measurement of the minority carrier mobility in the base of heterojunction bipolar transistors using a magnetotransport method*, Applied Physics Letters, **67**(13), 1883.
- [71] Y. BETSER AND D. RITTER (1996), *Electron transport in heavily doped bases of InP/GaInAs HBT's probed by magneto transport experiments*, IEEE Transactions on Electron Devices, **43**(8), 1187.
- [72] E. HARMON, M. LOVEJOY, M. MELLOCH, M. LUNDSTROM, D. RITTER AND R. HAMM (1993), *Minority-carrier mobility enhancement in  $p^+$ -InGaAs lattice matched to InP*, Applied Physics Letters, **63**(5), 636.
- [73] B. LYE, H. YOW, P. HOUSTON AND C. BUTTON (1996), *Electron mobility enhancement in heavily doped GaAs:C heterojunction bipolar transistors*, Electronics Letters, **32**(25), 2351.
- [74] U. STRAUSS, A. HEBERLE, X. ZHOU, W. RUEHLE, T. LAUTERBACH, K. BACHEM AND N. HAEGEL (1993), *Minority-carrier lifetime in heavily doped GaAs:C*, Japanese Journal of Applied Physics, Part 1: Regular Papers and Short Notes, **32**(1B), 495.
- [75] B.-C. LYE, P. HOUSTON, H.-K. YOW AND C. BUTTON (1998), *GaInP/AlGaAs/GaInP double heterojunction bipolar transistors with zero conduction band spike at the collector*, IEEE Transactions on Electron Devices, **45**(12), 2417.
- [76] Q. YANG, D. SCOTT, T. CHUNG AND G. STILLMAN (2000), *Minority carrier lifetime degradation in carbon-doped base of InGaP/GaAs heterojunction bipolar transistors grown by low-pressure metalorganic chemical vapor deposition*, Applied Physics Letters, **77**(2), 271.

- [77] T. NOZU, T. SUGIYAMA, S. HONGO AND K. MORIZUKA (1999), *A new method for evaluation of surface recombination in heterojunction bipolar transistors by magnetotransport*, Solid-State Electronics, **43**, 1347.
- [78] S. W. KURNICK AND R. N. ZITTER (1956), *Photoconductive and photoelectromagnetic effects in InSb*, Journal of Applied Physics, **27**(3), 278.
- [79] R. NOTTENBURG, Y. CHEN, T. TANBUN-EK, R. LOGAN AND D. HUMPHREY (1989), *High performance InP/InGaAs heterostructure bipolar transistors grown by metalorganic vapor phase epitaxy*, Applied Physics Letters, **55**(2), 171.
- [80] A. W. HANSON, S. A. STOCKMAN AND G. E. STILLMAN (1992), *InP/In<sub>0.53</sub>Ga<sub>0.47</sub>As heterojunction bipolar transistors with a carbon-doped base grown by MOCVD*, IEEE Electron Device Letters, **13**(10), 504.
- [81] E. KUPHAL, K. MAUSE, K. MIETHE, A. EISENBACH, F. FIEDLER AND A. CORBET (1995), *Electron diffusion length in InGaAs:Zn derived from heterostructure bipolar transistors*, Solid-State Electronics, **38**(4), 795.
- [82] I. TAN, G. SNIDER, L. CHANG AND E. HU (1990), *A self-consistent solution of Schrodinger-Poisson equations using a nonuniform mesh*, Journal of Applied Physics, **68**(8), 4071.
- [83] G. SNIDER (2006), *WWW Homepage*, <http://www.nd.edu/~gsnider/>, accessed: 15th May 2006.
- [84] S. HAYWOOD, A. LIM, R. GUPTA, S. EMERY, J. HOGG, V. HEWER, P. STAVRINO, M. HOPKINSON AND G. HILL (2003), *Demonstration of a blueshift in type II asymmetric InP/InAsP/InGaAs multiple quantum wells*, Journal of Applied Physics, **94**(5), 3222.
- [85] B. KANEGSBURG AND E. KANEGSBURG (2006), *Parameters in ultrasonic cleaning for implants and other critical devices*, Journal of ASTM International, **3**(4), 8.
- [86] M. N. STEKOL'SHCHIKOV, L. M. KRIVTSOVA AND M. I. RATNER (1987), *Evaluation of solvency of hydrocarbon solvents*, Chemistry and Technology of Fuels and Oils, **23**(6), 292.
- [87] R. PETHRICK AND K. RANKIN (1999), *Criteria for uniform thin film formation for polymeric materials*, Journal of Materials Science: Materials in Electronics, **10**(2), 141.
- [88] SHIPLEY (2005), *Microposit S1800 Series Photoresists*, [www.cnse.ucr.edu/capabilities/spin\\_files/S1800seriesDataSheet.pdf](http://www.cnse.ucr.edu/capabilities/spin_files/S1800seriesDataSheet.pdf), accessed: 24th January 2005.
- [89] K. MIN-GU AND P. HYUNG-HO (2002), *Surface preparation and effective contact formation for GaAs surface*, 2nd International Seminar on Semiconductor Surface Passivation, volume 67 of *Vacuum (UK)*, Elsevier, Ustron, Poland, 91.

- [90] H. CHONG, W. TAN AND A. BRYCE (2007), *Reflectivity of deep-etched InGaAs-InP waveguide Bragg reflectors*, Physica Status Solidi (C), **4**, 1646.
- [91] R. WILLIAMS (1990), *Modern GaAs Processing Methods*, Artech House, Boston, MA.
- [92] M. BROZEL AND C. STILLMAN (editors) (1996), *Properties of Gallium Arsenide*, 3rd edition, EMIS Datareviews, Inspec, London.
- [93] A. STANO (1987), *Chemical etching characteristics of InGaAs/InP and InAlAs/InP heterostructures*, Journal of the Electrochemical Society, **134**(2), 448.
- [94] S. UEKUSA, K. OIGAWA AND M. TACANO (1985), *Preferential etching of InP for submicron fabrication with HCl/H<sub>3</sub>PO<sub>4</sub> solution*, Journal of the Electrochemical Society, **132**(3), 671.
- [95] S. MURAD, S. BEAUMONT, M. HOLLAND AND C. WILKINSON (1995), *Selective reactive ion etching of InGaAs and InP over InAlAs in SiCl<sub>4</sub>/SiF<sub>4</sub>/HBr plasmas*, Journal of Vacuum Science and Technology B: Microelectronics Processing and Phenomena, **13**(6), 2344.
- [96] P. BHATTACHARYA (editor) (1993), *Properties of Lattice-Matched and Strained Indium Gallium Arsenide*, 1st edition, EMIS Datareviews, Inspec, London.
- [97] G. LUCOVSKY, P. RICHARD, D. TSU, S. LIN AND R. MARKUNAS (1986), *Deposition of silicon dioxide and silicon nitride by remote plasma enhanced chemical vapor deposition*, Journal of Vacuum Science and Technology A (Vacuum, Surfaces, and Films), **4**(3), 681.
- [98] B. LUO, F. REN, C. WU, S. PEARTON, C. ABERNATHY AND K. MACKENZIE (2002), *Influence of PECVD deuterated SiN<sub>x</sub> on GaAs MESFETs and GaAs/AlGaAs HBTs*, Solid-State Electronics, **46**(9), 1359.
- [99] H. ZHOU, K. ELGAID, C. WILKINSON AND I. THAYNE (2006), *Low-hydrogen-content silicon nitride deposited at room temperature by inductively coupled plasma deposition*, Japanese Journal of Applied Physics, Part 1: Regular Papers and Short Notes and Review Papers, **45**(10 B), 8388.
- [100] NORDIC PACKAGING (2005), *The Nordic Electronics Packaging Guideline*, <http://extra.ivf.se/ngl/>, accessed: 16th September 2005.
- [101] J.-L. LEE, Y.-T. KIM AND J. Y. LEE (1998), *Microstructural evidence on direct contact of Au/Ge/Ni/Au ohmic metals to InGaAs channel in pseudomorphic high electron mobility transistor with undoped cap layer*, Applied Physics Letters, **73**(12), 1670.
- [102] D. CAFFIN, C. BESOMBES, J. BRESSE, P. LEGAY, G. LE ROUX, G. PATRIARCHE AND P. LAUNAY (1997), *Base metallization stability in InP/InGaAs heterojunction*

*bipolar transistors and its influence on leakage currents*, Journal of Vacuum Science and Technology B (Microelectronics and Nanometer Structures), **15**(4), 854.

- [103] A. KATZ, W. DAUTREMONT-SMITH, S. CHU, P. THOMAS, L. KOSZI, J. LEE, V. RIGGS, R. BROWN, S. NAPHOLTZ, J. ZILKO AND A. LAHAV (1989), *Pt/Ti/p-In<sub>0.53</sub>Ga<sub>0.47</sub>As low-resistance nonalloyed ohmic contact formed by rapid thermal processing*, Applied Physics Letters, **54**(23), 2306.
- [104] I.-H. KIM, S. H. PARK, T.-W. LEE AND M.-P. PARK (1997), *A study on Au/Ni/Au/Ge/Pd ohmic contact and its application to AlGaAs/GaAs heterojunction bipolar transistors*, Applied Physics Letters, **71**(13), 1854.
- [105] Y.-T. LYU, K.-L. JAW, C.-T. LEE, C.-D. TSAI, Y.-J. LIN AND Y.-T. CHERNG (2000), *Ohmic performance comparison for Ti/Ni/Au and Ti/Pt/Au on InAs/graded InGaAs/GaAs layers*, Materials Chemistry and Physics, **63**(2), 122.
- [106] S. THOMS AND D. MACINTYRE (2007), *Tilt-corrected stitching for electron beam lithography*, Microelectronic Engineering, **84**(5–8), 793.
- [107] N. MATINE, M. DVORAK, J. PELOUARD, F. PARDO AND C. BOLOGNESI (1998), *InP in HBTs by vertical and lateral wet etching*, 10th International Conference on Indium Phosphide and Related Materials, Tsukuba, Jpn, 195–198.
- [108] H. SCHUMACHER, J. HAYES, R. BHAT AND M. KOZA (1987), *OMCVD grown InP/InGaAs heterojunction bipolar transistors*, International Electron Devices Meeting, New York, 852–853.
- [109] R. NOTTENBURG, H. TEMKIN, M. PANISH AND R. HAMM (1986), *High gain InGaAs/InP heterostructure bipolar transistors grown by gas source molecular beam epitaxy*, Applied Physics Letters, **49**(17), 1112.
- [110] R. NOTTENBURG, Y.-K. CHEN, M. PANISH, R. HAMM AND D. HUMPHREY (1988), *High-current-gain submicrometer InGaAs/InP heterostructure bipolar transistors*, IEEE Electron Device Letters, **9**(10), 524.
- [111] W. HO, M. CHANG, N. SHENG, N. WANG, P. ASBECK, K. WANG, R. NUBLING, G. SULLIVAN AND J. HIGGINS (1990), *A multifunctional HBT technology*, 12th Annual GaAs IC Symposium Technical Digest 1990, New Orleans, LA, USA, 67–70.
- [112] T. OKA, T. TANOUÉ, H. MASUDA, K. OUCHI AND T. MOZUME (1995), *InP/InGaAs heterojunction bipolar transistor with extremely high  $f_t$ ; over 200 GHz*, Electronics Letters, **31**(23), 2044.
- [113] J. ZHI, S. YONG-BO, C. WEI, L. XIN-YU, X. AN-HUAI AND Q. MING (2008), *High-speed InGaAs/InP double heterostructure bipolar transistor with high breakdown voltage*, Chinese Physics Letters, **25**(7), 2683.

- [114] W. MÖNCH (2001), *Semiconductor Surfaces and Interfaces*, berlin edition, Surface Sciences, Springer.
- [115] R. F. PIERRET (1988), *Modular Series on Solid State Devices*, Volume I: *Semiconductor Fundamentals*, Addison–Wesley, Reading, MA.
- [116] W. SHOCKLEY (1939), *On the Surface States Associated with a Periodic Potential*, *Physical Review*, **56**(4), 317.
- [117] W. SHOCKLEY AND W. T. READ (1952), *Statistics of the Recombinations of Holes and Electrons*, *Physical Review*, **87**(5), 835.
- [118] R. GREENE (1975), *Carrier scattering at elemental and compound semiconductor interfaces*, *Critical Reviews in Solid State and Materials Sciences*, **5**(3), 345.
- [119] A. DODABALAPUR, T. CHANG, B. TELL AND K. BROWN-GOEBELER (1992), *Growth of InAlAs/InGaAs and InGaAlAs/InGaAs heterojunction bipolar transistors on Si-implanted InP substrates by molecular beam epitaxy*, *Journal of Applied Physics*, **71**(5), 2449.
- [120] S. YAMAHATA, K. KURISHIMA, T. KOBAYASHI AND Y. MATSUOKA (1995), *InP/InGaAs collector-up heterojunction bipolar transistors fabricated using Fe-ion-implantation*, *Seventh International Conference on Indium Phosphide and Related Materials*, Hokkaido, Japan, 652–655.
- [121] G. WALKER AND E. CONWAY (1972), *Electrical Contacts to Ion Cleaned n-type Gallium Arsenide*, *IEEE Transactions on Parts, Hybrids and Packaging*, **8**(4), 49.
- [122] K. CHEUNG (2001), *Plasma Charging Damage*, 1st edition, Springer, New York.
- [123] J.-Z. YU, N. MASUI, Y. YUBA, K. GAMO, S. NAMBA, T. HARA, M. HAMAGAKI AND Y. AOYAGI (1989), *Induced defects in GaAs etched by low energy ions in electron beam excited plasma (EBEP) system*, *Japanese Journal of Applied Physics*, Part 1 (Regular Papers and Short Notes), **28**(11), 2391.
- [124] Z. DENG, R. KWOK, W. LAU AND L. CAO (1999), *Band gap state formation in InP (110) induced by 10 and 100 eV argon ion bombardment*, *Journal of Applied Physics*, **86**(7), 3676.
- [125] Q. ZHAO, Z. DENG, R. KWOK AND W. LAU (2000), *Damage of InP (110) induced by low energy Ar<sup>+</sup> and He<sup>+</sup> bombardment*, *Journal of Vacuum Science and Technology A*, **18**(5), 2271.
- [126] C. J. SANDROFF, M. S. HEGDE, L. A. FARROW, C. C. CHANG AND J. P. HARBISON (1989), *Electronic passivation of GaAs surfaces through the formation of arsenic-sulfur bonds*, *Applied Physics Letters*, **54**(4), 362.

- [127] M. CARPENTER, M. MELLOCH, M. LUNDSTROM AND S. TOBIN (1988), *Effects of  $Na_2S$  and  $(NH_4)_2S$  edge passivation treatments on the dark current-voltage characteristics of GaAs pn diodes*, Applied Physics Letters, **52**(25), 2157.
- [128] R. IYER, R. R. CHANG AND D. L. LILE (1988), *Sulfur as a surface passivation for InP*, Applied Physics Letters, **53**(2), 134.
- [129] R. IYER AND D. L. LILE (1991), *Role of polysulfides in the passivation of the InP surface*, Applied Physics Letters, **59**(4), 437.
- [130] S. GAYEN, W. C. ERMILER AND C. J. SANDROFF (1991), *Theoretical study of GaAs surface passivation with Se*, Journal of Chemical Physics, **94**(1), 729.
- [131] V. N. BESSOLOV, A. F. IVANKOV AND M. V. LEBEDEV (1995), *Sulfide passivation of III-V semiconductors: The starting electronic structure of a semiconductor as a factor in the interaction between its valence electrons and the sulfur ion*, Journal of Vacuum Science and Technology B, **13**(3), 1018.
- [132] V. N. BESSOLOV, M. V. LEBEDEV, N. M. BINH, M. FRIEDRICH AND D. R. T. ZAHN (1998), *Sulphide passivation of GaAs: the role of the sulphur chemical activity*, Semiconductor Science and Technology, **13**, 611.
- [133] ZHI-JIN, W. PROST, S. NEUMANN AND F. TEGUDE (2004), *Sulfur and low-temperature  $SiN_x$  passivation of self-aligned graded-base InGaAs/InP heterostructure bipolar transistors*, Journal of Vacuum Science and Technology B, **22**(3), 1060.
- [134] D. CAFFIN, L. BRICARD, J. COURANT, L. HOW KEE CHUN, B. LESCAUT, A. DUCHENOIS, M. MEGHELLI, J. L. BENCHIMOL AND P. LAUNAY (1997), *Passivation of InP-Based HBTs for High Bit Rate Circuit Applications*, 9th International Conference on Indium Phosphide and Related Materials, IEEE, 637–640.
- [135] C. BAEK, T. OH AND B. KANG (2005), *Effect of surface treatment on electrical properties of AlGaAs/GaAs heterojunction bipolar transistor*, Solid-State Electronics, **49**(8), 1335.
- [136] A. KAPILA, V. MALHOTRA, L. CAMNITZ, K. SEAWARD AND D. MARS (1995), *Passivation of GaAs surfaces and AlGaAs/GaAs heterojunction bipolar transistors using sulfide solutions and  $SiN_x$  overlayer*, Journal of Vacuum Science and Technology B (Microelectronics and Nanometer Structures), **13**(1), 10.
- [137] R. DRIAD, Z. H. LU, S. CHARBONNEAU, W. R. MCKINNON, S. LAFRAMBOISE, P. J. POOLE AND S. P. MCALISTER (1998), *Passivation of InGaAs surfaces and InGaAs/InP heterojunction bipolar transistors by sulfur treatment*, Applied Physics Letters, **73**(5), 665.
- [138] Z. JIN, S. NEUMANN, W. PROST AND F.-J. TEGUDE (2004), *Surface recombination mechanism in graded-base InGaAs-InP HBTs*, IEEE Transactions on Electron Devices, **51**(6), 1044.

- [139] H. MYERS (1997), *Introductory Solid State Physics*, 2nd edition, Taylor and Francis, London.
- [140] S. I. YI, C.-H. CHUNG AND W. H. WEINBERG (1997), *Dissociative adsorption of hydrogen sulfide on GaAs(100)-(2×4) and GaAs(100)-(4×2) surfaces*, *Journal of Vacuum Science and Technology A: Vacuum, Surfaces, and Films*, **15**(3 Pt 1), 1168.
- [141] C.-H. CHUNG, S. YI AND W. WEINBERG (1997), *Adsorption state of hydrogen sulfide on the GaAs (001)-(4×2) surface*, *Journal of Vacuum Science and Technology A*, **15**(3), 1163.
- [142] H. OIGAWA, J. FAN, Y. NANNICHI, K. ANDO, K. SAIKI AND A. KOMA (1988), *Stabilization of GaAs surface/interface by sulfur treatment*, 20th (1988 International) Conference on Solid State Devices and Materials, Tokyo, Japan, 263–266.
- [143] D. JILES (1998), *Introduction to Magnetism and Magnetic Materials*, 2nd edition, Chapman and Hall, London.
- [144] J. D. LIVINGSTON (1996), *Driving Force: The Natural Magic of Magnets*, Harvard University Press, Cambridge, Massachusetts.
- [145] B. TERRIS AND T. THOMSON (2005), *Nanofabricated and self-assembled magnetic structures as data storage media*, *Journal of Physics D (Applied Physics)*, **38**(12), 199.
- [146] J. HOWARD (1985), *Thin films for magnetic recording technology: a review*, *Journal of Vacuum Science and Technology A (Vacuum, Surfaces, and Films)*, **3**(3), 657.
- [147] R. DESIKAN, C. R. LEFURGY, S. W. KECKLER AND D. BURGER (2002), *On-chip MRAM as a High-Bandwidth, Low-Latency Replacement for DRAM Physical Memories*, Technical Report TR-02-47, Department of Computer Sciences, University of Texas at Austin.
- [148] T. M. MAFFITT, J. K. DEBROSSE, J. A. GABRIC, E. T. GOW, M. C. LAMOREY, J. S. PARENTEAU, D. R. WILLMOTT, M. A. WOOD AND W. J. GALLAGHER (2006), *Design considerations for MRAM*, *IBM Journal of Research and Development*, **50**(1), 25.
- [149] W. J. GALLAGHER AND S. S. P. PARKIN (2006), *Development of the magnetic tunnel junction MRAM at IBM: From first junctions to a 16-Mb MRAM demonstrator chip*, *IBM Journal of Research and Development*, **50**(1), 5.
- [150] C. BROWNLIE, S. MCVITIE, J. CHAPMAN AND C. WILKINSON (2006), *Lorentz microscopy studies of domain wall trap structures*, *Journal of Applied Physics*, **100**(3), 33902.

- [151] B. LYE, P. HOUSTON, C. BUTTON AND J. DAVID (1998), *Electrical and optical characterisation of heavily doped GaAs:C bases of heterojunction bipolar transistors*, Solid-State Electronics, **42**(1), 115.
- [152] A. S. SEDRA AND K. C. SMITH (1998), *Microelectronic Circuits*, 4th edition, Oxford University Press, New York.
- [153] M. KURATA, R. KATOH AND J. YOSHIDA (1985), *Ring oscillator circuit simulation with physical model for GaAs/GaAlAs heterojunction bipolar transistors*, IEEE Transactions on Electron Devices, **32**(6), 1086.